



universität  
wien

# DISSERTATION / DOCTORAL THESIS

Titel der Dissertation / Title of the Doctoral Thesis

Talbot-Lau Schemes and Bragg Diffraction: Theory and  
Applications in High-Mass Matter-Wave Interferometry

verfasst von / submitted by

Filip Bartłomiej Kiałka

angestrebter akademischer Grad / in partial fulfilment of the requirements for the degree of  
Doktor der Naturwissenschaften (Dr. rer. nat.)

Wien, 2021 / Vienna 2021

Studienkennzahl lt. Studienblatt /  
degree programme code as it appears on the  
student record sheet:

UA 796 605 411

Dissertationsgebiet lt. Studienblatt /  
field of study as it appears on the student  
record sheet:

Physik

Betreut von / Supervisor:

Univ.-Prof. Dr. Markus Arndt

Betreut von / Supervisor:

Prof. Dr. Klaus Hornberger  
(Universität Duisburg-Essen)



# Talbot-Lau Schemes and Bragg Diffraction: Theory and Applications in High-Mass Matter-Wave Interferometry

Der Fakultät für Physik  
der Universität Duisburg-Essen

vorgelegte Dissertation

zum Erwerb des akademischen Grades eines  
Doktors der Naturwissenschaft (Dr. rer. nat)

Filip Bartłomiej Kiałka  
aus Krapkowice, Polen

Wien, 2. März 2021

# Abstract

This thesis describes theoretical work carried out in connection with the high-mass matter-wave interference experiments at the University of Vienna. Its scope ranges from the simulation and analysis of experimental data to the proposal of a trapped interference scheme applicable to a variety of matter-wave platforms.

The first main result of the thesis is the phase-space description of a near-field interferometer with any number of gratings. This theory is used to analyze a four-grating Talbot-Lau interferometer, in which passive compensation of low-frequency vibrations and of the Coriolis force are expected. The compensation is numerically confirmed and its effectiveness is compared to existing techniques.

The second main result is the demonstration of Bragg diffraction of complex molecules on optical gratings, to which the author contributed the basic experimental design, simulations, and the interpretation of the data. This demonstration is a first step towards applying large momentum transfer coherent manipulation techniques to the interference of heavy molecules and clusters.

The third main result is a new interference scheme for matter waves in toroidal confinement. The beam splitting and recombination in this scheme rely on the free evolution in the waveguide and require no interaction with the matter waves. The scheme is within reach of state-of-the-art experiments with Bose-Einstein condensates, where it could be used to measure weak atom-atom interactions or magnetic field gradients.



## Zusammenfassung

Diese Dissertation beschreibt theoretische Arbeiten, die im Zusammenhang mit den Molekül-Interferenz-Experimenten an der Universität Wien durchgeführt wurden. Die erzielten Ergebnisse reichen von der Simulation und Analyse experimenteller Daten bis zum Vorschlag eines neuen Interferenzschemas für Atome und Moleküle in toroidalen Fallengeometrien.

Das erste Hauptergebnis der Arbeit ist die Phasenraumbeschreibung eines Nahfeldinterferometers mit einer beliebigen Anzahl von Gittern. Diese Theorie wird verwendet, um ein Talbot-Lau-Interferometer mit vier Gittern zu analysieren, bei dem eine passive Kompensation niederfrequenter Schwingungen und der Coriolis-Kraft erwartet wird. Die Kompensation wird numerisch bestätigt und ihre Effizienz mit bestehenden Techniken verglichen.

Das zweite Hauptergebnis ist die experimentelle Demonstration von Bragg-Beugung komplexer Moleküle an optischen Gittern, zu der der Autor das grundlegende experimentelle Design, Simulationen und die Interpretation der Daten beigetragen hat. Dieses Experiment stellt einen ersten Schritt in Richtung kohärenter Manipulationstechniken mit großem Impulsübertrag für schwere Moleküle und Cluster dar.

Das dritte Hauptergebnis ist ein neues Interferenzschema für Materiewellen in toroidalen Fallengeometrien. Die Erzeugung und Rekombination der Superposition erfolgt in diesem Schema durch die freie Zeitentwicklung im Wellenleiter und erfordert keine Wechselwirkung mit externen Feldern. Das Schema kann mit Bose-Einstein-Kondensaten realisiert werden und erlaubt, schwache Atom-Atom-Wechselwirkungen oder Magnetfeldgradienten zu messen.

# Contents

<b>Preface</b>	<b>ix</b>
<b>I Talbot-Lau interference</b>	<b>1</b>
<b>1 Introduction</b>	<b>3</b>
1.1 The Talbot and Lau effects . . . . .	4
1.2 Types of diffraction gratings . . . . .	7
1.3 Multi-loop interferometer schemes . . . . .	9
<b>2 Talbot-Lau interferometers with arbitrary number of gratings</b>	<b>11</b>
2.1 Interference pattern and signal . . . . .	11
2.2 Visibility and shift . . . . .	18
2.3 Graphical interpretation . . . . .	21
2.4 Classical description . . . . .	23
2.5 Applications . . . . .	25
2.6 Notes on implementation . . . . .	27
<b>3 The four-grating Talbot-Lau interferometer</b>	<b>33</b>
3.1 Visibility . . . . .	33
3.2 Transmission . . . . .	37
3.3 Vibration sensitivity . . . . .	38
3.4 Coriolis force compensation . . . . .	39
<b>4 Comparison of two- and three-grating interferometers</b>	<b>45</b>
4.1 Figure of merit . . . . .	45
4.2 Numerical optimization . . . . .	47
<b>5 Conclusions (Part I)</b>	<b>51</b>

<b>II Bragg diffraction and trapped interference</b>	<b>53</b>
<b>6 Introduction</b>	<b>55</b>
6.1 Bragg diffraction . . . . .	56
6.2 Trapped interference . . . . .	58
<b>7 Diffraction of point particles on optical lattices</b>	<b>59</b>
7.1 Problem formulation . . . . .	59
7.2 Analytic solution methods . . . . .	65
7.3 Numerical solution . . . . .	77
7.4 Classical dynamics . . . . .	77
<b>8 Demonstration of Bragg diffraction of massive molecules</b>	<b>81</b>
8.1 Experiment design . . . . .	81
8.2 Diffraction image simulation . . . . .	84
8.3 Experimental data and analysis . . . . .	88
<b>9 Talbot-Lau interference in toroidal traps</b>	<b>99</b>
9.1 Particle in a curved waveguide . . . . .	100
9.2 Interference scheme . . . . .	101
9.3 Imperfections . . . . .	106
9.4 Proposed realization with a BEC . . . . .	111
<b>10 Conclusions (Part II)</b>	<b>115</b>
<b>A Hamiltonians in comoving frames</b>	<b>119</b>
<b>B Theory of Talbot-Lau interference (inertial-frame description)</b>	<b>121</b>
<b>C Bragg approximation via adiabatic elimination</b>	<b>125</b>
<b>D Least-squares fitting of diffraction images</b>	<b>129</b>
<b>Bibliography</b>	<b>133</b>
<b>Reprints of selected publications</b>	<b>145</b>
Concepts for long-baseline high-mass matter-wave interferometry . .	147
Bragg diffraction of large organic molecules . . . . .	157
Orbital angular momentum interference of trapped matter waves . . .	167



# Preface

Autumn of 2011 was an exciting time to become a physicist. I remember Prof. Marek Demiański starting my first physics lecture by taking out the day's newspaper and holding it high for everyone to see. The front page read

FASTER-THAN-LIGHT NEUTRINOS BAFFLE PHYSICISTS.

“If this turns out to be true, you will have an amazing challenge to face”, he said. It did not, but I must admit I faced some amazing challenges nevertheless. Prophetically, it was on the same lecture that I first learned about the work of Markus Arndt: The fullerene diffraction experiment was given as an example of how far the reign of quantum mechanics can stretch. I remember the experiment (and the promise of viruses coming next) having quite an impact on me and my colleagues. The effect proved to last and made me join the extended group of Markus and Klaus in 2016.

Since then, I have worked in two great teams and become indebted to more people than I can realistically thank. Among them to my supervisors Klaus Hornberger and Markus Arndt, as well as to the entire Duisburg and Viennese groups and the administration. Special gratitude is due for those who had the patience to work with me directly. In addition to Markus and Klaus, this includes Ben, Yaakov, and the Calzone team of Christian, Ksenija, and Stephan. Taking a step back, I must thank Krzysztof Sobków and Prof. Andrzej Wysmołek, both of whom opened the right door for me at the right time. Here's to you, and to all those “I quit” emails I never sent!

Over on the other side of the dining hall was a chemistry table (...). I went over and said, *Do you mind if I join you?* They can't say no, so I started eating with them for a while. And I started asking, *What are the important problems of your field?* And after a week or so, *What important problems are you working on?* And after some more time I came in one day and said, *If what you are doing is not important, and if you don't think it is going to lead to something important, why are you at Bell Labs working on it?* I wasn't welcomed after that; I had to find somebody else to eat with!

R. Hamming [1]

# **Part I**

## **Talbot-Lau interference**





# Chapter 1

## Introduction

Matter-wave diffraction and interference are among the oldest experimentally established quantum phenomena. First observed for electrons in 1927 [2, 3], they predate unambiguous demonstrations of the particulate nature of light by nearly 50 years [4]. Since their discovery, matter-wave phenomena have only increased in importance and are now relevant for many areas of physics and technology. These areas range from laboratory tests of fundamental physics to gravitational-wave astronomy and geological prospecting or navigation [5, 6]. The relevance of matter-wave interferometry will continue to increase, fueled by recent achievements which have opened up new regimes of coherence time [7], particle mass [8], and precision [9, 10].

In this work, we will mostly focus on one of the frontiers of matter-wave interferometry: that of high particle mass. High-mass matter-wave interferometry has been pursued in Vienna starting with the seminal fullerene diffraction experiment in 1999 [11]. This line of research has since progressed through a number of increasingly challenging experiments [12, 13, 14], currently culminating in the interference of particles with masses exceeding<sup>1</sup> 25 000 Da [8]. In addition to the pursuit of record masses, high-mass interference experiments have been used for quantum-assisted metrology of atoms [15], fullerenes [16, 17], and biologically relevant molecules [18], for decoherence studies [19, 20], and more. The breadth of applications reflects the unique ability of high-mass interference experiments to delocalize particles virtually independently of their internal structure.

Current record-setting high-mass interference experiments are appreciably more complex than the paradigmatic double slit diffraction, both in terms of the experimental apparatus and its theoretical description. The qualitative jump occurred in 2002 with the shift from far-field, single-grating diffraction to

---

<sup>1</sup>Throughout the thesis, we will express masses in daltons (Da): a synonym of the unified atomic mass units (u), which has become standard in the literature of our subfield.

near-field diffraction in a three-grating Talbot-Lau interferometer (TLI) [12]. In high-mass interference, the TLI offers two key advantages over far-field setups: it has a higher mass acceptance for the same interferometer length and works with uncollimated beams of any width. The latter is important because creating intense beams of highly massive particles is challenging. The TLI configuration is still in use today<sup>2</sup>, although compared to the setup of 2002 a number of grating, source, and detection innovations have been made. The record-breaking Long-baseline Universal Matter-wave Interferometer (LUMI) additionally boasts an order-of-magnitude greater length.

In this thesis, we will investigate ways to go beyond the TLI setup as currently used. In this first part, we will largely restrict ourselves to the existing optical toolbox of high-mass matter-wave interferometry. That is, we only consider gratings and detection mechanisms which are either already in use or very likely to work. In particular, in Chapter 4 we will find the optimal two- and three-grating setups, intended as an upgrade of LUMI. In Chapter 3, we will investigate the benefits of departing from a three-grating TLI by introducing additional gratings. These phenomenological discussions build on Chapter 2, in which we systematically formulate the theory of a TLI with an arbitrary number, type, period, and spacing of gratings.

Before proceeding with the somewhat technical derivations of Chapter 2, we give a qualitative introduction to the physical phenomena at work in a TLI. We will discuss the single-grating Talbot effect and the double-grating Lau effect, as well as basic diffraction mechanisms. We do so to show the simple physics which is hardly discernible in the abstract phase-space treatment of Chapter 2. An understanding of the underlying physics pays off, as it allows us to apply the same elementary concepts in different ways. This is illustrated by the beam-splitter-free interference scheme of Chapter 9, which follows from an elementary description of the Talbot pattern produced by a phase grating.

## 1.1 The Talbot and Lau effects

The Talbot effect is the near-field self-imaging of a single diffraction grating [22], which can be described as follows. Consider a particle of mass  $m$ , whose initial state is given by a one-dimensional periodic wavefunction,

$$\psi(t = 0, x + d) = \psi(t = 0, x), \quad (1.1)$$

---

<sup>2</sup>In our group, the term TLI is reserved for an interferometer consisting of three mechanical gratings [21]. Here, we will refer to all Talbot-Lau-type interferometers as TLIs, irrespectively of the number and type of gratings.

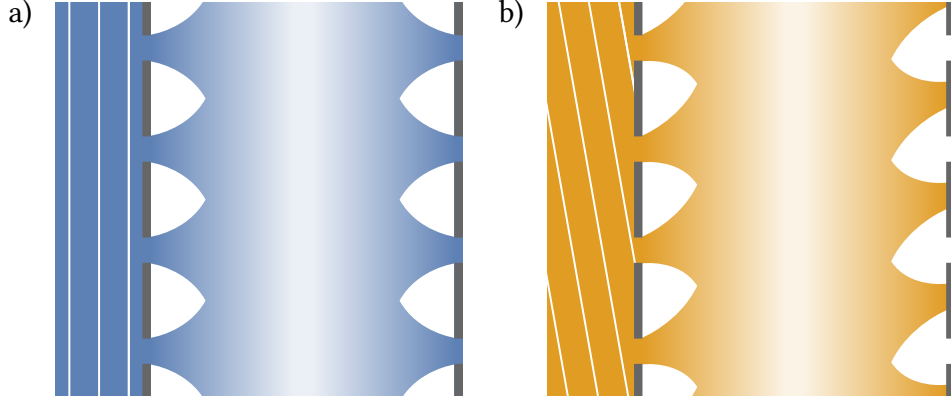


Figure 1.1: Illustration of the Talbot effect for plane-wave illumination at normal (a) and slanted (b) incidence. The two-grating Talbot-Lau setup shown transmits plane-wave components which produce Talbot patterns offset by integer multiples of the grating period. As a result, a high-contrast pattern is formed downstream of the second grating even when the original illumination is uncollimated.

where  $d$  is the period. Since the wavefunction is periodic, it can be decomposed in a Fourier series

$$\psi(t=0, x) = \sum_{j=-\infty}^{\infty} \psi_j e^{2\pi i j x / d}. \quad (1.2)$$

Assuming a free Hamiltonian  $H = -\hbar^2 \partial_x^2 / 2m$ , the time-evolution of  $\psi$  is

$$\psi(t, x) = \sum_{j=-\infty}^{\infty} \psi_j e^{2\pi i j x / d} \exp\left(-i \frac{\pi j^2 \hbar t}{m d^2}\right), \quad (1.3)$$

which is periodic in time (up to a spatial shift) with a period referred to as the Talbot time

$$T_T = \frac{m d^2}{\hbar}. \quad (1.4)$$

For we have

$$\psi(T_T, x) = \sum_{j=-\infty}^{\infty} \psi_j e^{2\pi i j x / d} \exp(-i \pi j^2) = \sum_{j=-\infty}^{\infty} \psi_j e^{2\pi i j x / d} \exp(-i \pi j) \quad (1.5a)$$

$$= \sum_{j=-\infty}^{\infty} \psi_j e^{2\pi i j (x - d/2) / d} = \psi\left(0, x - \frac{d}{2}\right). \quad (1.5b)$$

To observe the Talbot revivals, one has to prepare a space-periodic initial state. This can be done by illuminating a periodic structure (a diffraction grating

with period  $d$ ) with a plane wave at normal incidence. The case of non-normal incidence can be reduced to the normal-illumination case by moving to a reference frame comoving with the particle<sup>3</sup>. In the comoving frame, the state initially has no position dependence and becomes periodic upon traversing the grating (in this reference frame the grating is moving, but this does not spoil its space-periodicity). Therefore, Eq. (1.5) implies that revivals occur in the comoving frame. Back in the lab frame, this means that for non-normal incidence the revivals occur as they travel along the wavevector of the original illumination (see Fig. 1.1b). Crucially, this results in washing out of the Talbot pattern if the illumination is not collimated.

The collimation requirement can be relaxed thanks to the Lau effect [23, 24], which occurs when a second identical grating is placed at the location of the Talbot image. As shown in Fig. 1.1b, the second grating blocks the plane-wave components of the illumination which produce misaligned Talbot patterns. With those components filtered out, repeating the evolution for another Talbot time produces a high-contrast pattern. That is because the patterns produced by the transmitted plane-wave components align and add in intensity if the original illumination is incoherent. The two-grating Talbot-Lau setup creates a high-visibility pattern while conserving as much of the incoming particle flux as possible. In particular, it has a much higher transmission than a simple collimator consisting of two consecutive slits. Because of this, the Talbot-Lau setup is often used in combination with low-intensity sources, such as those in high-mass or in antimatter interference [25].

The two-grating Talbot-Lau setup is the simplest example of what we will refer to as a direct-detection TLI. In order to record the pattern produced by an interferometer of this type, the particles must be deposited on a surface and imaged with a microscope. Alternatively, the pattern can be detected by placing an additional grating in the plane of the self-image and moving it perpendicularly to the fringes. This repeatedly covers and uncovers the density maxima, producing an oscillating flux which is measured with a particle-counting detector. We will refer to setups employing this detection scheme as scanning-grating TLIs.

An important special case of the Talbot effect occurs when the phase of the initial state is periodic, but its modulus is constant. In this situation, the revival of the phase after multiples of the Talbot time does not result in a measurable intensity pattern. To see how a density modulation can arise in this case, one

---

<sup>3</sup>We review the problem of changing reference frames in quantum mechanics in Appendix A. For a particle with a transverse momentum component equal to  $p_0$ , the transformation referred to here is  $U(t) = \exp(ip_0 tp/\hbar m) \exp(-ip_0 x/\hbar) \exp(ip_0^2 t/2\hbar m)$ .

must consider the evolution (1.3) for  $T_T/2$ . Beginning as in Eq. (1.5), we obtain

$$\psi\left(\frac{T_T}{2}, x\right) = \sum_{j=-\infty}^{\infty} \psi_j e^{2\pi i j x/d} \exp\left(-\frac{i\pi j^2}{2}\right) = \sum_{\text{even } j} \psi_j e^{2\pi i j x/d} - i \sum_{\text{odd } j} \psi_j e^{2\pi i j x/d} \quad (1.6a)$$

$$= \frac{e^{-i\pi/4}}{\sqrt{2}} \left[ (1+i) \sum_{\text{even } j} \psi_j e^{2\pi i j x/d} + (1-i) \sum_{\text{odd } j} \psi_j e^{2\pi i j x/d} \right] \quad (1.6b)$$

$$= \frac{e^{-i\pi/4}}{\sqrt{2}} \left[ \psi(0, x) + i \sum_{j=-\infty}^{\infty} \psi_j e^{2\pi i j x/d} \exp(-i\pi j) \right] \quad (1.6c)$$

$$= \frac{e^{-i\pi/4}}{\sqrt{2}} \left[ \psi(0, x) + i \psi\left(0, x - \frac{d}{2}\right) \right] \quad (1.6d)$$

Therefore, if the initial state is  $\psi(0, x) = e^{i\phi(x)}$  for a real  $\phi(x)$ , we will have

$$\left| \psi\left(\frac{T_T}{2}, x\right) \right|^2 = \sin\left(\phi(x) - \phi\left(x - \frac{d}{2}\right)\right) + \text{const.} \quad (1.7)$$

In an appropriate parameter regime, a grating formed by a standing light wave will only imprint a phase onto the matter wave. If the grating is formed using a laser with wavelength  $\lambda = 2\pi/k$ , this phase will be  $\phi(x) = \phi_0 \cos^2(kx)$ , in which  $\phi_0$  is real [26]. Inserting this into Eq. (1.7) gives

$$\left| \psi\left(\frac{T_T}{2}, x\right) \right|^2 = \sin(\phi_0 \cos(2kx)) + \text{const.} \quad (1.8)$$

The above equation illustrates the mechanism of pattern formation in TLIs with optical phase gratings. However, the significance of Eq. (1.6) extends beyond conventional Talbot-Lau interferometry. We will show in Chapter 9 that the emergence of a balanced superposition at half the Talbot time could be used to perform a beam-splitter-free interferometric sequence.

## 1.2 Types of diffraction gratings

The theoretical approach of Chapter 2 does not require specifying the types of gratings used. In fact, it does not even require specifying whether the particle-grating interaction is treated using quantum or classical mechanics. Nevertheless, we give a brief overview of the possible grating choices here for the sake of concreteness and to set the stage for the more experimentally-focused Chapters 3 and 4.

High-mass interference experiments currently employ combinations of the three basic grating types: mechanical masks, optical phase gratings, and optical depletion gratings. The mechanical gratings in use today are typically silicon nitride membranes with evenly-spaced rectangular openings etched using a photolithographic process. The period of such gratings is typically in the few-hundred nanometer range. For example, the mechanical gratings of the LUMI experiment have a 266 nm period, and gratings with periods down to 100 nm have been used before [11]. Mechanical gratings are a simple way to obtain small periods and thus large grating momenta. However, their usefulness is limited by the dispersion forces acting between the particles and the walls of the slit. The particle-grating interaction leads to a strong dependence of the diffraction on the forward velocity of the particle. This washes out the interference pattern, because the moderate intensity of high-mass beam sources does not allow for strict velocity selection [27]. Additionally, in many cases the particles stick to and clog the grating, suppressing transmission completely [21]. For these reasons, mechanical gratings are being gradually replaced by optical ones in the interference of record-high masses.

Optical gratings for high-mass matter waves come in two basic types: those which only modulate the phase of the matter wave and those which additionally modulate the amplitude. Both types are usually realized using a standing wave of laser light. In both cases, the phase modulation is a result of the dipole-force interaction between the light and the particle. To additionally achieve amplitude modulation (in what is then referred to as an optical depletion grating), one must post-select particles which have or have not absorbed a photon. Photon absorption will happen preferentially at the antinodes of the standing light wave, providing a periodic amplitude modulation. The post-selection is easy if the particle is ionized or neutralized upon photon absorption, as then a simple electrode will separate the charge classes [14]. If the molecule fragments upon photon absorption, it can be discarded at the detection stage using a mass filter [28]. Because the probability of photon absorption and the phase of dipole interaction are functions of the light intensity, the period of a standing-wave optical grating will be equal to half of the laser wavelength. In the LUMI experiment, a 532 nm green standing light wave thus creates an optical phase grating with a period of 266 nm. Finally, the probability of photon absorption as well as the dipole interaction phase are inversely proportional to the interaction time with the grating. This makes the diffraction patterns produced by optical gratings velocity-dependent. However, the velocity dependence here is weaker than in the case of mechanical gratings, resulting in good compatibility with high-mass interference.

### 1.3 Multi-loop interferometer schemes

The basic experiment in matter-wave interferometry with atoms and neutrons is the far-field Mach-Zehnder interferometer. It consists of three gratings or pulses, whose role is to consecutively split, mirror, and recombine the wavepacket. By adding additional mirrors between the split and recombination stages, the geometry of the interferometer arms can be changed almost arbitrarily. By choosing the right geometry, the interferometer can be made selectively insensitive to rotation or external forces, as well as to a combination or gradients of the two [29, 30]. Such insensitive configurations typically involve the two arms undulating and crossing each other to form multiple loops of different sizes (in this terminology, a basic Mach-Zehnder interferometer would be a one-loop scheme).

The simplest example of such a multi-loop interferometer is the “two-loop”, “figure-eight”, or “butterfly” interferometer, in which the arms form two identical loops [31]. It consists of two beam splitters and two mirrors in each arm and is insensitive to uniform accelerations. It has found applications in atomic gyroscopes [32–34], gradiometers [35], in Stark shift measurements [36], and for vibration cancellation [37]. This and other multi-loop schemes have also been proposed for the detection of gravitational waves [38, 39] and for probing scalar dark matter [40]. On the opposite extreme from the two-loop interferometer, schemes with more than 50 loops have been demonstrated [41]. In general terms, such highly-undulating schemes trade sensitivity for bandwidth. That is, they are highly sensitive to signals oscillating at the frequency of the undulation while suppressing off-resonant signals. This is beneficial in some applications, as illustrated by the above examples.

In high-mass interference experiments, it would be desirable to tailor the properties of TLIs in the same way it is possible with multi-loop far-field schemes. In particular, a “two-loop” TLI setup could be useful for compensating low-frequency vibrations and the Coriolis force due to the rotation of the Earth, both of which pose a major challenge in high-mass interference experiments. However, it is not immediately clear how a near-field interferometer could form multiple loops. Unlike in a far-field setup, the free evolution in a TLI is typically far too short for the diffraction orders to separate in space and to form clearly visible interferometer arms. The lack of discernible arms and mirrors to manipulate them makes it difficult to draw a simple analogy between near- and far-field interferometers. This apparent difficulty is compounded by the usual intuitive description of a TLI. In it, each grating plays a qualitatively different role [21]: The first grating acts as an array of point sources to prepare coherence for the second grating, the second grating produces the Talbot pattern, and the third grating is used to detect it. From this perspective, it is not obvious what

would be the role of any additional gratings or where should they be placed.

In the next chapter, we show that multi-loop TLIs can be constructed in analogy to far-field setups and that they exhibit similar features as their far-field counterparts. Later, in Chapter 3, we discuss the two-loop near-field interferometer in detail.



## Chapter 2

# Talbot-Lau interferometers with arbitrary number of gratings

In this chapter, we expand the phase-space description of a TLI [26, 42] to accommodate any number of gratings with arbitrary periods and distances between them. Importantly, we will treat the evolution of the incident wavepacket in its (possibly noninertial) center-of-mass frame. This results in a description of near-field interference which closely resembles the treatments of far-field interferometers. This correspondence will allow us to conclude that multi-loop TLIs can be similarly effective in the compensation of external forces as their far-field counterparts. In addition to this, performing the calculations in the comoving frame results in significantly more compact derivations compared to the lab-frame description, which we present in Appendix B.

### 2.1 Interference pattern and signal

#### Hamiltonian in the comoving frame

We consider a particle of mass  $m$  flying along the  $z$  axis with velocity  $v$  and impinging on a series of  $k$  diffraction gratings. Since the particle's forward kinetic energy is much larger than the external and grating potentials typically involved, we will assume that the motion along the  $z$  axis is uniform and can be treated classically. We further assume that the bars of all gratings are aligned with the  $y$  axis well enough so that diffraction in this direction can be neglected and the motion treated classically. Motion along the  $x$  axis will be treated quantum-mechanically, assuming a Hamiltonian

$$H = \frac{p^2}{2m} - F(t)x, \quad (2.1)$$

in which  $F(t)$  is a possibly time-dependent, homogeneous external force.

The following calculations will be greatly simplified if we perform them in the reference frame comoving with the center of mass of the wavepacket. The latter follows the trajectory

$$\xi(t) = \frac{1}{m} \int_0^t dt' \int_0^{t'} dt'' F(t''). \quad (2.2)$$

We review the procedure of changing the reference frame in quantum mechanics in Appendix A. Using the transformation rules derived there, we find the unitary transformation to the comoving frame

$$U = \exp\left(\frac{i\xi(t)p}{\hbar}\right) \exp\left(-\frac{ix}{\hbar} \int_0^t dt' F(t')\right) \exp\left(\frac{i}{2m\hbar} \int_0^t dt' \left[\int_0^{t'} dt'' F(t'')\right]^2\right), \quad (2.3)$$

as well as the transformed Hamiltonian

$$H_{\text{cm}} = \frac{p^2}{2m}. \quad (2.4)$$

As expected, the Hamiltonian in the comoving frame is that of the free particle.

Calculations in the comoving frame are simpler but their results must be interpreted with caution. In the description of a typical experiment, the forward velocity spread in the beam cannot be neglected. To account for it, one averages the pattern derived for a fixed  $v$  by intensity over the velocity distribution. However, different velocity classes have different trajectories (2.2), and therefore the results obtained for them are with respect to different frames of reference. This means that results for different velocities cannot be directly compared or averaged, unless the quantity in question is frame-independent or is transformed back into the lab frame. The same precaution applies to any external parameters the force  $F$  might depend on, such as the voltage applied to a deflection electrode. When in doubt, we can compare the results obtained in the comoving frame with those from an inertial-frame calculation, presented in Appendix B.

## Transformations of the Wigner function

We will calculate the evolution of the transverse state  $\rho$  of the particle in the Wigner representation,

$$w(x, p) = \frac{1}{2\pi\hbar} \int ds e^{ips/\hbar} \left\langle x - \frac{s}{2} \left| \rho \right| x + \frac{s}{2} \right\rangle. \quad (2.5)$$

The primary benefit of using the Wigner function is the ease of computing the quantum and the classical predictions side by side and to the same level of approximation. We discuss this in more detail in Section 2.4. In addition to this, the phase-space formalism is also a natural starting point for including decoherence [42].

As a first step, we derive the transformations of the Wigner function induced by the gratings and by the free evolution between them. We will denote these transformations by  $GT_i$  and  $FF_i$ , respectively. To find  $FF_i$ , we note that the free evolution of the Wigner function is the same as that of a classical phase-space density [30]. That is,

$$(FF_i w)(x, p) = w(x', p'), \quad (2.6)$$

where  $x, p$  and  $x', p'$  are related by the classical equations of motion. For the free flight after the  $i$ -th grating, we have

$$x = x' + \frac{p'}{m} T_i, \quad (2.7a)$$

$$p = p', \quad (2.7b)$$

where  $T_i$  is the flight time. Expressing the primed coordinates on the right-hand side of Eq. (2.6) by  $x$  and  $p$  gives

$$(FF_i w)(x, p) = w\left(x - \frac{p}{m} T_i, p\right). \quad (2.8)$$

Diffraction at the  $i$ -th grating is described by a convolution

$$(GT_i w)(x, p) = \int dp_i K_i(x - \Delta x_i, p - p_i) w(x, p_i), \quad (2.9)$$

in which  $\Delta x_i$  is the position of the grating in the comoving frame and  $K_i$  is the transformation kernel. The latter is obtained from the transmission function  $t_i(x)$  of the grating as [26, 42]

$$K_i(x, p) = \frac{1}{2\pi\hbar} \int ds_i e^{ips_i/\hbar} t_i\left(x - \frac{s}{2}\right) t_i^*\left(x + \frac{s}{2}\right). \quad (2.10)$$

The  $x$ -periodic transmission kernel can be decomposed in a Fourier series,

$$K_i(x, p) = \frac{1}{2\pi\hbar} \sum_{n_i=-\infty}^{\infty} e^{2\pi i n_i x / d_i} \int ds_i e^{ips_i/\hbar} B_{n_i}^{(i)}\left(\frac{s_i}{d_i}\right), \quad (2.11)$$

where  $d_i$  is the period of the  $i$ -th grating and  $B_n^{(i)}$  are known as the Talbot coefficients. To express the latter in terms of the grating transmission function, we invert the decomposition (2.11),

$$B_n^{(i)}(\xi) = \frac{1}{d_i} \int_{-d_i/2}^{d_i/2} dx e^{-2\pi i n_i x / d_i} \int dp e^{-ip\xi d_i/\hbar} K_i(x, p). \quad (2.12)$$

We then substitute the definition (2.10) of the kernel, yielding

$$B_{n_i}^{(i)}(\xi) = \frac{1}{d_i} \int_{-d_i/2}^{d_i/2} dx e^{-2\pi i n_i x/d_i} t_i \left( x - \frac{\xi d_i}{2} \right) t_i^* \left( x + \frac{\xi d_i}{2} \right). \quad (2.13)$$

From Eq. (2.13) we infer the following properties of the Talbot coefficients, which will be useful in subsequent calculations,

$$B_{-n}(-\xi) = B_n^*(\xi), \quad (2.14a)$$

$$B_n^*(\xi) = B_n(\xi) \quad \text{when} \quad t(-x) = t(x), \quad (2.14b)$$

$$B_n(\xi + 1) = (-1)^n B_n(\xi), \quad (2.14c)$$

$$|t_i(x)|^2 = \sum_{n=-\infty}^{\infty} e^{2\pi i n x/d_i} B_n^{(i)}(0). \quad (2.14d)$$

## Derivation of the interference pattern

The initial state of the particle just in front of the first grating will be

$$w_0(x, p) = \frac{\theta(X_0/2 - |x|)}{X_0} D(p), \quad (2.15)$$

where  $\theta$  is the Heaviside theta,  $X_0$  is the width of the illuminated area, and  $D(p)$  is a distribution of the momenta in the particle beam. To calculate the state after  $k$  diffraction gratings and free flights, we must apply  $k$  compositions of the transformations  $GT_i$  and  $FF_i$  to the above state. A single composition of  $GT_i$  and  $FF_i$  takes the form

$$(FF_i GT_i w)(x, p) = \int dp_i K_i \left( x - \Delta x_i - \frac{p}{m} T_i, p - p_i \right) w \left( x - \frac{p}{m} T_i, p_i \right). \quad (2.16)$$

Applying the above transformation  $k$  times to  $w_0(x, p)$  and integrating over momentum to obtain the particle density gives

$$w_k(x) = \int dp (FF_k GT_k \dots FF_1 GT_1 w_0)(x, p) \quad (2.17a)$$

$$\begin{aligned} &= \frac{1}{X_0} \int dp dp_k K_k \left( x - \Delta x_k - \frac{p}{m} T_k, p - p_k \right) \\ &\quad \times \int dp_{k-1} K_{k-1} \left( x - \Delta x_{k-1} - \frac{p_k}{m} T_{k-1} - \frac{p}{m} T_k, p_k - p_{k-1} \right) \\ &\quad \times \dots \\ &\quad \times \int dp_1 K_1 \left( x - \Delta x_1 - \frac{p_2}{m} T_1 - \frac{p_3}{m} T_2 + \dots - \frac{p}{m} T_k, p_2 - p_1 \right) \\ &\quad \times \theta \left( \frac{X_0}{2} - \left| x - \frac{p_2}{m} T_1 - \frac{p_3}{m} T_2 - \dots - \frac{p}{m} T_k \right| \right) D(p_1). \end{aligned} \quad (2.17b)$$

We now expand the grating kernels in terms of Talbot coefficients using Eq. (2.11), obtaining

$$\begin{aligned}
w_k(x) = & \frac{1}{X_0} \frac{1}{(2\pi\hbar)^k} \sum_{n_1, \dots, n_k \in \mathbb{Z}} e^{i(\kappa x - \phi_k)} \\
& \times \int ds_k \dots ds_1 B_{n_1}^{(1)}\left(\frac{s_1}{d_1}\right) \dots B_{n_k}^{(k)}\left(\frac{s_k}{d_k}\right) \\
& \times \int dp \exp\left\{\frac{ip}{\hbar} \left(s_k - \frac{hT_k}{m} \left[\frac{n_1}{d_1} + \dots + \frac{n_k}{d_k}\right]\right)\right\} \\
& \times \int dp_k \exp\left\{\frac{ip_k}{\hbar} \left(-s_k + s_{k-1} - \frac{hT_{k-1}}{m} \left[\frac{n_1}{d_1} + \dots + \frac{n_{k-1}}{d_{k-1}}\right]\right)\right\} \\
& \times \dots \\
& \times \theta\left(\frac{X_0}{2} - \left|x - \frac{p_2}{m}T_1 - \frac{p_3}{m}T_2 - \dots - \frac{p}{m}T_k\right|\right) \int dp_1 e^{ip_1(-s_1)/\hbar} D(p_1). \quad (2.18)
\end{aligned}$$

In Eq. (2.18), we have introduced two quantities which depend on the integers  $n_1, \dots, n_k$  and characterize the terms in the summation. These are the wavenumbers

$$\kappa = \sum_{i=1}^k \frac{2\pi n_i}{d_i}, \quad (2.19)$$

and the phases

$$\phi_k = \sum_{i=1}^k \frac{2\pi n_i}{d_i} \Delta x_i. \quad (2.20)$$

To arrive at the final form of the pattern, we carry out the integrations in Eq. (2.18) starting from the innermost. For a broad beam<sup>1</sup>, the integrals over  $p_2, \dots, p$  can be approximated by Dirac deltas. This gives

$$w_k(x) = \frac{\theta(X_0/2 - |x|)}{X_0} \sum_{\kappa} e^{i\kappa x} P_{\kappa}, \quad (2.21a)$$

$$P_{\kappa} = \sum_{\frac{n_1}{d_1} + \dots + \frac{n_k}{d_k} = \frac{\kappa}{2\pi}} e^{-i\phi_k} B_{n_1}^{(1)}\left(\frac{s_1}{d_1}\right) \dots B_{n_k}^{(k)}\left(\frac{s_k}{d_k}\right) \tilde{D}(s_1), \quad (2.21b)$$

where

$$s_i = \frac{h}{m} \left[ T_i \left( \frac{n_1}{d_1} + \dots + \frac{n_i}{d_i} \right) + \dots + T_k \left( \frac{n_1}{d_1} + \dots + \frac{n_k}{d_k} \right) \right] \quad (2.22)$$

and  $\tilde{D}(s_1)$  is the Fourier transform of the initial momentum distribution,

$$\tilde{D}(s_1) = \int dp_1 e^{-ip_1 s_1/\hbar} D(p_1). \quad (2.23)$$

---

<sup>1</sup>Technically in the limit of infinite  $X_0$ .

Equation (2.21) gives the probability of detecting the particle at position  $x$  in the comoving frame and constitutes the final result for a direct-detection interferometer. We have grouped the terms in the summation by their wavenumbers, as in practice we are usually interested in the individual Fourier components  $P_\kappa$  of the pattern.

### Signal in a scanning-grating interferometer

Oftentimes the most practical way to detect the fringe pattern produced by a TLI is by means of a movable mask. To do this, an additional grating is placed in the plane of the interference pattern and scanned perpendicularly to the fringes. This repeatedly covers and uncovers the density maxima, producing an oscillating flux of particles which is measured and constitutes the signal. The latter is proportional to the transmission of the interferometer

$$I(x_S) = \int dx w_k(x) |t_{k+1}(x - \Delta x_{k+1} - x_S)|^2, \quad (2.24)$$

in which  $x_S$ ,  $\Delta x_{k+1}$ , and  $t_{k+1}(x)$  are respectively the position, offset, and the transmission function of the mask. Expanding  $|t_{k+1}(x)|$  and  $w_k(x)$  using Eqs. (2.14d) and (2.21a) gives

$$I(x_S) = \sum_{\kappa, n_{k+1}} \left( \frac{1}{X_0} \int_{-X_0/2}^{X_0/2} dx e^{i(\kappa + 2\pi n_{k+1}/d_{k+1})x} \right) e^{-2\pi i n_{k+1} x_S / d_{k+1}} B_{n_{k+1}}^{(k+1)}(0) \times e^{-2\pi i n_{k+1} \Delta x_{k+1} / d_{k+1}} P_\kappa. \quad (2.25)$$

For large  $X_0$ , the integral over  $x$  in Eq. (2.25) approximates a Dirac delta, imposing a constraint

$$\kappa + \frac{2\pi n_{k+1}}{d_{k+1}} = \sum_{i=1}^{k+1} \frac{2\pi n_i}{d_i} = 0. \quad (2.26)$$

We will refer to the above as the last-grating condition. It picks up those components of the pattern whose period is a unit fraction of the period of the detection mask. This ensures that the resulting signal has the periodicity of the last grating. In the same large  $X_0$  limit, the interference signal becomes

$$I(x_S) = \sum_{n_{k+1}=-\infty}^{\infty} e^{-2\pi i n_{k+1} x_S / d_{k+1}} I_{n_{k+1}}, \quad (2.27a)$$

$$I_{n_{k+1}} = \sum_{\frac{n_1}{d_1} + \dots + \frac{n_k}{d_k} = -\frac{n_{k+1}}{d_{k+1}}} e^{-i\phi_{k+1}} B_{n_1}^{(1)}\left(\frac{s_1}{d_1}\right) \dots B_{n_k}^{(k)}\left(\frac{s_k}{d_k}\right) B_{n_{k+1}}^{(k+1)}(0) \tilde{D}(s_1), \quad (2.27b)$$

where  $\phi_{k+1}$  is defined analogously as in Eq. (2.20).

## Uncollimated illumination and phase gratings

The expressions for the pattern and signal simplify if the initial beam is uncollimated, i.e., when  $D(p_0)$  is very wide. We can then approximate  $\tilde{D}(s_1)$  with a Dirac delta and thus omit it in Eqs. (2.21b) and (2.27b) for the interference pattern and signal. This requires restricting the summations in these equations to  $n_i$  satisfying

$$s_1 = \frac{h}{m} \sum_{i=1}^k \frac{n_i}{d_i} (T_i + \dots + T_k) = 0. \quad (2.28)$$

We will refer to the above as the uncollimated-illumination condition. As shown in Section 2.3, it has a straightforward graphical interpretation when the  $n_i$  are understood as diffraction orders.

When phase gratings are used in all inner positions ( $i = 2, \dots, k$ ), the averages  $P_0$  and  $I_0$  of the interference pattern and signal simplify to

$$P_0 = B_0^{(1)}(0)B_0^{(2)}(0) \dots B_0^{(k)}(0), \quad (2.29a)$$

$$I_0 = P_0 B_0^{(k+1)}(0). \quad (2.29b)$$

To see this, note that the Talbot coefficient  $B_{n_i}^{(i)}(0)$  of a perfectly transmissive grating is only nonzero for  $n_i = 0$  (see the property (2.14d)). Then,  $\kappa = 0$  implies  $s_k = 0$  via their definitions (2.19) and (2.22), and  $s_k = 0$  implies  $n_k = 0$  via the above property of  $B_{n_i}^{(i)}$ . This in turn means  $n_1/d_1 + \dots + n_{k-1}/d_{k-1} = 0$  as  $\kappa = 0$ , which gives  $s_{k-1} = 0$ , etc.

## Multi-loop TLIs

The Fourier components  $P_\kappa$  and  $I_{n_{k+1}}$  of the interference pattern and signal are sums indexed by as many integers  $n_i$  as the interferometer has gratings (see Eqs. (2.21b) and (2.27b)). For a given Fourier component, these indices have to satisfy the constraint (2.19) on  $\kappa$  and the uncollimated-illumination condition (2.28). In a scanning-grating interferometer, they must additionally fulfill the last-grating condition (2.26). This gives two linearly independent equations in the case of a direct-detection interferometer and three in the case of a scanning-grating one. As a result, two-grating direct-detection interferometers and three-grating scanning-mask ones are special. For them, the equations for  $n_i$  can have at most one solution, and the sums in Eqs. (2.21b) and (2.27b) for the Fourier components  $P_\kappa$  and  $I_{n_{k+1}}$  collapse to a single term. We will refer to those setups as single-loop TLIs.

Direct-detection interferometers with more than two-gratings and scanning-mask interferometers with more than three gratings will be referred to as multi-loop TLIs. In these setups, each Fourier component of the interference pattern

or signal is a sum of an a priori infinite number of terms. These terms interfere with each other, leading to a highly complicated dependence of the Fourier components  $P_\kappa$  and  $I_{n_{k+1}}$  on parameters such as the particle velocity. The presence of many terms<sup>2</sup> makes the treatment of multi-loop setups more subtle than that of single-loop TLLs and motivates the use of recoil diagrams, which we discuss in Section 2.3. In practice, the decay of the Talbot coefficients with increasing  $n$  means that usually considering a small number of low- $n$  terms is sufficient. We give an example of this in Chapter 3 when discussing the four-grating TLL.

## 2.2 Visibility and shift

### Monochromatic beam

The pattern or signal measured in an interference experiment is usually characterized by its visibility and spatial shift. To introduce these quantities in the case of the interference pattern, we rewrite the complex Fourier decomposition in Eq. (2.21a) as a real one:

$$w_\kappa(x) = \sum_{\kappa} e^{i\kappa x} P_\kappa = P_0 + \sum_{\kappa>0} 2|P_\kappa| \cos(\kappa x + \text{Arg } P_\kappa), \quad (2.30)$$

where for clarity we have neglected the finite extent of the pattern. To obtain Eq. (2.30), we have used that  $P_{-\kappa} = P_\kappa^*$ . To see the latter, note that changing the sign of  $\kappa$  is equivalent to changing the sign of all  $n_i$  which in turn changes the sign of  $s_i$  and of the  $\phi_k$  for every term. The former conjugates the Talbot coefficients via the property (2.14a), resulting in  $P_{-\kappa} = P_\kappa^*$ .

The sinusoidal visibility of interference fringes with a spatial frequency  $\kappa$  is defined as

$$V_\kappa = \left| \frac{2P_\kappa}{P_0} \right|, \quad (2.31)$$

In most cases, the magnitude of the Fourier components  $P_\kappa$  decreases quickly with increasing  $\kappa$  and all but one can be neglected. When this is the case, the modulation of the interference pattern is approximately sinusoidal and Eq. (2.31) is a good approximation of the interferometric visibility. If the assumption of a single dominating spatial frequency is not well satisfied, the sinusoidal visibility can still be measured, but may exceed unity.

The spatial shift of the interference pattern (2.30) is  $\text{Arg } P_\kappa$ . In a multi-loop scheme,  $P_\kappa$  will be a sum of multiple terms, each entering with a different phase

---

<sup>2</sup>From now on, the word *term* used without further specification will refer to terms in the sums in Eqs. (2.21b) and (2.27b) for the Fourier components  $P_\kappa$  and  $I_{n_{k+1}}$ .



(see Eq. (2.21b)). If the Talbot coefficients are real<sup>3</sup>, these phases will be equal to  $\phi_k$ , defined as in Eq. (2.20). To calculate the latter, we assume that the gratings are stationary in the lab frame. Their positions in the comoving frame are then determined by the center-of-mass trajectory (2.2), that is,

$$\Delta x_i = -\xi(T_1 + \dots + T_{i-1}) \quad (2.32)$$

and  $\Delta x_1 = 0$ . Inserting the positions (2.32) into the definition (2.20) of  $\phi_k$  gives the shifts of the terms with respect to the comoving frame. To transform them into the lab frame, we add the final position of the comoving frame, equal to the end point of the trajectory. This gives

$$\phi_k^{\text{lab}} = - \sum_{i=2}^k \frac{2\pi n_i}{d_i} \xi(T_1 + \dots + T_{i-1}) + \kappa \xi(T_1 + \dots + T_k), \quad (2.33)$$

where the wavenumber  $\kappa$  converts the frame's position to a phase shift.

The interference signal (2.27a) in a scanning-grating interferometer can be written as a real series analogously to Eq. (2.30). This motivates an expression for the sinusoidal visibility of the signal which is analogous to Eq. (2.31), but with the Fourier coefficients  $I_{n_{k+1}}, I_0$  in place of  $P_\kappa$  and  $P_0$ . To obtain the shifts of the terms contributing to the interference signal, we note that the latter is a frame-independent quantity. The shifts will therefore be given simply by the phases  $\phi_{k+1}$ , defined as in Eq. (2.20). Inserting the grating positions (2.32) into the latter gives

$$\phi_{k+1} = - \sum_{i=2}^{k+1} \frac{2\pi n_i}{d_i} \xi(T_1 + \dots + T_{i-1}). \quad (2.34)$$

For a scanning-grating interferometer, both the shift of the pattern and of the signal can be calculated. In order for the description to be consistent, these shifts must be equal for every term. To verify this, we substitute  $\kappa = -2\pi n_{k+1}/d_{k+1}$  from the last-grating condition (2.26) in the phases (2.33) of the pattern terms, obtaining the phases (2.34) of the signal terms.

As an additional verification, we use Eq. (2.34) to reproduce the shift of the interference signal in a three-grating, scanning-mask TLI. We assume equal periods  $d_i = d$  and  $T_1 = T$ ,  $T_2 = NT + \tau$ , where  $N$  is an integer and  $\tau$  is a small detuning. If the particles are subject to a constant external force  $F = ma$ , the center-of-mass trajectory is

$$\xi(T_1 + \dots + T_i) = \frac{a(T_1 + \dots + T_i)^2}{2}. \quad (2.35)$$

---

<sup>3</sup>This can usually be ensured by taking the grating transmission functions to be even (see property (2.14b)).

From the incoherent illumination and last-grating conditions, we have  $n_1 = -N$ ,  $n_2 = N + 1$ ,  $n_3 = -1$  for the lowest-frequency Fourier component  $L_1$ . Since this is a single-loop configuration, this is the only contributing term and the phase  $\phi_3$  from Eq. (2.34) is simultaneously the shift of the pattern. Using the above trajectory and  $n_i$  with Eq. (2.34) reproduces the known result [26]

$$\phi_3 = -\frac{\pi a}{d} [N(N+1)T^2 + 2(N+1)T\tau + \tau^2]. \quad (2.36)$$

As a final consistency check, we repeat the derivation of the interference pattern and signal in an inertial frame and show that the results agree with those obtained above. This is described in Appendix B.

## Velocity averaging

The visibilities and shifts introduced above depend on the forward velocity of the particle. As a result, they are not directly measurable unless the velocity distribution in the beam is extremely narrow or a velocity-resolving detection technique is used. What is accessible instead is the visibility and shift of the velocity-averaged pattern or signal. If we denote the distribution of the velocities in the beam by  $\rho(v)$ , the sinusoidal visibility of the averaged pattern is

$$\bar{V}_\kappa = \left| \frac{2 \int dv \rho(v) P_\kappa(v)}{\int dv \rho(v) P_0(v)} \right|, \quad (2.37)$$

and an analogous expression holds for the visibility of the averaged signal. We stress that in Eq. (2.37), the integration is inside the absolute value and the order of these operations can not be changed<sup>4</sup>. Furthermore, the transmission  $P_0$  or the average of the signal  $S_0$  are in general functions of velocity (for example due to velocity-dependent opening fractions of material gratings) and must be averaged as well.

To obtain the shift of the velocity-averaged pattern, we note that for an arbitrary real function  $f(v)$

$$\int dv f(v) \cos(\kappa x + \varphi(v)) = \text{Re} \left\{ e^{i\kappa x} \int dv f(v) e^{i\varphi(v)} \right\} = C \cos(\kappa x + \gamma), \quad (2.38)$$

where  $C e^{i\gamma} = \int dv f(v) e^{i\varphi(v)}$ ,  $C \in \mathbb{R}$ . Taking the velocity average of the pattern Eq. (2.30) and applying the above gives the shift of the averaged pattern,

$$\bar{\Phi}_\kappa = \text{Arg} \int dv \rho(v) P_\kappa(v). \quad (2.39)$$

---

<sup>4</sup>Averaging the visibility instead of taking the visibility of the averaged signal is the single most frequent source of inconsistencies between visibility calculations.

In a single-loop interferometer,  $P_\kappa$  collapses to a single term and we have  $P_\kappa = \exp(-i\phi_k^{\text{lab}})|P_\kappa|$ , in which the phase is given by Eq. (2.33) and the modulus is a product of Talbot coefficients (see Eq. (2.21b)). If the latter is approximately constant in the relevant velocity range, it factors out in Eq. (2.39) resulting in a simple expression for the shift of the averaged pattern,

$$\bar{\Phi}_\kappa = \text{Arg} \int dv \rho(v) \exp(-i\phi_k^{\text{lab}}(v)). \quad (2.40)$$

The shift of a velocity-averaged interference signal is obtained analogously.

Going beyond Eq. (2.40) and including the modulus  $|P_\kappa|$  can be problematic for light particles, for which the Talbot coefficients oscillate rapidly as a function of velocity<sup>5</sup>. These oscillations are caused by the arguments  $s_i/d_i$ , which are inversely proportional to the velocity and mass of the particle. The mean values of the Talbot coefficients vary slowly as a result of the velocity dependence of the grating transmission functions. To suppress the fast oscillations and facilitate numerical calculations, we can replace the Talbot coefficients  $B_n(\xi)$  with their one-period averages

$$\bar{B}_n(v) = \int_0^1 d\xi B_n(\xi), \quad (2.41)$$

where the right-hand side depends on  $v$  parametrically.

## 2.3 Graphical interpretation

It is instructive to visualize the terms contributing to the interference pattern or signal using recoil diagrams. To draw the latter, we treat the integers  $n_i$  as diffraction orders, resulting in momentum transfers of  $n_i h/d_i$  at the respective gratings. For every term, this allows us to draw a classical trajectory through the interferometer, as shown in Fig. 2.1. In such a diagram, the wavenumber  $\kappa$  of the term is proportional to the slope of the segment before the optional last grating. If the end of the trajectory is placed at the origin of the  $x$  axis, the  $s_i$  become the  $x$  coordinates of the intersections of the trajectory with the gratings. In particular, the uncollimated-illumination condition  $s_1 = 0$  then means that the trajectory and its  $x$ -mirrored partner form a closed loop. For terms which satisfy the last-grating condition (2.26), the trajectory extends beyond the last grating with a zero slope.

In addition to the above properties, we find that the area of a recoil diagram is proportional to the phase the corresponding term acquires as a result of constant

---

<sup>5</sup>For example, in a deflection measurement with barium atoms in LUMI, the Talbot coefficient of the second grating oscillates between zero and a finite value up to 400 times over the relevant velocity range of  $200 \text{ m s}^{-1}$  to  $700 \text{ m s}^{-1}$ .

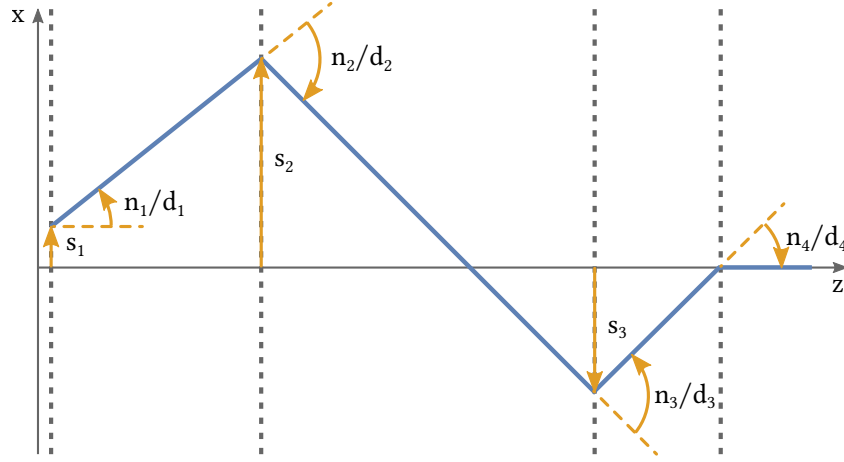


Figure 2.1: In both the quantum and the classical description of a near-field interferometer, the fringe pattern can be obtained by summing contributions corresponding to classical particle trajectories. Each of the latter is described by a series of diffraction orders  $n_i$ , which together with the ratios of grating periods  $d_i$  define a recoil diagram, as shown above.

acceleration. To see this, note that diffraction at the  $i$ -th grating contributes to the (signed) area of the recoil diagram like a triangle of base  $n_i h(T_i + \dots + T_k)/d_i m$  and height  $v(T_i + \dots + T_k)$ . Adding up contributions from all gratings gives the area enclosed by the diagram with respect to a centerline passing through the origin of the trajectory. If the diagram is not closed ( $s_1 \neq 0$ ), a more natural choice of the centerline is the one located symmetrically between the trajectory's start and end points. Shifting the centerline from the origin to the center of the diagram subtracts the area of the rectangle  $s_1 v(T_1 + \dots + T_k)$ . With this correction, the area of the trajectory becomes

$$A = \sum_{i=1}^k \frac{n_i h v}{2 d_i m} (T_i + \dots + T_k)^2 - s_1 v(T_1 + \dots + T_k). \quad (2.42)$$

We now show that the phase (2.33) of a pattern term in the case of constant acceleration  $a$  is proportional to the area (2.42). To do this, we first substitute the accelerating trajectory (2.35) and the definition (2.19) of  $\kappa$  into  $\phi_k^{\text{lab}}$ . We then transform the resulting expression, obtaining

$$\phi_k^{\text{lab}} = \pi a \sum_{i=1}^k \frac{n_i}{d_i} [(T_1 + \dots + T_k)^2 - (T_1 + \dots + T_{i-1})^2] \quad (2.43a)$$

$$= \pi a \sum_{i=1}^k \frac{n_i}{d_i} (T_i + \dots + T_k) [2(T_1 + \dots + T_k) - (T_i + \dots + T_k)] = -\frac{am}{\hbar v} A. \quad (2.43b)$$

The introduction of recoil diagrams makes the phase-space description of near-field interferometers under incoherent illumination analogous to the treatment of far-field interferometers. In particular, the classical trajectories in a recoil diagram and its  $x$ -mirrored partner correspond closely to the arms of a far-field interferometer. In both cases, the interference pattern arises at the intersection of the trajectories or arms and its period is inversely proportional to the intersection angle<sup>6</sup>. Furthermore, the shift of the pattern thus produced is given by the same phase (2.20) (cf. Eq. (5) in Ref. [43]), which for a constant external force is proportional to the signed area enclosed by the arms. Because the shifts are equal, we expect multi-loop TLIs (on the level of individual terms) to be as effective as their far-field counterparts in the compensation of external forces and their gradients. We give a concrete example of this in Chapter 3 by considering the four-grating, “two-loop” TLI.

In addition to their conceptual significance, the recoil diagrams have a number of direct applications. They allow us to find promising interferometer schemes given any set of grating periods, as viable schemes will tend to have closed loops utilizing small diffraction orders. We can also use them to find ways to detune an interferometer so as to suppress terms with undesirable properties, as discussed in Section 3.1.

## 2.4 Classical description

An important qualitative difference between far- and near-field interferometers is that the observation of fringes in the latter does not necessarily prove the wave nature of the particles involved. An extreme example is obtained by sending the distances between all the interferometer elements (the diffraction gratings and the detector) to zero. In this limiting case, one would necessarily observe fringes for classical and quantum particles alike, being just a shadow of the diffraction gratings. To rule out a classical shadow, a pattern obtained in a near-field interferometer must be compared to the one predicted by classical mechanics. Only when the observed pattern is stronger than what can be classically explained, one can claim to have demonstrated a quantum superposition.

Fortunately, the classical prediction can be obtained analogously to the quantum one. The only differences are the use of a classical phase-space density in place of the Wigner function and the substitution of the grating kernel

---

<sup>6</sup>The period is inversely proportional to the difference of the transverse momentum components of the interfering beams, which is proportional to their intersection angle when the latter is small.

in Eq. (2.9) by a classical one. The classical kernel is [26]

$$K'(x, p) = |t(x)|^2 \delta\left(p + \int_{-\infty}^{\infty} dt \frac{\partial V(t, x)}{\partial x}\right), \quad (2.44)$$

in which  $\delta$  is a Dirac delta,  $V(t, x)$  is the grating potential experienced by the particle, and  $t(x)$  is the transmission function of the grating. The  $|t(x)|^2$  term in Eq. (2.44) masks the classical distribution with the transmission of the grating, while the Dirac delta shifts it in momentum by the value of the classical impulse. The use of a classical distribution function instead of a Wigner function requires no further changes. In particular, the initial state (2.15) just in front of the first grating stays the same as we assume no initial coherence in the beam. Obtaining the classical prediction is therefore as easy as substituting the kernel (and thus the Talbot coefficients) in Eqs. (2.21b) and (2.27b). The ease of obtaining the classical prediction is one of the key advantages of the phase-space description of near-field matter-wave interference.

The classical Talbot coefficients are defined analogously as the quantum ones in Eq. (2.12), but using the classical kernel  $K'$  in place of the quantum  $K$ . Their derivation for different types of gratings can be found in Ref. [26]. Here we only review one property of these coefficients which will be useful later. For classical Talbot coefficient  $C_n$  corresponding to the quantum  $B_n$ , we have

$$C_n(0) = B_n(0). \quad (2.45)$$

This follows from the definitions (2.10) and (2.44) of the kernels, from which we get

$$B_n(0) = \frac{1}{d_i} \int_{-d_i/2}^{d_i/2} dx e^{-2\pi i n_i x / d_i} \int dp K(x, p) = \frac{1}{d_i} \int_{-d_i/2}^{d_i/2} dx e^{-2\pi i n_i x / d_i} |t(x)|^2 \quad (2.46a)$$

$$= \frac{1}{d_i} \int_{-d_i/2}^{d_i/2} dx e^{-2\pi i n_i x / d_i} \int dp K'(x, p) = C_n(0). \quad (2.46b)$$

The property (2.45) is the formal statement of the zero-spacings limit invoked at the beginning of this section. To see this, note that from the definition (2.22) of  $s_i$  we have that the arguments of the Talbot coefficients in the expressions (2.21b) and (2.27b) approach zero when the interferometer length vanishes. Combined with Eq. (2.45), this implies that in the zero-spacings limit the quantum and the classical predictions coincide.

## 2.5 Applications

### Vibration sensitivity

The effect of vibrations on an interferometer depends on their frequency, mode, and on the observable in question. Drifts slower than the integration time<sup>7</sup> do not diminish the visibility of the interference pattern. They can nevertheless affect deflection measurements, for which the phase stability of the pattern is necessary. Vibrations faster than the integration time will in general lead to visibility loss, which is treated in two limiting cases below.

The first case is that of independent translational grating vibrations, which we describe following Ref. [21]. We take the grating positions to be

$$\Delta x_i = A_i \sin(\varphi_i), \quad (2.47)$$

in which  $A_i, \varphi_i$  are the amplitude and phase of the vibration of the grating  $i$ . Inserting these positions into the phase (2.20) gives the instantaneous spatial shifts of the terms of the interference pattern or signal. We then average the latter over the random phases  $\varphi_1, \dots, \varphi_l$ , where  $l$  is the number of gratings including the optional mask. In this way, we find that each term in the expansion of the interference pattern or signal is suppressed by a factor

$$R = \frac{1}{(2\pi)^l} \prod_{i=1}^l \int_0^{2\pi} d\varphi_i \exp\left\{ \frac{2\pi i n_i A_i \sin(\varphi_i)}{d_i} \right\} = \prod_{i=1}^l J_0\left( \frac{2\pi n_i}{d_i} A_i \right), \quad (2.48)$$

in which  $J_0$  is the zeroth-order Bessel function of the first kind.

An opposite extreme is the case of phase-stable, common-mode translational grating vibrations with frequency  $\omega$ . In this case the grating shifts are

$$\Delta x_i = A \sin(\omega[T_1 + \dots + T_{i-1}] + \varphi). \quad (2.49)$$

The term-dependent suppression factor is then

$$R = \frac{1}{2\pi} \int_0^{2\pi} d\varphi \exp\left\{ 2\pi i A \sum_{i=1}^l \frac{n_i}{d_i} \sin(\omega[T_1 + \dots + T_{i-1}] + \varphi) \right\} \quad (2.50a)$$

$$= J_0\left( 2\pi A \sqrt{\sum_{i=1}^l \left(\frac{n_i}{d_i}\right)^2 + 2 \sum_{i<j} \frac{n_i n_j}{d_i d_j} \cos(\omega[T_i + \dots + T_{j-1}])} \right). \quad (2.50b)$$

Unlike in the case of independent grating vibrations, the suppression factor (2.50b) depends on the particle velocity (via the flight times  $T_i$ ). As a result,

---

<sup>7</sup>In the LUMI experiment, the integration time is typically a few seconds.

one must know the velocity dependence of the pattern or signal terms in order to calculate the total visibility loss for a velocity-averaged pattern or signal. This requires specifying the types and parameters of all gratings in the interferometer. However, an approximate visibility reduction can be calculated given only the velocity distribution if we neglect the dependence of the pattern or signal terms on the velocity. One can then simply average the suppression factor (2.50b) with the velocity distribution in the beam. This is justified when the vibration-free pattern or signal is approximately constant in the relevant velocity range.

### Coriolis force compensation

Observing high-mass interference in a long-baseline horizontal setup such as LUMI would not be possible without compensating the Coriolis force due to the rotation of the Earth. In LUMI, the compensation is achieved by means of a constant grating roll [44]. Tilting the gratings away from vertical introduces a small gravitational acceleration component in the plane of diffraction, which can be used to compensate other forces acting on the particle. Compensation of the Coriolis force achieved in this way is not exact, because the latter force is velocity-dependent while gravity is not. It is nevertheless good enough to recover close to maximum contrast in many practical situations (see Ref. [44] and Section 3.4).

The technique generalizes straightforwardly to a multi-loop interferometer. For a constant acceleration  $a$ , the shifts (2.33) of the pattern terms are proportional to  $a/v^2$ , where  $v$  is the velocity of the particle. To find the grating roll  $\theta$  which makes the shifts stationary as a function of velocity, we note that

$$\partial_v \phi_k^{\text{lab}} \propto \partial_v \left( \frac{a}{v^2} \right) = \partial_v \left( \frac{g \sin \theta - 2\Omega_y v}{v^2} \right) = \frac{2}{v^2} \left( \Omega_y - \frac{g \sin \theta}{v} \right), \quad (2.51)$$

where  $-2\Omega_y v$  is the  $x$  component of the Coriolis acceleration and  $\Omega_y$  is the vertical<sup>8</sup> (in the lab frame) component of the Earth's angular velocity. The component of the angular velocity lying in the plane of the interferometer results in a Coriolis force acting along the grating bars and thus can be neglected. Setting the expression (2.51) to zero gives the optimal roll angle  $\theta_v$  for Coriolis-force compensation at velocity  $v$ ,

$$\sin \theta_v = \frac{\Omega_y v}{g}. \quad (2.52)$$

---

<sup>8</sup>Strictly speaking, one should take here the component parallel to the grating bars, but since the resulting roll angle will be small, the vertical component is a good approximation.



Assuming optimal compensation at velocity  $v_0$ , the shift (2.33) of a pattern term becomes

$$\phi_k^{\text{lab}} = -\frac{\Omega_y(v_0 - 2v)}{2v^2} \left[ \sum_{i=2}^k \frac{2\pi n_i}{d_i} (L_1 + \dots + L_{i-1})^2 - \kappa (L_1 + \dots + L_k)^2 \right], \quad (2.53)$$

where  $L_i = T_i/v$  are the distances between the gratings. Equation (2.53) captures the imperfect nature of the compensation and allows us to see when the technique is likely to become insufficient. We discuss this in further detail in Section 3.4 when analyzing the four-grating TLI.

## 2.6 Notes on implementation

In order to make quantitative predictions using the theory presented in this chapter, one has to implement it in software for numeric or symbolic calculations. In this section we present some guidance on how to do so, based on the experience of having implemented the formalism as a MATHEMATICA package. Some parts of the following discussion are also relevant for back of the envelope calculations (especially the following subsection) or for understanding the occasional discrepancies with previous results.

### Dimensionless parameters and similarity

The first step in making the formalism of this chapter suitable for numeric or symbolic computation is moving to dimensionless quantities<sup>9</sup>. The interferometer properties we want to calculate, such as visibility or transmission, are dimensionless themselves. That means they must be functions of dimensionless parameters only [45]. Identifying those parameters has advantages beyond making the problem amenable to machine computation. Most importantly, it allows us to identify equivalent (or similar in the language of dimensional analysis) combinations of dimensionful parameters. Simple examples of equivalent parameter combinations include those in which the power of a laser grating varies in proportion to its vertical radius. All these combinations will have the same peak light intensity in the grating and will (within the approximations we use) result in identical interferometer performance. Identifying a complete set of dimensionless parameters is a way to find all such equivalence relations. It will also allow us to quickly tell which experimental parameters have to change

---

<sup>9</sup>An adept of MATHEMATICA might argue that the latter can now integrate dimensionful quantities and will even update the units correctly. A veteran will know that this is nowhere near reliable enough for a project as big as this.

and how in order to accommodate, for example, an increase in particle mass. Finally, knowing all the dimensionless parameters gives us an overview of which physical mechanisms in the interferometer are affected by which experimental parameters and to what extent.

To find a complete set of dimensionless parameters<sup>10</sup>, we inspect the quantities appearing in Eq. (2.37) for the visibility of the velocity-averaged pattern and gather all dimensionful quantities into dimensionless groups. A complete set of dimensionless parameters obtained in this way is shown in Table 2.1. These parameters together determine all the dimensionless properties of an interferometer.

### Finding the term indices $n_i$

The first step in the calculation of the interference pattern or signal is finding the sets of  $n_i$  which define the terms in Eqs. (2.21b) and (2.27b). This is done by solving the uncollimated-illumination and last-grating conditions (2.26) and (2.28) with a constraint  $\kappa \geq 0$ . The latter is used to exclude terms which differ only by an overall sign, as the factor of 2 in the formula for visibility already accounts for those. Additionally, a constraint on the magnitude of  $n_i$  must be included in order to obtain a finite number of solutions. The resulting equations and constraints can be solved easily using a symbolic computation package, for example with `Solve` in `MATHEMATICA`. We group the terms found in this way by their wavenumbers  $\kappa$  and usually restrict our attention to those with the lowest value<sup>11</sup>. To ensure that we have included all the relevant terms, we add more by increasing the constraint on the magnitude of  $n_i$  until the quantities of interest no longer change.

### Talbot coefficients

The Talbot coefficients are best taken from Ref. [26] or later sources in order to avoid the sign error found in earlier publications in the  $B_n$  of optical phase gratings with absorption. This error is discussed in Ref. [26] (p. 98) and is sometimes the reason for discrepancy with older visibility calculations. Another common reason for discrepancies is neglecting the velocity dependence of the phase  $\phi_0$  imprinted at the antinode of an optical grating.

In contrast to the analytic Talbot coefficients for optical gratings, the full coefficients for mechanical gratings can only be obtained numerically. The

<sup>10</sup>We say parameter, because there is also a dimensionless variable,  $v/v_0$  which is integrated over and does not enter the final result.

<sup>11</sup>In general, the smallest  $\kappa$  is not known in advance, and thus we cannot directly solve for the terms corresponding to it.

Quantity	Measures	Appears in
$\frac{d_i}{d}$	Ratios of grating periods. $d$ is a length scale associated with the grating period, such as the smallest or the average period.	The last-grating condition (2.26) and the uncollimated-illumination condition (2.28).
$\frac{L_i}{L}$	Ratios of distances between the gratings. $L$ is a length scale such as the total interferometer length or the smallest of the distances between the gratings.	As above.
$\frac{Lh}{v_0 m d^2}$	Interferometer length. $v_0$ is the most probable particle velocity. This is proportional to the ratio of the interferometer length to the Talbot length $v_0 T_T$ .	Arguments of Talbot coefficients, all grating types.
$\frac{\Delta v}{v_0}$	Velocity spread. $\Delta v$ is any linear measure of variation, such as standard deviation.	Distribution of velocities in the beam.
$\frac{\Omega_y L^2}{v_0 d}$	Interferometer rotation. This is proportional to the displacement of the gratings as a result of rotation during the transit of a particle through the interferometer.	Phase shift (2.53) due to the Coriolis force.
$f$	Nominal opening fraction of a mechanical grating.	Talbot coefficients of mechanical gratings.
$\frac{h c \alpha' b^2}{v_0^2 m d^6}$	Mechanical grating thickness. $\alpha'$ is the polarizability volume of the particle and $b$ is the thickness of the grating.	Effective opening fraction of a mechanical grating using Eq. (2.55) (see Page 30).
$\frac{\alpha' P}{h c v_0 w_y}$	Phase modulation. $P$ and $w_y$ are power and vertical size of the optical grating.	Talbot coefficients of optical gratings.
$\frac{\sigma \lambda}{\alpha'}$	Absorption cross section. $\lambda$ is the wavelength of the grating laser and $\sigma$ is the absorption cross-section. This is proportional to the ratio of the average number of absorbed photons to the dipole-force phase. Cf. $\beta$ in Ref. [26].	Talbot coefficients of optical depletion gratings and of optical phase gratings with absorption.

Table 2.1: Dimensionless parameters of a TLI with mechanical or optical gratings and in the presence of the Coriolis force. To obtain a complete set of dimensionless groups, the last four quantities must be included multiple times if they are different for different gratings. Note that a different result for the mechanical grating thickness would follow from Eq. (2.58).

knowledge how to do it is rather fragmented in the literature, we therefore provide a quick summary here. The first step is estimating the effective opening fraction, which can be done in two ways. In both approaches, the effective opening fraction has the form

$$f' = f - \frac{2x_c}{d}, \quad (2.54)$$

where  $x_c$  is a critical impact parameter such that the particle will not be detected if it enters the grating closer than  $x_c$  to the slit wall. The two methods differ in how  $x_c$  is obtained.

The first method takes  $x_c$  as the impact parameter below which the classical trajectory of the particle hits the grating bar. For a grating with thickness  $b$  interacting with the particle via the retarded Casimir-Polder potential<sup>12</sup>  $V(x) = -C_4x^{-4}$ , this distance is given by [47]

$$x_c = \left( \frac{18b^2C_4}{mv^2} \right)^{1/6}. \quad (2.55)$$

A possible shortcoming of this method is that the deflection of molecules which barely escape collision with the grating will be quite strong. In most cases strong enough for them to miss the detector at the end of the interferometer. This means that Eq. (2.55) most likely underestimates the effective critical distance.

A way to address this is to set  $x_c$  equal to a distance below which particle deflection exceeds a maximum detectable angle  $\theta_c$ . To do this, one estimates the deflection upon grating transit as [48]

$$\theta \approx -\frac{V'(x)b}{mv^2}, \quad (2.56)$$

which is a good approximation as long as the higher-order term is negligible; that is,

$$\frac{V''(x)v^2m - [V'(x)]^2}{6m^2v^2} \left( \frac{b}{v} \right)^2 \ll 1. \quad (2.57)$$

Using the same Casimir-Polder potential then gives

$$x_c = \left( \frac{4bC_4}{mv^2\theta_c} \right)^{1/5}. \quad (2.58)$$

---

<sup>12</sup>The strongly retarded form of the Casimir-Polder potential is valid for distances much larger than the particle's largest resonant excitation wavelength [46]. It proved sufficient for describing the diffraction of fullerenes on gratings with a 991 nm period [27], but must be used with caution for smaller periods and for particles with larger polarizability.

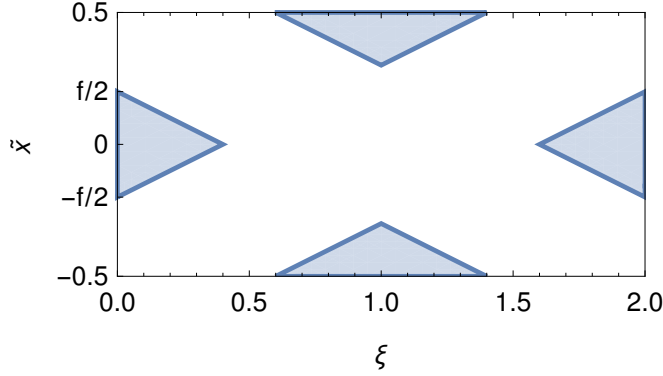


Figure 2.2: For a material grating with opening fraction  $f$ , the integrand in Eq. (2.61) is only nonzero within the shaded regions.

By design, the latter will usually give a larger cutoff distance and thus a smaller opening fraction than Eq. (2.55).

For easy reference, we include the  $C_4$  constant as found in Ref. [46], p. 180.

$$C_4 = \frac{3\hbar c\alpha'}{16\pi} \int_1^\infty dv \left[ \left( \frac{2}{v^2} - \frac{1}{v^4} \right) \frac{\varepsilon v - \sqrt{\varepsilon\mu - 1 + v^2}}{\varepsilon v + \sqrt{\varepsilon\mu - 1 + v^2}} - \frac{1}{v^4} \frac{\mu v - \sqrt{\varepsilon\mu - 1 + v^2}}{\mu v + \sqrt{\varepsilon\mu - 1 + v^2}} \right], \quad (2.59)$$

where  $\varepsilon$  and  $\mu$  are static electric and magnetic relative permittivities of the grating material, and  $\alpha'$  is the polarizability volume of the particle. The latter is a SI quantity expressing the proportionality between the dipole moment  $\boldsymbol{\mu}$  induced by an electric field  $\boldsymbol{E}$  as [49]

$$\boldsymbol{\mu} = 4\pi\varepsilon_0\alpha'\boldsymbol{E}. \quad (2.60)$$

The permittivity integral in Eq. (2.59) is sometimes omitted in applications. To give an idea of the resulting error, we note that if one takes  $\mu = 1$  and  $\varepsilon = 7.5$  for silicon nitride, the integral evaluates to about 1.2.

The effective opening fraction determines the Talbot coefficient at zero argument via  $B_n(0) = f' \operatorname{sinc}(\pi n f')$  [26]. This is all that is needed if the mechanical grating is used in the first or last positions. If it is used in the middle, the full Talbot coefficients need to be obtained via numerical integration. This is done starting from the definition (2.13) of  $B_n$  by noting that for even  $t(x)$  the integrand is hermitian. The latter allows us to restrict the integration to positive  $\tilde{x} = x/d$ ,

$$B_n(\xi) = 2 \operatorname{Re} \int_0^{1/2} d\tilde{x} e^{-2\pi i n \tilde{x}} t\left(\tilde{x} - \frac{\xi}{2}\right) t^*\left(\tilde{x} + \frac{\xi}{2}\right). \quad (2.61)$$

For  $f' < 1/2$ , expressing  $t(x)$  in the eikonal approximation [26] and noting that the integrand is only nonzero in the regions shown in Fig. 2.2 gives

$$B_n(\xi) = 2 \operatorname{Re} \int_0^{(f'-\xi)/2} d\tilde{x} \exp \left\{ -2\pi i n \tilde{x} - \frac{ibC_4}{\hbar v} \left[ \left( \frac{f'}{2} - \tilde{x} + \frac{\xi}{2} \right)^{-4} + \left( \frac{f'}{2} + \tilde{x} - \frac{\xi}{2} \right)^{-4} - \left( \frac{f'}{2} - \tilde{x} - \frac{\xi}{2} \right)^{-4} - \left( \frac{f'}{2} + \tilde{x} + \frac{\xi}{2} \right)^{-4} \right] \right\} \quad (2.62)$$

when  $\xi \in [0, f']$  or  $\xi \in [1-f', 1]$ , otherwise  $B_n(\xi) = 0$ . For all  $\xi$  outside of the  $[0, 1]$  interval, the coefficient is then obtained using the periodicity property (2.14c).

## Chapter 3

# The four-grating Talbot-Lau interferometer

In this chapter, we analyze the four-grating TLI, which could be useful for passive compensation of low-frequency vibrations and of the Coriolis force due to the rotation of the Earth. We will assume that the interferometer is illuminated by an uncollimated source and that the last grating is scanned to detect the interference pattern.

Each of the four gratings of the interferometer could be of a different type, leading to a large number of possible configurations. Here, we will focus on two possibilities inspired by the current form and by the ongoing upgrade of the LUMI experiment [21]. That is, on the mixed mechanical-optical setup with 28 kDa oligoporphyrins or strontium atoms, and on the all-optical setup with 100 kDa or 500 kDa hafnium clusters. The former configuration will have two mechanical diffraction gratings in the first and last positions, and an optical phase grating with a wavelength of 532 nm in the middle. For the all-optical setup, we will assume that 266 nm wavelength photoionizing depletion gratings are used in all positions, and we will allow for the laser powers of the internal and external gratings to be different. For both interferometer types, we will denote the common period of the gratings by  $d$  and the particle flight time between the first and the second grating by  $T$ . Unless otherwise noted, the total length of the interferometer will be 2 m when relevant.

### 3.1 Visibility

The first step in the calculation of the visibility of the interference signal is the identification of the relevant terms. We do this as described in Section 2.6. The solutions with  $\sum_{i=1}^4 |n_i| \leq 8$  are shown in Table 3.1. There, we sort the terms


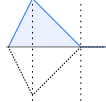
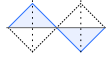
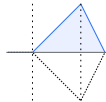
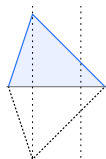
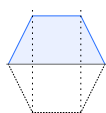
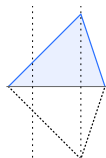
No.	$\sum_{i=1}^4  n_i $	$n_i$	$ \kappa d/2\pi $	Recoil diagram
1	4	1, -1, -1, 1	1	
2	6	2, -3, 1, 0	0	
3	6	1, -2, 2, -1	1	
4	6	0, 1, -3, 2	2	
5	8	3, -4, 0, 1	1	
6	8	2, -2, -2, 2	2	
7	8	1, 0, -4, 3	3	

Table 3.1: Lowest- $n$  terms contributing to the signal in a four-grating Talbot-Lau interferometer. These are all terms for which  $\sum_{i=1}^4 |n_i| \leq 8$ , excluding the trivial one  $n_i = 0$ .

by  $\sum_{i=1}^4 |n_i|$ : a heuristic metric motivated by the decay of the Talbot coefficients with  $n$ . We will restrict ourselves to fringes with the lowest spatial frequency; i.e., those with  $\kappa d/2\pi = 1$ . This leaves us with terms 1, 3, and 5, which we respectively refer to as the trapezoidal, figure-eight, and triangular terms. The constant background in the interferometer signal is due to terms with  $\kappa d/2\pi = 0$ ; i.e., the trivial term  $n_i = 0$  and term 2 in Table 3.1, which we refer to as the top term. The latter as well as the inverse top term (No. 4 in Table 3.1) vanish for the mechanical-optical setup because of the property of the phase gratings discussed in Section 2.1.

The visibilities of the three- and four-grating interferometers in the absence of external forces are compared in Fig. 3.1 for the mechanical-optical configuration and in Fig. 3.2 for the all-optical configuration. There, we also plot the



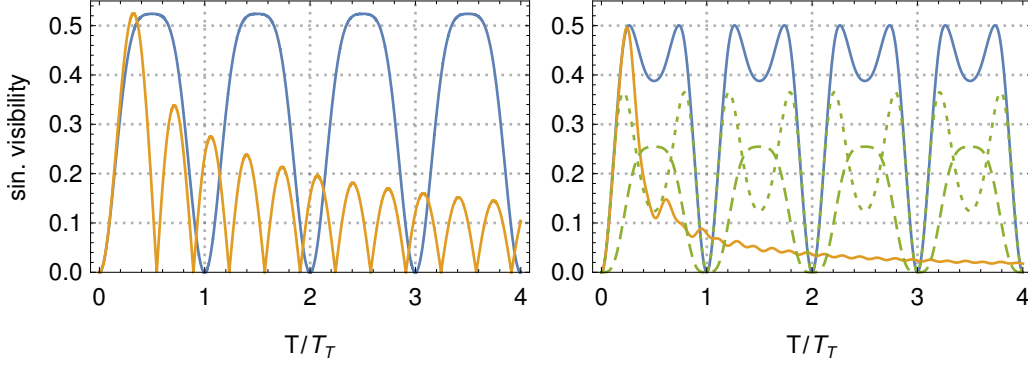


Figure 3.1: Quantum (blue) and classical (orange) sinusoidal visibilities as a function of grating separation<sup>1</sup> in three- (left) and four-grating (right) interferometers in a mechanical-optical configuration. On the right, contributions to the quantum visibility from the trapezoidal (dotted) and the figure-eight (dashed) terms are shown. The peak phase modulation of the phase gratings is  $\phi_0 = 3$  and the opening fraction of the mechanical gratings is  $f = 0.42$ .

visibilities of the trapezoidal and figure-eight terms. Because of the lack of external forces, the phases of both terms are zero and they interfere constructively. The contribution of the triangular term is small, reaching at most 2 percentage points of visibility for the mechanical-optical setup and at most 8 percentage points for the all-optical setup. In Fig. 3.2 the sinusoidal visibility significantly exceeds unity. As discussed in Section 2.2, this is a sign that the assumption of a single dominating spatial frequency is not well satisfied. This is caused by the inverse top and big trapezoidal terms (4 and 6 in Table 3.1), which produce higher-frequency fringes with a combined visibility of about 0.7.

Both in the mechanical-optical and all-optical configurations, the dependence of the visibility on the flight time  $T$  between the gratings is similar for the three- and four-grating interferometers. However, the total flight time is  $4T$  in a four-grating setup compared to  $2T$  in a three-grating one. Therefore, for a fixed particle velocity and interferometer length,  $T/T_T$  is half as large in a four-grating configuration as in a three-grating one. This has important implications for the applicability of the four-grating and other multi-loop setups, especially for experiments which are de-Broglie-wavelength limited. For experiments which are not de-Broglie-wavelength limited,  $T/T_T$  is large and can be halved

<sup>1</sup>The ratio  $T/T_T$  can change as a result of changing interferometer length or changing particle velocity. These two ways are not equivalent, because velocity of the particle also enters the transmission functions of the gratings (in the case of optical phase gratings through  $\phi_0$ , which is inversely proportional to velocity).

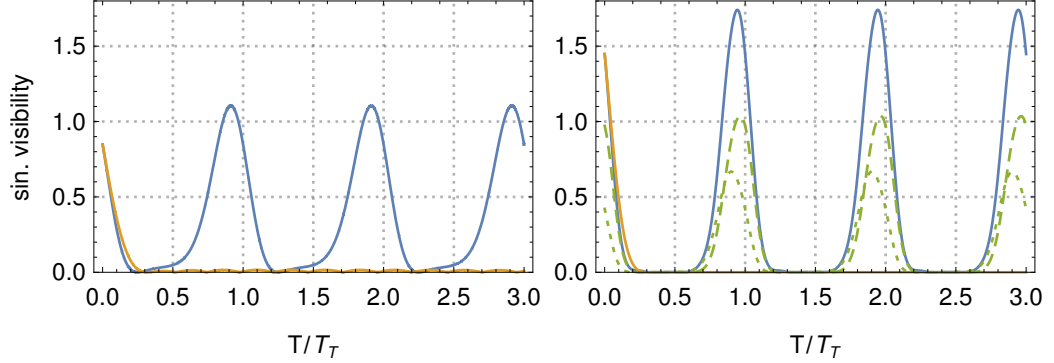


Figure 3.2: As in Fig. 3.1 but for interferometers with optical depletion gratings. The peak phase modulation and the mean number of absorbed photons are  $\phi_0 = 4$  and  $n_0 = 8$ , respectively.

without losing the ability to distinguish the quantum pattern from a classical one. However, high-mass interference experiments often operate in the  $T/T_T \sim 1$  regime, in which  $T/T_T$  cannot be further decreased without substantial loss of distinguishability between the quantum and the classical patterns. In this case, changing from a three-grating configuration to a four-grating one would require halving the velocity of the particles, which might be a significant challenge.

In the presence of a uniform external force, fringes resulting from the dominating trapezoidal and figure-eight terms are affected differently. This is a consequence of the difference in enclosed areas as defined in Eq. (2.42). Fringes due to the positive-area trapezoidal term are displaced proportionally to the magnitude of the applied force and to the inverse square of the particle velocity. Fringes due to the zero-area figure-eight term, on the other hand, remain unaffected. If the external force or the velocity spread in the molecular beam is small, this leads to visibility oscillations as the two sets of fringes slide against and interfere with each other. If the force or the velocity spread is large, the trapezoidal-term fringes are washed out completely, reducing the visibility to that of the figure-eight term.

If necessary, the visibility oscillation resulting from interference of the two terms can be eliminated by detuning the interferometer. This can be achieved by changing the grating separation to  $L + \delta L, 2L, L - \delta L$ , where  $\delta L \ll L$  [30] (see Fig. 3.3). This suppresses the trapezoidal term in exchange for introducing a slight acceleration sensitivity to the figure-eight term. The suppression follows from the uncollimated-illumination condition (2.28), which the trapezoidal term fails to satisfy in the detuned interferometer. The acceleration sensitivity arises as the two loops of the eight figure are no longer identical and thus the enclosed

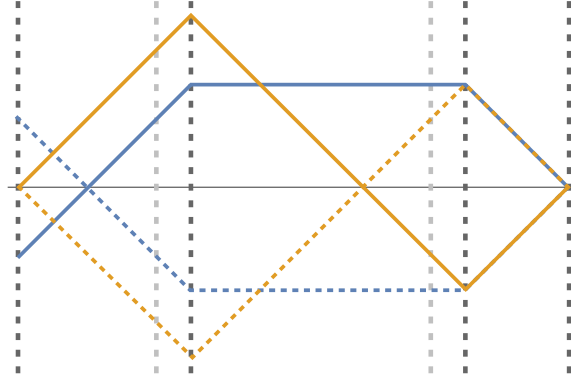


Figure 3.3: Detuning the four-grating interferometer by moving the middle two gratings. This suppresses the trapezoidal term (blue) by violating the uncollimated-illumination condition (2.28). The figure-eight term is retained, but imbalancing the two loops introduces a nonzero signed area and thus slight acceleration sensitivity.

area does not vanish. Alternatively, the interferometer can be detuned by increasing the spacing between the two middle gratings while decreasing their period [50]. The benefit of this detuning is that it does not compromise the insensitivity of the figure-eight term to acceleration. Finally, another possibility is to selectively dephase the trapezoidal terms using additional standing-wave pulses [51].

## 3.2 Transmission

Switching from a three-grating setup to a four-grating one affects the transmission of the interferometer in two ways. First, the transmission is decreased by the effective opening fraction of the new grating (equal to unity for phase gratings). In addition to that, moving to a four-grating configuration might require changing the operating parameters, which can affect the transmission of all gratings in the setup. The prime example of such a parameter is particle velocity, which influences the transmission of all absorptive gratings. Similarly, a change in the laser grating intensities will affect the transmission of optical depletion gratings.

In the mechanical-optical configuration, the extra phase grating is perfectly transmissive and thus only the second mechanism applies. For an experiment which is de-Broglie-wavelength limited, switching to a four-grating configuration requires halving the particle velocity, which decreases the transmission of the mechanical gratings. This can be seen from the Eq. (2.54) for the effective

opening fraction and Eqs. (2.55) and (2.58) for the critical distance. Halving the velocity increases the latter and thus the opening fraction reduction (which can be as large as 40% for fullerene experiments with a 100 nm period grating) by 26%.

In the all-optical configuration, both reasons for the change in transmission apply. Introducing an additional depletion grating decreases the flux through the interferometer by a factor

$$B_0(0) = e^{-n_0/2} J_0\left(\frac{n_0}{2}\right), \quad (3.1)$$

where  $n_0$  is the mean number of photons absorbed at the antinodes. The above follows from property (2.14d) combined with the Talbot coefficients of a depletion grating [26]. The factor (3.1) decays quickly with  $n_0$  and decreases the transmission of the interferometer, which in most cases is already low for three-grating setups. For example, we will show that the maximum of visibility for a three-grating all-optical interference of 100 kDa hafnium clusters traveling at  $200 \text{ m s}^{-1}$  occurs with  $n_0 \approx 28$  at the external and  $n_0 \approx 13$  at the internal grating. This results in a total transmission of only 0.2%. One can estimate that switching to a four-grating configuration in this situation, which would require halving the particle velocity and adding another grating, would decrease the transmission by a further order of magnitude.

### 3.3 Vibration sensitivity

The effect of vibrations on a multi-loop setup depends on their amplitude, mode, and frequency and will be different for different terms. For three-grating setups, the most stringent stability requirements typically result from independent grating vibrations [21]. To evaluate their influence on the four-grating interferometer, we use Eq. (2.48) and plot the visibility reduction in Fig. 3.4. Since the latter is a strong function of  $n_i$ , the trapezoidal term is affected less than a three-grating setup, and the figure-eight term is affected more. However, for moderate vibration amplitudes the difference is likely too small to be of practical concern.

To investigate the sensitivity of the four-grating setup to common-mode vibrations, we use Eq. (2.50b). Since in this case the reduction is velocity-dependent, we average it over a Gaussian velocity distribution while treating the magnitudes of the terms as constant. The result is shown in Fig. 3.5. We find that the figure-eight term is significantly less sensitive to low-frequency common-mode vibrations than the trapezoidal term or the three-grating setup. This is expected from the acceleration-compensating property of the figure-eight term and has previously been observed in far-field interferometers for

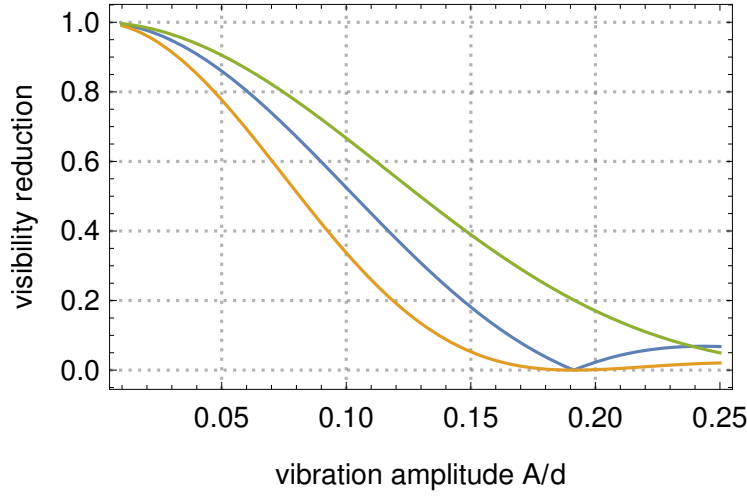


Figure 3.4: Visibility reduction in three- (blue) and four-grating interferometers (figure-eight term in orange, trapezoidal in green) as a result of independent translational grating vibrations with amplitude  $A$ .

neutrons [37]. Multi-loop configurations could thus complement or supersede the use of pendular suspensions for the suppression of low-frequency vibrations.

### 3.4 Coriolis force compensation

One of the main benefits of the four-grating configuration is its partial insensitivity to constant accelerations, and thus to the Coriolis force. Compensating the latter was already necessary for achieving the recent mass record [8], and will remain a prerequisite for all future high-mass interference experiments in a horizontal configuration. The currently employed compensation technique is the “grating roll trick”, described in Section 2.5. We will use it as a point of reference for discussing the usefulness of the cancellation achieved in a four-grating setup.

The grating-roll technique necessarily offers only an approximate compensation of the Coriolis force. Nevertheless, we find that in existing and in near-future high-mas interference experiments it allows for almost complete recovery of maximal visibility. This is shown in Fig. 3.6, where we take the record-breaking mechanical-optical setup [8] as an example of an existing experiment and an all-optical interferometer for 100 kDa hafnium clusters as an example of a near-future one. In these two cases, the maximal visibility in a

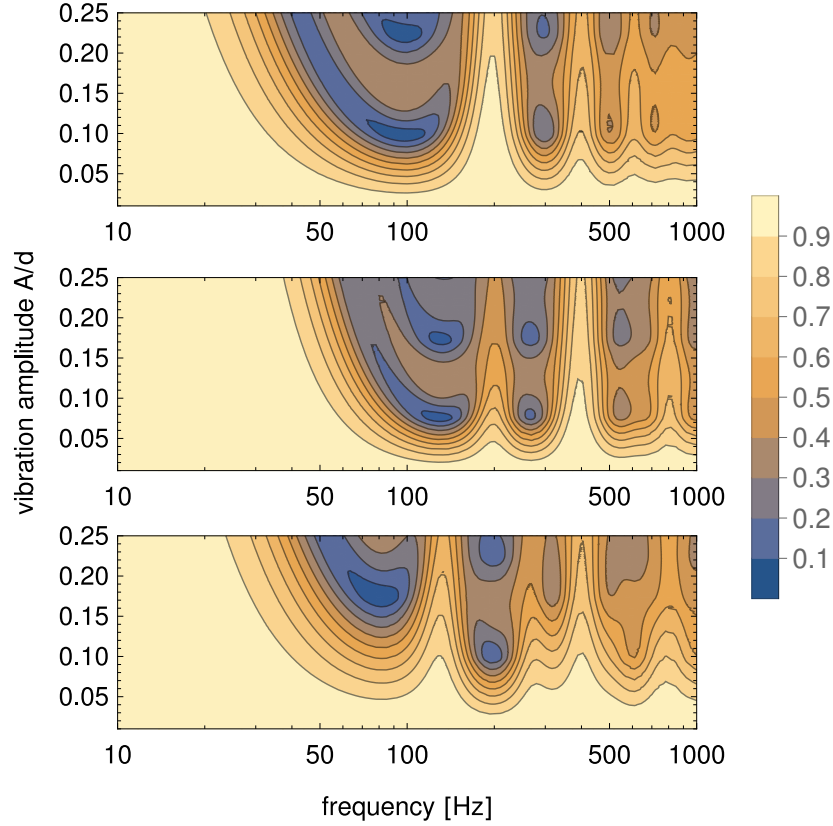


Figure 3.5: Visibility reduction in three- (top) and four-grating interferometers (middle: figure-eight term, bottom: trapezoidal term) as a result of common-mode translational grating vibrations. We assume a Gaussian velocity distribution with a mean of  $200 \text{ m s}^{-1}$  and standard deviation of 10% of the mean.

four-grating setup is similar as in a three-grating one<sup>2</sup>. Therefore, the potential benefit from switching to a four-grating configuration in these two scenarios is small.

We expect the gain from using the four-grating configuration to be significant when the Coriolis force compensation achieved using the roll trick is insufficient. The residual phase shift (2.53) after applying the latter is proportional to the length of the interferometer squared and to the inverse of the particle velocity. This suggests that the roll trick might become insufficient as the velocity of the particles is decreased. This is an important scenario, as decreasing particle velocity is needed to maximize the mass of the interfering particles or the

<sup>2</sup>Strictly speaking, the all-optical four-grating setup can achieve a higher visibility than its three-grating counterpart. However, this requires laser grating intensities which significantly reduce the particle flux, as discussed in Section 3.2.

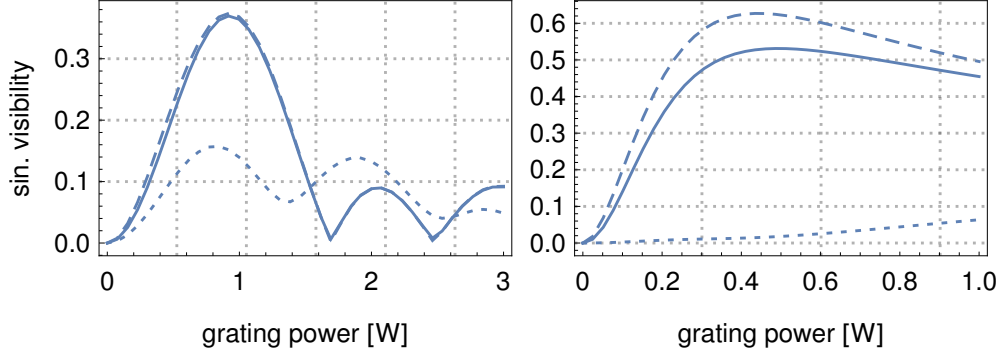


Figure 3.6: Dependence of visibility on the middle grating power in a three-grating interferometer showing Coriolis force compensation using the grating roll technique. Left: 28 kDa oligoporphyrin interference in a mechanical-optical setup (LUMI). Right: 100 kDa hafnium cluster interference in an all-optical setup. The dashed line shows the visibility without Coriolis force, the dotted one is the visibility with the gratings aligned to gravity (no compensation), and the continuous one is with the gratings tilted by angle (2.52) to compensate the Coriolis force. For oligoporphyrin interference, we take the experimental parameters of  $261 \text{ m s}^{-1}$  mean velocity with a spread of 21% (standard deviation) [8], as well as an absorption cross section  $\sigma = 6.8 \times 10^{-17} \text{ cm}^2$  and a polarizability volume  $\alpha' = 1317 \text{ \AA}^3$ . For cluster interference, we assume a mean velocity of  $200 \text{ m s}^{-1}$  with a spread of 40%, as well as  $\alpha' = 1150 \text{ \AA}^3$  and  $\sigma = 9.1 \times 10^{-15} \text{ cm}^2$ . The latter are obtained as in Appendix A of Ref. [48] using bulk electric permittivity [52]. The power of the external gratings in the all-optical setup is held constant at 1 W and all vertical grating radii are taken to be  $700 \text{ }\mu\text{m}$  ( $1/e^2$  intensity). The length of the interferometer is 1.96 m.

superposition distance (in which case light particles would be used). In Fig. 3.7, we compare the performance of the grating-roll technique to a four-grating setup in these two cases of the low-velocity limit. We find that the three-grating setup indeed loses a significant portion of maximal visibility despite the roll trick. However, in this case the four-grating setup does not offer a significant improvement. That is primarily because the acceleration-insensitive term only accounts for a half to a third of the maximal visibility in the four-grating setup (see Figs. 3.1 and 3.2). The visibility in both setups is further decreased by the large velocity spread.

The second case in which we expect the limitations of the roll trick to show is that of an increased interferometer length. In Fig. 3.7, we compare the three- and four-grating configurations for an interferometer with a total length of 20 m.

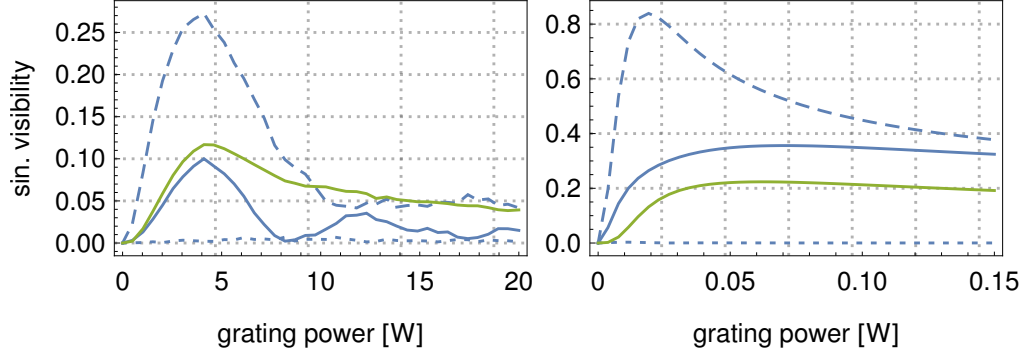


Figure 3.7: Dependence of visibility on the middle grating power in a three- (blue) and four-grating (green) interferometers in the low particle velocity limit. Left: Interference of strontium atoms in a mechanical-optical setup (LUMI). Right: Interference of 500 kDa hafnium clusters in an all-optical setup. We assume mean velocities of  $30 \text{ m s}^{-1}$  with a spread of 50% for the atoms and  $40 \text{ m s}^{-1}$  ( $20 \text{ m s}^{-1}$  for the four-grating setup) with 40% spread for the clusters. For the latter we take  $\alpha' = 5770 \text{ \AA}^3$  and  $\sigma = 4.5 \times 10^{-14} \text{ cm}^2$  [48, 52], while for strontium we neglect the absorption and take  $\alpha' = 29.6 \text{ \AA}^3$ . The remaining parameters are the same as in Fig. 3.6, with the exception of the external grating power for the four-grating setup, which is 0.4 W. In the four-grating setup, the gratings are aligned to gravity.

In this case, the visibility of the three-grating setup is decreased to the extent that observing interference would be essentially impossible for atoms and heavy clusters alike. The multigrating configuration performs relatively well in this limit even at moderate velocities. As a result, the four-grating scheme could be necessary for TLIs with a length of the order of 10 m.

The above result invites the question if such long interferometers are likely to be built in a horizontal configuration. One of the ultimate limitations on the length of a horizontal interferometer is the vertical free fall, which determines the minimum diameter of the interferometer chamber. In a 20 m interferometer, the flight time of particles traveling at  $80 \text{ m s}^{-1}$  is 250 ms. This corresponds to about 30 cm of free fall if the particles start with zero vertical velocity. This is unpractically large, but can be reduced by directing the particle beam slightly upwards so that the particle trajectory peaks in the middle of the interferometer. In this case, the trajectory would be approximately 8 cm tall and thus much easier to accommodate. However, what remains problematic is the vertical dispersion of the beam, which grows with the square of the interferometer length. In the same example, the vertical separation of the  $80 \text{ m s}^{-1}$  and  $100 \text{ m s}^{-1}$



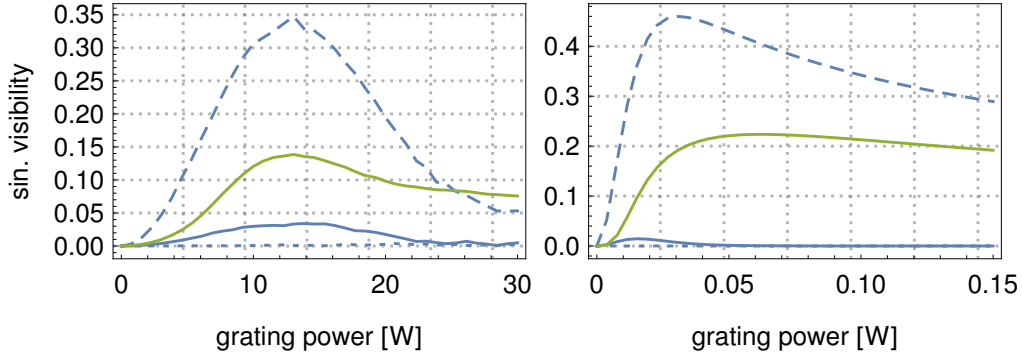


Figure 3.8: Like Fig. 3.7, but for a 20 m long interferometer. Left: strontium atoms traveling at  $100 \text{ m s}^{-1}$ . Right: 500 kDa hafnium clusters traveling at  $80 \text{ m s}^{-1}$ . In both cases, we assume a 25% velocity spread.

velocity classes would exceed 10 cm at the end of the interferometer. This would inevitably lead to strong velocity selectivity, which puts considerable limitations on the minimum source brightness.

An alternative to a horizontal setup is a vertical one in which the particles are trapped and cooled before being either launched upwards or dropped towards the diffraction gratings. To achieve the same free evolution time as for particles traveling at  $80 \text{ m s}^{-1}$  in a 20 m long horizontal setup, a drop height of 30 cm would suffice. If the particles are launched upwards instead, this reduces to about 8 cm. Such reduction in interferometer length is clearly desirable and makes the development of trapping and cooling techniques applicable to highly massive particles a priority.

Finally, we note that in a vertical arrangement, the Coriolis force would be less detrimental to interference than in a long-baseline horizontal setup. That is because in a vertical setup, the Coriolis force can be made approximately perpendicular to the grating vector. If the grating laser is coaxial with the particle beam, orthogonality is guaranteed because the Coriolis force is perpendicular to the velocity of the particle<sup>3</sup>. If the gratings are perpendicular to the particle beam, orthogonality can be achieved by rotating them around the interferometer axis such that grating slits are oriented in the East–West direction. In both setups, the orthogonality of the Coriolis force and the grating vector is approximate, because we have neglected the small transverse velocity components of the particle. However, the Coriolis force resulting from those is relatively small and

<sup>3</sup>In this setup, the Coriolis force still affects the overlap of the wavepackets at the end of the interferometer. However, this is a higher-order effect than the dephasing due to Coriolis force in a horizontal setup.

can be compensated using standard methods.

# Chapter 4

## Comparison of two- and three-grating interferometers

The discussion in the previous chapter illustrates some of the difficulties in comparing dissimilar interferometer schemes. In this chapter, we make those difficulties explicit and show how to address them. The following treatment complements our published work [48] with a detailed justification of the signal-to-noise figure of merit. We also discuss how the latter can be extended to include metrological experiments and different sources of uncertainty. We end with a discussion of the results and limitations of the current approach.

### 4.1 Figure of merit

The first problem we face when comparing interferometer schemes is the lack of an adequate metric or figure of merit. The visibility of the interference pattern or signal is most often used for this purpose, but its limitations are easily seen: an interferometer with unit visibility is not worth much if its transmission is essentially zero. High visibility and transmission at the same time are also not sufficient if they occur in a parameter regime for which the classical visibility is large. A good figure of merit should capture how well an interferometer serves its purpose, and so in the first step we must define the latter.

Here and in Ref. [48], we focus on interference experiments aiming to demonstrate quantum superpositions of massive particles. For such a demonstration to succeed, the difference between the quantum and the classical signals has to be larger than any uncertainty involved. Assuming that statistical uncertainty dominates, we can introduce a figure of merit  $N$  proportional to the number of baseline counts necessary for the quantum-classical difference to exceed the shot noise. Baseline counts are a product of source intensity (in the relevant

velocity class and solid angle), detection efficiency, and integration time. Equivalently, they are equal to the number of counts the experiment would register with no gratings in place. Referring to baseline counts allows us to capture the differences in interferometer transmission: A setup which wastes more particles will require more baseline counts to achieve the same shot noise level. Another benefit of using  $N$  is the ability to treat imaging setups on equal footing with scanning-grating interferometers.

For a scanning grating interferometer, the above figure of merit can be introduced as follows. Assume that the total data-taking time and the source and detection efficiency are such that without gratings we would register  $N$  counts. Then assume that the scanning grating position  $x_s$ , for which the signal  $S(x_s)$  attains a maximum, can be found using a negligible portion of these counts. With this information available, the amplitude of the interference signal can be measured in the most count-efficient way by integrating for half of the data-taking time at the maximum and for the other half at the minimum of the signal. The expectation value of the number of counts registered at the maximum is then

$$\langle N_+ \rangle = \frac{N}{2} \max S(x_s), \quad (4.1)$$

and analogously at the minimum  $\langle N_- \rangle = N \min S(x_s)/2$ . The expectation value of the measured amplitude is then

$$\langle N_+ - N_- \rangle \approx NS_\kappa, \quad (4.2)$$

where  $S_\kappa$  is the dominant term in the decomposition of the signal, Eq. (2.27a). A result analogous to Eq. (4.2) holds in the classical scenario. The difference between the amplitudes obtained in the quantum and in the classical case is

$$\langle N_+ - N_- \rangle - \langle N_+ - N_- \rangle^{\text{cl}} = N (S_\kappa - S_\kappa^{\text{cl}}), \quad (4.3)$$

where the superscript cl denotes the classical predictions. The variance of the amplitude measurement assuming Poissonian counting statistics is

$$\text{Var}(N_+ - N_-) = NS_0. \quad (4.4)$$

That is because the variance of a sum of independent measurements is the sum of variances, and the variance of a Poissonian variable is equal to its mean. Equation (4.4) holds both in the quantum and in the classical case, because the constant term  $S_0$  is the same in both cases (this follows from the equality (2.45) of quantum and classical Talbot coefficients at zero argument). The standard error of the amplitude measurement is thus  $\sqrt{NS_0}$  in both cases. Dividing the

signal (4.3) by this value of error gives us a signal-to-noise type figure of merit. Equating it to unity and solving for  $N$  gives

$$N = \frac{S_0}{(S_\kappa - S_\kappa^{\text{cl}})^2}. \quad (4.5)$$

For a direct-detection interferometer, an analogous expression for  $N$  can be obtained following a similar argument [48].

It must be noted that  $N$  is only a lower bound on the number of baseline counts necessary for the quantum-classical discrimination task to succeed. The reasons for that are twofold. First, a signal-to-noise ratio of more than unity is certainly desirable, which inflates  $N$  accordingly. Second, we have assumed an impossible optimal protocol for measuring the amplitude. In it, the locations of the maximum and the minimum of the signal are known and the entire count budget can be spent on determining their values. This is not the case in practice, and measuring the amplitude to the same precision as in this ideal case would probably require at least an order of magnitude more counts. Therefore, one must not put too much weight on the value of  $N$  for any single interferometer configuration (unless  $N$  is extremely high, then one is safe to conclude that the configuration is not viable). However, the ratios of  $N$  for different interferometer configurations are representative of the differences in baseline counts necessary to achieve the same quantum-classical distinguishability.

If the need arises, the above approach can be extended in the following ways. First, one can include the systematic uncertainty if there are reasons to believe it exceeds the statistical error. This can be the case for particle species for which the optical properties are highly uncertain. Including systematic uncertainty would require restricting the (typically numerical) minimization of  $N$  to the parameter regimes in which the signal exceeds a certain threshold value. This cutoff value would need to be found by estimating the response of the signal to variation in the uncertain parameters. Second, the figure of merit  $N$  can be adapted to experiments with a metrological focus, for which the classically-predicted signal is irrelevant. This is as easy as omitting the classical signal term from the definition (4.5) of  $N$ . The resulting metric captures the ratio of the quantum signal to the shot noise, which determines the theoretical limit on the precision of an experiment. With this modification,  $N$  would be suitable for comparison of metrological setups.

## 4.2 Numerical optimization

The second problem we face when comparing interferometer schemes or looking for optimal configurations is the large number of possibilities. Even if we

Particle	$m$ [kDa]	$\alpha'_{266}$ [ $\text{\AA}^3$ ]	$\sigma_{266}$ [ $\text{cm}^2$ ]	$\alpha'_{532}$ [ $\text{\AA}^3$ ]	$\sigma_{532}$ [ $\text{cm}^2$ ]
Insulin <sup>a</sup>	5.8	600	$4 \times 10^{-17}$	600	0
Trp <sub>50</sub> <sup>b</sup>	10	1000	$9.1 \times 10^{-16}$	1000	0
GFP <sup>ac</sup>	27	2700	$4 \times 10^{-17}$	2700	0
Silver	100	2500	$6.9 \times 10^{-15}$	5200	$2.1 \times 10^{-16}$
Cesium	100	-2200	$6.5 \times 10^{-15}$	-22000	$2.4 \times 10^{-14}$
Silver	300	7400	$2.1 \times 10^{-14}$	15400	$6.2 \times 10^{-16}$
Cesium	300	-6700	$1.9 \times 10^{-14}$	-65000	$7.2 \times 10^{-14}$

<sup>a</sup> Absorption cross sections correspond to that of the photocleavable group [53].

<sup>b</sup> See Ref. [54].

<sup>c</sup> Green Fluorescent Protein

Table 4.1: Parameters of the molecules and clusters used for the comparison of two- and three-grating interferometer setups shown in Fig. 4.1. Reproduced from Ref. [48].

consider only one grating of each basic type (mechanical, optical phase, and optical depletion), we arrive at 12 possible two- and three-grating combinations, listed in Fig. 4.1. If we include four-grating interferometers, this number more than doubles. Each grating configuration can then be combined with a number of sources, including metal clusters of different composition and size, as well as natural and artificial macromolecules. Each setup-source combination should then be optimized over laser grating powers for every particle velocity to find the best working parameters. Only once this is done, we can conclude that certain interferometer schemes perform better than others.

In Ref. [48], we have used numerical optimization to tackle this complexity with the aim of making the best possible use of the 2 m baseline of LUMI. At the core of our approach was the theory from Chapter 2, implemented as a MATHEMATICA package. In anticipation of the treatment of four-grating setups presented in Chapter 3, we have restricted our attention to two- and three-grating setups. We have also limited ourselves to the gratings already in use at LUMI (266 nm period mechanical and optical phase gratings) in addition to a 133 nm period optical depletion grating, which could be obtained by frequency-doubling the phase grating<sup>1</sup>. We have considered seven different sources, including a range of biomolecules as well as metal clusters. The optical properties of the chosen particles are shown in Table 4.1. For each combination of source and grating sequence, we have numerically minimized the figure of

<sup>1</sup>This choice of grating types surely does not exhaust the promising possibilities. Noteworthy candidates include a 266 nm period optical depletion grating for clusters of metals with a low work function.

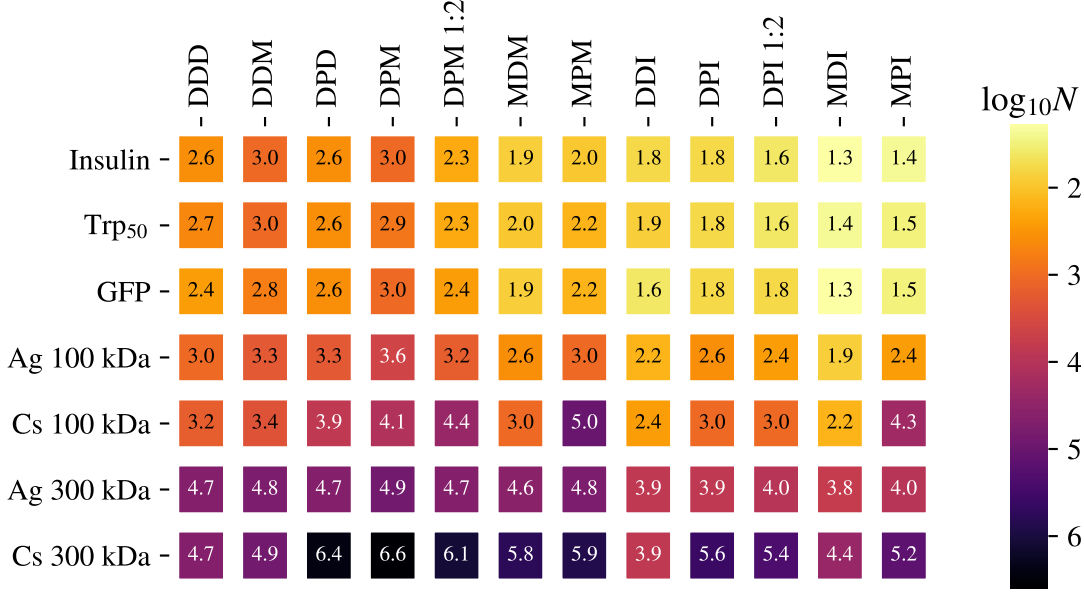


Figure 4.1: Comparison of two- and three-grating interferometer schemes in terms of the figure of merit  $N$ , introduced in Section 4.1 (smaller is better).  $N$  is proportional to the number of baseline counts necessary to distinguish quantum interference from classical fringes in a given setup.  $D$ ,  $P$ , and  $M$  stand for optical depletion, optical phase, and mechanical gratings.  $I$  denotes space-resolving detection allowing for direct imaging of the interferometer pattern. The distance between the first and second grating is equal to the distance between the second and the third (or a detector for imaging setups), unless 1 : 2 is noted. For 1 : 2 setups, the second distance is twice as large as the first. The mean velocity of the particles is optimized over a range of  $30 \text{ m s}^{-1}$  to  $600 \text{ m s}^{-1}$  and the velocity spread is kept at 5% of the mean (standard deviation). Reproduced from Ref. [48].

merit  $N$  over the mean particle velocity and over the powers of all laser gratings. To decrease the size of the parameter space, the powers of the first and third laser gratings were kept equal (where applicable). The results are shown in Fig. 4.1.

The biggest gap we find is between scanning-grating and direct-detection setups. The latter typically need about an order of magnitude less baseline counts to achieve the same degree of quantum-classical distinguishability<sup>2</sup>. Direct-detection setups have been expected to be more count efficient than

<sup>2</sup>Additionally, we expect the detection efficiency to be higher in direct-detection setups than in scanning-grating setups. This means that the former accumulate baseline counts faster

their scanning-grating counterparts. However, this is the first time that this advantage has been quantified. Finally, we note that the difference in  $N$  between the two interferometer types can be estimated analytically. To do this, we use that the constant term of the signal (2.27) is smaller than that of the pattern (2.21) by  $B_0^{(3)}(0)$ , while the modulation amplitude is multiplied by  $B_{n_3}^{(3)}(0)$  in the quantum and by  $C_{n_3}^{(3)}(0)$  in the classical case. Since  $B_n^{(i)}(0) = C_n^{(i)}(0)$ ,  $N$  changes by a factor  $[B_{n_3}^{(3)}(0)]^2/B_0^{(3)}(0)$ . This factor reproduces the observed difference in  $N$  when its dependence on velocity is weak; that is, when  $[B_{n_3}^{(3)}(0)]^2/B_0^{(3)}(0)$  changes little over the velocity spread in the beam.

We now restrict our attention to the scanning-grating setups. Among these, the mechanical-depletion-mechanical and the mechanical-phase-mechanical configurations stand out in terms of performance for biomolecules and silver clusters. However, these setups might be incompatible with clusters or large molecules due to clogging of the mechanical gratings [21]. This is likely to be most severe at the first grating, which is exposed to the largest particle flux. To alleviate the clogging issue, we could replace the first mechanical mask with an optical depletion gating. Among the setups which implement this, the asymmetric depletion-phase-mechanical one performs very well overall and is only one grating substitution away from the existing LUMI setup. Going further, the most reliable approach to the interference of highly massive clusters might be to avoid mechanical gratings altogether. In this case, the triple-depletion setup is the best choice.

It is worth noticing that the asymmetric depletion-phase-mechanical scheme systematically outperforms its symmetric counterpart. The advantage of the asymmetric setup lies in using lower-order diffraction at the second grating to close the interferometer. Whereas the symmetric setup requires fourth-order diffraction, the asymmetric one uses third-order diffraction. Similar advantages should always be sought when considering TLIs with unequal grating periods.

Finally, two remarks are in order regarding the results of Ref. [48]. First, the analysis predates the grating-roll technique of Coriolis force compensation. The loss of visibility due to the Coriolis force thus inflates the number of counts necessary to achieve distinguishability. This is especially pronounced for the most massive particles<sup>3</sup>. The second caveat is the assumption that for each setup the optimal laser intensity can be reached. For insulin and GFP achieving optimal  $N$  requires upwards of 20 W of UV light for a grating radius of 150  $\mu\text{m}$ . This could limit the real-world applicability of such interferometers.

---

for the same source intensity. As a result, the difference in data taking time is likely to be even larger than the difference in baseline counts.

<sup>3</sup>While the Coriolis force does not depend on mass, highly massive particles require a longer flight time, which increases Coriolis dephasing.



# Chapter 5

## Conclusions (Part I)

The three-grating Talbot-Lau interferometer (TLI) has been the basis for high-mass interference experiments for almost 20 years. Most recently, the scheme has been employed in the record-breaking LUMI experiment [8]. In this part of the thesis, we have looked into the potential benefits of departing from the TLI configuration in LUMI and in future experiments by changing the type or the number of the diffraction gratings. We have first turned to the latter possibility, which required generalizing the existing phase-space description of pattern formation in a TLI to include an arbitrary number of gratings. We have done this in Chapter 2.

The most important feature of the generalized theory is the graphical interpretation of the expressions for the interference pattern or signal. It allows one to write down the complete pattern in any Talbot-Lau interferometer (including asymmetric or magnifying setups) essentially by finding closed-loop classical trajectories. These trajectories visualize the “coprime integers  $r, s$ ” of Ref. [26] and earlier works, and naturally generalize to interferometers with any number and period of gratings. The diagrammatic approach also makes it easier to design interferometers with desirable properties, such as those which suppress unwanted parasitic trajectories.

In Chapter 3, we have used the generalized theoretical approach to analyze a near-field interferometer analogous to the figure-eight far-field interferometer [31]. We found that it is in many ways equivalent to two three-grating TLIs performed one after another. In particular, the four-grating setup will require twice as much free evolution time as a three-grating setup to produce a pattern with a similar visibility. This makes it suboptimal for the interference of record-breaking masses, in which the available coherent evolution time is a limiting factor. In atomic gravity gradiometers, the doubled evolution time requirement is one of the reasons why the two-loop configuration is often substituted by two three-pulse interferometers operating side-by-side [55].

The two-loop scheme is valued for its insensitivity to constant forces and low-frequency vibrations. We found that these advantages carry over from the far-field scheme to its near-field counterpart. However, we find that usually only about half of the maximal visibility in a four-grating setup benefits from the insensitivity. This bounds the effectiveness of a two-loop scheme as a compensation technique for vibrations or the Coriolis force to about 50% in most scenarios. As a result, the two-loop scheme compares unfavorably to existing methods of compensating the Coriolis force for interferometers with a total length of a few meters. For an order of magnitude longer interferometer, the existing techniques would be insufficient for observing interference, and the four-grating interferometer could be a viable alternative. However, with its increased baseline requirement halving the achievable particle mass, a different approach such as a velocity-resolved measurement or a vertical setup may prove more practical.

In Chapter 4 we have quantified the benefit of direct imaging of the interference pattern and of using different grating-type combinations in an update of the LUMI experiment. To do this, we have introduced a figure of merit proportional to the source and detection efficiency needed to demonstrate quantum interference with a given setup. This allowed us to include the effects of varying interferometer transmission when comparing and optimizing two- and three-grating schemes. Using this approach, we have shown that direct imaging of the interference pattern could save an order of magnitude in integration time (assuming a spatially-resolving detector with the same efficiency as the detectors used in scanning-grating interferometers). The analysis of Chapter 4 also influenced the upgrade of the LUMI experiment to a configuration with three optical depletion gratings, currently underway [21].

## **Part II**

# **Bragg diffraction and trapped interference**



# Chapter 6

## Introduction

In the first part of the thesis, we have analyzed new interferometers utilizing the existing toolbox of high-mass matter-wave optics. In this part, we will focus instead on expanding this toolbox. In particular, we will look for techniques which increase the momentum transferred to the particles upon beam splitting or the overall evolution time without increasing the interferometer length.

The momentum transfer and the evolution time together with the velocity of the particles determine the spacetime area enclosed by the arms of a matter-wave interferometer. Since the enclosed area scales the sensitivity of the interferometer to external forces, methods to increase it are highly valued in all areas of matter-wave interferometry. In particular, this includes beam splitters and mirrors with high momentum transfer and methods for suspension or trapping of the particles during the interferometer sequence. In high-mass matter-wave interference, increasing momentum transfer and evolution time is important for two additional reasons. First, high momentum transfer could allow for the construction of a far-field Mach-Zehnder interferometer for heavy particles. The clear separation of the arms in such an interferometer would allow for new applications, such as genuine quantum metrology<sup>1</sup> or Aharonov-Bohm-type experiments. Second, an increased evolution time would allow for demonstrating quantum superpositions of even higher masses. In this case, the prolonged evolution is necessary for the quantum dynamics to clearly diverge from the classical prediction.

In matter-wave optics, a proven way to achieve large momentum transfer is to use strong one-dimensional optical lattices to diffract or guide the matter waves. This includes the techniques of Bragg diffraction and Bloch oscillations, which have been widely adopted in the field of atom interferometry. In the fol-

---

<sup>1</sup>The deflection of the molecular or atomic beam measured in our current experiments is a classical phenomenon. In a fully quantum scheme, one would interferometrically measure a phase applied to one of the superposition components.

lowing section, we provide a brief overview of the theoretical and experimental development of these techniques. Then, in Chapters 7 and 8, we discuss the modern theory of Bragg diffraction and the experimental demonstration of the technique with heavy molecules.

In Chapter 9, we focus on the goal of increasing evolution time and propose an interference scheme for particles in periodic confinement. The scheme is inspired by the formation of a Talbot pattern behind a phase grating and motivated by the recent progress in creating smooth toroidal traps for atoms. We briefly review this as well as historical progress in the interference of trapped matter waves in Section 6.2.

## 6.1 Bragg diffraction

The next two chapters focus on the theory and experimental demonstration of Bragg diffraction of large molecules. The term Bragg diffraction originates in X-ray crystallography and has a precise meaning there, as well as in the diffraction of neutrons or near-visible light [56]. It denotes the diffraction on an regular array of weak scatterers, in which the interference of many reflected waves leads to a strong dependence of the total reflection amplitude on the incidence angle.

The same physical picture does not always apply to the diffraction of atoms or molecules by “thick” optical potentials, which is nevertheless generally referred to as Bragg diffraction. The main difference lies in the amplitude of the modulation of the scattering potential. To appreciate the difference, let us consider the parameter  $q$  defined as the ratio of the depth of the grating potential to the recoil energy. Bragg diffraction of neutrons will then be characterized by  $q$  of the order of  $10^{-5}$  [57]. On the other hand, large momentum transfer atom optics will typically employ  $q$  of the order of  $10^2$  [58]. Qualitatively, this means that in the atomic case the potential will have (or will be very close to having) a classical turning point.

The first theoretical descriptions of atomic Bragg diffraction [59, 60] were based on perturbation theory and were only accurate to leading order in  $q$ . To achieve high-order diffraction with grating pulses of moderate duration, atomic diffraction experiments quickly increased the potential depth beyond the regime of validity of the leading-order solution. The breakdown of the latter was first addressed by S. Dürr and coworkers [61], who proposed a solution combining the adiabatic theorem with numerical diagonalization of a truncated Hamiltonian. Their approach can be used to obtain the solution to any order in  $q$  when the potential is switched on and off adiabatically. For sudden switching, a nonperturbative solution based on the Mathieu equation was found by M. Horne

and coworkers [57]. The qualitative difference between these two types of grating boundaries only appears for large  $q$  and was first demonstrated in Ref. [62]. There, it was shown that smooth switching is necessary for achieving high-order Bragg diffraction with moderate interaction times. Corrections to the adiabatic solution were first derived using a generalization of the procedure of adiabatic elimination [58]. Recently, an alternative approach using Landau-Zener theory and including small detunings from the Bragg condition was presented [63]. Previously, the treatments of off-resonant diffraction were either entirely numerical<sup>2</sup> [64], limited to low diffraction orders [65], or used semi-phenomenological models [66]. In Chapter 7, we fill a minor gap in the available treatments of Bragg diffraction by combining the approaches of Refs. [57, 61, 63] to give a nonperturbative solution in the case of adiabatic switching of the potential.

Bragg diffraction of atoms was first demonstrated experimentally in 1988 [67]. About 30 years later, it became one of the main tools in large-momentum-splitting atom interferometry [68]. Interferometers consisting only of Bragg pulses were the first to reach  $100\hbar k$  splitting [69] and continue to be used in state-of-the-art applications [9]. First demonstrated with atoms in 1996 [70, 71], Bloch oscillations became widely used in atom interferometry around the same time as high-order Bragg diffraction. This is not accidental, as Bloch oscillations are essentially a sequence of high-fidelity, first-order Bragg transitions. Combined with low-order initial diffraction, they were first used in 2008 to obtain large momentum transfer [72] and in 2009 to demonstrate large-momentum beam splitting [73, 74]. The combined approach has since become common and is employed in many of the recent headline atom-interferometric experiments [7, 10]. Starting in 2013, a technique using two gratings moving in opposite directions (referred to as double Bragg diffraction) was developed [75, 76]. It has recently been extended to symmetric Bloch oscillations, in which two lattices are used to split and guide the matter waves throughout the interferometric sequence [77]. In Chapter 8, we present the first demonstration of Bragg diffraction of heavy molecules [78]. This demonstration is a first step towards employing Bloch oscillations and other advanced lattice techniques for the manipulation of high-mass particles.

---

<sup>2</sup>Importantly, the authors of Ref. [64] have found that the efficiency of Bragg-based matter-wave optics is fundamentally limited by the initial momentum width of the wavepacket. This is one of the factors contributing to the increased adoption of Bose-Einstein condensates as sources for atom interferometry.

## 6.2 Trapped interference

The basic promise of trapped matter-wave interference schemes is a long coherent evolution time made possible by the suspension of the interfering particles against gravity. Coherent splitting and holding of matter waves was first demonstrated in 2004 with Bose-Einstein condensates in double-well potentials [79]. These early experiments (see also Ref. [80]) could reach a coherent hold time of a few milliseconds. They were soon followed by interferometers using optical pulses to manipulate condensates in stationary traps [81–83], which could reach coherence times of the order of 10 ms. In 2006, hold times of many seconds were demonstrated for thermal clouds of atoms using Bloch oscillations [84], albeit without interference. First interferometers incorporating Bloch-oscillation holds were reported in 2012 [85], reaching coherence times of the order of 100 ms. The coherence times achievable in setups of this type successively increased [86], recently culminating in the 20 s coherent hold time of Ref. [7]. In the trapping of Bose-Einstein condensates, notable progress involves traps based on time-averaged adiabatic potentials [87, 88]. Using this technique, toroidal traps with picokelvin roughness have recently been demonstrated [89]. In Chapter 9, we show that very smooth toroidal traps can be used for matter-wave interference without beam splitting or mirror pulses.



# Chapter 7

## Diffraction of point particles on optical lattices

### 7.1 Problem formulation

#### The polarizable point particle approximation

We will treat the interaction of molecules with light in the polarizable point particle approximation. That is, we will assume that the particle responds to an applied electric field  $E$  by inducing a dipole moment

$$\mu = \alpha E. \quad (7.1)$$

This approximation is standard in high-mass matter-wave interference as well as in the treatments of atomic Bragg diffraction<sup>1</sup>. We further assume that the polarizability  $\alpha$  is scalar and real, in which case the particle-light interaction is conservative and described by the Hamiltonian [26]

$$H_{\text{int}} = -\frac{\text{Re}\{\alpha\}}{4}|E|^2. \quad (7.2)$$

We will express  $\alpha$  in terms of the polarizability volume [49]

$$\alpha' = \frac{\text{Re}\{\alpha\}}{4\pi\epsilon_0}. \quad (7.3)$$

Using Eq. (7.3) and the definition of light intensity  $I = c\epsilon_0|E|^2/2$ , we write the interaction Hamiltonian as

$$H_{\text{int}} = -\frac{2\pi\alpha'}{c}I. \quad (7.4)$$

---

<sup>1</sup>In the atomic case, this approximation applies, because the lattice is usually far detuned from the atomic transition. The excited state can then be adiabatically eliminated, which results in a linear response to the electric field.

We now assume that the lattice is formed by retroreflecting the beam of a laser with wavelength  $\lambda = 2\pi/k$  and power  $P$ , directed along the  $x$  axis. The intensity experienced by the particle will then be

$$I(x, y, z) = \frac{8P}{\pi w_z w_y} \exp\left(-\frac{2z^2}{w_z^2} - \frac{2y^2}{w_y^2}\right) \cos^2(kx), \quad (7.5)$$

where we have assumed that the molecular beam is narrow enough so that the dependence of the intensity radii  $w_y$ ,  $w_z$  on  $x$  can be neglected.

### Hamiltonian in the lab and comoving frames

We consider a particle of mass  $m$ , flying predominantly along the  $z$  axis and impinging on a standing light wave with intensity (7.5). We will denote the largest velocity component (along the  $z$  axis) as  $v$ . Following the same argument as in the treatment of the Talbot-Lau interferometer in Section 2.1, we start by reducing the problem to one dimension. That is, we approximate the movement of the particle along the  $z$  axis as uniform, and we neglect the free fall during grating transit. Using Eqs. (7.4) and (7.5) we then find the Hamiltonian for the motion along the axis of the optical lattice

$$H_{\text{lab}} = \frac{p^2}{2m} + V(t) \cos^2(kx), \quad (7.6a)$$

$$= \frac{p^2}{2m} + \frac{V(t)}{4} (e^{2ikx} + e^{-2ikx}) + \text{const.}, \quad (7.6b)$$

with

$$V(t) = -\frac{16P\alpha'}{c w_z w_y} e^{-2v^2 t^2 / w_z^2}. \quad (7.7)$$

In the diffraction of atoms on far-detuned standing light waves, the Hamiltonian has the same form (7.6). However, the amplitude of the potential is  $V(t) = \hbar\Omega^2(t)/\Delta$ , where  $\Omega(t)$  is the single-photon Rabi frequency and  $\Delta$  is the detuning [58]. The potential can therefore be either attractive or repulsive depending on the sign of the detuning. The dynamics are the same in both cases, because changing the sign of the potential in Eq. (7.6a) is equivalent to a shift of the  $x$  axis by  $\pi/2k = \lambda/4$  and the addition of a constant.

For some treatments of the diffraction problem it is convenient to have the initial state of the particle always centered around  $p = 0$ . This can be achieved by performing the calculations in an inertial frame which is initially comoving with the particle. Assuming the particle is initially moving with mean transverse velocity  $v_0$ , the unitary transformation to the comoving frame will



Figure 7.1: The division of the momentum space into even (blue) and odd (orange) subspaces.

be (see Appendix A)

$$U_{\text{cm}} = \exp\left\{i \frac{v_0 t p}{\hbar}\right\} \exp\left\{-i \frac{v_0 m x}{\hbar}\right\} \exp\left\{i \frac{m v_0^2 t}{2\hbar}\right\}. \quad (7.8)$$

The Hamiltonian in the comoving frame is then analogous to Eq. (7.6), but with the grating moving with velocity  $-v_0$ ,

$$H_{\text{cm}} = \frac{p^2}{2m} + \frac{V(t)}{4} (e^{2ik(x+v_0 t)} + e^{-2ik(x+v_0 t)}). \quad (7.9)$$

## Hamiltonian in the momentum representation

Expressing the Hamiltonian (7.6) in the momentum representation highlights its block structure as well as its connections to problems in other areas of physics. Following Ref. [63], we write

$$H_{\text{lab}} = \int_{-\hbar k/2}^{\hbar k/2} dp [H_{\text{lab}}^{\text{even}}(p) + H_{\text{lab}}^{\text{odd}}(p)], \quad (7.10a)$$

$$H_{\text{lab}}^{\text{even}}(p) = \sum_{n \in \mathbb{Z}_{\text{even}}} \left[ \frac{(p + n\hbar k)^2}{2m} |p + n\hbar k\rangle \langle p + n\hbar k| + \frac{V(t)}{4} (|p + (n+2)\hbar k\rangle \langle p + n\hbar k| + \text{h.c.}) \right], \quad (7.10b)$$

where h.c. stands for hermitian conjugate and the summation is over even integers. The odd Hamiltonian  $H_{\text{lab}}^{\text{odd}}(p)$  is the same as  $H_{\text{lab}}^{\text{even}}(p)$ , but with the sum restricted to odd  $n$ . All the Hamiltonians introduced above act within orthogonal subspaces of the Hilbert space (the even and odd subspaces are illustrated in Fig. 7.1) and thus commute. That is, for any  $p_1, p_2 \in (-\pi/2, \pi/2]$

$$[H_{\text{lab}}^{\text{even}}(p_1), H_{\text{lab}}^{\text{even}}(p_2)] = [H_{\text{lab}}^{\text{odd}}(p_1), H_{\text{lab}}^{\text{odd}}(p_2)] = [H_{\text{lab}}^{\text{even}}(p_1), H_{\text{lab}}^{\text{odd}}(p_2)] = 0 \quad (7.11)$$

Therefore, we can think of the Hilbert space as consisting of shifted even and odd momentum eigenstate ladders, which the time evolution does not couple. This lack of coupling results from assuming the lattice being formed by a perfectly monochromatic and collimated laser beam and is a great simplification.

The Hamiltonians governing the time evolution within each ladder have a band-diagonal form. For example, the Hamiltonian of the non-shifted even subspace is

$$H_{\text{lab}}^{\text{even}}(0) = \hbar\omega_r \begin{pmatrix} \ddots & & & & & & & \\ & \ddots & & & & & & \\ & & q(t) & 4 & q(t) & & & \\ & & & q(t) & 1 & q(t) & & \\ & & & & q(t) & 0 & q(t) & \\ & & & & & q(t) & 1 & q(t) \\ & & & & & & q(t) & 4 & q(t) \\ & & & & & & & \ddots & \ddots & \ddots \end{pmatrix}, \quad (7.12)$$

where we have introduced the recoil frequency and the dimensionless lattice depth

$$\omega_r = \frac{\hbar k^2}{2m}, \quad q(t) = \frac{V(t)}{4\hbar\omega_r}. \quad (7.13)$$

Hamiltonian (7.12) is a Jacobi operator which arises in the classical mechanics of coupled harmonic oscillators and in many other discrete one-dimensional problems. As a result, many of its properties are known both in the finite [90] and in the infinite-dimensional cases [91]. In quantum optics, Eq. (7.12) truncated to an  $N$ -dimensional subspace is the Hamiltonian of an  $N$ -level atom interacting with  $N - 1$  laser fields in the rotating wave approximation [92, 93]. It is one of the standard models considered in the theory of coherent atomic excitation [94].

The non-shifted ladders are special from a physical perspective, because they consist of states satisfying the Bragg condition. To see this, we note that the optical lattice has a period  $\lambda/2$ , and so the Bragg condition reads

$$\lambda \sin \theta = n\lambda_{\text{dB}}, \quad (7.14)$$

where  $n \in \mathbb{Z}$ ,  $\lambda_{\text{dB}}$  is the de Broglie wavelength, and  $\theta$  is the angle between the particle momentum and the lattice planes. For a particle with momentum  $p_{\text{tot}}$ , Eq. (7.14) is equivalent to

$$p_{\text{tot}} \sin \theta = n\hbar k, \quad (7.15)$$

which means that the component of the particle's momentum along the lattice axis is an integer multiple of the photon momentum. This corresponds exactly to the domain of  $H_{\text{lab}}^{\text{even}}(0)$  for even  $n$  and to the domain of  $H_{\text{lab}}^{\text{odd}}(0)$  for odd  $n$ . From now on, we will thus refer to states satisfying Eq. (7.15) and to the subspaces which contain them as (Bragg-)resonant.

The resonant subspaces are also special from a more abstract perspective as the only ones respecting the parity symmetry (changing  $x$  to  $-x$ ) of the

optical lattice Hamiltonian (7.6). This allows us to decompose them further into symmetric and antisymmetric subspaces which will be conserved by the time evolution. The latter are spanned by the states

$$|n^\pm\rangle = \frac{1}{\sqrt{2}} (|n\hbar k\rangle \pm |-n\hbar k\rangle), \quad (7.16)$$

where for  $n = 0$  we have only  $|0^+\rangle = |0\rangle$ . In the basis (7.16), the Hamiltonian in the odd resonant subspace becomes

$$H_{\text{lab}}^{\text{odd}}(0) = H_{\text{lab}}^{\text{odd}+} + H_{\text{lab}}^{\text{odd}-} \quad (7.17)$$

with [63]

$$H_{\text{lab}}^{\text{odd}\pm} = \hbar\omega_r \sum_{n \in \mathbb{N}_{\text{odd}}} (n^2 \pm \delta_{1n} q(t)) |n^\pm\rangle\langle n^\pm| + q(t) (|n + 2^\pm\rangle\langle n^\pm| + \text{h.c.}), \quad (7.18)$$

in which  $\delta_{1n}$  is the Kronecker delta. The Hamiltonian in the even resonant subspace decomposes similarly [63]. In non-resonant ladders, a decomposition using basis states  $|p + n\hbar k\rangle \pm |p - n\hbar k\rangle$  analogous to (7.16) is possible, but it is not conserved by the time evolution and therefore far less useful.

The additional symmetry in the Bragg-resonant subspaces makes the time evolution within them much easier to treat analytically. As a consequence, virtually all analytical thick-grating treatments are restricted to this case (with the notable exception of Ref. [63], which includes ladders shifted by  $|p| \ll \hbar k$ , albeit with restrictions).

## The Raman-Nath equations

The block structure of the Hamiltonian (7.6) allows one to reduce the time-dependent Schrödinger equation to a set of ordinary differential equations. They are referred to as the Raman-Nath equations, after an analogous set of equations arising in the diffraction of light on acoustic waves in dielectrics [95]. These equations are the starting point for many approximate solutions of the diffraction problem, and can take a number of equivalent forms.

The basic form of the Raman-Nath equations is obtained by considering the resonant subspace, in which every state can be written as<sup>2</sup>

$$|\psi(t)\rangle = \sum_{j=-\infty}^{\infty} c_j(t) |j\rangle, \quad (7.19)$$

---

<sup>2</sup>We note that the following procedure is exactly the same as the first steps in time-dependent perturbation theory [96] or in the original proof of the adiabatic theorem [97].

where we write  $|j\rangle \equiv |j\hbar k\rangle$  for the Bragg-resonant momentum eigenstates. Inserting Eq. (7.19) into the time-dependent Schrödinger equation with Hamiltonian (7.6b) gives

$$i\dot{c}_j = j^2 c_j + q(\tau)(c_{j-2l} + c_{j+2l}), \quad (7.20)$$

where a dot denotes a derivative with respect to dimensionless time

$$\tau = \omega_r t. \quad (7.21)$$

The diagonal terms in the Raman-Nath equations can be removed by including the free evolution of the momentum eigenstates in the ansatz (7.19). Equivalently, this can be seen as working in the interaction picture with respect to the free Hamiltonian. Using

$$|\psi(\tau)\rangle = \sum_{j=-\infty}^{\infty} e^{ij^2\tau} d_j |j\rangle \quad (7.22)$$

with the Hamiltonian (7.6b) gives

$$i\dot{d}_j = q(\tau)(e^{4i(j-1)\tau} d_{j-2} + e^{4i(j+1)\tau} d_{j+2}). \quad (7.23)$$

This form of the Raman-Nath equations lends itself to the treatment with averaging methods borrowed from classical mechanics, as discussed in Ref. [75]. Removing only one diagonal element with an ansatz

$$|\psi(\tau)\rangle = \sum_{j=-\infty}^{\infty} e^{in^2\tau} g_j |j\rangle \quad (7.24)$$

gives

$$i\dot{g}_j = (j^2 - n^2)g_j + q(\tau)(g_{j-2} + g_{j+2}), \quad (7.25)$$

which is a convenient starting point for deriving the Bragg approximation using adiabatic elimination (see Ref. [58] and Appendix C).

Finally, a form of Raman-Nath equations which is especially well suited for numerical calculations is the one following from an ansatz

$$|\psi(\tau)\rangle = \sum_{j=-\infty}^{\infty} f_j(\tau) |j/l\rangle, \quad (7.26)$$

where  $l \in \{1/2, 1, 2, \dots\}$  determines the spacing of the basis states. For  $l = 1/2$  we obtain a ladder with a  $2\hbar k$  spacing, sufficient for calculating the diffraction of plane waves. For  $l \gg 1$  we obtain a dense grid which can be used to approximate the evolution of wavepackets with finite momentum width. However, even with large  $l$  the momentum of the initial state cannot be changed continuously. To

alleviate this, we switch to the comoving frame in which the particle is initially at rest. Using the ansatz (7.26) with Hamiltonian (7.9) gives

$$i\dot{c}_j = \left(\frac{j}{l}\right)^2 c_j + q(\tau)(c_{j-2l}e^{4i\eta\tau} + c_{j+2l}e^{-4i\eta\tau}), \quad (7.27)$$

where we have introduced the dimensionless initial momentum of the particle

$$\eta = \frac{mv_0}{\hbar k}. \quad (7.28)$$

The time-dependence of  $q(\tau)$  in the above equations is most often given by a Gaussian pulse. We will parametrize it as

$$q(\tau) = q_{\max} e^{-2\tau^2/\sigma^2} \quad (7.29)$$

with  $q_{\max}, \sigma > 0$ . Up to the irrelevant sign, this corresponds to the standing light wave potential (7.7) when

$$q_{\max} = \frac{8P\alpha'm\lambda^2}{h^2 c w_z w_y}, \quad \sigma = \frac{w_z \omega_r}{v} = \frac{\pi w_z}{4L_T} = \frac{\pi \hbar w_z}{m v \lambda^2}, \quad (7.30)$$

where  $L_T = vT_T$  is the Talbot length.

## 7.2 Analytic solution methods

We now review the major analytic approaches to solving the diffraction problem, with an emphasis on methods applicable to strong optical lattices. In practice, quantitative predictions and modeling usually rely on numerical methods. Nevertheless, knowledge of the analytic approaches is necessary to be able to navigate and utilize the different diffraction regimes.

To the best of our knowledge, the last attempt at a cohesive classification of the matter-wave diffraction regimes is the one in Ref. [62]. There, the authors delineate three diffraction regimes: Bragg or “thick grating”, Raman-Nath or “thin grating”, and “channeling”. Diffraction in the Bragg regime results in only two diffraction orders and is strongly dependent on the incidence angle. The opposite is true in the Raman-Nath regime, where dependence on the incidence angle is weak and many diffraction orders are populated. In the channeling regime, the diffraction is the same as in the Bragg regime if the grating pulse has a sufficiently smooth envelope, but the same as in the Raman-Nath regime if the envelope has sharp boundaries<sup>3</sup>. In the Raman-Nath and Bragg regimes,

---

<sup>3</sup>The name “channeling” refers to this Raman-Nath-like diffraction, which can be understood as resulting from the guiding of the particles by the valleys of the potential.

the profile of the pulse has no qualitative influence on diffraction. In this classification, the Bragg regime occupies  $q < 1$ , while  $4\sqrt{2q}\sigma < 1$  gives the Raman-Nath regime, and the rest of the parameter space is the channeling regime.

Even though this classification could be updated to reflect new developments and terminology (such as the “quasi-Bragg” regime of Ref. [58] and later works), this is beyond the scope of this thesis. Instead, we propose to view matter-wave diffraction as a coherent control problem on the one hand, and as a scattering problem on the other. From the coherent-control perspective, we expect analytic solutions in the limits of instantaneous and of adiabatic switching of the driving potential. From the scattering perspective, we expect analytic solutions when the scattering potential is weak (perturbation theory) or when the deflection is small (eikonal approximation). These four approximations are discussed next.

## The Mathieu equation

We first consider the time-independent version of the problem, that is with the depth of the potential taken to be constant in time. The Schrödinger equation with the optical lattice Hamiltonian (7.6) is then stationary and reads

$$\left[ -\frac{\hbar^2 \partial_x^2}{2m} + V \cos^2(kx) \right] \psi(x) = E \psi(x). \quad (7.31)$$

This equation is known as the Mathieu equation, the standard form of which is [98]

$$\frac{d^2 w}{du^2} + [a - 2q \cos(2u)] w = 0. \quad (7.32)$$

The above corresponds to the Schrödinger equation (7.31) for

$$u = kx \quad a = \frac{E - V/2}{\hbar\omega_r}, \quad (7.33)$$

and for  $q = V/(4\hbar\omega_r)$  as used thus far. The Mathieu equation arises in numerous mathematical and engineering applications. As a result, many of its properties are known and scientific calculation packages typically include routines for the calculation of its eigenvalues and solutions (the Mathieu functions).

A first important property of the Mathieu equation is its eigenvalue spectrum, shown in Fig. 7.2 as a function of  $q$ . In the literature on the Mathieu equation, the spectrum is referred to as the *stability diagram*, because it shows the combinations of  $q$  and  $a$  for which bounded solutions exist. Because bounded solutions are normalizable (and thus physical), the stability diagram is simultaneously the spectrum of the optical lattice Hamiltonian (7.6). To interpret it properly, one



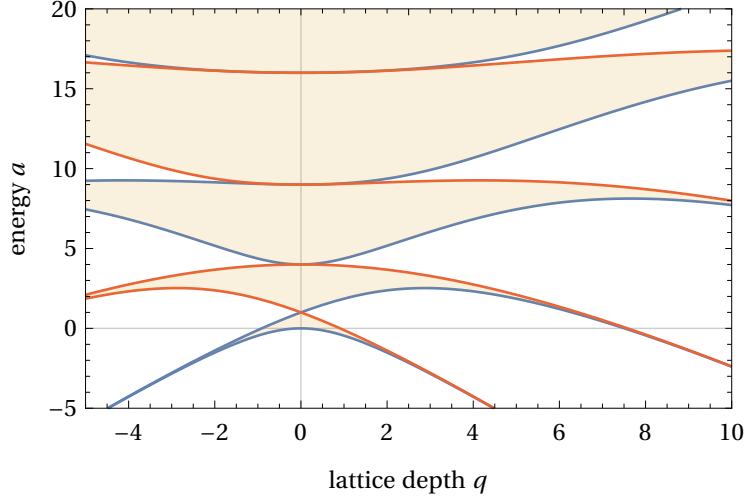


Figure 7.2: The spectrum of the optical lattice Hamiltonian (7.6a) as a function of the dimensionless lattice depth  $q$ .  $a$  is the energy in units of photon recoil energy, with the mean value of the potential subtracted. The blue curves show the threshold eigenvalues  $a_0(q), a_1(q), \dots$  (from the bottom) corresponding to symmetric Bragg-resonant states. Analogously, the eigenvalues  $b_1(q), b_2(q), \dots$  of antisymmetric Bragg-resonant states are shown in red.

must remember that in the dimensionless energy  $a$  the mean value  $V/2$  of the lattice potential is subtracted. From Fig. 7.2, we see that the Hamiltonian has a continuous spectrum which divides into energy bands for  $|V| > 0$ .

Of particular importance are the threshold eigenvalues, corresponding to the edges of the energy bands. In standard notation, the eigenvalues making up the lower edges of the bands for  $q > 0$  are denoted  $a_0(q), a_1(q), \dots$ , whereas the upper edges are  $b_1(q), b_2(q), \dots$ . Their corresponding eigenstates are known as the integer-order Mathieu functions of the first kind, denoted by  $ce_j$  and  $se_j$  respectively for  $a_j$  and  $b_j$ . These eigenstates are important because they are orthonormal and complete in the Bragg-resonant subspace<sup>4</sup>.

In addition to spanning the subspace of Bragg-resonant states, the functions  $ce_j$  and  $se_j$  converge to the (anti)symmetric basis of it in the limit of vanishing potential. This basis was introduced in Eq. (7.16) and in the position space is

<sup>4</sup>To see this, note that the  $ce_n$  and  $se_n$  are complete and orthonormal in the subspace of functions which are  $\pi$  or  $2\pi$  periodic [98]. This subspace is exactly the Bragg-resonant subspace, because the latter is spanned by states  $\langle u|n\rangle \propto \exp(inu)$ , which are  $\pi$ -periodic for even  $n$  and  $2\pi$ -periodic for odd  $n$ .

simply given by

$$\langle x|n^+\rangle = \frac{1}{\sqrt{\pi}} \cos(nkx), \quad (7.34a)$$

$$\langle x|n^-\rangle = \frac{1}{\sqrt{\pi}} \sin(nkx). \quad (7.34b)$$

Knowing that the Mathieu functions reduce to sines and cosines for  $q = 0$  [98], we introduce the Mathieu-function states such that

$$\langle x|a_n(q)\rangle = \frac{1}{\sqrt{\pi}} \text{ce}_n(kx, q) \xrightarrow{q \rightarrow 0} \langle x|n^+\rangle, \quad (7.35a)$$

$$\langle x|b_n(q)\rangle = \frac{1}{\sqrt{\pi}} \text{se}_n(kx, q) \xrightarrow{q \rightarrow 0} \langle x|n^-\rangle. \quad (7.35b)$$

An exception is the state  $|a_0(q)\rangle$ , which must be defined as

$$\langle x|a_0(q)\rangle = \sqrt{\frac{2}{\pi}} \text{ce}_0(kx, q) \quad (7.36)$$

in order to converge to  $\langle x|0^+\rangle = 1/\sqrt{\pi}$ . That is because  $\text{ce}_0(kx, 0) = 1/\sqrt{2}$  in the conventional normalization [98]. For further discussion and visualization of the Mathieu states, as well as an in-depth discussion of the high- $q$  regime, we refer the reader to Ref. [57].

### Square-pulse grating: diabatic approximation

In reality, the optical lattice always has a finite extent, and thus  $q$  must be time-dependent. Including the time dependence of  $q$  is relatively easy in the usual limiting cases of sudden or adiabatic switching. We first turn to the former case, which corresponds to a grating with a sharp square profile.

We assume that the interaction begins at  $\tau = 0$  with the potential changing infinitely fast from 0 to a constant value  $V_0 = 4\hbar\omega_r q_0$ . A Bragg-resonant initial state  $|\psi(0)\rangle = |n\rangle$  can then be decomposed in the basis of the Mathieu-function states corresponding to the potential depth  $q_0$ . The time evolution in the basis of Mathieu states is straightforward, as they are the eigenstates of the lattice Hamiltonian. We have

$$|\psi(t)\rangle = \sum_{j=0}^{\infty} e^{-ia_j\tau} \langle a_j(q_0)|n\rangle |a_j(q_0)\rangle + \sum_{i=1}^{\infty} e^{-ib_i\tau} \langle b_i(q_0)|n\rangle |b_i(q_0)\rangle, \quad (7.37)$$

in which we have ignored a global phase due to the average value of the potential. The overlaps  $\langle a(q_0)|n\rangle$  and  $\langle b(q_0)|n\rangle$  are easily obtained as the Fourier

coefficients of the Mathieu functions<sup>5</sup>. At the end of the interaction (or at any point during the interaction), we can change the basis again to the free-particle states  $|l\rangle$  to calculate the populations of the diffraction orders. We have (suppressing temporarily the argument  $q_0$  of the Mathieu states)

$$\begin{aligned}
|\langle l|\psi(\tau)\rangle|^2 &= 2 \sum_{j_1, j_2=0}^{\infty} \left| \langle a_{j_1}|n\rangle \langle a_{j_2}|n\rangle \langle l|a_{j_1}\rangle \langle l|a_{j_2}\rangle \right| \cos((a_{j_1} - a_{j_2})\tau) \\
&+ 2 \sum_{i_1, i_2=1}^{\infty} \left| \langle b_{i_1}|n\rangle \langle b_{i_2}|n\rangle \langle l|b_{i_1}\rangle \langle l|b_{i_2}\rangle \right| \cos((b_{i_1} - b_{i_2})\tau) \\
&+ 2 \sum_{j=0, i=1}^{\infty} \left| \langle a_j|n\rangle \langle b_i|n\rangle \langle l|a_j\rangle \langle l|b_i\rangle \right| \cos((a_j - b_i)\tau) \\
&+ \text{const.}
\end{aligned} \tag{7.38}$$

As discussed in the previous section, for small  $q_0$  the wavefunctions of the Mathieu states  $|a_n(q_0)\rangle$  and  $|b_n(q_0)\rangle$  converge to sines and cosines of  $nkx$ . They will therefore only overlap significantly with  $|\pm n\rangle$ . In this case, most of the terms in Eq. (7.38) can be neglected, leaving [57, 58]

$$|\langle \pm n|\psi(\tau)\rangle|^2 = \text{const.} \pm 2 \sum_{j=0, i=1}^{\infty} |\langle a_n(q_0)|n\rangle|^2 |\langle b_n(q_0)|n\rangle|^2 \cos(\Omega_n(q_0)\tau). \tag{7.39}$$

As a function of time, the population will thus oscillate between the initial state and its specular reflection with the frequency given by

$$\Omega_n(q) = a_n(q) - b_n(q). \tag{7.40}$$

This phenomenon is referred to as the *pendellösung* and is universally associated with Bragg diffraction. A plot of the pendellösung frequency  $\Omega_n(q)$  is shown in Fig. 7.3.

The easiest way to obtain an analytic approximation of the pendellösung frequency is to use tabulated small- $q$  expansions of  $a_n$  [99] and  $b_n$  [100]. Inserting these into Eq. (7.40), one directly obtains  $\Omega_n$  up to twentieth order in  $q$  for  $n \leq 10$ . Beyond that, one can use the iterative procedure of Ref. [58] to obtain the expansion of  $\Omega_n$  to any order in  $q$ . Alternatively,  $\Omega_n$  is easily calculated numerically to any precision, as functions calculating  $a_n$  and  $b_n$  ship with most numerical software distributions<sup>6</sup>.

<sup>5</sup>For example, `mathieu_even_coef` and `mathieu_odd_coef` in SciPy, the scientific library in Python.

<sup>6</sup>For example, `MathieuCharacteristicA` and `MathieuCharacteristicB` in MATHEMATICA or `mathieu_a` and `mathieu_b` in SciPy.

### Smooth-pulse grating: adiabatic or quasi-Bragg approximation

The second case in which the time dependence of  $q$  can be treated analytically is the limit of adiabatic switching of the interaction. This is also the most important case for experimental applications, as it allows for large-momentum-transfer matter-wave optics with manageable interaction times. Compared to square pulses, it exhibits significantly lower losses and better control of diffraction phases [58, 63]. The treatment below uses the adiabatic theorem to describe Bragg diffraction in a way that was pioneered in Ref. [61] and later significantly expanded in Ref. [63].

Let us assume that the particle is initially in the resonant, free-particle state  $|n\rangle$ . We will refer to this and other interaction-free eigenstates as bare states, as is customary in the applications of the adiabatic theorem. The instantaneous eigenstates of the time-dependent Hamiltonian are then referred to as the dressed states. In our case, these are the Mathieu states  $|a_j(q)\rangle$ ,  $|b_j(q)\rangle$ , where  $q$  is now a slowly-varying function of time.

Since the grating pulse has a finite duration, the bare states coincide with the dressed states in the asymptotic past and future. We can therefore decompose the initial state in the basis of dressed states

$$|\psi(t \rightarrow -\infty)\rangle = \frac{1}{\sqrt{2}} (|n^+\rangle + |n^-\rangle) = \frac{1}{\sqrt{2}} (|a_n(0)\rangle + |b_n(0)\rangle). \quad (7.41)$$

The dressed states  $|a_n(0)\rangle$  and  $|b_n(0)\rangle$  will evolve independently from each other, because they belong to the conserved symmetric and antisymmetric subspaces. For even  $n$ , the Hamiltonians governing their evolution are the commuting  $H_{\text{lab}}^{\text{even}+}(0)$  and  $H_{\text{lab}}^{\text{even}-}(0)$  (and analogously  $H_{\text{lab}}^{\text{odd}+}(0)$  and  $H_{\text{lab}}^{\text{odd}-}(0)$  for odd  $n$ ). The spectra of these Hamiltonians are discrete and nondegenerate, as shown in<sup>7</sup> Fig. 7.2. We can thus invoke the adiabatic theorem in its simplest formulation<sup>8</sup> [97]. From it, we infer that an adiabatic grating pulse will not lead to transitions between the dressed states. Instead, the latter will only acquire a

<sup>7</sup>There, the  $a_j(q)$  (shown in blue) are the spectrum of  $H_{\text{lab}}^{\text{even}+}(0)$  for even  $j$  and of  $H_{\text{lab}}^{\text{odd}+}(0)$  for odd  $j$ , etc.

<sup>8</sup>Beyond the simplest formulation, there are adiabatic theorems which allow for degenerate states and a mixed continuous-discrete spectrum [101, 102], as well as those which do not assume an energy gap at all [103]. These formulations are of as much theoretical as of practical importance. For example, they lead to quantum control protocols which use quickly-varying Hamiltonians to approximate adiabatic evolution better than a slowly-varying Hamiltonian [104].

dynamic phase<sup>9</sup>, such that

$$|\psi(\tau)\rangle = \frac{1}{\sqrt{2}} \left( \exp\left\{-i \int_{-\infty}^{\tau} d\tau' a_n(\tau')\right\} |a_n(\tau)\rangle + \exp\left\{-i \int_{-\infty}^{\tau} d\tau' b_n(\tau')\right\} |b_n(\tau)\rangle \right), \quad (7.42)$$

where  $a_n(\tau)$  and  $b_n(\tau)$  are shorthands for  $a_n(q(\tau))$  and  $b_n(q(\tau))$ . After the grating pulse decays, the dressed states again coincide with the bare states and we can write

$$|\psi(t \rightarrow \infty)\rangle = \frac{1}{\sqrt{2}} \left( \exp\left\{-i \int_{-\infty}^{\infty} d\tau' a_n(\tau')\right\} |n^+\rangle + \exp\left\{-i \int_{-\infty}^{\infty} d\tau' b_n(\tau')\right\} |n^-\rangle \right) \quad (7.43a)$$

$$= \cos\left(\frac{1}{2} \int_{-\infty}^{\infty} d\tau' \Omega_n(\tau')\right) |n\rangle - i \sin\left(\frac{1}{2} \int_{-\infty}^{\infty} d\tau' \Omega_n(\tau')\right) |-n\rangle, \quad (7.43b)$$

where the pendellösung frequency is as defined in Eq. (7.40).

From Eq. (7.43b) we see that at most two bare states are populated at the end of the grating pulse. This means that Bragg diffraction in the adiabatic regime is strictly lossless, independently of the peak grating strength. During the grating pulse only two dressed states, but in general many bare states are populated. This is a qualitative difference with respect to the Bragg diffraction on weak potentials (discussed next), in which only two bare states are macroscopically populated throughout the grating pulse. Because of this difference and its significant practical implications, most recent works on the topic refer to the adiabatic Bragg diffraction as quasi-Bragg diffraction [58, 63, 75]. That is to tell it apart from the weak-potential “deep-Bragg” regime.

Physically, Bragg diffraction arises because the optical lattice lifts the degeneracy between the symmetric and the antisymmetric components of a Bragg-resonant state. The degeneracy is lifted because the maxima of the  $\cos^2(kx)$  potential coincide with the maxima of the symmetric component (whose probability density is proportional to  $\cos^2(nkx)$ ), but with the minima of the antisymmetric component (whose probability density is proportional to  $\sin^2(nkx)$ ). As a result, the symmetric component experiences a stronger potential and its energy is increased more than the energy of the antisymmetric component. Crucially, this alignment and antialignment of maxima repeats periodically only if the period of the lattice is an integer multiple of the period of the state. That is, if the state is Bragg-resonant. If it is not, the maxima of the potential will coincide with the maxima of the symmetric and antisymmetric components

---

<sup>9</sup>The geometric phase is zero, because the trajectory of the system in the (one-dimensional) parameter space encloses a zero area [105].

equally often, and there will be no average difference in the potential these two components see. This means that the lattice does not lift the degeneracy between the symmetric and antisymmetric components of off-resonant states. As a result, in the adiabatic approximation there is no diffraction of off-resonant states.

An important question remaining is how gentle must the grating pulse be in order to drive an approximately adiabatic evolution. For a Hamiltonian  $H(t)$  containing no terms which oscillate in time, the evolution starting from an eigenstate  $|E_n\rangle$  will be adiabatic if<sup>10</sup>

$$\max_t \left| \frac{\langle E_m(t) | \hbar \partial_t H | E_n(t) \rangle}{[E_n(t) - E_m(t)]^2} \right| \ll 1 \quad \text{for all } m \neq n. \quad (7.44)$$

The quasi-Bragg approximation is just the adiabatic approximation applied to the time-dependent lattice Hamiltonian (7.6). Therefore, the conditions for its validity are obtained by imposing Eq. (7.44) separately on the evolution of the symmetric ( $|a_n\rangle$ ) and the antisymmetric ( $|b_n\rangle$ ) component of the initial state. The Hamiltonians governing the evolution of these components have different forms for even and odd  $n$ , which results in a total of four slightly different conditions. To give an example, for the odd- $n$  symmetric component we get

$$\max_\tau \left| \frac{\langle a_m(\tau) | \partial_\tau H_{\text{lab}}^{\text{odd}+} | a_n(\tau) \rangle}{\hbar \omega_r [a_m(\tau) - a_n(\tau)]^2} \right| \ll 1 \quad \text{for all odd } m \neq n. \quad (7.45)$$

Using the odd Hamiltonian (7.18), we obtain

$$\begin{aligned} \max_\tau \left| \frac{\dot{q}(\tau)}{[a_m(\tau) - a_n(\tau)]^2} \left[ \sum_{j=0}^{\infty} \langle j^+ | a_n(\tau) \rangle \langle a_m(\tau) (|j+2^+ \rangle + |j-2^+ \rangle) \right. \right. \\ \left. \left. + \langle a_m(\tau) | 1^+ \rangle \langle 1^+ | a_n(\tau) \rangle \right] \right| \ll 1 \quad \text{for all odd } m \neq n. \end{aligned} \quad (7.46)$$

The overlaps between the dressed and bare states are easy to calculate numerically as Fourier coefficients of the Mathieu functions. Additionally, for moderate  $q$  the above condition can be simplified by considering only  $m = n \pm 2$  and the term with  $j = n$ . Nevertheless, Eq. (7.46) and similar conditions remain rather cumbersome.

In practice, the duration of the pulse is made as short as possible and including corrections to the adiabatic evolution is sometimes necessary. These corrections come in two forms: modifications of the pendellösung frequency (7.40)

<sup>10</sup>The validity conditions of the adiabatic approximation have been subject to controversy following the inconsistency brought up in Ref. [106]. What we report here is based on Ref. [107] and seems to be the presently accepted view.

and losses to intermediate diffraction orders. Both arise as a result of coupling between the dressed states (within their respective (anti)symmetric subspaces). These corrections can be derived in a number of ways, and are a subject of ongoing research. One general approach is to use “adiabatic perturbation theories”, as discussed in Ref. [108]. Alternatively, an iterative scheme based on adiabatic elimination can be used to obtain an expansion of the pendellösung frequency in  $q$  and  $\dot{q}$ , yielding non-adiabatic corrections [58]. One can also use results from Landau-Zener theory to obtain corrections resulting from the interaction between neighboring dressed states [63].

Using the nonadiabatic corrections derived in Ref. [58], we can give a plausible adiabaticity condition which is much easier to use than Eq. (7.46). By requiring that the lowest-order (in  $\dot{q}/q$ ) correction to the pendellösung frequency is small gives

$$\left| \frac{\dot{q}}{q} \right| \ll 4 \left( \sum_{j=1}^{n-1} j^{-1} \right)^{-1}. \quad (7.47)$$

The right-hand side of the above inequality is the  $(n-1)$ st harmonic number, usually denoted as  $H_{n-1}$ . For Gaussian pulses of the form (7.29), the inequality translates to

$$\sigma \gg \sum_{j=1}^{n-1} \frac{1}{j} \approx \log\left(n - \frac{1}{2}\right) + \frac{1}{24(n-1)^2} + 0.577..., \quad (7.48)$$

where the approximation follows from one of the well-known upper bounds on  $H_n$  [109] and is accurate to at least 0.005 for  $n \geq 3$ . The offset 0.577... is the Euler-Mascheroni constant  $\gamma$ . The condition Eq. (7.48) is much more convenient for back-of-the-envelope calculations than Eq. (7.46), but potentially less reliable. That is because it only bounds the nonadiabatic phase corrections, and not the losses.

## Weak grating: the Bragg approximation

The Bragg approximation is a solution of the diffraction dynamics to leading order in the grating strength  $q$ . The expression for the pendellösung frequency in this approximation is [58–60]

$$\Omega_n(q) = \frac{2q^n}{4^{n-1}[(n-1)!]^2}. \quad (7.49)$$

In principle, Eq. (7.49) can be obtained by treating the stationary Schrödinger equation (7.31) using time-independent perturbation theory. While possible<sup>11</sup>,

<sup>11</sup>The expressions for arbitrary-order corrections to energies and wavefunctions in time-independent perturbation theory are readily available [110].

this is highly inefficient, because the pendellösung frequency depends only on the difference of the energy corrections to the symmetric and antisymmetric states  $|n^\pm\rangle$ . This difference vanishes up to order  $n - 1$ , while the corrections to the energies and to the wavefunctions do not. A direct solution would thus involve an exponential number of terms which cancel in the final result.

A more efficient, indirect way of obtaining Eq. (7.49) is by adiabatic elimination of the intermediate states  $|n - 1\rangle, \dots, |-n + 1\rangle$  (assuming  $n > 0$ ). We do this in Appendix C, loosely following Ref. [58]. Yet another way is to invoke the  $N$ -level atom analogy [59, 60] and use the (perturbative) expression for the  $n$ -photon Rabi frequency<sup>12</sup>. The results from all these approaches can be verified using the tabulated expansions of Mathieu eigenfunctions  $a_n(q)$  and  $b_n(q)$ , which give the pendellösung frequency directly via Eq. (7.40).

Intuitively, the physics behind diffraction in the Bragg regime is that of tunneling. When the lattice potential is turned on, the initial state  $|n\rangle$  is no longer an eigenstate of the Hamiltonian and begins to disperse. With sufficient time, the particle can tunnel through the energy-forbidden states to the degenerate  $|-n\rangle$  state on the opposite side of the energy parabola. This picture agrees with the sharp decrease of the pendellösung frequency with  $n$ : The width of the potential barrier increases with the diffraction order, which suppress the tunneling rate immensely<sup>13</sup>.

An important qualitative feature of the Bragg regime is the vanishing difference between sudden and adiabatic pulses. That is because for very small  $q$  the difference between the bare and the dressed states becomes negligible. In particular, this means that sudden switching of the potential does not excite additional dressed states, because their overlap with the initial state is small.

It is justified to ask how small  $q$  must be for Eq. (7.49) to hold. This can always be checked by comparing the approximate expression with the exact value (7.40), as we do in Fig. 7.3. However, a rough analytic expression for the limit of the Bragg approximation is useful for back-of-the envelope calculations. A simple limitation on  $q$  is obtained from the derivation of Eq. (7.49) by adiabatic elimination (see Appendix C). Adiabatic elimination requires that  $q$  is much smaller than the smallest energy gap between  $|\pm n\rangle$  and the intermediate states.

<sup>12</sup>By comparing Eq. (7.25) to Eq. (15.10-2) in Ref. [94], we see that the analogy holds for cumulative detunings  $\Delta_j = j^2 - n^2$  and Rabi frequencies  $\Omega_j = 2q(\tau)$ . Inserting these into Eq. (15.11-6) in Ref. [94] gives the pendellösung frequency (7.49).

<sup>13</sup>This behavior is reminiscent of the dynamics of a particle in a double well potential and of a popular lecture demonstration in which many pendulums of different lengths are attached to a common base. In the latter, if two of the pendulums have the same length and one is excited, the energy can be seen to flow from one resonant pendulum to the other and back with little excitation of the non-resonant ones.



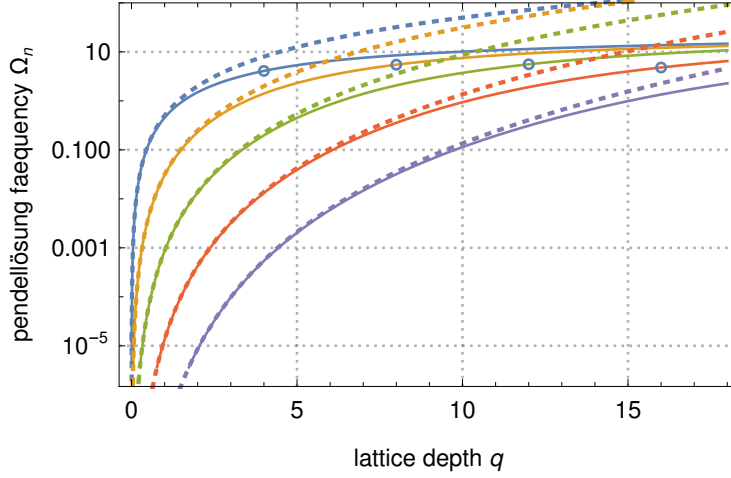


Figure 7.3: Pendellösung frequency for diffraction orders  $n = 2, \dots, 6$  (from top to bottom). The continuous lines show the exact result (7.40), while the dotted lines show the Bragg approximation (7.49). Circles on the exact curves show the limit (7.50) of the validity of the Bragg approximation.

This gives

$$q \ll 4(n-1). \quad (7.50)$$

This condition is illustrated in Fig. 7.3 with dots on the exact-solution curves for  $q = 4(n-1)$ . For the diffraction orders shown, we find that this condition consistently predicts the values of  $q$  for which the relative error of the approximation reaches a fixed value. In Ref. [58], the authors derive a different condition by requiring that the  $q^{n+2}$  correction to Eq. (7.49) is small. This gives

$$q \ll \frac{2(n^2 - 1)}{\sqrt{n+2}}. \quad (7.51)$$

We find that Eq. (7.51) limits the absolute error of the approximation more consistently, but the relative error less consistently than Eq. (7.50). A comparison of the exact and approximate pendellösung frequencies with experimental values can be found in Ref. [111].

### Thin grating: the eikonal and Raman-Nath approximations

The last approximation applies when the transverse motion of the particle within the grating can be neglected. For any grating strength and initial transverse momentum of the particle, this becomes a good approximation when the grating is sufficiently thin. The approximation is introduced by dropping the kinetic

term in the Hamiltonian (7.6a). Up to a global phase, the evolution operator is then

$$U = \exp \left\{ -\frac{i \cos(2kx)}{2\hbar} \int_{-\infty}^{\infty} V(t) dt \right\} = \sum_{n=-\infty}^{\infty} (-i)^n J_n \left( \frac{1}{2\hbar} \int_{-\infty}^{\infty} V(t) dt \right) e^{2inkx}, \quad (7.52)$$

where  $J_n$  are the Bessel functions of the first kind.

Equation (7.52) is referred to as the Raman-Nath [58] or Bessel-function approximation [59], or as Kapitza-Dirac scattering [5]. It can be thought of as a result of applying the “elementary eikonal” approximation<sup>14</sup> [47] to the  $\cos^2(kx)$  standing-wave potential. In the diffraction described by Eq. (7.52), the orders are arranged symmetrically around the initial beam and their populations do not depend on the incidence angle. This approximation has been sufficient to describe all the diffraction elements used in high-mass interferometry so far [47].

Approximation (7.52) holds when the kinetic-energy term in the Hamiltonian can be neglected in comparison to the potential term. For pure states extending over many grating periods, this is the case when  $V(t)$  is much larger than the instantaneous transverse kinetic energy spread  $\Delta E_k(t)$ . Importantly, the action of Eq. (7.52) inflates  $\Delta E_k$  leading to a breakdown of the approximation for long grating pulses. To find an approximate bound on the interaction time, we note that the action of the evolution operator (7.52) implies a momentum transfer with a magnitude

$$\Delta p(t) \approx \left| k \int_{-\infty}^t dt' V(t') \right|. \quad (7.53)$$

This is justified by noting that  $J_n(x)$  are small for arguments  $x < n$ . The time dependence of  $\Delta E_k(t)$  can then be estimated taking into account the initial transverse momentum  $p_0$ , giving

$$\Delta E_k(t) \approx \begin{cases} \frac{(|p_0| + \Delta p(t))^2}{2m} & \text{when } |p_0| < \Delta p(t), \\ \frac{2|p_0|\Delta p(t)}{m} & \text{otherwise,} \end{cases} \quad (7.54a)$$

$$(7.54b)$$

where the first case corresponds to the state extending onto both arms of the kinetic-energy parabola and the second to it remaining on one. Equation (7.54) further assumes that the initial transverse kinetic energy spread can be neglected compared to the one resulting from diffraction.

---

<sup>14</sup>This approximation is “elementary”, because it neglects the motion of the particle entirely. This is in contrast to the conventional eikonal method in optics or in scattering theory, which treats the motions as uniform instead.

To obtain a practical criterion, we specialize to the case of a Gaussian pulse of the form (7.29). Inserting it into Eq. (7.53) and integrating over time gives

$$\Delta p(t = \infty) = 2\sqrt{2\pi}q_{\max}\sigma\hbar k. \quad (7.55)$$

Inserting the momentum transfer into Eq. (7.54) and requiring that  $\Delta E_k(t = \infty) \ll V(0)$  gives the conditions

$$\sigma \ll \frac{2\sqrt{q_{\max}} - |\eta|}{2\sqrt{2\pi}q_{\max}} \quad \text{when} \quad |\eta| < 2\sqrt{2\pi}q_{\max}\sigma, \quad (7.56a)$$

$$\sigma \ll \frac{1}{2\sqrt{2\pi}|\eta|} \quad \text{otherwise,} \quad (7.56b)$$

where again  $\eta = p_0/\hbar k$ . These conditions generalize the  $4\sqrt{2q}\sigma < 1$  of Ref. [62] to nonzero incidence angle.

### 7.3 Numerical solution

The numerical solution of the Schrödinger equation with Hamiltonian (7.6a) is relatively straightforward. That is because of the block structure of the Hamiltonian, which allows for the reduction of the problem to a system of linear ordinary differential equations. A convenient starting point for the numerical solution are the Raman-Nath equations in the form (7.27). We use these combined with the Gaussian grating pulse given in Eq. (7.29). The resulting equations are easily truncated, written in matrix form, and integrated using any ordinary differential equation solver. Depending on the context, we have used either `NDSolve` from `MATHEMATICA` or the Schrödinger equation solver `sesolve` from `QU TIP`, the Quantum Toolbox in Python [112, 113].

Examples of the results are shown in Fig. 7.4, where we plot the efficiency understood as the fraction of the population found in the target state at the end of the grating pulse. For an initial state  $|\psi(0)\rangle = |n\rangle$ , this is  $|\langle -n|\psi(t \rightarrow \infty)\rangle|^2$ . As expected, we see that the efficiency oscillates both as a function of interaction time and of lattice depth. Importantly, an interaction time  $\sigma > 0.1$  is necessary to see diffraction largely irrespective of the desired order. We also notice that for the interaction times shown, high-order diffraction requires strong potentials with classical turning points. This can be seen by noting that a particle in state  $|n\rangle$  will have a classical turning point when  $q > n^2/4$ .

### 7.4 Classical dynamics

In this section we consider the classical analogue of the diffraction problem. A classical counterpart of a plane wave initial state is an ensemble of particles

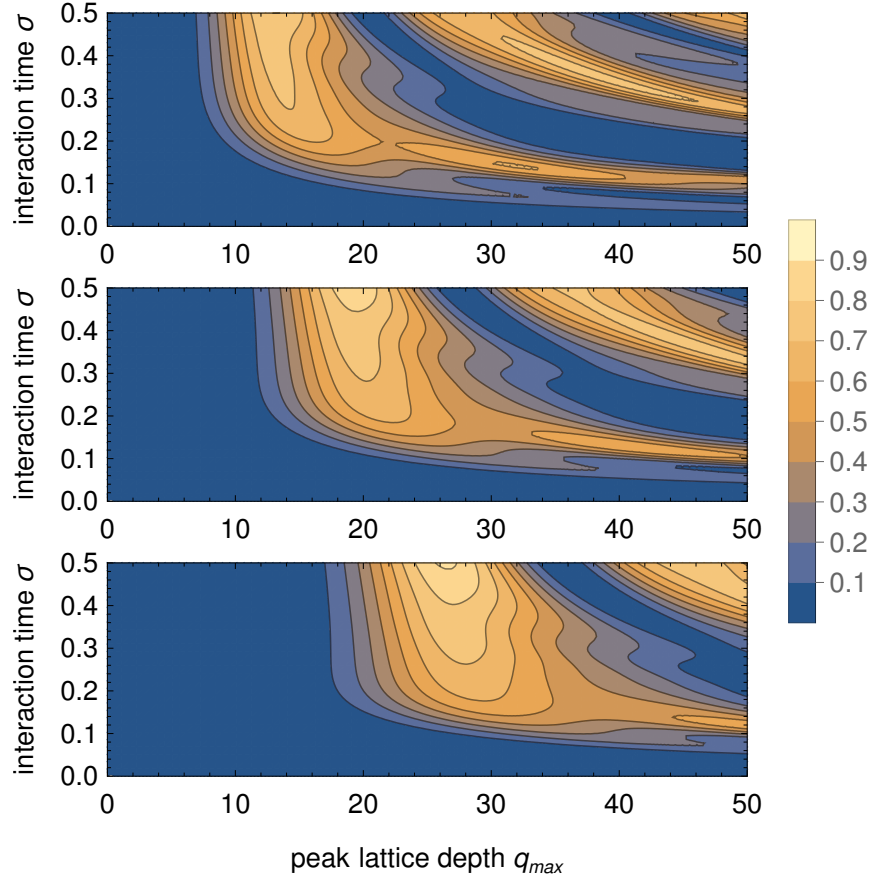


Figure 7.4: Efficiency of fourth-, fifth-, and sixth-order diffraction (from the top) as a function of dimensionless grating thickness  $\sigma$  and peak grating strength  $q_{\max}$ .

moving with the same velocity and distributed evenly in space. Since the problem is periodic in  $x$ , it suffices to consider particles distributed within one period  $(0, \pi/k]$ . The trajectory of each particle is found by integrating the Newton's equations

$$\frac{dx}{dz} = \frac{v_x}{v_z}, \quad (7.57a)$$

$$\frac{dv_x}{dz} = -\frac{1}{mv_z} \frac{dV}{dx}. \quad (7.57b)$$

Specializing to the case of the Gaussian pulse of the form (7.7)

$$V(z) = V(0)e^{-2z^2/w_z^2} \cos^2(kx), \quad (7.58)$$

and introducing the dimensionless coordinates  $\tilde{x} = kx/\pi$ ,  $\tilde{z} = z/w_z$ , we obtain

$$\frac{d\tilde{x}}{d\tilde{z}} = \tilde{v}_x \quad (7.59a)$$

$$\frac{d\tilde{v}_x}{d\tilde{z}} = \beta e^{-2\tilde{z}^2} \sin(2\pi\tilde{x}), \quad (7.59b)$$

where

$$\tilde{v}_x = \frac{k w_z v_x}{\pi v_z}, \quad \beta = \frac{V(0)k^2 w_z^2}{\pi m v_z^2}. \quad (7.60)$$

The classical evolution is therefore determined by two dimensionless parameters: the interaction strength  $\beta$  and the initial transverse velocity  $\tilde{v}_x$ . To find the correspondence between these and the quantum parameters  $q_{\max}$ ,  $\sigma$ ,  $\eta$ , we first use the definitions (7.13) and (7.30) and get

$$\beta = \frac{8}{\pi} q_{\max} \sigma^2. \quad (7.61)$$

We then use the definition (7.28) of  $\eta$  to obtain

$$\tilde{v}_x(z \rightarrow -\infty) = \frac{2}{\pi} \eta \sigma. \quad (7.62)$$

To solve Eq. (7.59) for an ensemble of  $N$  particles at once, we introduce indices  $v_i, x_i$ ,  $i = 1, 2, \dots, N$  and a vector  $X$  such that  $X_{v_i}, X_{x_i}$  are the velocity and position of particle  $i$ . The derivative  $dX/d\tilde{z}$  is then given by Eq. (7.59a) for the velocity indices and by Eq. (7.59b) for the position indices. The initial conditions are given by  $X_{x_i} = i/N$ , which gives evenly spaced particles, and by Eq. (7.62). We solve the initial value problem obtained in this way using the `solve_ivp` routine from `SciPy`. Example trajectories for a fixed interaction time and a few potential depths are shown in Fig. 7.5. There, we also show the histograms of the particles' final transverse momenta in units of  $\hbar k$ , obtained analogously as  $\eta$  in Eq. (7.62).

Based on Fig. 7.5 we can already expect some qualitative similarities between the classical and the quantum dynamics. For example, we see that as a function of potential depth, the momentum of the outgoing particles oscillates between  $\pm p_0$ , where  $p_0$  is the initial transverse momentum<sup>15</sup>. However, the full extent of the similarity can only be appreciated in a side-by-side comparison, which we present in Section 8.3 when analyzing the experimental data. More examples of classical trajectories and a discussion of the long-interaction limit can be found in Ref. [114].

<sup>15</sup>The restriction of outgoing transverse momenta to  $\pm p_0$  is a result of the approximate conservation of forward kinetic energy and is understandably predicted both by quantum and by classical mechanics.

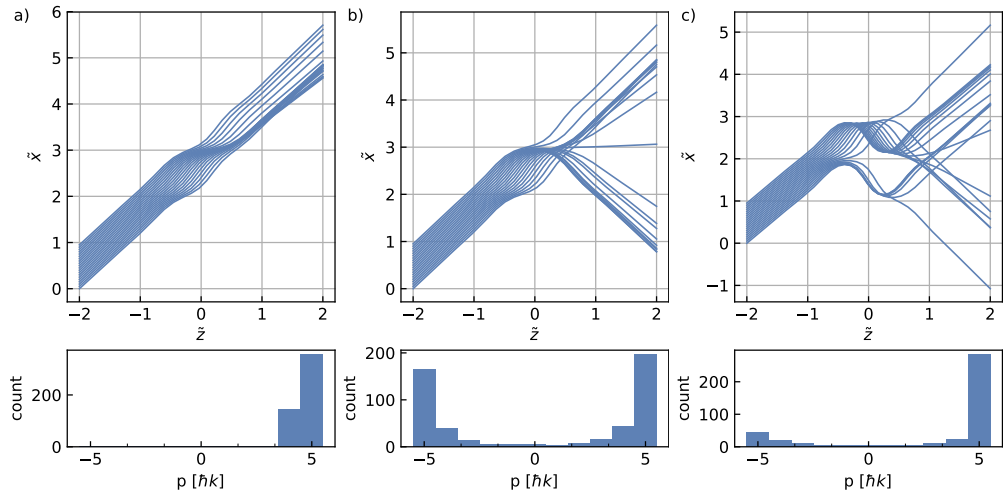


Figure 7.5: Classical trajectories of particles in a sinusoidal potential (top) and the histograms of final velocities (bottom) for three different potential depths,  $q_{\max} = 12, 14, 25$  respectively in (a), (b), and (c). The initial transverse momentum of the particles is  $\eta = 5$ , and the grating thickness is  $\sigma = 0.38$ . The parameters in (b) correspond to our ciprofloxacin diffraction experiment in Fig. 8.5 for molecules traveling at  $250 \text{ m s}^{-1}$ . We calculate 500 trajectories evenly spaced in one grating period, plotting one in 25 in the top figures.

## Chapter 8

# Demonstration of Bragg diffraction of massive molecules

In this chapter, we describe the experimental demonstration of the Bragg diffraction of organic molecules with a mass of a few hundred Da [78]. We will focus on the author's contributions to the experimental design, simulation, and data analysis. The measurements were performed by Christian Brand, Ksenija Simonović, Stephan Troyer, and Christian Knobloch.

### 8.1 Experiment design

For Bragg diffraction to occur, the particle must have a nonzero velocity component along the axis of the optical lattice. This can be obtained in three basic experimental configurations illustrated in Fig. 8.1. In the configuration shown in panel (a), the lattice is moving coaxially with the particle beam. This is the

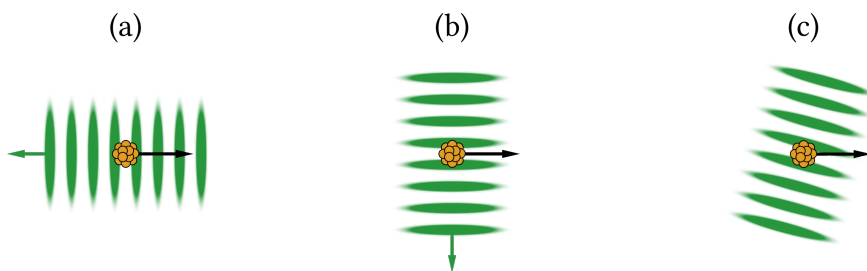


Figure 8.1: Illustration of the basic possible configurations for a Bragg diffraction experiment. a) Coaxial particle and laser beams, grating moving in the lab frame. b) Perpendicular particle and laser beams, grating moving in the lab frame. c) Particle and laser beams at an angle, grating stationary in the lab frame.

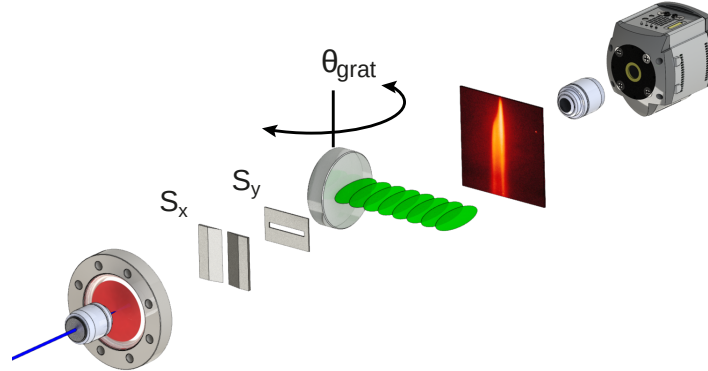


Figure 8.2: Far-field diffraction setup used for the demonstration of molecular Bragg diffraction. The consecutive elements are (from bottom left): laser desorption source, horizontal delimiter  $S_x$ , vertical delimiter  $S_y$ , laser grating, screen, objective, and a CCD camera. Image reprinted from Ref. [78].

configuration typically employed in present-day atom interferometers. There, the moving lattice is obtained using two frequency-shifted, counterpropagating light fields. Unlike the other two configurations, it is only compatible with pulsed particle beams, which limits its applicability to high-mass interference.

In the configuration shown in panel (b), the particle beam is strictly perpendicular to a moving optical lattice. This configuration is rarely used, but has a number of advantages. First, the velocity component which determines the order of Bragg diffraction is independent of the particle's forward velocity. This could be especially important for high-mass interference experiments, which can usually afford only moderate velocity selection. Second, this configuration allows one to employ some advanced multi-lattice splitting techniques, such as double-Bragg diffraction [75].

In the configuration shown in panel (c), a moving optical lattice is avoided by tilting the grating with respect to the particle beam. This is the configuration used in our experiment, as well as in early atomic Bragg diffraction experiments [67, 115]. This configuration has two properties which make it disadvantageous in the long run. First, the particle's forward velocity simultaneously influences the transverse momentum component and the grating interaction time (provided the grating is not pulsed). Second, it relies on moving mechanical parts while requiring the orientation of the mirror to be stable on a microradian level. In our case, with measurement times reaching 30 hours, this level of stability proved challenging to achieve.

A schematic view of the experimental setup is shown in Fig. 8.2. In simplified terms, the apparatus consists of a laser desorption source, a pair of delimiters,



Particle	$m$ [Da]	$\alpha'_{\text{st}}$ [ $\text{\AA}^3$ ]	$\alpha'_{532}$ [ $\text{\AA}^3$ ]	$\sigma_{532}$ [ $\text{cm}^2$ ]	$(\alpha'/\sigma\lambda)_{532}$
PcH <sub>2</sub> <sup>a</sup>	515	101 [117]		$9.6 \times 10^{-18} \text{ }^\dagger$	0.20
TPP <sup>b</sup>	614	105 [118]		$1.7 \times 10^{-17} \text{ }^\dagger$	0.11
C <sub>60</sub>	720	89–98 <sup>‡</sup>	87 <sup>‡</sup>	$2.8 \times 10^{-18} \text{ }^\ddagger$	0.58
C <sub>70</sub>	40	109–123 <sup>‡</sup>	114 <sup>‡</sup>	$2.5 \times 10^{-17} \text{ }^\ddagger$	0.09
$\beta$ -carotene	537	211–229 [18]	83 [18]	$6.9 \times 10^{-18} \text{ }^\dagger$	0.23
DBATT <sup>c</sup>	376	69 <sup>d</sup>	54 <sup>d</sup>	$9.6 \times 10^{-18} \text{ }^\dagger$	0.11
Ciprofloxacin	331	44 [119]	38.9 <sup>d</sup>	$<3.0 \times 10^{-20} \text{ }^\S$	>28

<sup>a</sup> Phthalocyanine. <sup>b</sup> Thiamine pyrophosphate. <sup>c</sup> Dibenzanthanthrene. <sup>‡</sup> Ref. [120].  
<sup>d</sup> Calculated by Armin Shayeghi. <sup>†</sup> Obtained from PhotochemCAD absorption spectra using Eq. (A1) from Ref. [48]. Except DBATT: spectral data from Ref. [121]. <sup>§</sup> This is an upper bound corresponding to the absorption cross section at 390 nm in a methanol solution [122].

Table 8.1: Candidate molecules for the experimental demonstration of Bragg diffraction. The parameters listed are: mass, static and optical polarizability volume, absorption cross section, and a dimensionless parameter reflecting the ratio of dipole phase to the number of absorbed photons. In the last column, the static polarizability is used in place of the optical one when the latter is not available.

the laser grating, and a fluorescent detection stage. The total length of the particle beam is 2.1 m with the grating located about 1.5 m downstream from the source. The grating itself is formed by retroreflecting a 532 nm laser with up to 30 W of power. The 7 mm thickness of the grating is achieved using a cylindrical lens, resulting in a vertical radius of the grating (about 50  $\mu\text{m}$ ) being much smaller than the horizontal one. This achieves a high peak light intensity, but makes precise alignment necessary. The delimiters are located directly in front of the grating and are used for collimation, as well as for velocity selection. A detailed description of the setup can be found in Refs. [78, 116].

## Choice of the molecule

The choice of candidate molecules for the demonstration experiment is largely dictated by the laser desorption source and by the fluorescence detection stage. To be compatible with the source, the molecule must withstand the thermal strain of desorption without fragmenting. As the detection offers no mass resolution, the integrity of the desorbed molecules must be verified independently (see the Supplemental Material to Ref. [78]). To be detected, the molecule must absorb

at the excitation laser wavelength<sup>1</sup> and fluoresce strongly and long enough while adsorbed on a quartz plate. From the molecules which are known or expected to be compatible with the source and detection setups, we shortlisted the candidates shown in Table 8.1.

In addition to the source and detection requirements, the molecule should have a low absorption at the grating wavelength. That is to avoid scrambling of the diffraction pattern by the recoils of the absorbed photons. Since absorption can be made less significant in a molecule with higher polarizability by decreasing light intensity, the molecules must be compared using the ratio of the dipole-force phase to the mean number of absorbed photons. This ratio is proportional to the parameter  $\alpha'/\sigma\lambda$ , introduced in Table 2.1. A quick glance singles out ciprofloxacin, which was thus used to obtain the most representative diffraction patterns. However, because of low detection efficiency it was not possible to use it for series of multiple measurements or for alignment. In these cases, phthalocyanine was used.

### Choice of grating parameters

The necessary thickness of the grating was determined using the Raman-Nath simulations shown in Fig. 7.4. From these, we infer that a dimensionless interaction time  $\sigma \gtrsim 0.25$  is necessary for high-efficiency diffraction. This holds largely independently of the diffraction order or grating power. To satisfy this condition for fast ciprofloxacin molecules traveling at about  $350 \text{ m s}^{-1}$ , we require  $w_z \gtrsim 6.5 \text{ mm}$ . This motivates the experimental value  $w_z \approx 7 \text{ mm}$ . The available grating power in the experiment is  $30 \text{ W}$ , which focused to such  $w_z$  and  $w_y = 45 \mu\text{m}$  gives  $q_{\text{max}} \approx 35$ . According to Fig. 7.4, this should easily allow us to reach sixth-order diffraction.

## 8.2 Diffraction image simulation

A simulation of the diffraction image is performed by building on the simple procedure for integrating the Raman-Nath equations described in Section 7.3. The parameters necessary for the simulation are listed in Table 8.2. The simulation procedure is as follows

1. For an extended source, calculate the  $x$  positions of the point sources that will be used to approximate it. The source is assumed to have a Gaussian profile and the spacing between the samples is smaller around the peak

---

<sup>1</sup>In the present experiment, 661 nm excitation was used for phthalocyanine and 420 nm or 266 nm for ciprofloxacin [116].

Element	Parameters
Particle	polarizability mass
Source	radius x position <sup>a</sup>
Delimiter	z position width height
Grating	y position z position y offset <sup>b</sup> z radius y radius wavelength power incidence angle
Detector	y position z position height
Simulation	momentum grid spacing x grid points y grid points interaction region depth source points

<sup>a</sup> Averaged over for an extended source (see caption).

<sup>b</sup> Optional. Grating is assumed to have infinite extent if not given, but grating y radius still determines light intensity.

Table 8.2: Parameters entering the simulation of the diffraction images. The origin of the coordinate system is taken at the center of source. If the source has a finite size, many images with nonzero  $x$  positions are generated and averaged. If the simulation is to include the weighing of velocity classes, a velocity distribution must additionally be specified.

than it is in the tails. An adequate list of samples is obtained by taking evenly spaced samples in the  $(0, 1)$  interval and mapping them with the quantile function of the Gaussian distribution (`norm.ppf` from `SciPy`).

2. Calculate the vertical positions of the image lines on the screen. The number of lines is a parameter of the simulation ( $y$  grid points), and the lines are evenly spaced starting from the detector  $y$  position and extending to this position decreased by detector height.
3. For each point source and line
  - a) Calculate the forward velocity component  $v_z$  of the molecular velocity class arriving at this height on the screen. We assume that the source is located at the origin, and the  $z, y$  positions of the delimiter and the landing site on the screen are  $z_1, y_1$  and  $z_2, y_2$ , respectively. The velocity  $v_z$  is found by solving for the leading coefficient of the free fall parabola  $y = az + bz^2$ . One obtains

$$b = \frac{y_1 z_2 - y_2 z_1}{z_1 z_2 (z_1 - z_2)}. \quad (8.1)$$

The velocity  $v_z$  then follows from the condition  $d^2 y / dt^2 = 2bv_z^2 = -g$ , where  $g$  is the gravitational acceleration. Introducing  $\Delta y = y_2 - z_2 y_1 / z_1$ ; i.e., the vertical distance from the infinite-velocity line, we have

$$v_z = \sqrt{\frac{g z_2 (z_1 - z_2)}{2 \Delta y}}. \quad (8.2)$$

- b) Prepare the initial state in the plane of the delimiter, immediately after it. We model the two distinct horizontal and vertical delimiters with a single delimiter placed at their average  $z$  position. The initial state is prepared in position space. Its modulus squared is Gaussian with a standard deviation equal to the width of the delimiter (a parameter of the simulation). Its phase is quadratic in  $x$  and corresponds to a paraxially-approximated spherical wave originating at the current point source location.
  - c) Calculate the dimensionless scattering parameters  $\sigma, q_{\max}, \eta$ . If the grating  $y$  offset is given, the light intensity entering  $q_{\max}$  is scaled to correspond to the height at which the molecules pierce the grating. Otherwise the vertical variation of intensity is neglected and peak intensity is used.

- d) Transform the state to momentum space using a fast Fourier transform and perform the diffraction calculation as described in Section 7.3.
  - e) Propagate the result from the end of the interaction region to the  $z$  position of the screen and transform to position space. The propagation is performed by multiplying with a transfer function in the Fresnel approximation<sup>2</sup>.
4. For each point source, stack the lines vertically and average all the point-source diffraction images by intensity. The averaging is performed with Gaussian weights to reflect the assumed profile of the source. Note that by changing the weights one can adjust (within limits) the effective source size without redoing any time-consuming calculations.
  5. Apply a vertical Gaussian blur to the resulting image to account for the finite vertical extent of the source and of the delimiter.
  6. Weigh the image vertically using an experimental height-intensity distribution or a postulated velocity-intensity distribution. Care has to be taken when using a velocity distribution, as the mapping between  $v_z$  and position on the screen is not linear, and therefore the transformation linking the two distributions is not a simple point substitution. The height distribution  $\rho(y)$  is related to the velocity distribution  $\rho(v)$  via

$$\rho(y) = \left| \frac{dv}{dy} \right| \rho(v) \approx \left| \frac{dv_z}{dy} \right| \rho(v_z), \quad (8.3)$$

where the approximation is justified because the  $v_z$  is much bigger than the transverse velocity components.

The above procedure proved accurate enough to qualitatively reproduce the data, despite making a number of approximations which we now discuss. First, the initial state prepared after the delimiter is Gaussian in intensity, even though the slit is square. Initial versions of the simulation used a square profile, but the ringing artifacts thus introduced take an excessive number of point-source images to average out. A better result was achieved using a Planck-taper profile [123], but ultimately a Gaussian was chosen as it allows one to obtain the observed, nearly-Gaussian profile of the molecular beam even with quick point-source simulations.

Second, the vertical position of the delimiter is neglected, because to first approximation it only changes the position of the image on the screen. The

---

<sup>2</sup>Even though the experiment in which the measurements were made is referred to as the “far-field setup”, the Fraunhofer approximation is not fully justified in its description.

forward velocity component is independent of the vertical position of the delimiter (see Eq. (8.2)), but the magnitude of the particle's velocity at the source is not. However, we assume that the  $v_z$  is large enough and the delimiter is approximately at the same height as the source, so that the initial vertical velocity component is small for all molecules reaching the screen. The approximation in Eq. (8.3) is then justified.

An important part of the simulation procedure is verifying if the simulation grid is large and dense enough to accurately represent the evolution of the quantum state. To do this, we first note that the grid is defined by two parameters: the number of points and their separation in momentum space. From these, the size of the grid in momentum space as well as its size and point separation in position space follow. The two grid parameters must be chosen such that four conditions are met: the grid has to be large enough and dense enough in position and in momentum space. The size conditions are easy to check, as the expected position and momentum extent of the state is known. For point density we use the following criteria

1. At least two grid points per  $2\pi$  of phase of the initial state over its spatial extent.
2. At least two grid points per  $2\pi$  of phase of the propagation kernel for the highest momentum component we expect (equal to the initial transverse momentum of the particle). The most stringent requirement here is set by the slow velocity classes.

## 8.3 Experimental data and analysis

### Early ciprofloxacin data

The first high-quality diffraction image obtained with ciprofloxacin is shown in Fig. 8.3 (a). The data is consistent with the population oscillating between two diffraction orders in addition to small losses in the lower part of the image (see Fig. 8.3 (c)). Based on the incidence angle and the 57 cm drift length between the grating and the screen, we would expect a separation of  $17(6) \mu\text{m}$  between the diffracted and the undiffracted beams. This is slightly smaller than seen in the data, but within the uncertainty if we include a finite collimation angle, as discussed next.

The separation between the beams appears to increase from top to the bottom of the image; that is, with decreasing forward velocity. This suggests that the momentum transfer is approximately constant, and the increasing separation is a result of increasing flight time for the lower velocity classes. The entire diffracted

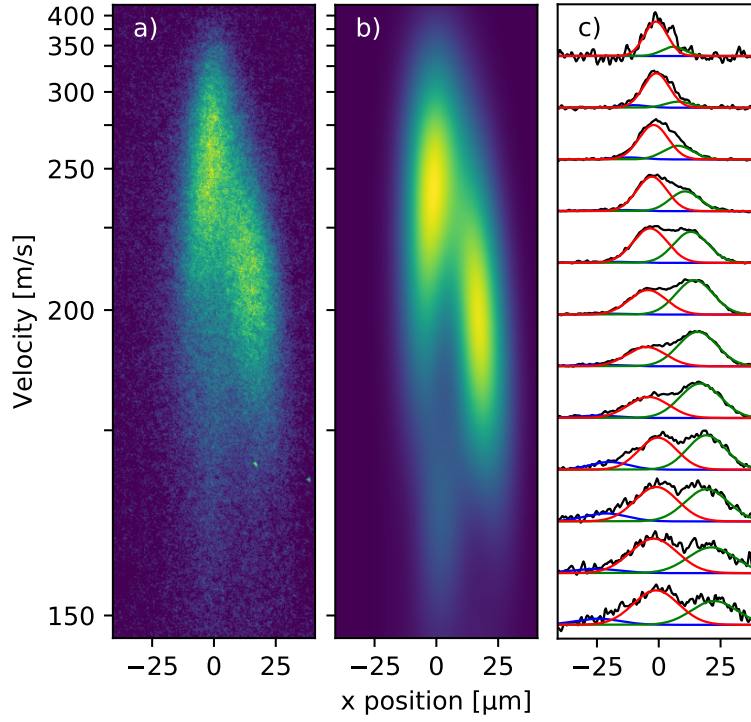


Figure 8.3: a) False-color diffraction image of ciprofloxacin at an incidence angle of  $15(5)\mu\text{rad}$ . The grating power is  $29.3(2)\text{W}$  and the grating radii are  $w_y = 44(1)\mu\text{m}$ ,  $w_z = 7.05(5)\text{mm}$ . The delimiters  $S_x$  and  $S_y$  are set to  $8\mu\text{m}$  and  $45\mu\text{m}$ , respectively. The velocity axis is taken from the simulation (b), as the velocity distribution in the beam is not known. b) Simulated diffraction image fitted to the data in (a), yielding an incidence angle of  $18(2)\mu\text{rad}$  and a vertical grating offset of  $90(10)\mu\text{rad}$  (see text). The simulation uses Raman-Nath equations (7.27) with  $l \approx 300$  truncated to  $|j| \leq 2048$ . The source radius is  $12\mu\text{m}$  (standard deviation) and is approximated by averaging 9 point source images. c) Vertically binned experimental data (black) with Gaussian fits to the diffraction orders (red, green, blue). The data is smoothed with a Gaussian filter with a radius of 1 camera pixel, corresponding to about  $0.4\mu\text{m}$ . Stephan Troyer performed the fit in panel (c).

structure is thus most likely a single diffraction order. The broad resonance is a result of three factors: a natural width of the Bragg resonance resulting from a finite  $\sigma$ , the wide opening of  $S_y$  leading to weak velocity selection, and a relatively broad collimation angle. The latter is between  $3\ \mu\text{rad}$  and  $10\ \mu\text{rad}$  and can only be estimated crudely. That is because it is very sensitive to the source size and to the exact transmission profile of the  $S_x$  delimiter, which are not well known<sup>3</sup>.

The velocity distribution in the beam is not known a priori, so the magnitude of the momentum transfer cannot be inferred from the data in a straightforward way. However, expecting a peak velocity of about  $200\ \text{m s}^{-1}$  we can calculate that  $25\ \mu\text{m}$  separation between the peaks on a screen  $57\ \text{cm}$  away corresponds to a momentum transfer of about  $4\hbar k$ ; that is, second-order diffraction. Importantly, this is the highest-order diffraction that could have been observed in this setup for any incidence angle. This disagrees with the prediction we made based on Fig. 7.4 that  $30\ \text{W}$  of power should be sufficient to observe diffraction up to sixth order. We have suspected that this could be caused by a vertical misalignment of the molecular and the light beams. If the molecules were only skimming the edge of the grating, they would experience significantly smaller light intensity than at the center. This would in turn decrease the maximal diffraction order.

To investigate that, we have performed a least-squares fit of the numerically simulated diffraction image to the observed one, as described in Appendix D. We have obtained the best agreement with the data for a vertical offset of  $90(10)\ \mu\text{rad}$  between the centers of the  $S_y$  delimiter and the grating. This means that the grating was most likely significantly below the molecular beam, and that a big portion of the molecules only experienced a vanishing light intensity. Neglecting free fall between the delimiter and the grating, we estimate that the molecules passing near the bottom of the  $S_y$  would experience about 12% of the peak intensity (and molecules passing higher up would experience even less). This corresponds to  $q_{\text{max}} \approx 4$ , for which second order of diffraction is the highest possible, as confirmed by a simple Raman-Nath simulation.

---

<sup>3</sup>The desorption laser is focused to a  $1.3\ \mu\text{m}$  radius, but depending on the thickness of the molecular layer on the desorption window the effective source size can be many times larger. The lower bound on the collimation radius comes from assuming a point source, and the upper bound is from a source size estimated as in the Supplemental Material to Ref. [78]. We suspect that the effective transmission of the  $S_x$  might deviate from a simple boxcar function, because using the latter made it very hard to recreate the experimental profile of the undiffracted beam in a simulation.



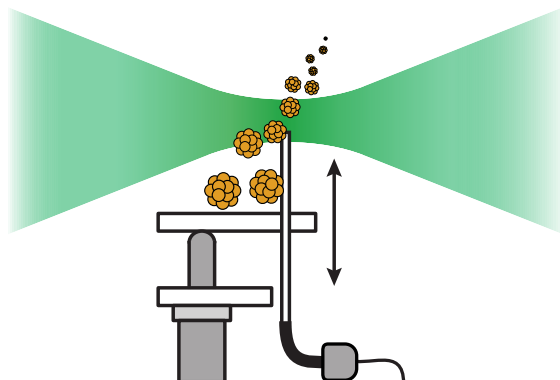


Figure 8.4: Aligning the grating and the molecular beam using an optical fiber mounted on a scanning stage. Adapted from a figure prepared by Christian Brand.

### New ciprofloxacin data

In order to decrease the vertical offset between the molecular and the laser beams, it was necessary to develop a new in-vacuum alignment technique [124]. The technique employs a cleaved optical fiber inserted into the laser beam on a scanning arm (see Fig. 8.4). By measuring the light intensity coupled into the fiber while moving its tip through the beam, the center of the grating can be found. Once this is done, the fiber tip is held in place and the molecular beam is aligned using the shadow of the fiber tip visible in the molecular pattern. This allows for very good alignment and its verification between experimental runs. The details of the technique can be found in Refs. [116, 124].

In addition to improved alignment, the second experiment uses a slightly larger vertical grating radius of  $55(5)\mu\text{m}$  and a smaller  $S_y$  opening of  $25\mu\text{m}$  in order to make the intensity experienced by the molecules even more uniform (to cope with the decreased flux, the excitation wavelength in the detection stage had to be changed). As the 30 W grating laser was no longer available, the new experiment uses a grating power of  $14.6(2)\text{ W}$  which results in  $q_{\text{max}} \approx 14$ . Based on the simple Raman-Nath simulations in Fig. 7.4, we expect to see up to about 20% efficiency of fifth order diffraction with this grating depth. This finds confirmation in the data, shown in Fig. 8.5 (a). The separation of  $50\mu\text{m}$  at  $250\text{ m s}^{-1}$  corresponds to a momentum transfer of about  $10\hbar k$ ; i.e., fifth order diffraction.

The improved alignment, smaller  $S_y$  opening, and the resulting clear separation of the diffracted beam simplified the fitting of the simulated image (Fig. 8.5b). In particular, we were able to neglect the variation of light intensity with height, which decreased the number of fitting parameters by removing the grating offset.

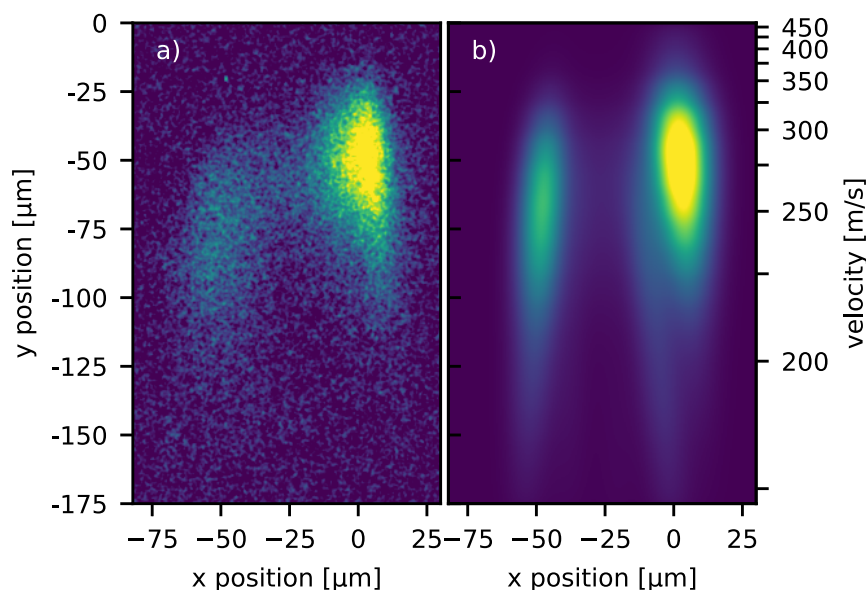


Figure 8.5: a) False-color diffraction image of ciprofloxacin at an incidence angle of  $-43(5)\mu\text{rad}$  and with the  $S_x$  delimiter set to  $14\mu\text{m}$  (remaining parameters as discussed in the text). b) Simulated diffraction image fitted to the data in (a), yielding an incidence angle of  $-44\mu\text{m}$ . The simulation uses Raman-Nath equations (7.27) with  $l = 700$  truncated to  $|j| \leq 8192$ . The source radius is  $12\mu\text{m}$  (standard deviation) and is approximated by averaging 50 point source images.

The remaining two parameters (incidence angle and peak velocity) were found by matching the position of the diffracted beam. The incidence angle was chosen so that the separation between the diffracted and the undiffracted beams in the simulation matched the data. This gave essentially the experimental incidence value of  $-44\mu\text{m}$ . Then, the vertical alignment of the two figures was found by matching the heights at which the diffracted peaks reach half of their maximal intensities. With the vertical alignment in place, we could weigh the simulation with the empirical height-intensity distribution, yielding the final simulated image. Since the forward velocities in the simulation are known, the vertical alignment also determines the forward velocities in the experimental image. This allowed us to calculate the most probable velocity in the beam<sup>4</sup> of  $250\text{ m s}^{-1}$ . Throughout the process, the source size was kept at the value of  $12\mu\text{m}$  found

<sup>4</sup>More precisely, aligning the two images first gives us the velocity corresponding to the highest intensity on screen, which is  $270\text{ m s}^{-1}$ . To obtain the probability distribution of velocities in the beam, we have to multiply the intensity distribution by the inverse of the Jacobian from Eq. (8.3). The peak of the transformed distribution is then the most probable velocity in the beam.

when analyzing the first ciprofloxacin data.

### Phthalocyanine power and incidence scans

Because of the tilted-grating configuration of our experiment, the interaction time and the initial transverse momentum change simultaneously as a function of vertical position in a diffraction image. In order to isolate the dependence on just one diffraction parameter, it is necessary to take a series of diffraction images and focus on a single forward velocity class. However, taking multiple consecutive diffraction images is not feasible with ciprofloxacin because of the low detection efficiency and thus long integration time. This can be alleviated by switching to the dye molecules phthalocyanine, for which series of diffraction images as a function of incidence angle and of power have been obtained. The downside of using phthalocyanine is its measurable absorption at the grating wavelength, which is difficult to account for theoretically<sup>5</sup>. Additionally, even for phthalocyanine the beam could only be collimated to a transverse momentum spread of multiple photon momenta, which clouds the analysis.

The dependence of the diffraction of phthalocyanine on grating power is shown in Fig. 8.6. As the power is increased, we observe two major effects: the increasing separation between the diffracted and the undiffracted beams, and the oscillating population transfer between the two beams (the intensity of the diffracted beam exceeds that of the undiffracted one for  $P \approx 4$  W and again for  $P \approx 10$  W). While the oscillating momentum transfer is expected from the dependence of the pendellösung frequency on power, the increasing separation is not. Indeed, the momentum transfer depends only on the initial transverse momentum  $\eta$ , which is held constant. This expectation is confirmed by a simple plane-wave simulation shown in Fig. 8.6 (e).

The most probable cause of the discrepancy lies in the broad collimation of the molecular beam. As can be seen from the 0 W trace in Fig. 8.6 (d), the momentum spread in the beam amounts to nearly  $5\hbar k$ . This is broad enough to explain the appearance of multiple diffraction orders. In particular, with the incidence angle corresponding to a mean transverse momentum of  $3\hbar k$ , we can expect diffraction orders as low as the first. As a result, consecutively higher diffraction orders become populated as the power is increased, leading to an appearance of a continuously increasing momentum transfer.

The dependence of the diffraction of phthalocyanine on the incidence angle is shown in Fig. 8.7. For plane-wave illumination, we would expect the separation between the diffracted and the undiffracted beams to be proportional

---

<sup>5</sup>We estimate that molecules traveling at about  $150 \text{ m s}^{-1}$  will absorb about one photon on average for the typical beam size we use and 10 W of power (see Supplemental Material of Ref. [78]).

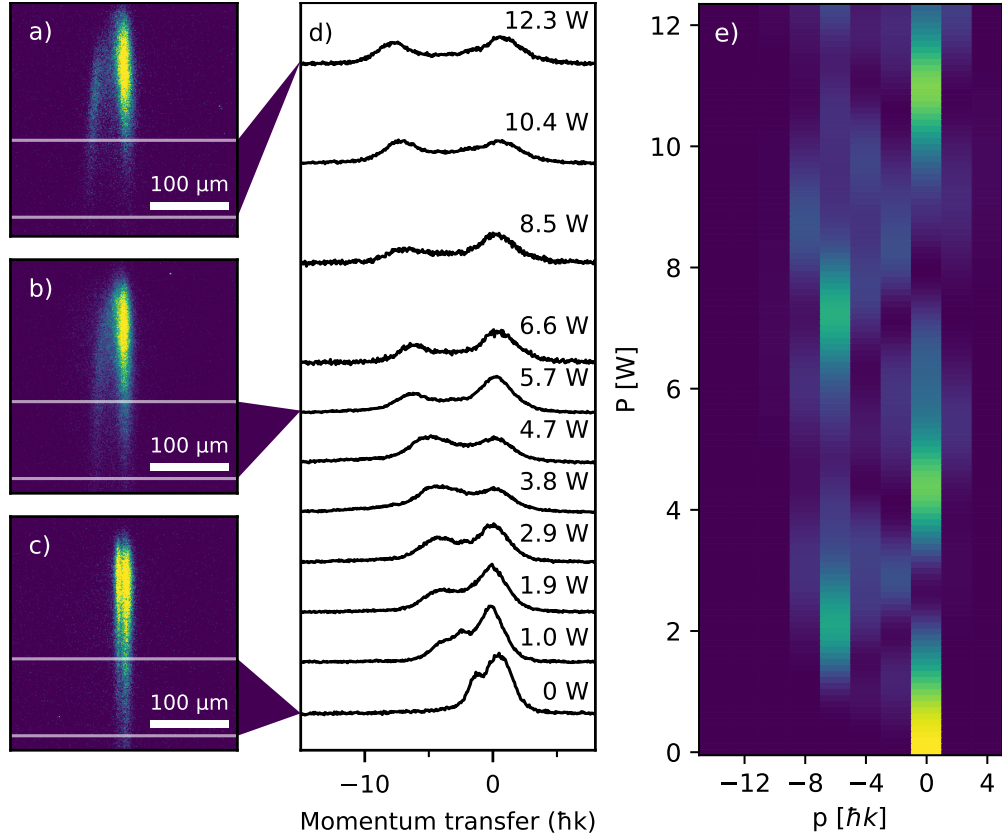


Figure 8.6: a, b, c) False-color diffraction images of phthalocyanine at different grating powers. The incidence angle is about  $30 \mu\text{rad}$ , which corresponds to  $\eta \approx 3$  for the low velocities shown in (d). The double peak at 0 W is accidental and caused by a hole in the collimation delimiter. d) Integrated intensity profiles showing the dependence of diffraction on grating power for velocities from  $143 \text{ m s}^{-1}$  to  $175 \text{ m s}^{-1}$ . e) The dependence of momentum transfer on laser power, calculated using the Raman-Nath equations for plane-wave illumination and a velocity of  $160 \text{ m s}^{-1}$ . The vertical laser grating radius is  $w_y = 54(2) \mu\text{m}$  and (in the data) the collimation slit width is  $12.5 \mu\text{m}$ . Stephan Troyer performed the velocity fitting (as described in the Supplemental Material of Ref. [78]) and prepared the panels a–d.

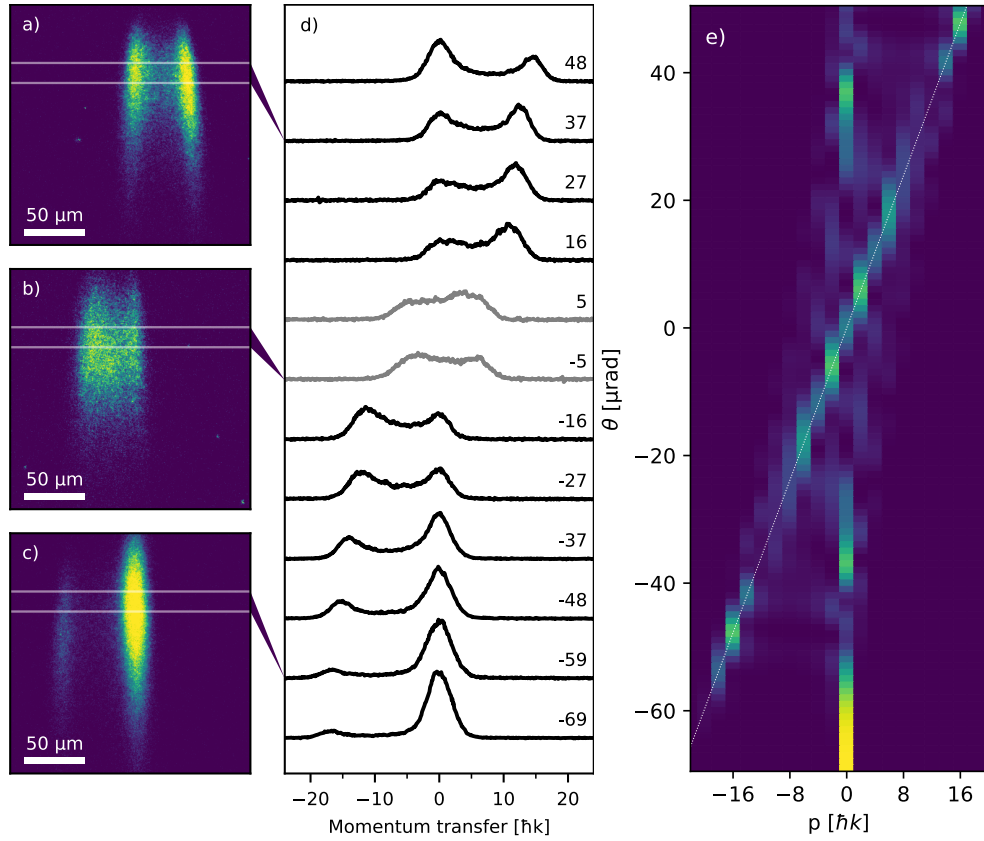


Figure 8.7: a, b, c) False-color diffraction images of phthalocyanine at different incidence angles. d) Integrated intensity profiles for velocities from  $234 \text{ m s}^{-1}$  to  $255 \text{ m s}^{-1}$ . The profiles are manually aligned to center the undiffracted peak (that is the right peak for negative incidence and the left peak for positive incidence). The alignment of the small-angle profiles (shown in gray) is ambiguous and thus we align them by their center of mass. e) The dependence of momentum transfer on grating incidence, calculated using the Raman-Nath equations for plane-wave illumination and a velocity of  $244 \text{ m s}^{-1}$ . The dotted line shows the geometric reflection condition. The vertical laser grating radius is  $w_y = 65(5) \mu\text{m}$  and (in the data) the collimation slit width is  $14.8 \mu\text{m}$ . Stephan Troyer performed the velocity fitting and prepared the panels a–d.

to the incidence angle. This expectation is confirmed by a numerical calculation shown in Fig. 8.7 (e), in which the Bragg resonances fall on the geometric reflection line. In the data, the dependence of the separation of the peaks on the incidence is clearly compressed. For example, upon changing the incidence angle from  $-16\ \mu\text{rad}$  to  $-69\ \mu\text{rad}$  the separation increases by a factor of only 1.5 instead of the expected 4.3.

We believe that this is again a result of moderate collimation of the molecular beam. From the  $-69\ \mu\text{rad}$  profile we can read that the momentum spread in the beam approaches  $10\hbar k$ . Because of this, the  $16\hbar k$  diffraction visible in the simulation in Fig. 8.7 (e) can be seen even for angles much smaller and much larger than the resonant  $48\ \mu\text{rad}$ . This effectively flattens the dependence of peak separation on the incidence angle.

## Comparison with classical dynamics

In Fig. 8.8 we compare the quantum and the classical dynamics as a function of all three diffraction parameters: the incidence angle, the interaction time, and the grating depth. The parameters in these figures are chosen to match the corresponding experiments; that is, the phthalocyanine angle and power scans, and the ciprofloxacin image in Fig. 8.5. Importantly, the quantum images only show the plane waves with transverse momenta equal to even multiples of  $\hbar k$ , omitting the unpopulated odd- $\hbar k$  plane waves in between. This approximately accounts for the effective momentum resolution available in our experiments. Because the collimation of the molecular beam always spans multiple photon recoils, the stepwise nature of the momentum transfer is not clearly visible in our data. Given this coarse momentum resolution, we find that the dependence of quantum and classical dynamics on all diffraction parameters is nearly identical. We must therefore conclude that the presented data do not show clearly quantum behavior (which has been demonstrated under the same conditions and in the same experimental setup on other occasions [125]).

Importantly, the close correspondence between the coarse-grained quantum and classical dynamics is not specific to our choice of grating parameters. By performing numerical comparisons like the one in Fig. 8.8, we find that it is instead generic and holds in a large portion of the  $\sigma$ - $q_{\text{max}}$  parameter space. In particular, experiments demonstrating atomic Bragg diffraction [67, 126] or channeling [62], as well as Bragg-based atom interferometers [115] operate in this regime<sup>6</sup>. However, in these experiments the atomic beams are typically collimated to below a photon recoil, which makes the quantum nature of the

---

<sup>6</sup>Experiments which are deep in the classical regime include the manipulation of molecular gases with optical lattices created by ultrashort laser pulses [127].

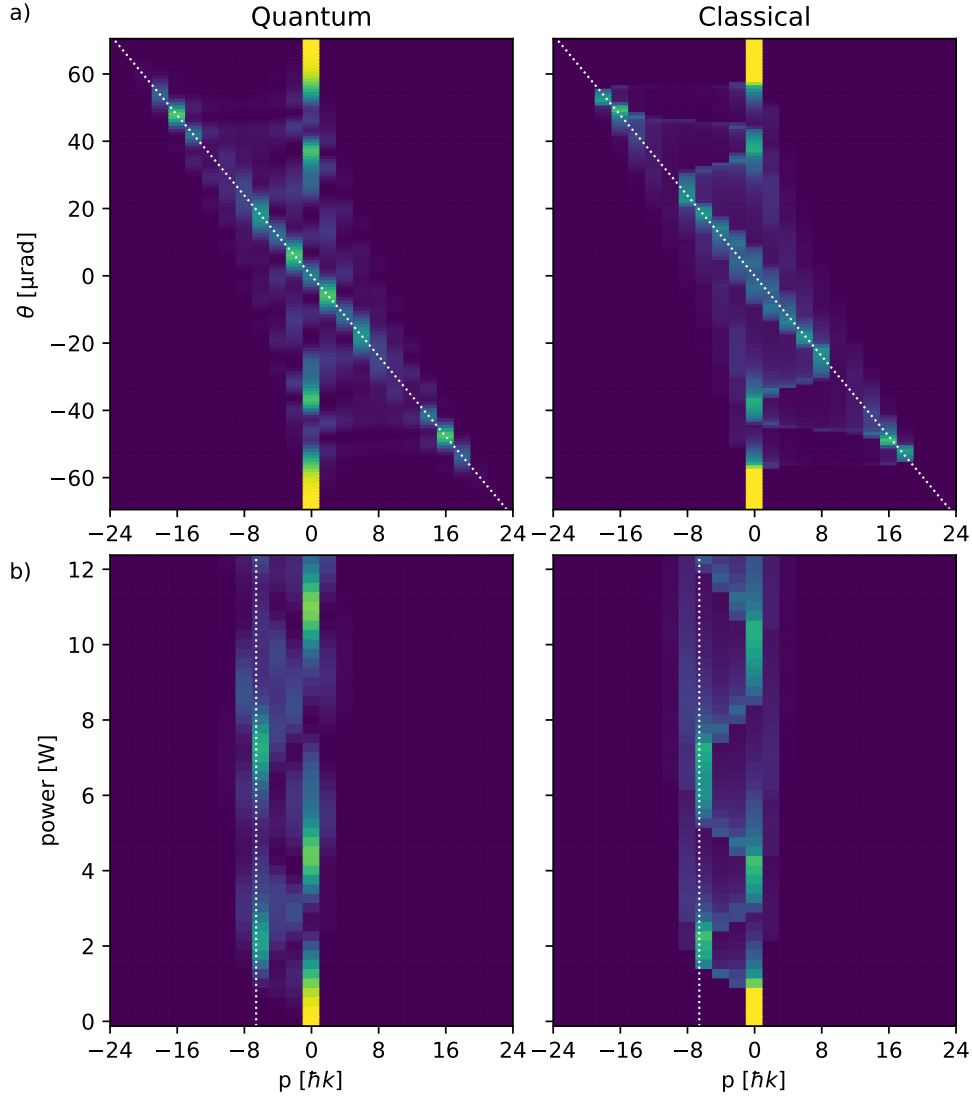


Figure 8.8: Diffraction efficiency assuming plane-wave illumination as a function of incidence angle (a) and grating power (b) in quantum and in classical mechanics. The parameters are chosen to match the phthalocyanine measurements: the angle scan (Fig. 8.7) in (a) and the power scan (Fig. 8.6) in (b). In the quantum plots, we do not show odd  $p$ , for which the population is identically zero. To match this, the classical momenta (which change continuously) are grouped into  $2\hbar k$  bins. The simulations are performed as described in Sections 7.3 and 7.4.

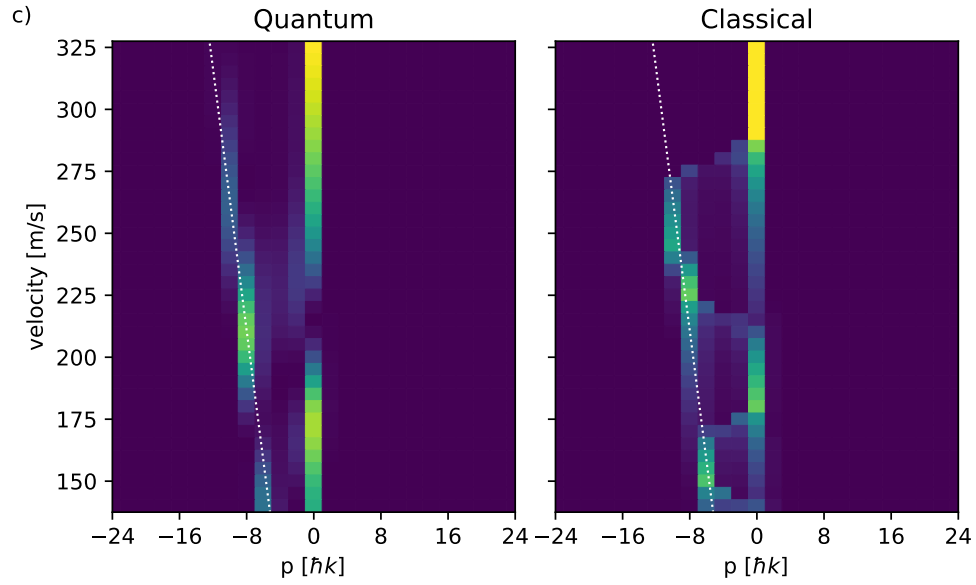


Figure 8.8: (Continued.) Diffraction efficiency as a function of forward velocity of the particle. The parameters are the same as in the ciprofloxacin diffraction image (Fig. 8.5).

observed phenomena evident. The observation of a quantum–classical difference without sub-recoil momentum resolution is possible, but requires extremely long interaction times ( $\sigma \geq 5$ ), which are usually only achievable with Bose-Einstein condensates [128].



## Chapter 9

# Talbot-Lau interference in toroidal traps

The physical limitation on the mass of a particle interfering in a Talbot-Lau interferometer is determined by the required periodicity of the initial state and the available coherent evolution time. In order to increase the latter, high-mass interference experiments are likely to follow the trajectory of their high-precision, atom-interfering counterparts: transitioning from horizontal-beam setups into vertical-beam fountain configurations, and ultimately to guided interferometers. The defining feature of the latter is that the matter waves are confined in trapping potentials for most or all of the interference time. Anticipating that, it is worthwhile to consider the ways in which the Talbot-Lau interference scheme could generalize to a guided scenario.

An interesting way to perform matter-wave interference in a trap follows from the description of the Talbot effect in Section 1.1. There, we stressed that the Talbot revivals of a quantum state are a result of the periodicity of the initial condition. This periodicity combined with the Hamiltonian of a free particle yields a commensurate energy spectrum, which in turn implies a periodic time evolution. In existing free-flight interferometers, the periodicity of the initial state is achieved using a diffraction grating. However, for guided matter waves an intriguing way to enforce periodicity is to trap the particle in a closed-loop waveguide. Combined with free evolution along the trap, this would result in a spontaneous Talbot effect and could allow for an interferometer scheme without diffraction elements or deformations of the trap.

We find that an interference scheme based on this idea is possible, even though it is unlikely to be optimal for the interference of record-breaking masses. That is because in this configuration the Talbot time is determined by the size of the trap, which cannot be decreased indefinitely. Nevertheless, we find the scheme to be a compelling macroscopic demonstration of the discreteness of

orbital angular momentum, and to offer some unique metrological possibilities.

In this chapter we largely follow our published work on the subject [129], but place much more emphasis on the conceptual similarities to Talbot-Lau interference. Additionally, we discuss the effect of imperfections in more detail and present simplified derivations of the main effects. We start by analyzing the Hamiltonian of a particle confined in a tight waveguide and showing that the Eq. (1.6), obtained in the context of Talbot-Lau interference, implies spontaneous beam splitting in toroidal waveguides. We then show that a complete interference scheme with sensitivity to external phase as well as to gauge fields is possible. The discussion is closed by a consideration of relevant imperfections and a numerical simulation of concrete proposed realization of the scheme with a noninteracting Bose-Einstein condensate (BEC). We choose to focus on cold atoms for the final proposal as with present technology the scheme would be the easiest to implement using this platform.

Finally, we want to highlight that the interference scheme we propose is related to experiments and proposals across many different fields. Most importantly to the experiments utilizing interferometric manipulation of orientational quantum revivals to control molecular alignment [130]. However, we also draw on the recent proposal to use orientational quantum revivals for a mesoscopic demonstration of quantum interference [131]. On the other hand, related work on center-of-mass revivals can be found in the context of toroidally-shaped quantum dots [132].

## 9.1 Particle in a curved waveguide

Equation (1.6) shows that a periodic state will evolve into a balanced superposition of two shifted copies of itself after half of the Talbot time  $T_T$ . However, this calculation only holds for a free-particle Hamiltonian. To investigate under what conditions the motion of a particle trapped in a waveguide is free (in the longitudinal direction), we analyze the Hamiltonian for a general curved waveguide. Analyzing the general Hamiltonian is also necessary to derive the leading-order corrections to the desirable free-particle dynamics, which we do later in this chapter.

We will assume that the waveguide follows a smooth and torsion-free curve  $\mathbf{r}(s)$ , which we parametrize by its arc-length  $s$ . The Hamiltonian is then expressed conveniently in the local Frenet-Serret coordinate system associated with the curve. To introduce it, we let  $\mathbf{t} = \mathbf{r}'$  (a prime denotes derivative with respect to  $s$ ) be the tangent vector of the curve. Then  $\kappa = |\mathbf{t}'|$  is the curvature and  $\mathbf{n} = \mathbf{t}'/\kappa$ ,  $\mathbf{b} = \mathbf{t} \times \mathbf{n}$  are the normal and binormal vectors. Using these, we

can define a local coordinate system  $(s, u, v)$  in which an arbitrary vector  $\mathbf{x}$  is given by  $\mathbf{x}(s, u, v) = \mathbf{r}(s) + u\mathbf{n}(s) + v\mathbf{b}(s)$ .

The Frenet-Serret coordinate system is curvilinear, and thus the normalization condition for a wavefunction  $\psi$  includes a nontrivial Jacobian<sup>1</sup>,

$$1 = \int ds du dv (1 - \kappa(s)u) |\psi(s, u, v)|^2. \quad (9.1)$$

From now on, we absorb it into the wavefunction and work with the rescaled  $\chi = \sqrt{f}\psi$ , where  $f(s, u) = 1 - \kappa(s)u$ . This will allow us to deform the waveguide (and thus the coordinate system) without having to re-enforce the normalization condition. With the preparation in place, we can express the Hamiltonian for the rescaled wavefunction  $\chi$  as [133, 134]

$$H = -\frac{\hbar^2}{2m} \left[ \partial_s \frac{1}{f^2} \partial_s + \partial_u^2 + \partial_v^2 + \frac{\kappa^2}{4f^2} + \frac{5(f')^2}{4f^4} - \frac{f''}{2f^3} \right] + V_u(u) + V_v(v), \quad (9.2)$$

where we have assumed that the trapping potential  $V$  separates  $V(s, u, v) = V_u(u)V_v(v)$ .

We now take the tight-confinement limit by expanding the Hamiltonian (9.2) to leading order in  $u$ . We do this by neglecting higher-than-leading powers of the ratios of  $u$  to the characteristic length scales at which  $\kappa$  and its derivatives change. These small quantities are:  $\kappa u$ ,  $\kappa' u / \kappa$ , and  $\kappa'' u / \kappa^2$ . The expansion gives

$$H \approx -\frac{\hbar^2}{2m} \left( \partial_s^2 + \partial_u^2 + \partial_v^2 + \frac{\kappa^2}{4} \right) + \frac{m\omega_{\perp}^2}{2} u^2 + V_v(v) \quad (9.3a)$$

$$- \frac{\hbar^2}{2m} \left[ 2\kappa u \left( \partial_s^2 + \frac{\kappa^2}{4} \right) + 2\kappa' u (1 + 3\kappa u) \partial_s + \frac{\kappa'' u}{2} \right], \quad (9.3b)$$

where we have also expanded the radial trapping potential  $V_u \approx m\omega_{\perp}^2 u^2 / 2$ . In Eq. (9.3), the terms in the first line are zeroth-order in the small quantities, whereas those in the second line are first-order. We will use the first-order terms in Section 9.3 to estimate the necessary transverse confinement, but first we focus on the zeroth-order ones.

## 9.2 Interference scheme

Equation (9.3a) gives the Hamiltonian of the particle neglecting the transverse extent of its state. We see that in this tight-confinement limit, the transverse

<sup>1</sup>In addition to being curvilinear, the coordinate system is local. This means that it is not well defined arbitrarily far away from the waveguide. For Eq. (9.1) to make sense, we must assume that the curvature of the waveguide is gentle compared to the transverse extent of the state  $\psi$ . This is not a limitation for us, as we will mostly be interested in the tight confinement limit.

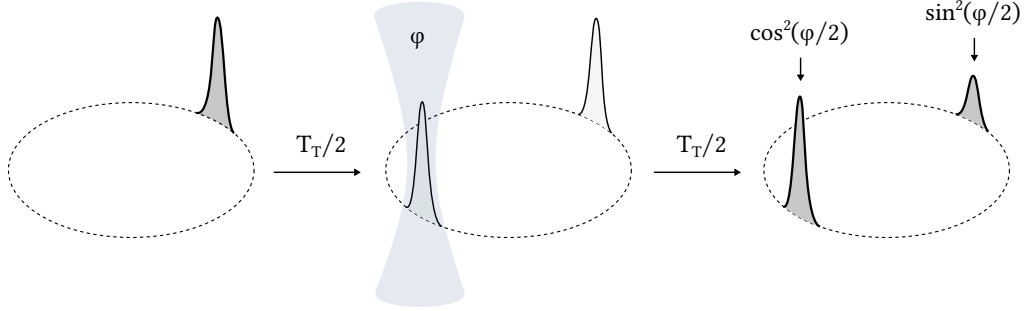


Figure 9.1: Beam-splitter-free interference in a toroidal trap. The free evolution leads to spontaneous coherent splitting of a localized wavepacket, and applying a phase to one of the components interferometrically controls the position of the revival.

and longitudinal dynamics decouple. The longitudinal motion is governed by the Hamiltonian

$$H_s = -\frac{\hbar^2}{2m} \left( \partial_s^2 + \frac{\kappa^2}{4} \right), \quad (9.4)$$

which describes a free particle when  $\kappa$  is constant; i.e., when the waveguide is toroidal. This means that a particle localized in a tight toroidal trap will exhibit the free-evolution beam splitting shown in Eq. (1.6). We now argue that in this case of toroidal trap not only beam splitting, but a full interferometric scheme is possible.

Since Eq. (1.6) holds for any state  $\chi(s)$  given the Hamiltonian (9.4), it is in fact a statement about the evolution operator  $U(T_T/2)$ ,

$$U\left(\frac{T_T}{2}\right)\chi(s) = \frac{e^{-i\pi/4}}{\sqrt{2}} \left[ \chi(s) + i\chi\left(s - \frac{d}{2}\right) \right], \quad (9.5)$$

where  $T_T$  is the Talbot time (1.4) and  $d$  is the spatial period of the state. If we imprint a phase  $e^{i\varphi}$  onto one of the superposition components above and then apply  $U(T_T/2)$  again, we get

$$U\left(\frac{T_T}{2}\right) \frac{e^{-i\pi/4}}{\sqrt{2}} \left[ \chi(s) + ie^{i\varphi}\chi\left(s - \frac{d}{2}\right) \right] = \frac{-i}{2} \left[ (1 - e^{i\varphi})\chi(s) + i(1 + e^{i\varphi})\chi\left(s - \frac{d}{2}\right) \right] \quad (9.6a)$$

$$= e^{i\varphi/2} \left[ \cos\left(\frac{\varphi}{2}\right)\chi\left(s - \frac{d}{2}\right) - \sin\left(\frac{\varphi}{2}\right)\chi(s) \right]. \quad (9.6b)$$

Therefore, imprinting a phase onto one of the superposition components in Eq. (9.5) interferometrically controls the position of the revival. This observation is at the core of the proposed interference scheme, shown in Fig. 9.1.

The most important (and the longest) time scale in the proposed protocol is the time necessary for the spontaneous beam splitting to occur. It is equal to half the Talbot time (1.4), which depends on the spatial period  $d$  of the state. For an initial state which is well localized in a circular trap with radius  $R$ , the latter is<sup>2</sup>  $d = 2\pi R$ , resulting in a Talbot time

$$T_T = \frac{m(2\pi R)^2}{h} = \frac{2\pi m R^2}{\hbar}. \quad (9.7)$$

A small but feasible trap might have  $R \approx 5 \mu\text{m}$ , which gives a Talbot time of  $2.5 \text{ ms Da}^{-1}$ . With coherence times of the order of a second, this proposed interference scheme could be thus applied to atoms and other light particles with masses of the order of 1 kDa or less.

Another important time scale is that of wavepacket dispersion. Not only does it determine the spreading of the initial state, but also the lifetime of the well-separated configuration in the middle of the interferometer protocol. It therefore determines the time one has to apply the phase  $\varphi$ . In the simplest scenario, the initial state will be prepared in an isotropic harmonic trap with the same frequency as the radial confinement and quickly transferred into the ring. Using the standard result for the dispersion of a Gaussian wavepacket, we can then argue that the components of the superposition will remain well separated for<sup>3</sup>  $t_d \approx 2/\omega_\perp$ . The ratio of time scales  $t_d/T_T$  can be expressed using the width of the initial state  $\sigma = \sqrt{\hbar/m\omega_\perp}$  as

$$\frac{t_d}{T_T} = \frac{1}{\pi} \left( \frac{\sigma}{R} \right)^2 = \frac{1}{\pi} (\sigma\kappa)^2. \quad (9.8)$$

In the tight confinement limit these time scales will therefore be vastly separated. A rule-of-thumb estimate with  $\sigma\kappa \sim 10^{-1}$  and  $T_T$  of the order of a second gives  $t_d \sim 10 \text{ ms}$ . This is short, but still much longer than a typical interaction of a particle with a grating in a Talbot-Lau interferometer, which is of the order of  $0.1 \mu\text{s}$  [21].

We now consider the possible origins of the phase difference in such an interferometer scheme. One natural choice is imprinting  $\varphi$  using a far-detuned

---

<sup>2</sup>The period  $d$  could be made smaller than the circumference of the trap by preparing an initial state with many identical lobes spaced regularly around the ring. This is an interesting possibility, but we leave it out for simplicity.

<sup>3</sup> $1/\omega_\perp$  is the time in which the ground state of a harmonic oscillator with frequency  $\omega_\perp$  doubles its width. We add a factor of two to account for the time of focusing, in addition to defocusing, of the wavepackets.

laser pulse. Since  $t_d$  can be much longer than a grating transit time in free-flight matter-wave interferometry, the magnitude of phase imprinted in this way could certainly be large enough to have a measurable effect. Alternatively, the trap could be tilted to introduce a gravitational phase shift between the two components. Assuming a tilt angle  $\theta$ , the magnitude of such phase shift would be

$$\varphi_g \approx \frac{2mgRt_d \sin \theta}{\hbar}. \quad (9.9)$$

For  $R \approx 5 \mu\text{m}$  and 1 mrad tilt, this is about  $0.15 \text{ rad Da}^{-1}$  and thus likely a measurable shift.

In a realization of the interferometer scheme with cold atoms, the phase difference could also arise due to atom-atom interactions. In order to obtain high-contrast interference, the interactions between the particles must be strongly suppressed throughout most of the interferometric sequence (see Section 9.4). Such suppression could be achieved using Feshbach tuning in select atomic species [135]. However, when the two superposition components are well separated, a weak magnetic field gradient along the separation axis would result in a measurable phase. This is a result of an opposite detuning of the two superposition components from the zero crossing of the Feshbach resonance. We can crudely estimate this phase using the self-interaction term of the Gross-Pitaevskii equation (9.40). The self-interaction potential is

$$V_{\text{int}} = \frac{4\pi\hbar^2 a N |\psi|^2}{m}, \quad (9.10)$$

where  $a$  and  $N$  are the scattering length and the number of atoms. Approximating  $N|\psi|^2$  with the mean atom density  $n$  gives

$$\varphi_{\text{int}} \approx \frac{V_{\text{int}} t_d}{\hbar} = \frac{4\pi\hbar\Delta a n t_d}{m}, \quad (9.11)$$

where  $\Delta a$  is the difference of the effective scattering lengths of the two wavepackets. With a high but achievable value  $n = 5 \times 10^{15} \text{ cm}^{-3}$  for a noninteracting condensate of  $^{39}\text{K}$  [136], this gives a phase of about  $50 \text{ rad } a_0^{-1}$ , where  $a_0$  is the Bohr radius. Therefore, the scheme could allow one to measure small scattering lengths with an accuracy of the order of  $10^{-2} a_0$ , an order of magnitude better than the state-of-the-art time-of-flight [137] or spectroscopic [138] measurements for  $^{39}\text{K}$ .

Introducing a magnetic field has one further effect on the interference scheme if the particle has a nonzero charge  $q$ . If we denote the tangential component of the vector potential by  $A(s)$ , the free longitudinal Hamiltonian (9.4) becomes

$$H_s = \frac{1}{2m} [i\hbar\partial_s + qA(s)]^2 \quad (9.12)$$

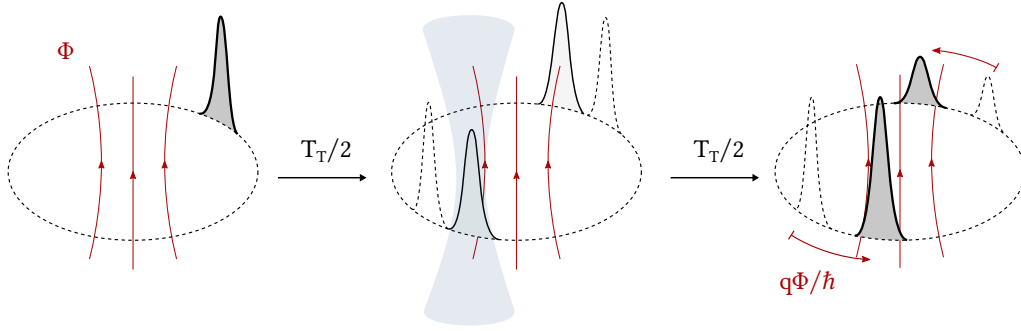


Figure 9.2: Performing the interference scheme with a charged particle in the presence of a magnetic field causes the pattern to rotate by an angle equal to the Aharonov-Bohm phase. Similar effect occurs for particles possessing an electrical or a magnetic dipole moment, as discussed in the text.

For now we specialize to the case of  $A(s) = \text{const.}$ , for which

$$H_s = -\frac{\hbar^2}{2m} \partial_s^2 + \frac{i\hbar q A}{m} \partial_s. \quad (9.13)$$

The two terms in the Hamiltonian commute, and the latter simply generates translations,

$$\exp\left(\frac{qAt}{m} \partial_s\right) \chi(s) = \exp\left(\frac{qAt}{m} \partial_s\right) \sum_{j=-\infty}^{\infty} \chi_j e^{2\pi i j s/d} = \sum_{j=-\infty}^{\infty} \chi_j \exp\left\{\frac{2\pi i j}{d} \left(s + \frac{qAt}{m}\right)\right\} \quad (9.14a)$$

$$= \chi\left(s + \frac{qAt}{m}\right). \quad (9.14b)$$

Therefore, the evolution by Hamiltonian (9.13) consists of the time-periodic free evolution discussed thus far, superimposed with a uniform rotation. At the end of the interferometric sequence, the rotation angle  $qAT_T/mR$  is equal to the Aharonov-Bohm phase  $q\Phi/\hbar$ , where  $\Phi = 2\pi RA$  is the circulation of the vector potential around the trap (and thus the flux of the magnetic field through the ring). The proposed interferometer scheme could therefore be used to demonstrate the Aharonov-Bohm and related effects, or for the measurement of magnetic fields. We illustrate the rotation effect in Fig. 9.2.

Importantly, for the rotation to occur, the magnetic field must be switched on quickly and only after the particle begins to evolve freely in the ring. To see this, we assume that before releasing into the ring the particle is held and cooled in a stationary trap. This means that the initial state is centered around zero kinetic momentum (the gauge-invariant momentum which determines the

kinetic term of the Hamiltonian). If the field is on during cooling this means  $\langle i\hbar\partial_s + qA \rangle = 0$ , whereas if the field is off this means  $\langle i\hbar\partial_s \rangle = 0$ . Therefore, in the field-on case the particle starts with a canonical momentum  $\langle -i\hbar\partial_s \rangle = qA$ , which exactly cancels the rotation shown in Eq. (9.14). Unless the particle is in a field-free region, this observation means that the rotation effect has a classical analog. The corresponding classical system is a charged bead constrained to move on a ring. If the flux of the magnetic field through the ring changes, it will induce a rotational electric field and accelerate the bead.

Finally, we show that for any magnetic field the tangential vector potential component  $A(s)$  can be made constant using a suitable gauge transformation. This makes the argument of the previous paragraph apply to any spatial dependence of the magnetic field. For a gauge transformation of the form  $A \mapsto A + \partial_s \phi$ , we find that it is sufficient to take

$$\phi(s) = \frac{s}{2\pi R} \int_0^{2\pi R} ds' A(s') - \int_0^s ds' A(s'). \quad (9.15)$$

The above  $\phi(s)$  satisfies the periodic boundary condition  $\phi(0) = \phi(2\pi R)$  and can be extended smoothly to a function on the entire space. After a gauge transformation with such  $\phi$ , the tangential component of the vector potential is

$$A(s) + \partial_s \phi = \frac{1}{2\pi R} \int_0^{2\pi R} ds' A(s') = \text{const.} \quad (9.16)$$

Additionally, we note that an analogous rotation effect can be obtained for particles carrying a dipole moment. The dipole can be either electric or magnetic, and could be either permanent or induced. In the case of an electric dipole  $\boldsymbol{\mu}$ , the treatment is the same as for a charged particle, but with  $qA$  replaced by  $(\boldsymbol{\mu} \times \mathbf{B}) \cdot \mathbf{t}$  [139, 140]. The rotation angle at the end of the interferometric sequence is then equal to the He-McKellar-Wilkens phase [139, 141]. In the case of a magnetic dipole  $\boldsymbol{\mu}_m$ , we would substitute  $qA$  with  $(\boldsymbol{\mu}_m \times \mathbf{E}/c^2) \cdot \mathbf{t}$  and the resulting angle would be equal to the Aharonov-Casher phase [142].

### 9.3 Imperfections

In this section, we analyze the robustness of the proposed interference scheme to a number of imperfections. First, we consider the effects of technical limitations: a tilt of the trap and its nonzero ellipticity. Second, we analyze the influence of the centrifugal barrier, which is a source of dephasing inherent to the scheme. For these three imperfections we will derive corrections to the energy spectrum, which in the unperturbed case is

$$E_j^{(0)} = \frac{\hbar^2 j^2}{2mR^2}, \quad (9.17)$$



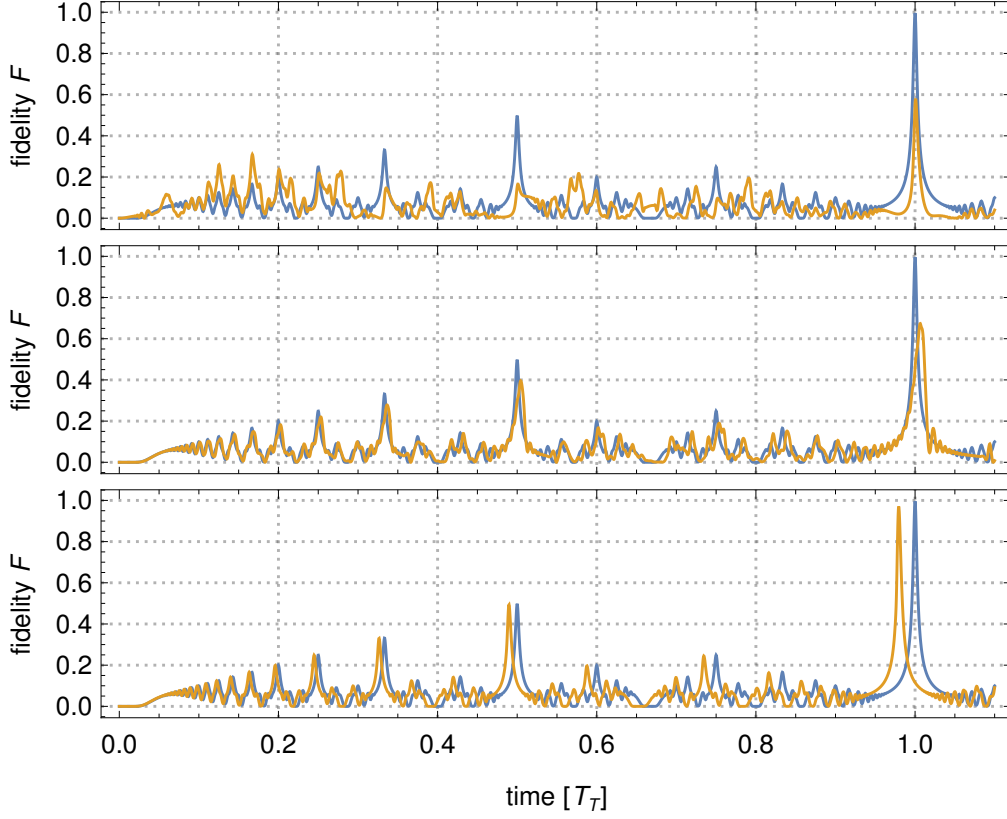


Figure 9.3: Fidelity of the revival in a toroidal trap in the presence of imperfections. The blue curves correspond to the ideal case of a one-dimensional revival. The orange curves show the influence of a tilt of 1 mrad (top), the centrifugal barrier (middle), and an elliptical deformation of the trap with an eccentricity of 0.5 (bottom). The parameters of the setup correspond to a realization with a noninteracting BEC of  $^{39}\text{K}$ , discussed in Section 9.4.

with corresponding eigenstates

$$\langle s|j\rangle = \frac{1}{\sqrt{2\pi R}} e^{ijs/R}. \quad (9.18)$$

Whenever the obtained energy corrections deviate from quadratic dependence on  $j$ , both the visibility and the timing of the revival will be affected. Disentangling those two effects analytically proves to be difficult. We therefore evaluate their effect numerically, by plotting the fidelity of the revival as a function of time. We define fidelity as the overlap of the final and the  $\pi$ -rotated initial state.

If the initial is

$$|\chi(0)\rangle = \sum_{j=-\infty}^{\infty} c_j |j\rangle, \quad (9.19)$$

then the overlap will be

$$F(t) = \left| \int_0^{2\pi R} ds \chi^* \left( 0, s - \frac{d}{2} \right) \chi(t, s) \right|^2 = \left| \sum_{j=-\infty}^{\infty} c_j c_j^* e^{i(\pi j - E_j t/\hbar)} \right|. \quad (9.20)$$

The first imperfection we consider is the presence of a potential of the form  $V(s) = V_0 \cos(s/R)$  throughout the interferometric sequence. Such potential could arise, for example, due to a permanent tilt of the trap. In this case, we would have  $V_0 = mgR \sin \theta$  for a tilt angle  $\theta$ . We can quickly see that a potential of this form does not shift the energies of the eigenstates  $|j\rangle$  to first order in  $V_0$ . That is because  $\langle j|V(s)|j\rangle = 0$ . To find the second-order correction we note that

$$\langle j|V(s)|k\rangle = \frac{V_0}{2} (\delta_{k,j-1} + \delta_{k,j+1}), \quad (9.21)$$

where  $\delta_{kj}$  is the Kronecker delta. Using this and the unperturbed energies (9.17), we find the second-order corrections

$$E_j^{(2)} = \frac{mR^2 V_0^2}{4\hbar^2} \left( j^2 - \frac{1}{4} \right)^{-1} = \frac{m^3 g^2 R^4 \sin^2 \theta}{4\hbar^2} \left( j^2 - \frac{1}{4} \right)^{-1}. \quad (9.22)$$

In Fig. 9.3, we show the effect of this correction for  $\theta = 1$  mrad and the parameters of the BEC setup we discuss in detail in Section 9.4. These are  $m = 39$  Da for potassium and  $R = 5.9 \mu\text{m}$ .

The next imperfection is the dephasing due to the centrifugal barrier. This will predominantly affect the high angular momentum states, which will be pushed outwards by the centrifugal force. Because of the larger equilibrium radius, the high- $j$  states will experience a different trapping potential than the low- $j$  states and gradually dephase. To quantify this effect, we must go beyond the one-dimensional treatment used thus far. We do this by considering the full Hamiltonian (9.3), specializing for now to a perfectly circular waveguide. Substituting  $\kappa = 1/R$  in Eq. (9.3) gives

$$H = -\frac{\hbar^2}{2m} \left( \partial_s^2 + \partial_u^2 + \frac{2u}{R} \left[ \partial_s^2 + \frac{1}{4R^2} \right] + \partial_v^2 \right) + \frac{m\omega_{\perp}^2}{2} u^2 + V_v(v). \quad (9.23)$$

In the dynamics described by Eq. (9.23), the out-of-plane motion (in the  $v$  coordinate) still separates. To see the separation of the longitudinal and radial motion, we write down the stationary Schrödinger equation for the in-plane dynamics,

$$\left\{ -\frac{\hbar^2 \partial_s^2}{2m} + \left( 1 + \frac{2u}{R} \right)^{-1} \left[ -\frac{\hbar^2}{2m} \left( \partial_u^2 + \frac{u}{2R^3} \right) + \frac{m\omega_{\perp}^2}{2} u^2 - E^{(su)} \right] \right\} \chi(s, u) = 0. \quad (9.24)$$

It admits separable solutions of the form

$$\chi_j(s, u) = \frac{e^{ijs/R}}{\sqrt{2\pi R}} \xi_j(u). \quad (9.25)$$

Inserting the above ansatz into Eq. (9.24) gives the equation for the radial state  $\xi_j$ ,

$$\left[ -\frac{\hbar^2 \partial_u^2}{2m} + \frac{m\omega_\perp^2}{2} (u + u_j)^2 \right] \xi_j(u) = \left( E_j^{(su)} - E_j^{(0)} + \frac{m\omega_\perp^2}{2} u_j^2 \right) \xi_j(u), \quad (9.26)$$

in which the  $j$ -dependent equilibrium position is

$$u_j = \frac{\hbar^2}{m^2 \omega_\perp^2 R^3} \left( j^2 - \frac{1}{4} \right). \quad (9.27)$$

Equation (9.26) describes a harmonic oscillator, and so its right-hand side must be equal to  $\hbar\omega_\perp n$  (since  $\omega_\perp$  does not depend on  $j$ , the constant  $\hbar\omega_\perp/2$  can be neglected). From this, we infer that the eigenvalues  $E^{(su)}$  of the in-plane motion are

$$E_{jn}^{(su)} = \hbar\omega_\perp n + E_j^{(0)} - \frac{m\omega_\perp^2}{2} u_j^2 = \hbar\omega_\perp n + E_j^{(0)} - \frac{\hbar^4}{2m^3 \omega_\perp^2 R^6} \left( j^2 - \frac{1}{4} \right)^2. \quad (9.28)$$

In Fig. 9.3, we show the effect of these corrections for  $\omega_\perp = 6.4$  kHz, corresponding to the BEC realization of Section 9.4.

The final imperfection we analyze is an elliptical deformation of the trap. We will parametrize the deformation with the eccentricity  $\varepsilon$ , which is 0 for a circle and between 0 and 1 for an ellipse. Nonzero eccentricity is especially likely in optical traps as a result of residual astigmatism in the trap-generating optics. An elliptical trap is also the simplest example in which the curvature potential  $\kappa^2(s)/4$  does not vanish. Alas, finding the leading-order correction in eccentricity is not as easy as inserting the curvature of the ellipse into the Hamiltonian Eq. (9.4). That is because the arc length  $s$  depends on the eccentricity, and through it also the normalization condition and the momentum operator  $-i\hbar\partial_s$ . To perform a systematic expansion in  $\varepsilon$ , we must therefore first move to a parametrization of the ellipse which does not depend on the eccentricity. To do this, we replace the arc length  $s$  with the eccentric anomaly  $\beta \in [-\pi, \pi)$ . Using the latter, an ellipse in the  $xy$  plane of the trap is parametrized as

$$x = R \cos \beta \quad y = R \sqrt{1 - \varepsilon^2} \sin \beta. \quad (9.29)$$

The line element is then

$$\frac{\partial s}{\partial \beta} = \sqrt{\left( \frac{\partial x}{\partial \beta} \right)^2 + \left( \frac{\partial y}{\partial \beta} \right)^2} = R \sqrt{1 - \varepsilon^2 \cos^2 \beta} \equiv \tilde{f}(\beta), \quad (9.30)$$

and the curvature is [143]

$$\kappa(\beta) = \sqrt{R(1 - \varepsilon^2)} [\tilde{f}(\beta)]^{-3/2}. \quad (9.31)$$

The normalization condition using the new longitudinal coordinate reads

$$1 = \int ds du dv |\chi(s, u, v)|^2 = \int d\beta du dv \tilde{f}(\beta) |\chi(\beta, u, v)|^2. \quad (9.32)$$

To make it  $\varepsilon$ -independent, we will use a rescaled wavefunction  $\zeta = \tilde{f}^{1/2} \chi$ . The Hamiltonian for  $\zeta$  will be<sup>4</sup>

$$H_\beta = \tilde{f}^{1/2} H \tilde{f}^{-1/2} = H_\beta^{(0)} + \varepsilon^2 H_\beta^{(2)}. \quad (9.33)$$

Applying the transformation to Hamiltonian (9.3) and expanding gives

$$H_\beta^{(0)} = -\frac{\hbar^2}{2m} \left[ \left( 1 + \frac{2u}{R} \right) \left( \frac{\partial_\beta^2}{R^2} + \frac{1}{4R^2} \right) + \partial_u^2 \right] + \frac{m\omega_\perp^2}{2} u^2, \quad (9.34)$$

in which we neglect the out-of-plane variable  $v$ , which remains decoupled from the dynamics in the plane of the trap. As expected, Eq. (9.34) is the same as the Hamiltonian for a circular trap, Eq. (9.23) (up to the constant  $1/4R^2$ , which we have omitted there). The unperturbed solutions are therefore again of the separable form (9.25),

$$\zeta_j = \frac{e^{ij\beta}}{\sqrt{2\pi}} \chi_j(u). \quad (9.35)$$

For the eccentricity term we obtain

$$\begin{aligned} H_\beta^{(2)} = & -\frac{\hbar^2}{4mR^2} \left[ 1 + \frac{3u}{R} + \left( 1 + \frac{5u}{R} \right) \cos(2\beta) \right] \partial_\beta^2 + \frac{\hbar^2 \sin(2\beta)}{2mR^2} \left( 1 + \frac{5u}{R} + \frac{9u^2}{R^2} \right) \partial_\beta \\ & - \frac{\hbar^2}{16mR^2} \left[ 1 + \frac{3u}{R} - \left( 1 + \frac{11u}{R} \right) \cos(2\beta) \right]. \end{aligned} \quad (9.36)$$

The expectation value of the above in the unperturbed states (9.35) will only have contributions from the non-oscillating terms, yielding

$$E_j^{(2)} = \frac{\hbar^2 \varepsilon^2}{8\pi m R^2} \left( 1 + \frac{3u_j}{R} \right) \left( j^2 - \frac{1}{4} \right). \quad (9.37)$$

As shown in Fig. 9.3, the corrections (9.37) affect mostly the timing of the revival, leaving the visibility largely unchanged. That is the case, because two of the three  $j$ -dependent terms in Eq. (9.37) are proportional to  $j^2$ . The remaining  $j^4$  term is suppressed by the small centrifugal offset  $u_j$ , resulting in relatively mild dephasing.

---

<sup>4</sup>The transformation of the Hamiltonian is justified as in Eq. (A.2), with the exception that the operator  $\tilde{f}^{-1/2}$  is time-independent and not unitary.

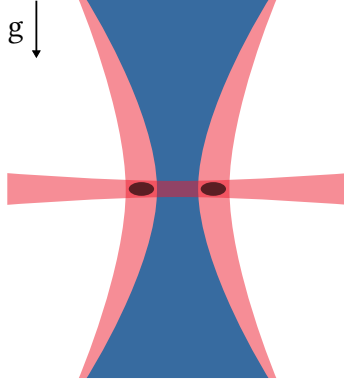


Figure 9.4: An optical torus trap as used in the proposed realization of the scheme with a BEC. The color of the beams corresponds to their detuning with respect to the atomic transition, and a cross section of the BEC is shown in black. The design of the trap is based on the setup in Ref. [144].

	Red	Blue	Sheet
Wavelength	830 nm	532 nm	830 nm
Dimensions <sup>a</sup>	13 $\mu\text{m}$	5.5 $\mu\text{m}$	5 $\mu\text{m} \times 200 \mu\text{m}$
Power	2 mW	2.5 mW	10 mW
Scattering rate	0.09 s <sup>-1</sup>	0.02 s <sup>-1</sup>	0.07 s <sup>-1</sup>

<sup>a</sup>  $e^{-2}$  intensity radii.

Table 9.1: Parameters of the laser beams forming the dipole trap in the proposed setup (see Fig. 9.4). Additionally, the rates of photon scattering from each beam are given.

## 9.4 Proposed realization with a BEC

We now propose a concrete setup in which the interferometer scheme discussed in this chapter could be realized. We focus on a realization with a BEC, because the long coherence times and ultra low temperatures make the demonstration of the scheme relatively easy using this platform.

Since we expect atom-atom interactions to be detrimental to revival visibility, we must choose an atomic species which is suitable for producing non-interacting condensates.  $^{39}\text{K}$  satisfies this criterion due to its Feshbach resonance structure [135] and additionally helps lower the required coherence time thanks to its low mass. The trap in our proposal is based on the optical dipole trap in Ref. [144]. It is formed by intersecting a horizontal light sheet with two coaxial Gaussian beams: one attractive (red detuned) and one repulsive (blue detuned),

as shown in Fig. 9.4. We decrease the dimensions of the setup by a factor of two compared to Ref. [144] to obtain a Talbot time of the order of 100 ms. We also adjust the laser powers in order to obtain trapping frequencies corresponding to at least 50 nK, while keeping the photon scattering rates below  $0.1 \text{ s}^{-1}$ . This limits the atom loss due to scattering to a percent level. The suggested parameters of the trapping beams as well as the expected scattering rates are shown in Table 9.1. In calculating the trapping potentials and the photon scattering, we follow Ref. [145]. For the parameters in Table 9.1, we obtain the trapping frequencies

$$\omega_z \approx 9.7 \text{ kHz} \sim 73 \text{ nK}, \quad \omega_\perp \approx 6.4 \text{ kHz} \sim 49 \text{ nK}, \quad (9.38)$$

as well as a trap radius  $R \approx 5.9 \mu\text{m}$ . For this configuration, the Talbot time from Eq. (9.7) is

$$T_T \approx 0.13 \text{ s}. \quad (9.39)$$

We now proceed to simulate the interference scheme in this setup using the Gross-Pitaevskii equation (GPE). To do this, we first reduce the three-dimensional and dimensionful GPE into a two-dimensional and dimensionless form. In doing so, we follow Ref. [146]. We start with a three-dimensional GPE

$$i\hbar\partial_t\psi = -\frac{\hbar^2}{2m}\nabla^2\psi + (V + NU_0|\psi|^2)\psi, \quad (9.40)$$

where  $N$  is the number of atoms,  $|\psi|^2$  is normalized to 1, and, for scattering length  $a$ ,

$$U_0 = \frac{4\pi\hbar^2 a}{m}. \quad (9.41)$$

If we take the inverse of the radial trapping frequency  $\omega_\perp$  as our unit of time and measure lengths in units of the width  $\sigma$  of the corresponding harmonic ground state, Eq. (9.40) becomes

$$i\partial_t\psi = -\frac{1}{2}\nabla^2\psi + (\tilde{V} + \delta|\psi|^2)\psi, \quad (9.42)$$

where

$$\tilde{V} = \frac{V}{\hbar\omega_\perp}, \quad \delta = 4\pi N \frac{a}{\sigma}. \quad (9.43)$$

In the weak-interactions limit and at sufficiently low temperature, the BEC will to a good approximation occupy the ground state of the out-of-plane motion. In this case, Eq. (9.42) can be reduced to a two-dimensional equation [146]

$$i\partial_t\psi = -\frac{1}{2}\nabla^2\psi + \left(\tilde{V} + \delta\sqrt{\frac{\omega_z}{2\pi\omega_\perp}}|\psi|^2\right)\psi, \quad (9.44)$$

where  $\omega_z$  is the frequency of the vertical confinement. The resulting equation can be solved using existing software libraries. We use a freely-available parallel Trotter-Suzuki solver with a Python interface [147].

The simulation is performed on a  $512 \times 512$  Cartesian grid with physical dimensions of  $20 \mu\text{m} \times 20 \mu\text{m}$ . The potential we use is exact, obtained from a sum of two Gaussian beams. The initial state in the simulation is isotropic and Gaussian with radius  $\sigma$ . We place it at the minimum of the radial trapping potential, so as to start in an approximate ground state of the radial motion<sup>5</sup>. The first step in simulating the interference scheme for a given interaction strength is finding the revival time. To do this, we first evolve the initial state for the analytically calculated Talbot time (9.39). Towards the end of the evolution, we frequently save snapshots of the state to find the dependence of the fidelity (9.20) on time in the vicinity of the revival. By locating the maximum of the fidelity, a correction to the analytic Talbot time is found. Once this is done, we redo the simulation starting from the initial state and evolving for half of the new Talbot time. The resulting state is then the starting point for the simulation of the interference pattern. To perform the latter, we apply a phase to one superposition component and evolve the state for a further  $T_T/2$ . The phase is applied by multiplying the wavefunction in the left half of the ring by  $\exp(i\varphi \cos^2(\beta - \pi))$ . Once we have computed the final states for a number of values of  $\varphi$ , we calculate the atom count imbalance for each state. To do this, we calculate  $N_R = |\psi(\beta)|^2 \cos^2 \beta$  (for  $|\beta| < \pi/2$ ) and  $N_L = |\psi(\beta)|^2 \cos^2(\beta - \pi)$  (for  $|\beta - \pi| < \pi/2$ ) and take

$$\Delta N = \frac{N_R - N_L}{N_R + N_L}. \quad (9.45)$$

We find that the interference scheme tolerates interaction strengths up to the equivalent of  $1 a_0$  scattering length for  $2 \times 10^4$  atoms. Although the atom density is already visibly distorted at this interaction strength, the visibility of the signal is only slightly affected (see Fig. 9.5). For stronger atom-atom interactions, a visible distortion of the interference signal occurs.

---

<sup>5</sup> A Gaussian of the radial coordinate is only an approximation of the ground state, as it does not account for interactions and because the radial trapping potential is not exactly harmonic. However, we find that this approximation is good enough for our purposes.

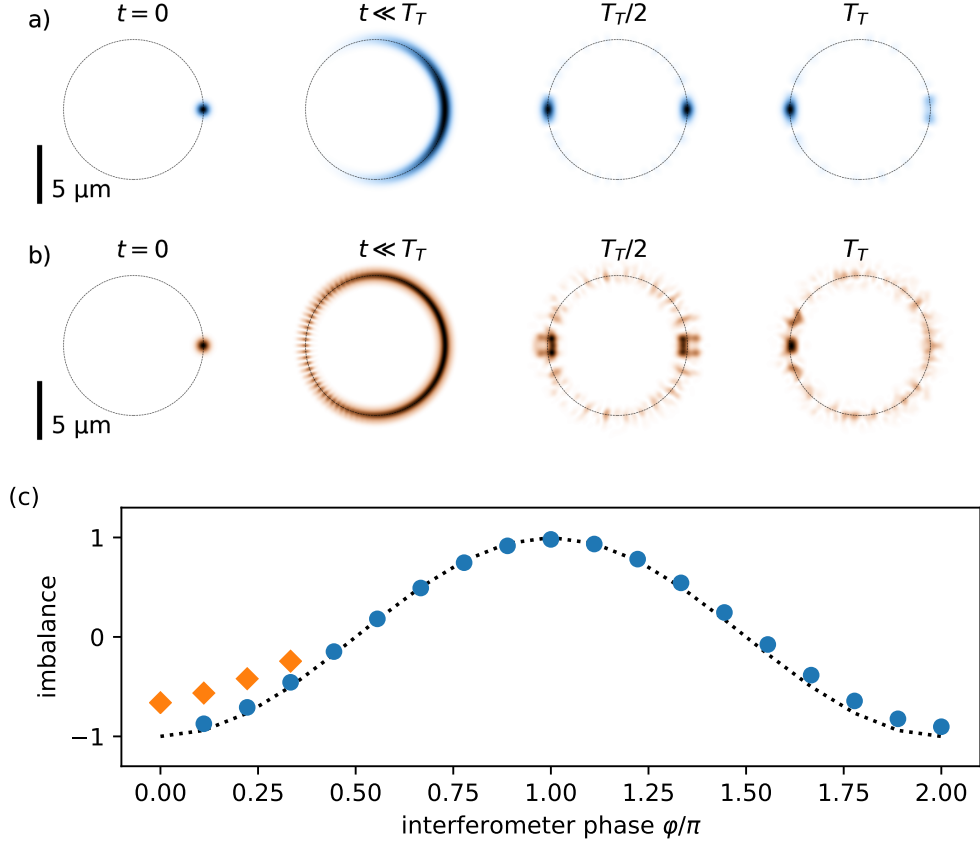


Figure 9.5: Simulation of the interference scheme realized using a noninteracting (a) and weakly interacting (b) BEC of  $^{39}\text{K}$  in an optical trap. (a,b) Snapshots of the particle density showing (left to right): the initial particle density and dispersion, balanced superposition at half the Talbot time, and a final interferometrically-controlled revival. At  $T_T/2$ , we apply a phase of  $\phi = \pi/3$  to the left superposition component. The Talbot time is found numerically to be 135.8 ms in (a) and 136.2 ms in (b). The scattering length in (b) is 1 Bohr radius and the BEC consists of  $N = 2 \times 10^4$  atoms. c) Interference signal as a function of external phase  $\phi$  in the non-interacting case (as in (a), dots) and in the interacting case (as in (b), diamonds). Plotted is the population imbalance defined in Eq. (9.45) (difference of the number of atoms in the two ports divided by the sum). The dotted line shows an ideal signal with unit visibility.



# Chapter 10

## Conclusions (Part II)

In the second half of the thesis, we have investigated matter-wave manipulation techniques which may be used in future high-mass interference experiments. We have first turned to Bragg diffraction, which is the basic component of state-of-the-art techniques using strong one-dimensional optical lattices to manipulate matter waves. In addition to regular Bragg diffraction, these techniques include double Bragg diffraction, as well as regular and symmetric Bloch oscillations used for beam splitting, acceleration, and suspension against gravity. Applying these techniques to high-mass matter-wave interferometry could allow for clear spatial separation of the superposition components, as well as for increased particle mass.

In Chapter 7, we have reviewed the theory of the diffraction of polarizable point particles on standing light-waves. We have put emphasis on adiabatic Bragg diffraction on strong lattices (also referred to as quasi-Bragg diffraction), which is the diffraction regime most often used in current applications. We have stressed that the stationary Schrödinger equation is exactly solvable for any lattice depth and matter-wave illumination angle. The solutions are given by the integer-order Mathieu functions of the first kind for Bragg-resonant illumination and by fractional-order Mathieu functions for off-resonant illumination. In adiabatic Bragg diffraction the population oscillates between the original and Bragg-reflected beams (the pendellösung oscillation) with a frequency proportional to the energy difference between the symmetric and antisymmetric components of the state. The energies of these components are the eigenvalues of the Mathieu equation, which are readily available in numerical packages and in the form of tabulated expansions. As a result, the pendellösung frequency can be immediately obtained to any precision both numerically and analytically. In the adiabatic limit, Bragg diffraction is lossless for any diffraction order or peak grating strength. However, the width of the Bragg resonances approaches zero in this limit, which illustrates that nonadiabatic corrections are needed to

describe realistic optical elements.

We have also clarified the difference between the quasi-Bragg and the deep-Bragg regimes: the latter is simply a perturbative solution of the diffraction problem to leading order in grating strength. In the deep-Bragg regime, only two diffraction orders are macroscopically populated throughout the diffraction pulse. This is in contrast to strong pulses in the quasi-Bragg regime, during which many diffraction orders are populated. However, their population vanishes at the end of the grating pulse as required by the adiabatic theorem.

In Chapter 8, we have described the first demonstration of Bragg diffraction of complex molecules. The experiment showed high-order diffraction, achieving  $\pi/2$  pulses with a momentum splitting of  $10\hbar k$  for ciprofloxacin and  $14\hbar k$  for phthalocyanine. The magnitude of the momentum transfer is on par with state-of-the-art single-pulse atomic Bragg diffraction, although the losses in our experiment are significantly larger. They are mostly a result of the broad collimation of the molecular beam, which translates to transverse momentum spreads significantly in excess of a photon recoil. The broad collimation also obscures the discrete nature of the momentum transfer, leading to strong similarity of our results to classical deflection. Finally, we were able to show that photon absorption is not an obstacle for high-order molecular Bragg diffraction: At least in the mass regime of a few hundred daltons, it can be mitigated by a suitable choice of the molecule.

Bragg diffraction and other lattice techniques are special among state-of-the-art methods for manipulating atoms with light, because they rely solely on the dipole force in far-detuned light fields. As we have demonstrated, this makes them immediately applicable to the manipulation of complex particles. As a result, momentum transfers of the order of  $10^4\hbar k$  as well as coherent guiding and suspension are potentially within reach of high-mass interference experiments. However, we must recognize that in their present form, lattice techniques fundamentally rely on a sub-recoil momentum spread of the manipulated particles. Unless these techniques can be modified to accept larger spreads, their adoption in high-mass interference will be limited by the availability of bright sub-recoil beams. From this perspective, the development of methods for transverse cooling of high-mass particle beams is a priority. That is in addition to the search for creative ways to adapt the lattice techniques to existing sources.

In Chapter 9, we have investigated a specific way to perform Talbot-like interference with trapped matter waves. We have shown that the free evolution in a toroidal waveguide leads to spontaneous beam splitting and recombination. This could allow one to perform an interference scheme with no matter-wave optics beyond the initial confinement and the toroidal trap. In this configuration, the necessary coherence time is proportional to the mass of the particle and to the radius of the trap squared. Since the size of the trap is not easily decreased

below a few micrometers, we think that this setup is mostly relevant for the interference of atoms or molecules with a mass up to about 1 kDa. We have argued that this scheme could be used to precisely measure external forces such as gravity, as well as weak interatomic forces. Additionally, the scheme could be performed with a charged or polar particle in an electromagnetic field in order to demonstrate a mesoscopic, Aharonov-Bohm-like effect.



# Appendix A

## Hamiltonians in comoving frames

Switching between the lab frame and inertial or noninertial comoving frames is relatively common practice in the theory of matter-wave interference. The general discussion of changing frames in quantum mechanics can be found, e.g., in Refs. [148–150]. Here, we briefly review the most useful formulas, following closely the Appendix of Ref. [151].

Let us assume that in reference frame  $A$  the Schrödinger equation reads

$$i\hbar\partial_t|\psi\rangle_A = H_A|\psi\rangle_A. \quad (\text{A.1})$$

In a unitarily-related frame  $B$  we have  $|\psi\rangle_B = U|\psi\rangle_A$  and the Schrödinger equation is

$$i\hbar\partial_t|\psi\rangle_B = i\hbar\partial_t U|\psi\rangle_A = (i\hbar(\partial_t U)U^\dagger + UH_AU^\dagger)U|\psi\rangle_A. \quad (\text{A.2})$$

Equation (A.2) will have the form (A.1) when

$$H_B = i\hbar(\partial_t U)U^\dagger + UH_AU^\dagger. \quad (\text{A.3})$$

We will be interested in the unitary transformation

$$U = \exp(i\xi(t)p/\hbar) \exp(-i\zeta(t)x/\hbar) \exp(i\varphi(t)/\hbar), \quad (\text{A.4})$$

where  $\xi, \zeta, \varphi$  are arbitrary real functions of time. It transforms the canonical coordinates in the following way

$$UxU^\dagger = \exp(i\xi(t)p/\hbar)x \exp(-i\zeta(t)p/\hbar) \quad (\text{A.5a})$$

$$= x + \exp(i\xi(t)p/\hbar)[x, \exp(-i\zeta(t)p/\hbar)] \quad (\text{A.5b})$$

$$= x + \exp(i\xi(t)p/\hbar)[x, p] \partial_p \exp(-i\zeta(t)p/\hbar) \quad (\text{A.5c})$$

$$= x + \xi(t), \quad (\text{A.5d})$$

$$UpU^\dagger = p + \zeta(t). \quad (\text{A.5e})$$

Transformation (A.4) is thus general enough to describe changing to any rigidly moving inertial or noninertial frame. To complete the transformation of the Hamiltonian, we note that the first term in Eq. (A.3) can be expressed as

$$i\hbar (\partial_t U) U^\dagger = -\dot{\xi}(t)p - \dot{\phi}(t) + \dot{\xi}(t)UxU^\dagger = -\dot{\xi}(t)p - \dot{\phi}(t) + \dot{\xi}(t)(x + \xi(t)). \quad (\text{A.6})$$

## Appendix B

### Theory of Talbot-Lau interference (inertial-frame description)

In this section, we validate the results of Section 2.1 by rederiving the interference pattern and signal in an inertial frame. Since the Hamiltonian (2.1) is at most quadratic in position and momentum, the evolution of the Wigner function between the gratings is again the same as for a classical phase-space density. However, in the inertial frame the coordinate transformation describing the free flight after the  $i$ -th grating reads

$$x' = x + \frac{p}{m} T_i + \xi_i, \quad (\text{B.1a})$$

$$p' = p + m\xi'_i, \quad (\text{B.1b})$$

in which  $\xi_i$  and  $\xi'_i$  are arbitrary position and velocity increments. The corresponding transformation  $\text{FF}_i$  of the Wigner function is

$$(\text{FF}_i w)(x, p) = w\left(x - \frac{p}{m} T_i - \zeta_i, p - m\zeta_i\right), \quad (\text{B.2})$$

where

$$\zeta_i = \xi_i - T_i \xi'_i. \quad (\text{B.3})$$

The grating transformation remains unchanged and is given by Eq. (2.9). A single composition of GT and FF takes the form

$$\begin{aligned} (\text{FF}_i \text{GT}_i w)(x, p) &= \int dp_i K_i\left(x - \Delta x_i - \frac{p}{m} T_i - \zeta_i, p - m\zeta'_i - p_i\right) \\ &\quad \times w\left(x - \frac{p}{m} T_i - \zeta_i, p_i\right). \end{aligned} \quad (\text{B.4})$$

We now apply the above composition  $k$  times to the initial state (2.15) and integrate over momentum to obtain the pattern. This gives

$$w_k(x) = \int dp (\text{FF}_k \text{GT}_k \dots \text{FF}_1 \text{GT}_1 w_0)(x, p) \quad (\text{B.5a})$$

$$\begin{aligned} &= \frac{1}{X_0} \int dp dp_k K_k \left( x - \Delta x_k - \frac{p}{m} T_k - \zeta_k, p - m \xi'_k - p_k \right) \\ &\quad \times \int dp_{k-1} K_{k-1} \left( x - \Delta x_{k-1} - \frac{p_k}{m} T_{k-1} - \frac{p}{m} T_k - \zeta_{k-1} - \zeta_k, \right. \\ &\quad \left. p_k - m \xi'_{k-1} - p_{k-1} \right) \\ &\quad \times \dots \\ &\quad \times \int dp_1 K_1 \left( x - \Delta x_1 - \frac{p_2}{m} T_1 - \frac{p_3}{m} T_2 + \dots \frac{p}{m} T_k - x_0, p_2 - m \xi'_1 - p_1 \right) \\ &\quad \times \theta \left( \frac{X_0}{2} - \left| x - \frac{p_2}{m} T_1 - \frac{p_3}{m} T_2 + \dots \frac{p}{m} T_k - x_0 \right| \right) D(p_1), \end{aligned} \quad (\text{B.5b})$$

where

$$x_0 = \zeta_1 + \zeta_2 + \dots + \zeta_k. \quad (\text{B.6})$$

Using Eq. (2.11) to expand the grating kernels gives

$$\begin{aligned} w_k(x) &= \frac{1}{X_0} \frac{1}{(2\pi\hbar)^k} \sum_{n_1, \dots, n_k} \exp \left\{ i\kappa x - i\phi_k - 2\pi i \sum_{i=1}^k \frac{n_i}{d_i} (\zeta_i + \dots + \zeta_k) \right\} \\ &\quad \times \int ds_k \dots ds_1 \exp \left\{ -\frac{im}{\hbar} \sum_i \xi'_i s_i \right\} B_{n_1}^{(1)} \left( \frac{s_1}{d_1} \right) \dots B_{n_k}^{(k)} \left( \frac{s_k}{d_k} \right) \\ &\quad \times \int dp \exp \left\{ \frac{ip}{\hbar} \left[ s_k - \frac{hT_k}{m} \left( \frac{n_1}{d_1} + \dots + \frac{n_k}{d_k} \right) \right] \right\} \\ &\quad \times \int dp_k \exp \left\{ \frac{ip_k}{\hbar} \left[ -s_k + s_{k-1} - \frac{hT_{k-1}}{m} \left( \frac{n_1}{d_1} + \dots + \frac{n_{k-1}}{d_{k-1}} \right) \right] \right\} \\ &\quad \times \dots \\ &\quad \times \theta \left( \frac{X_0}{2} - \left| x - \frac{p_2}{m} T_1 - \frac{p_3}{m} T_2 - \dots - \frac{p}{m} T_k - x_0 \right| \right) \int dp_1 e^{-ip_1 s_1/\hbar} D(p_1). \end{aligned} \quad (\text{B.7})$$

We now carry out the integrations starting from the innermost. For large  $X_0$  the



integrals over  $p_2, \dots, p$  can be approximated by Dirac deltas, resulting in

$$w_k(x) = \frac{\theta(X_0/2 - |x - x_0|)}{X_0} \sum_{\kappa} e^{i\kappa x} P_{\kappa}, \quad (\text{B.8a})$$

$$P_{\kappa} = \sum_{\substack{n_1 + \dots + n_k = \kappa \\ d_1 + \dots + d_k = \kappa}} e^{-i(\phi_k + \tilde{\phi})} B_{n_1}^{(1)}\left(\frac{s_1}{d_1}\right) \dots B_{n_k}^{(k)}\left(\frac{s_k}{d_k}\right) \tilde{D}(s_1), \quad (\text{B.8b})$$

where  $\phi_k$  and the  $s_i$  are defined as in the comoving frame (see Eqs. (2.20) and (2.22)), and the additional phase shift is

$$\tilde{\phi}_k = 2\pi \sum_{i=1}^k \left[ \frac{n_i}{d_i} (\zeta_i + \dots + \zeta_k) + \frac{ms_i}{h} \xi'_i \right]. \quad (\text{B.9})$$

The interference signal in a scanning-grating interferometer is obtained from the pattern in the same way as in the comoving frame calculation in Section 2.1. The resulting expression is the same as Eq. (2.27b), but with  $\phi_{k+1}$  replaced by  $\phi_{k+1} + \tilde{\phi}_k$ . That is, the additional shifts  $\tilde{\phi}_k$  of the pattern terms in the inertial frame are also visible in the signal.

The difference between the patterns obtained in the comoving and inertial frames lies in the way the trajectory of the particle enters the shift of the pattern. In the comoving frame, the motion of the particle together with the lab-frame positions of the gratings determine the grating shifts  $\Delta x_i$ . These then determine the shift of the pattern via the  $\phi_k$  phases. In the inertial frame, the  $\Delta x_i$  (and thus  $\phi_k$ ) only contain the positions of the gratings with respect to the lab frame. The motion of the particle enters instead through the additional shifts  $\tilde{\phi}_k$ .

To see that the shift of the pattern is the same in both cases, we first use the definition (2.22) of  $s_i$  to rewrite the second term in Eq. (B.9) as

$$\begin{aligned} \sum_{i=1}^k \frac{ms_i}{h} \xi'_i &= \sum_{i=1}^k \xi'_i \left[ \left( \frac{n_1}{d_1} + \dots + \frac{n_i}{d_i} \right) (T_i + \dots + T_k) + \frac{n_{i+1}}{d_{i+1}} (T_{i+1} + \dots + T_k) \right. \\ &\quad \left. + \dots + \frac{n_k}{d_k} T_k \right] \end{aligned} \quad (\text{B.10a})$$

$$\begin{aligned} &= \sum_{i=1}^k \frac{n_i}{d_i} \left[ (\xi'_1 + \dots + \xi'_i) (T_i + \dots + T_k) + \xi'_{i+1} (T_{i+1} + \dots + T_k) \right. \\ &\quad \left. + \dots + \xi'_k T_k \right] \end{aligned} \quad (\text{B.10b})$$

$$= \sum_{i=1}^k \frac{n_i}{d_i} \left[ T_i (\xi'_1 + \dots + \xi'_i) + \dots + T_k (\xi'_1 + \dots + \xi'_k) \right]. \quad (\text{B.10c})$$

Combining Eq. (B.9) with Eqs. (B.3) and (B.10c) gives

$$\tilde{\phi}_k = \sum_{i=1}^k \frac{2\pi n_i}{d_i} \left[ \xi_i + \dots + \xi_k + T_i(\xi'_1 + \dots + \xi'_{i-1}) + \dots + T_k(\xi'_1 + \dots + \xi'_{k-1}) \right]. \quad (\text{B.11})$$

Finally, we rewrite the pattern shift (2.33) obtained in the comoving frame as

$$\phi_k^{\text{lab}} = \sum_{i=1}^k \frac{2\pi n_i}{d_i} [\xi(T_1 + \dots + T_k) - \xi(T_1 + \dots + T_{i-1})]. \quad (\text{B.12})$$

The trajectory  $\xi(T_1 + \dots + T_i)$  is the result of composing Eq. (B.1a)  $i$  times and starting from the origin of the phase space. This gives

$$\xi(T_1 + \dots + T_i) = \xi_1 + \dots + \xi_i + T_2 \xi'_1 + \dots + T_i(\xi'_1 + \dots + \xi'_{i-1}), \quad (\text{B.13})$$

which inserted into Eq. (B.12) gives Eq. (B.11) as expected.

## Appendix C

### Bragg approximation via adiabatic elimination

Based on the multilevel-atom analogy in atomic diffraction, we can expect that for small grating strength  $q$  only transitions between the pairwise degenerate states  $|p = \pm n\hbar k\rangle \equiv |\pm n\rangle$  will occur. The effective two-state description can be obtained for  $n > 1$  by adiabatic elimination of the intermediate states [58], as reviewed in this section. Our treatment follows the procedure of Ref. [58], Sec. II analytically to first order, filling some minor gaps. The approximate solution is only worthwhile for  $n \geq 3$ . For the lowest orders it is easy and far more

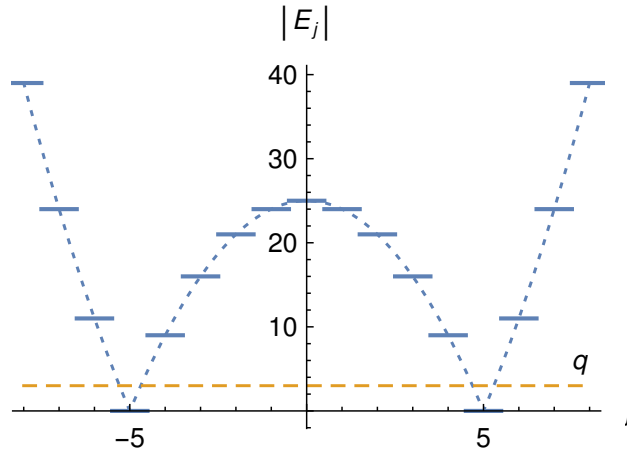


Figure C.1: Energies of momentum eigenstates  $|j\rangle$ , illustrating the multilevel-atom analogy in Bragg diffraction. The particle is initially in the state  $|n\rangle$ , here assuming  $n = 5$ . For small grating strength  $q$ , only transitions between the  $|\pm n\rangle$  states are resonant.

insightful to solve the problem via analytic diagonalization, like in Ref. [61].

Let us assume that at time  $\tau_0$  the particle is in the superposition of the  $|\pm n\rangle$  eigenstates,

$$|\psi(\tau_0)\rangle = g_n(\tau_0)|n\rangle + g_{-n}(\tau_0)|-n\rangle, \quad (\text{C.1})$$

where  $n > 0$ . We will subtract  $n^2\hbar\omega_r$  from the energy so that  $|\pm n\rangle$  correspond to the ground states in the multilevel atom analogy (see Fig. C.1). This is necessary for the simple adiabatic elimination (i.e., setting the derivatives of the fast degrees of freedom to zero) to yield the correct result [152]. With this subtraction, the evolution of the amplitudes  $g_j$  is given by Eq. (7.25). If the interaction energy  $q(\tau)/2$  is small compared to the  $|n\rangle \leftrightarrow |n-1\rangle$  energy spacing (see Fig. C.1), levels other than  $|\pm n\rangle$  are far-detuned and can be adiabatically eliminated. We do this by setting  $\dot{g}_j = 0$  for  $j \neq n$  in Eq. (7.25) and solving the resulting set of linear algebraic equations

$$0 = (j^2 - n^2)g_j + q(\tau)(g_{j-2} + g_{j+2}), \quad j = n-2, n-4, \dots, -n+2. \quad (\text{C.2})$$

We have truncated the a priori infinite set of equations to only the  $n-1$  intermediate states. The amplitudes of the outer states  $|\pm n \pm 2\rangle, |\pm n \pm 4\rangle, \dots$  can be taken to be zero without affecting the result to lowest order in  $q$ , as we justify later. Equation (C.2) is in matrix form

$$M \begin{pmatrix} g_{n-2} \\ g_{n-4} \\ \vdots \\ g_{-n+4} \\ g_{-n+2} \end{pmatrix} = \begin{pmatrix} -qg_n \\ 0 \\ \vdots \\ 0 \\ -qg_{-n} \end{pmatrix}, \quad (\text{C.3})$$

where  $M$  is a tridiagonal matrix

$$M = \begin{pmatrix} \Delta_{n-2} & q & & & & \\ q & \Delta_{n-4} & q & & & \\ & q & \Delta_{n-6} & q & & \\ & & \ddots & \ddots & \ddots & \\ & & & q & \Delta_{-n+4} & q \\ & & & & q & \Delta_{-n+2} \end{pmatrix}, \quad (\text{C.4})$$

with  $\Delta_{n-2j} = (n-2j)^2 - n^2 = -4j(n-j)$ . The solution of Eq. (C.3) for  $g_{\pm n \mp 2}$  is

$$g_{n-2} = -q (M_{1,1}^{-1}g_n + M_{1,n-1}^{-1}g_{-n}), \quad (\text{C.5a})$$

$$g_{-n+2} = -q (M_{n-1,1}^{-1}g_n + M_{n-1,n-1}^{-1}g_{-n}). \quad (\text{C.5b})$$

From the symmetry of  $M$  we must have  $M_{1,1}^{-1} = M_{n-1,n-1}^{-1}$ ,  $M_{1,n-1}^{-1} = M_{n-1,1}^{-1}$ . Using this and inserting Eq. (C.5) into the Raman-Nath equations (7.25) for  $g_{\pm n}$  gives

$$i\dot{g}_n = -q^2 (M_{1,1}^{-1}g_n + M_{1,n-1}^{-1}g_{-n}), \quad (\text{C.6a})$$

$$i\dot{g}_{-n} = -q^2 (M_{1,n-1}^{-1}g_n + M_{1,1}^{-1}g_{-n}). \quad (\text{C.6b})$$

The diagonal terms contribute a light shift, which is not relevant to our problem and can be removed by a substitution analogous to the one yielding Eq. (7.25). This leaves us with equations solved by Eq. (7.43b) with

$$\frac{\Omega_n}{2} = -q^2 M_{1,n-1}^{-1}. \quad (\text{C.7})$$

To obtain  $\Omega_n$ , we must therefore find the inverse  $M^{-1}$  of a tridiagonal matrix. This is in general a very hard task; however, we limit ourselves here to finding the solution to lowest order in  $q$ . To this end, we use the results of Ref. [153]. From their Corollary 2.1 we have

$$M_{j,j}^{-1} = \Delta_{n-2j}^{-1} + O(q^2), \quad (\text{C.8a})$$

$$M_{i,j}^{-1} = (-1)^{j-i} q^{j-i} \frac{z_{i-1}}{z_{j-1}} M_{j,j}^{-1} \quad \text{for } i < j, \quad (\text{C.8b})$$

where  $z_0 = 1$ ,  $z_1 = \Delta_{n-2}$  and

$$z_j = \Delta_{n-2j} z_{j-1} - q^2 z_{j-2}, \quad j = 2, 3, \dots, n-1. \quad (\text{C.9})$$

Using Eq. (C.8) we find the leading-order solution of Eq. (C.7) to be

$$\frac{\Omega_n}{2} = -q^2 \left[ (-1)^{n-2} q^{n-2} \left( \frac{M_{n-1,n-1}^{-1}}{z_{n-2}} \right)_{q=0} \right] = (-1)^{n-1} q^n \prod_{j=1}^{n-1} \frac{1}{\Delta_{n-2j}} = \frac{4}{[(n-1)!]^2} \left( \frac{q}{4} \right)^n, \quad (\text{C.10})$$

in agreement with Eq. (7.49).

We now argue that the truncation to the  $n-1$  equations (C.2) does not affect the above result. Let us assume we included  $2i$  more states, so that now we have a set of equations for  $g_{n+2i}, \dots, g_{n+2}, g_{n-2}, \dots, g_{-n+2}, g_{-n-2}, \dots, g_{-n-2i}$ . In the vicinity of  $g_{n-2}$ , the set of equations has the form

$$\begin{pmatrix} \ddots & \ddots & \ddots & & & & & & \\ & q & \Delta_{n+4} & q & & & & & \\ & & q & \Delta_{n+2} & 0 & & & & \\ & & & 0 & \Delta_{n-2} & q & & & \\ & & & & q & \Delta_{n-4} & q & & \\ & & & & & \ddots & \ddots & \ddots & \end{pmatrix} \cdot \begin{pmatrix} \vdots \\ g_{n+4} \\ g_{n+2} \\ g_{n-2} \\ g_{n-4} \\ \vdots \end{pmatrix} = \begin{pmatrix} \vdots \\ 0 \\ -qg_n \\ -qg_n \\ 0 \\ \vdots \end{pmatrix}, \quad (\text{C.11})$$

where we denote the extended matrix by  $\tilde{M}$ . To obtain  $\dot{g}_n$ , we need the solutions for  $g_{n-2}$  and  $g_{n+2}$  and therefore the matrix elements  $\tilde{M}_{1+i,n-1+i}^{-1}$ ,  $\tilde{M}_{1+i,n+i}^{-1}$ ,  $\tilde{M}_{i,n-1+i}^{-1}$ , and  $\tilde{M}_{i,n+i}^{-1}$ . There are now four terms of interest as we have two neighbors  $g_{n\pm 2}$  and two  $g_{-n}$  terms on the right-hand side of Eq. (C.11). To lowest order in  $q$  we have

$$\tilde{M}_{1+i,n-1+i}^{-1} = (-1)^n q^{n-2} \left[ \frac{\tilde{z}_i}{\tilde{z}_{n-2+i}} \tilde{M}_{n-1+i,n-1+i}^{-1} \right]_{q=0}, \quad (\text{C.12})$$

where the first two terms are the same as in  $M^{-1}$  because they depend only on the difference of indices [see Eq. (C.8b)] and  $i$  cancels out. The diagonal element is also the same as in  $M^{-1}$ , because in zeroth order it is just the inverse of the respective detuning [see Eq. (C.8a)],  $\tilde{M}_{n-1+i,n-1+i}^{-1} = M_{n-1,n-1}^{-1} = \Delta_{-n+2}^{-1}$ . Finally, for  $q = 0$  the additional detunings  $\Delta_{n+2i}, \dots, \Delta_{n+2}$  cancel in the ratio  $\tilde{z}_i/\tilde{z}_{n-2+i}$  yielding  $\tilde{M}_{1+i,n-1+i}^{-1} = M_{1,n-1}^{-1}$  as desired. The matrix elements  $\tilde{M}_{1+i,n+i}^{-1}$  and  $\tilde{M}_{i,n-1+i}^{-1}$  are  $O(q^{n-1})$ , while  $\tilde{M}_{i,n+i}^{-1}$  is  $O(q^n)$ , as can be seen from the difference of the indices. They are therefore of higher order than the term we already considered and do not enter the leading-order result. The argument proceeds in the same way for  $\dot{g}_{-n}$ . We have thus shown that Eq. (C.10) is accurate to leading order in  $q$  despite the finite number of states considered in Eq. (C.2).

## Appendix D

# Least-squares fitting of diffraction images

The simulation in Fig. 8.3 (b) is a least-squares fit to the data image in panel (a) of the same figure. The fit is performed over the following parameters: the incidence angle, the grating  $y$  offset, the peak of the molecular velocity distribution (its shape can be obtained from the data directly), and to a limited extent over source size. The remaining parameters (see Table 8.2) are held at their known or estimated experimental values. The fitting procedure is as follows

1. Pre-process the data by
  - a) Leveling the background<sup>1</sup>. This is done by masking the diffraction pattern, averaging the image along the  $y$  direction, and fitting a smoothing spline (`UnivariateSpline` from `SciPy`) to the noise floor. The floor is then subtracted from the image and the process repeated along the  $x$  axis.
  - b) Centering the pattern. This is done by finding the center of the undiffracted beam and shifting it to  $x = 0$ . The center is found by fitting a Gaussian to the  $y$ -average of a  $50\text{ }\mu\text{m}$  horizontal stripe at the top of the image.
2. Downsample the data. In our case by a factor of 7 to a resolution of  $140 \times 31$  (width  $\times$  height). This is done using `decimate` from `SciPy`. The smoothing filter used internally by `decimate` before downsampling is necessary for obtaining a low-noise result. The downsampling factor has to be low

---

<sup>1</sup>Initial background correction is done in the acquisition software, but it proved insufficient to obtain a good fit. Additional filtering is also crucial for obtaining a good vertical intensity distribution.

enough to conserve the physical content of the image, but high enough to filter out as much noise as possible.

3. Prepare a 3D array containing a selection of horizontal lines of the data image. In each consecutive slice of the array, the selection of lines is shifted vertically. We choose 21 lines separated by about 13  $\mu\text{m}$ .
4. Prepare the simulations
  - a) Sample the simulated images from a given range of incidence angles and grating offsets. We chose sampling points in regular intervals for each parameter. Then, for every parameter combination we calculate 21 horizontal lines of the diffraction image, separated by the same distance as the data lines selected in step 3. The simulations are calculated as described in Section 8.2 without vertical averaging or weighing with a velocity distribution (steps 5 and 6).
  - b) Downsample the simulated images in the  $x$  direction to match the resolution of the downsampled data. We downsample by a factor of 65, which requires the use of the finite impulse response smoothing filter in `decimate`.
5. Find the least-squares match; that is, for each simulated image
  - a) Normalize the simulation lines and multiply them by the sums of their respective data lines.
  - b) Subtract the theoretical image lines from the experimental ones and calculate the sum of squares.
  - c) Normalize the sum of squares by the sum of squares of the data lines.
  - d) Pick another (vertically shifted) set of data lines and repeat.

In practice the above steps are not done sequentially, but simultaneously using the array of shifted data lines prepared in step 3. The normalization in step 5b is necessary because different selections of lines contain different amounts of variability, as measured by their sum of squares.

6. Repeat step 5 for different source sizes and find the one which results in the smallest sum of squares. The source size can be changed (within a limited range) without repeating the simulations, as described in Section 8.2. The source size and the simulated image with the normalized sum of squares are chosen as the best fit.



Finally, to plot the fit alongside the data image we perform a simulation with 50 horizontal lines and weigh it with the empirical vertical intensity distribution. The latter is obtained by summing the image along the  $x$  axis and fitting a smoothing spline to the result. If a parametric fit is desired (for example to determine the peak velocity in the molecular beam), one has to use a Maxwell-Boltzmann distribution transformed as in Eq. (8.3) and convolved with a square or a Gaussian (to account for the finite opening of the  $S_y$ ).



# Bibliography

- [1] R. W. Hamming, *You and Your Research*, Transcription of the Bell Communications Research Colloquium Seminar, (Mar. 7, 1986) <https://www.cs.virginia.edu/~robins/YouAndYourResearch.html> (visited on 02/12/2021).
- [2] G. P. Thomson, “The Diffraction of Cathode Rays by Thin Films of Platinum”, *Nature* **120**, 802 (1927).
- [3] C. Davisson and L. H. Germer, “The Scattering of Electrons by a Single Crystal of Nickel”, *Nature* **119**, 558 (1927).
- [4] R. Loudon, “Non-classical effects in the statistical properties of light”, *Rep. Prog. Phys.* **43**, 913 (1980).
- [5] A. D. Cronin, J. Schmiedmayer, and D. E. Pritchard, “Optics and interferometry with atoms and molecules”, *Rev. Mod. Phys.* **81**, 1051 (2009).
- [6] G. M. Tino and M. A. Kasevich, eds., *Atom Interferometry*, Vol. 188, Proceedings of the International School of Physics "Enrico Fermi" (IOS Press, Amsterdam, 2014).
- [7] V. Xu et al., “Probing gravity by holding atoms for 20 seconds”, *Science* **366**, 745 (2019).
- [8] Y. Y. Fein et al., “Quantum superposition of molecules beyond 25 kDa”, *Nat. Phys.* **15**, 1242 (2019).
- [9] P. Asenbaum, C. Overstreet, M. Kim, J. Curti, and M. A. Kasevich, “Atom-Interferometric Test of the Equivalence Principle at the  $10^{-12}$  Level”, *Phys. Rev. Lett.* **125**, 191101 (2020).
- [10] L. Morel, Z. Yao, P. Cladé, and S. Guellati-Khélifa, “Determination of the fine-structure constant with an accuracy of 81 parts per trillion”, *Nature* **588**, 61 (2020).
- [11] M. Arndt et al., “Wave–particle duality of  $C_{60}$  molecules”, *Nature* **401**, 680 (1999).

- [12] B. Brezger et al., “Matter-Wave Interferometer for Large Molecules”, *Phys. Rev. Lett.* **88**, 100404 (2002).
- [13] S. Gerlich et al., “A Kapitza-Dirac-Talbot-Lau interferometer for highly polarizable molecules”, *Nat. Phys.* **3**, 711 (2007).
- [14] P. Haslinger et al., “A universal matter-wave interferometer with optical ionization gratings in the time domain”, *Nat. Phys.* **9**, 144 (2013).
- [15] Y. Y. Fein et al., “Quantum-Assisted Measurement of Atomic Diamagnetism”, *Phys. Rev. X* **10**, 011014 (2020).
- [16] S. Eibenberger, X. Cheng, J. P. Cotter, and M. Arndt, “Absolute Absorption Cross Sections from Photon Recoil in a Matter-Wave Interferometer”, *Phys. Rev. Lett.* **112**, 250402 (2014).
- [17] Y. Y. Fein, P. Geyer, F. Kialka, S. Gerlich, and M. Arndt, “Improved accuracy fullerene polarizability measurements in a long-baseline matter-wave interferometer”, *Phys. Rev. Research* **1**, 033158 (2019).
- [18] L. Mairhofer et al., “Quantum-assisted metrology of neutral vitamins in the gas phase”, *Angew. Chem. Int. Ed.* **56**, 10947 (2017).
- [19] K. Hornberger et al., “Collisional Decoherence Observed in Matter Wave Interferometry”, *Phys. Rev. Lett.* **90**, 160401 (2003).
- [20] L. Hackermüller, K. Hornberger, B. Brezger, A. Zeilinger, and M. Arndt, “Decoherence of matter waves by thermal emission of radiation”, *Nature* **427**, 711 (2004).
- [21] Y. Y. Fein, “Long-baseline universal matter-wave interferometry”, PhD thesis (University of Vienna, 2020).
- [22] H. F. Talbot, “Facts relating to optical science. No. IV”, *Philos. Mag.* **9**, 401 (1836).
- [23] E. Lau, “Beugungserscheinungen an Doppelrastern”, *Ann. Phys.* **437**, 417 (1948).
- [24] J. Jahns and A. W. Lohmann, “The Lau effect (a diffraction experiment with incoherent illumination)”, *Optics Communications* **28**, 263 (1979).
- [25] S. Sala et al., “First demonstration of antimatter wave interferometry”, *Sci. Adv.* **5**, eaav7610 (2019).
- [26] S. Nimmrichter, “Macroscopic Matter-wave Interferometry”, PhD thesis (University of Vienna, 2013).
- [27] B. Brezger, M. Arndt, and A. Zeilinger, “Concepts for near-field interferometers with large molecules”, *J. Opt. B* **5**, S82 (2003).

- [28] N. Dörre et al., “Photofragmentation Beam Splitters for Matter-Wave Interferometry”, *Phys. Rev. Lett.* **113**, 233001 (2014).
- [29] K.-P. Marzlin and J. Audretsch, “State independence in atom interferometry and insensitivity to acceleration and rotation”, *Phys. Rev. A* **53**, 312 (1996).
- [30] B. Dubetsky and M. A. Kasevich, “Atom interferometer as a selective sensor of rotation or gravity”, *Phys. Rev. A* **74**, 023615 (2006).
- [31] J. F. Clauser, “Ultra-high sensitivity accelerometers and gyroscopes using neutral atom matter-wave interferometry”, *Phys. BC* **151**, 262 (1988).
- [32] S. Wu, E. Su, and M. Prentiss, “Demonstration of an area-enclosing guided-atom interferometer for rotation sensing”, *Phys. Rev. Lett.* **99**, 173201 (2007).
- [33] J. K. Stockton, K. Takase, and M. A. Kasevich, “Absolute geodetic rotation measurement using atom interferometry”, *Phys. Rev. Lett.* **107**, 133001 (2011).
- [34] I. Dutta et al., “Continuous cold-atom inertial sensor with 1rad/sec rotation stability”, *Phys. Rev. Lett.* **116**, 183003 (2016).
- [35] I. Perrin et al., “Proof-of-principle demonstration of vertical-gravity-gradient measurement using a single-proof-mass double-loop atom interferometer”, *Phys. Rev. A* **99**, 013601 (2019).
- [36] B. Deissler, K. J. Hughes, J. H. T. Burke, and C. A. Sackett, “Measurement of the ac Stark shift with a guided matter-wave interferometer”, *Phys. Rev. A* **77**, 031604 (2008).
- [37] D. A. Pushin, M. G. Huber, M. Arif, and D. G. Cory, “Experimental realization of decoherence-free subspace in neutron interferometry”, *Phys. Rev. Lett.* **107**, 150401 (2011).
- [38] S. Dimopoulos, P. W. Graham, J. M. Hogan, M. A. Kasevich, and S. Rajendran, “Atomic gravitational wave interferometric sensor”, *Phys. Rev. D* **78**, 122002 (2008).
- [39] J. M. Hogan et al., “An atomic gravitational wave interferometric sensor in low earth orbit (AGIS-LEO)”, *Gen. Relativ. Gravit.* **43**, 1953 (2011).
- [40] S.-w. Chiow and N. Yu, “Multiloop atom interferometer measurements of chameleon dark energy in microgravity”, *Phys. Rev. D* **97**, 044043 (2018).
- [41] M. Jaffe, V. Xu, P. Haslinger, H. Müller, and P. Hamilton, “Efficient adiabatic spin-dependent kicks in an atom interferometer”, *Phys. Rev. Lett.* **121**, 040402 (2018).

- [42] K. Hornberger, J. E. Sipe, and M. Arndt, “Theory of decoherence in a matter wave Talbot-Lau interferometer”, *Phys. Rev. A* **70**, 053608 (2004).
- [43] J. Schmiedmayer et al., “Optics and interferometry with atoms and molecules”, in *Atom interferometry*, edited by P. R. Berman (Academic Press, San Diego, 1997), pp. 1–83.
- [44] Y. Y. Fein, F. Kialka, P. Geyer, S. Gerlich, and M. Arndt, “Coriolis compensation via gravity in a matter-wave interferometer”, *New J. Phys.* **22**, 033013 (2020).
- [45] A. A. Sonin, *The physical basis of dimensional analysis*, 2nd ed. (MIT Department of Mechanical Engineering, Cambridge, MA (USA), 2001).
- [46] S. Y. Buhmann, *Dispersion Forces I: Macroscopic Quantum Electrodynamics and Ground-State Casimir, Casimir–Polder and van der Waals Forces*, Vol. 247, Springer Tracts in Modern Physics (Springer-Verlag, Berlin Heidelberg, 2012).
- [47] S. Nimmrichter and K. Hornberger, “Theory of near-field matter-wave interference beyond the eikonal approximation”, *Phys. Rev. A* **78**, 023612 (2008).
- [48] F. Kialka et al., “Concepts for long-baseline high-mass matter-wave interferometry”, *Phys. Scr.* **94**, 034001 (2019).
- [49] P. Atkins, J. De Paula, and J. Keeler, *Atkins’ physical chemistry* (Oxford University Press, 2018).
- [50] L. A. Sidorenkov, R. Gautier, M. Altorio, R. Geiger, and A. Landragin, “Tailoring multiloop atom interferometers with adjustable momentum transfer”, *Phys. Rev. Lett.* **125**, 213201 (2020).
- [51] A. Tonyushkin and M. Prentiss, “Selective manipulation of degenerate interferometer loops by an atom-optics kicked rotor”, *Phys. Rev. A* **78**, 053625 (2008).
- [52] D. W. Lynch, C. G. Olson, and J. H. Weaver, “Optical properties of Ti, Zr, and Hf from 0.15 to 30 eV”, *Phys. Rev. B* **11**, 3617 (1975).
- [53] M. Debiossac et al., “Tailored photocleavable peptides: fragmentation and neutralization pathways in high vacuum”, *Phys. Chem. Chem. Phys.* **20**, 11412 (2018).
- [54] M. Marksteiner et al., “Gas-phase formation of large neutral alkaline-earth metal tryptophan complexes”, *J. Am. Soc. Mass Spectrom.* **19**, 1021 (2008).
- [55] J. M. McGuirk, “High precision absolute gravity gradiometry with atom interferometry”, PhD thesis (Stanford University, 2002).

- [56] T. K. Gaylord and M. G. Moharam, “Thin and thick gratings: terminology clarification”, *Appl. Opt.* **20**, 3271 (1981).
- [57] M. Horne, I. Jex, and A. Zeilinger, “Schrödinger wave functions in strong periodic potentials with applications to atom optics”, *Phys. Rev. A* **59**, 2190 (1999).
- [58] H. Müller, S.-w. Chiow, and S. Chu, “Atom-wave diffraction between the Raman-Nath and the Bragg regime: Effective Rabi frequency, losses, and phase shifts”, *Phys. Rev. A* **77**, 023609 (2008).
- [59] A. F. Bernhardt and B. W. Shore, “Coherent atomic deflection by resonant standing waves”, *Phys. Rev. A* **23**, 1290 (1981).
- [60] D. M. Giltner, R. W. McGowan, and S. A. Lee, “Theoretical and experimental study of the Bragg scattering of atoms from a standing light wave”, *Phys. Rev. A* **52**, 3966 (1995).
- [61] S. Dürr, S. Kunze, and G. Rempe, “Pendellösung oscillations in second-order Bragg scattering of atoms from a standing light wave”, *Quantum Semiclass. Opt.* **8**, 531 (1996).
- [62] C. Keller et al., “Adiabatic following in standing-wave diffraction of atoms”, *Appl. Phys. B* **69**, 303 (1999).
- [63] J.-N. Siemß et al., “Analytic theory for Bragg atom interferometry based on the adiabatic theorem”, *Phys. Rev. A* **102**, 033709 (2020).
- [64] S. S. Szigeti, J. E. Debs, J. J. Hope, N. P. Robins, and J. D. Close, “Why momentum width matters for atom interferometry with Bragg pulses”, *New J. Phys.* **14**, 023009 (2012).
- [65] S. Dürr and G. Rempe, “Acceptance angle for Bragg reflection of atoms from a standing light wave”, *Phys. Rev. A* **59**, 1495 (1999).
- [66] M. A. H. M. Jansen, K. F. E. M. Domen, H. C. W. Beijerinck, and K. A. H. van Leeuwen, “Off-resonance atomic Bragg scattering”, *Phys. Rev. A* **76**, 053629 (2007).
- [67] P. J. Martin, B. G. Oldaker, A. H. Miklich, and D. E. Pritchard, “Bragg scattering of atoms from a standing light wave”, *Phys. Rev. Lett.* **60**, 515 (1988).
- [68] H. Müller, S.-w. Chiow, Q. Long, S. Herrmann, and S. Chu, “Atom interferometry with up to 24-Photon-Momentum-Transfer beam splitters”, *Phys. Rev. Lett.* **100**, 180405 (2008).
- [69] S.-w. Chiow, T. Kovachy, H.-C. Chien, and M. A. Kasevich, “ $102\hbar k$  large area atom interferometers”, *Phys. Rev. Lett.* **107**, 130403 (2011).

- [70] M. Ben Dahan, E. Peik, J. Reichel, Y. Castin, and C. Salomon, “Bloch oscillations of atoms in an optical potential”, *Phys. Rev. Lett.* **76**, 4508 (1996).
- [71] S. R. Wilkinson, C. F. Bharucha, K. W. Madison, Q. Niu, and M. G. Raizen, “Observation of atomic Wannier-Stark ladders in an accelerating optical potential”, *Phys. Rev. Lett.* **76**, 4512 (1996).
- [72] M. Cadoret et al., “Combination of Bloch oscillations with a Ramsey-Bordé interferometer: New determination of the fine structure constant”, *Phys. Rev. Lett.* **101**, 230801 (2008).
- [73] P. Cladé, S. Guellati-Khélifa, F. Nez, and F. Biraben, “Large momentum beam splitter using Bloch oscillations”, *Phys. Rev. Lett.* **102**, 240402 (2009).
- [74] H. Müller, S.-w. Chiow, S. Herrmann, and S. Chu, “Atom Interferometers with scalable enclosed area”, *Phys. Rev. Lett.* **102**, 240403 (2009).
- [75] E. Giese, A. Roura, G. Tackmann, E. M. Rasel, and W. P. Schleich, “Double Bragg diffraction: A tool for atom optics”, *Phys. Rev. A* **88**, 053608 (2013).
- [76] H. Ahlers et al., “Double Bragg interferometry”, *Phys. Rev. Lett.* **116**, 173601 (2016).
- [77] Z. Pagel et al., “Symmetric Bloch oscillations of matter waves”, *Phys. Rev. A* **102**, 053312 (2020).
- [78] C. Brand et al., “Bragg diffraction of large organic molecules”, *Phys. Rev. Lett.* **125**, 033604 (2020).
- [79] Y. Shin et al., “Atom interferometry with Bose-Einstein condensates in a double-well potential”, *Phys. Rev. Lett.* **92**, 050405 (2004).
- [80] T. Schumm et al., “Matter-wave interferometry in a double well on an atom chip”, *Nat. Phys.* **1**, 57 (2005).
- [81] S. Wu, E. J. Su, and M. Prentiss, “Time domain de Broglie wave interferometry along a magnetic guide”, *Eur. Phys. J. D* **35**, 111 (2005).
- [82] O. Garcia, B. Deissler, K. J. Hughes, J. M. Reeves, and C. A. Sackett, “Bose-Einstein-condensate interferometer with macroscopic arm separation”, *Phys. Rev. A* **74**, 031601 (2006).
- [83] M. Horikoshi and K. Nakagawa, “Suppression of dephasing due to a trapping potential and atom-atom interactions in a trapped-condensate interferometer”, *Phys. Rev. Lett.* **99**, 180401 (2007).
- [84] G. Ferrari, N. Poli, F. Sorrentino, and G. M. Tino, “Long-lived Bloch oscillations with bosonic Sr atoms and application to gravity measurement at the micrometer scale”, *Phys. Rev. Lett.* **97**, 060402 (2006).



- [85] R. Charrière, M. Cadoret, N. Zahzam, Y. Bidel, and A. Bresson, “Local gravity measurement with the combination of atom interferometry and Bloch oscillations”, *Phys. Rev. A* **85**, 013639 (2012).
- [86] X. Zhang, R. P. del Aguila, T. Mazzoni, N. Poli, and G. M. Tino, “Trapped-atom interferometer with ultracold Sr atoms”, *Phys. Rev. A* **94**, 043608 (2016).
- [87] O. Zobay and B. M. Garraway, “Two-dimensional atom trapping in field-induced adiabatic potentials”, *Phys. Rev. Lett.* **86**, 1195 (2001).
- [88] I. Lesanovsky and W. von Klitzing, “Time-averaged adiabatic potentials: Versatile matter-wave guides and atom traps”, *Phys. Rev. Lett.* **99**, 083001 (2007).
- [89] S. Pandey et al., “Hypersonic Bose–Einstein condensates in accelerator rings”, *Nature* **570**, 205 (2019).
- [90] F. R. Gantmacher and M. G. Krein, *Oscillation matrices and kernels and small vibrations of mechanical systems*, Revised, AMS Chelsea Publishing (American Mathematical Society, 2002).
- [91] G. Teschl, *Jacobi operators and completely integrable nonlinear lattices*, Mathematical Surveys and Monographs (American Mathematical Society, 2000).
- [92] J. H. Eberly, B. W. Shore, Z. Białynicka-Birula, and I. Białynicki-Birula, “Coherent dynamics of N-level atoms and molecules. I. Numerical experiments”, *Phys. Rev. A* **16**, 2038 (1977).
- [93] Z. Białynicka-Birula, I. Białynicki-Birula, J. H. Eberly, and B. W. Shore, “Coherent dynamics of N-level atoms and molecules. II. Analytic solutions”, *Phys. Rev. A* **16**, 2048 (1977).
- [94] B. W. Shore, *The theory of coherent atomic excitation*, Vol. 2 (Wiley, New York, 1990).
- [95] C. V. Raman and N. S. Nagendra Nath, “The diffraction of light by high frequency sound waves: Part IV”, *Proc. Indian Acad. Sci.* **3**, 119 (1936).
- [96] D. Bohm, *Quantum theory*, Dover Books in Science and Mathematics (Dover Publications, 1989).
- [97] M. Born and V. Fock, “Beweis des Adiabatsatzes”, *Z. Physik* **51**, 165 (1928).
- [98] F. Arscott, *Periodic differential equations: An introduction to Mathieu, Lamé, and allied functions*, International Series of Monographs in Pure and Applied Mathematics (Macmillan, 1964).

- [99] O. Marichev and M. Trott, *Characteristic value of an even Mathieu function: Series representations*, Wolfram Functions, <https://functions.wolfram.com/MathieuandSpheroidalFunctions/MathieuCharacteristicA/06/01/01/> (visited on 12/10/2020).
- [100] O. Marichev and M. Trott, *Characteristic value of an odd Mathieu function: Series representations*, Wolfram Functions, <https://functions.wolfram.com/MathieuandSpheroidalFunctions/MathieuCharacteristicB/06/01/01/> (visited on 12/10/2020).
- [101] T. Kato, “On the adiabatic theorem of quantum mechanics”, J. Phys. Soc. Jpn. **5**, 435 (1950).
- [102] J. E. Avron, R. Seiler, and L. G. Yaffe, “Adiabatic theorems and applications to the quantum hall effect”, Commun.Math. Phys. **110**, 33 (1987).
- [103] J. E. Avron and A. Elgart, “Adiabatic theorem without a gap condition”, Comm Math Phys **203**, 445 (1999).
- [104] Z.-Y. Wang and M. B. Plenio, “Necessary and sufficient condition for quantum adiabatic evolution by unitary control fields”, Phys. Rev. A **93**, 052107 (2016).
- [105] M. V. Berry, “Quantal phase factors accompanying adiabatic changes”, Proceedings of the Royal Society of London. A. Mathematical and Physical Sciences **392**, 45 (1984).
- [106] K.-P. Marzlin and B. C. Sanders, “Inconsistency in the Application of the Adiabatic Theorem”, Phys. Rev. Lett. **93**, 160408 (2004).
- [107] M. H. S. Amin, “Consistency of the adiabatic theorem”, Phys. Rev. Lett. **102**, 220401 (2009).
- [108] G. Rigolin, G. Ortiz, and V. H. Ponce, “Beyond the quantum adiabatic approximation: Adiabatic perturbation theory”, Phys. Rev. A **78**, 052508 (2008).
- [109] J. Havil, *Gamma: Exploring Euler’s constant*, Princeton Science Library (Princeton University Press, Princeton, N.J., 2003).
- [110] L. Bracci and L. E. Picasso, “A simple iterative method to write the terms of any order of perturbation theory in quantum mechanics”, Eur. Phys. J. Plus **127**, 119 (2012).
- [111] D. Gochnauer, K. E. McAlpine, B. Plotkin-Swing, A. O. Jamison, and S. Gupta, “Bloch-band picture for light-pulse atom diffraction and interferometry”, Phys. Rev. A **100**, 043611 (2019).

- [112] J. Johansson, P. Nation, and F. Nori, “QuTiP: An open-source Python framework for the dynamics of open quantum systems”, *Comput. Phys. Commun.* **183**, 1760 (2012).
- [113] J. Johansson, P. Nation, and F. Nori, “QuTiP 2: A Python framework for the dynamics of open quantum systems”, *Comput. Phys. Commun.* **184**, 1234 (2013).
- [114] C. Keller, “Bewegung von Atomen in starken Lichtfeldern”, PhD thesis (University of Vienna, 1999).
- [115] D. M. Giltner, R. W. McGowan, and S. A. Lee, “Atom interferometer based on Bragg scattering from standing light waves”, *Phys. Rev. Lett.* **75**, 2638 (1995).
- [116] K. Simonović, “Optical tools for molecular quantum optics”, MSc Thesis (University of Vienna, Vienna, 2020).
- [117] R. Ramprasad and N. Shi, “Polarizability of phthalocyanine based molecular systems: A first-principles electronic structure study”, *Appl. Phys. Lett.* **88**, 222903 (2006).
- [118] S. Deachapunya et al., “Thermal and electrical properties of porphyrin derivatives and their relevance for molecule interferometry”, *J. Chem. Phys.* **126**, 164304 (2007).
- [119] K. Rajalakshmi, S. Gunasekaran, and S. Kumaresan, “Vibrational spectra, electronic and quantum mechanical investigations on ciprofloxacin”, *Indian J. Phys.* **88**, 733 (2014).
- [120] K. Hornberger et al., “Theory and experimental verification of Kapitza-Dirac-Talbot-Lau interferometry”, *New J. Phys.* **11**, 043032 (2009).
- [121] E. Clar, *Polycyclic hydrocarbons*, Vol. 2 (Springer-Verlag, Berlin Heidelberg, 1964).
- [122] M. A. Al-Omar, “Ciprofloxacin: Physical profile”, in *Profiles of drug substances, excipients and related methodology*, Vol. 31, edited by H. G. Brittain (Academic Press, Jan. 1, 2005), pp. 163–178.
- [123] D. J. A. McKechn, C. Robinson, and B. S. Sathyaprakash, “A tapering window for time-domain templates and simulated signals in the detection of gravitational waves from coalescing compact binaries”, *Class. Quantum Grav.* **27**, 084020 (2010).
- [124] C. Brand et al., “A fiber-based beam profiler for high-power laser beams in confined spaces and ultra-high vacuum”, *Opt. Express* **28**, 6164 (2020).
- [125] J. P. Cotter et al., “In search of multipath interference using large molecules”, *Sci. Adv.* **3**, e1602478 (2017).

- [126] A. E. A. Koolen, G. T. Jansen, K. F. E. M. Domen, H. C. W. Beijerinck, and K. A. H. van Leeuwen, “Large-angle adjustable coherent atomic beam splitter by Bragg scattering”, *Phys. Rev. A* **65**, 041601 (2002).
- [127] M. Shneider, P. Barker, and S. Gimelshein, “Molecular transport in pulsed optical lattices”, *Appl. Phys. A* **89**, 337 (2007).
- [128] M. Kozuma et al., “Coherent splitting of Bose-Einstein condensed atoms with optically induced Bragg diffraction”, *Phys. Rev. Lett.* **82**, 871 (1999).
- [129] F. Kialka, B. A. Stickler, and K. Hornberger, “Orbital angular momentum interference of trapped matter waves”, *Phys. Rev. Research* **2**, 022030 (2020).
- [130] M. Spanner, E. A. Shapiro, and M. Ivanov, “Coherent control of rotational wave-packet dynamics via fractional revivals”, *Phys. Rev. Lett.* **92**, 093001 (2004).
- [131] B. A. Stickler et al., “Probing macroscopic quantum superpositions with nanorotors”, *New J. Phys.* **20**, 122001 (2018).
- [132] A. S. Moskalenko, A. Matos-Abiague, and J. Berakdar, “Revivals, collapses, and magnetic-pulse generation in quantum rings”, *Phys. Rev. B* **74**, 161303 (2006).
- [133] P. Leboeuf and N. Pavloff, “Bose-Einstein beams: Coherent propagation through a guide”, *Phys. Rev. A* **64**, 033602 (2001).
- [134] S. Schwartz et al., “One-dimensional description of a Bose-Einstein condensate in a rotating closed-loop waveguide”, *New J. Phys.* **8**, 162 (2006).
- [135] C. Chin, R. Grimm, P. Julienne, and E. Tiesinga, “Feshbach resonances in ultracold gases”, *Rev. Mod. Phys.* **82**, 1225 (2010).
- [136] G. Roati et al., “ $^{39}\text{K}$  Bose-Einstein condensate with tunable interactions”, *Phys. Rev. Lett.* **99**, 010403 (2007).
- [137] C. D’Errico et al., “Feshbach resonances in ultracold  $^{39}\text{K}$ ”, *New J. Phys.* **9**, 223 (2007).
- [138] S. Falke et al., “Potassium ground-state scattering parameters and Born-Oppenheimer potentials from molecular spectroscopy”, *Phys. Rev. A* **78**, 012503 (2008).
- [139] M. Wilkens, “Quantum phase of a moving dipole”, *Phys. Rev. Lett.* **72**, 5 (1994).
- [140] H. Wei, R. Han, and X. Wei, “Quantum phase of induced dipoles moving in a magnetic field”, *Phys. Rev. Lett.* **75**, 2071 (1995).

- [141] X.-G. He and B. H. J. McKellar, “Topological phase due to electric dipole moment and magnetic monopole interaction”, *Phys. Rev. A* **47**, 3424 (1993).
- [142] Y. Aharonov and A. Casher, “Topological quantum effects for neutral particles”, *Phys. Rev. Lett.* **53**, 319 (1984).
- [143] E. W. Weisstein, *Ellipse*, MathWorld—A Wolfram Web Resource, <https://mathworld.wolfram.com/Ellipse.html> (visited on 01/15/2021).
- [144] G. E. Marti, R. Olf, and D. M. Stamper-Kurn, “Collective excitation interferometry with a toroidal Bose-Einstein condensate”, *Phys. Rev. A* **91**, 013602 (2015).
- [145] C. Foot, *Atomic physics*, Vol. 7, Oxford Master Series in Physics (Oxford University Press, Oxford; New York, 2004).
- [146] W. Bao, D. Jaksch, and P. A. Markowich, “Numerical solution of the Gross–Pitaevskii equation for Bose–Einstein condensation”, *J. Comput. Phys.* **187**, 318 (2003).
- [147] *Massively Parallel Trotter-Suzuki Solver*, GitHub, <https://github.com/trotter-suzuki-mpi> (visited on 01/16/2021).
- [148] E. Schmutzer and J. Plebański, “Quantum mechanics in non-inertial frames of reference”, *Fortschritte Phys.* **25**, 37 (1977).
- [149] W. H. Klink, “Quantum mechanics in noninertial reference frames”, *Annals of Physics* **260**, 27 (1997).
- [150] W. H. Klink and S. Wickramasekara, “Quantum mechanics in noninertial reference frames: Relativistic accelerations and fictitious forces”, *Annals of Physics* **369**, 66 (2016).
- [151] E. Peik, M. Ben Dahan, I. Bouchoule, Y. Castin, and C. Salomon, “Bloch oscillations of atoms, adiabatic rapid passage, and monokinetic atomic beams”, *Phys. Rev. A* **55**, 2989 (1997).
- [152] E. Brion, L. H. Pedersen, and K. Mølmer, “Adiabatic elimination in a lambda system”, *J. Phys. A* **40**, 1033 (2007).
- [153] Y. Huang and W. F. McColl, “Analytical inversion of general tridiagonal matrices”, *J. Phys. A: Math. Gen.* **30**, 7919 (1997).





## **Reprints of selected publications**





# Concepts for long-baseline high-mass matter-wave interferometry<sup>\*</sup>

Filip Kiałka<sup>1</sup>, Benjamin A Stickler<sup>1</sup>, Klaus Hornberger<sup>1</sup> ,  
Yaakov Y Fein<sup>2</sup>, Philipp Geyer<sup>2</sup>, Lukas Mairhofer<sup>2</sup>, Stefan Gerlich<sup>2</sup> and  
Markus Arndt<sup>2</sup> 

<sup>1</sup>Faculty of Physics, University of Duisburg-Essen, Lotharstraße 1, D-47048 Duisburg, Germany

<sup>2</sup>Faculty of Physics, University of Vienna, Boltzmanngasse 5, A-1090 Vienna, Austria

E-mail: markus.arndt@univie.ac.at

Received 28 June 2018, revised 10 October 2018

Accepted for publication 20 November 2018

Published 24 January 2019



## Abstract

Designing experiments which delocalize ever more complex and more massive particles requires a quantitative assessment of new interferometer configurations. Here, we introduce a figure of merit which quantifies the difference between a genuine quantum interference pattern and a classical shadow and use it to compare a number of near-field interferometer schemes. This allows us to identify the most promising setups for future tests of the quantum superposition principle, and to discuss the perspectives of interferometry with complex molecules and clusters.

Keywords: matter wave optics, quantum optics in phase space, interferometry with clusters and molecules

(Some figures may appear in colour only in the online journal)

## 1. Introduction

Matter-wave interference is a prominent example of fundamental quantum physics, with applications in quantum sensing and metrology [1, 2]. On the fundamental side, it is a direct test of the universality of the superposition principle and its possible breakdown beyond a certain mass and complexity limit [3–5]. Matter-wave interferometry has been used for quantum-enhanced measurements of gravitational effects [6–11] and in the search for dark energy [12]. Nanoparticle interferometry can enable new quantum tests of the weak equivalence principle [7, 13–15] in a range of internal particle properties and masses that cannot be compared in any other device so far [16]. Moreover, it has been suggested that certain candidates for dark matter might be best detected in nanoparticle interferometry [17, 18]. Matter-wave interference

experiments of the future aim to probe gravity-induced dephasing and decoherence [19–22, 26], and to test predictions of the Newton–Schrödinger equation [23] or the quantum nature of gravity [24, 25]. Interestingly, the influence of these phenomena tends to grow with the square of the mass of the delocalized particle. This also holds for a recent definition of macroscopicity, which quantifies the degree to which nonlinear extensions of quantum mechanics can be excluded [27].

On the applied side, a matter-wave interference pattern can be thought of as a free-flying nanometric ruler, the displacement of which can be measured with high sensitivity. In atom interferometry, this enables precise measurement of accelerations, such as those arising due to rotation or gravity [28–30]. Based on the same principle, macromolecule and nanoparticle interferometry can be developed for force sensing and used to measure molecular properties [31, 32]. This has been used to probe optical [33] and static [34] molecular polarizability, dipole moments [35], absolute optical absorption cross sections [36], and to distinguish molecular conformers [37, 38]. Extended to large peptides and proteins, such techniques can become a valuable tool for biophysical chemistry.

<sup>\*</sup> This special issue is honoring the 60th birthday of Wolfgang Schleich. Our contribution relates closely to his seminal research and teaching on quantum physics in phase space.



Original content from this work may be used under the terms of the Creative Commons Attribution 3.0 licence. Any further distribution of this work must maintain attribution to the author(s) and the title of the work, journal citation and DOI.

The instruments representing the state of the art in high-mass matter-wave physics are the Kapitza–Dirac–Talbot–Lau interferometer (KDTLI) [39] and the optical time-domain matter interferometer (OTIMA). KDTLI demonstrated quantum interference of bio-dyes, vitamins [34], and hot molecules with masses beyond 10 000 Da [40]. It was also used for many of the metrological applications mentioned above [33, 35, 37, 38]. OTIMA has demonstrated interference with molecular clusters [41, 42] and recently of molecules with masses beyond 6000 Da [16].

Both KDTLI and OTIMA rely on the near-field self-imaging of a diffractive element known as the Talbot–Lau effect [43, 44]. It is a two-grating phenomenon, in which the first grating prepares spatial coherence and the subsequent grating acts as the diffractive element. The Talbot–Lau scheme is especially suitable for high-mass interference because of the lack of bright coherent sources for molecules and clusters. Talbot–Lau interference is well-known in optics [45–47], has been demonstrated with atoms [48], and is also the basis for our present discussion. For a diffractive element with period  $d$ , the self-images occur at integer multiples of the Talbot length,  $L_T = d^2/\lambda_{dB}$ , where  $\lambda_{dB}$  is the de Broglie wavelength of the particle. The definition of  $L_T$  implies that pushing towards higher masses requires developments in slowing and cooling of heavy particles, but also an increase of the interferometer length. This motivates the present study of the long-baseline universal matter-wave interferometer, an instrument that is ten times longer than the current mass-record holder, the KDTLI. The goal of the new interferometer is to probe de Broglie wavelengths down to  $\lambda_{dB} = 20\text{--}30$  fm and demonstrate interference of masses beyond  $10^5$  Da.

The article is structured as follows: in section 2 we review the phase-space description of near-field interference, and derive a figure of merit that is later used to compare different interferometer setups. In section 3 we identify and discuss the most promising interferometer schemes for organic molecules, proteins, and atomic and molecular clusters. We end with a summary in section 4.

## 2. Phase-space description of near-field matter-wave interferometry

In this section, we describe the propagation of matter waves through a near-field interferometer and quantify the resulting interference pattern. We consider two- and three-grating setups and provide both a quantum and a classical description. Comparing these predictions is necessary to identify parameter ranges where quantum interference fringes are clearly distinguishable from a classical shadow [49].

Both descriptions are performed in the phase space  $(x, p)$  of the particle's motion in the direction perpendicular to the grating slits and the particle beam. We assume that the particle's forward motion can be separated and is thus constant, with velocity  $v$ . We further assume that the gratings are aligned to gravity, so that the particle falls freely along the grating slits. Gravity then only shifts the vertical position of the pattern, but does not reduce the fringe contrast.

The phase-space description allows us to derive the classical and quantum predictions based on the same approximations, and to insert the various beam-splitting components discussed in section 3. The phase-space description can also be extended to include decoherence events during free flight [50], measurement-induced beam splitting [51], and various metrological agents such as externally applied fields [34].

### 2.1. Quantum description

The transverse motional quantum state  $\hat{\rho}$  of the particle of mass  $m$  is represented with a Wigner function defined as [52]

$$w(x, p) = \frac{1}{2\pi\hbar} \int ds e^{ips/\hbar} \left\langle x - \frac{s}{2} \left| \hat{\rho} \right| x + \frac{s}{2} \right\rangle. \quad (1)$$

Assuming that the source uniformly illuminates an  $X_0$ -wide area of the first grating and that the momentum distribution in the beam is  $D(p)$ , the initial state can be written as

$$w_0(x, p) = \frac{D(p)}{X_0} \theta\left(\frac{X_0}{2} - |x|\right), \quad (2)$$

where  $\theta(x)$  is the Heaviside step function. After traversing the first grating, the state becomes

$$w_1(x, p) = \int dp_0 \mathcal{T}_1(x, p - p_0) w_0(x, p_0), \quad (3)$$

where the transformation kernel  $\mathcal{T}_1(x, p)$  is a Wigner transform of the first grating's transmission function  $t_1(x)$  calculated using the eikonal approximation [53]

$$\mathcal{T}_1(x, p) = \frac{1}{2\pi\hbar} \int ds e^{ips/\hbar} t_1\left(x - \frac{s}{2}\right) t_1^*\left(x + \frac{s}{2}\right). \quad (4)$$

Between the first and second grating, the molecule propagates for a time  $T_1$  under the influence of an external force causing transverse acceleration  $a$ . This corresponds to a transformation of the form

$$w'_1(x, p) = w_1\left(x - \frac{p}{m}T_1 + \frac{aT_1^2}{2}, p - maT_1\right). \quad (5)$$

For the second grating and second propagation, analogous transformations are performed, yielding  $w'_2(x, p)$ .

In a two-grating interferometer the particle is then detected using a spatially-resolving detector. The probability density of detection at position  $x$  is

$$P(x) = \int dp w'_2(x, p). \quad (6)$$

In the wide-illumination limit  $X_0 \rightarrow \infty$ , the probability density  $P(x)$  approaches a periodic function with a Fourier decomposition

$$P(x) = \frac{1}{X_0} \sum_{n=-\infty}^{\infty} \exp\left(-2\pi i n \frac{T_1}{T_2} \frac{x}{d_1}\right) P_n. \quad (7)$$

The  $P_n$  can be expressed in terms of the Fourier coefficients  $B_n^{(i)}(\xi)$  of the transformation kernels  $\mathcal{T}_i(x, p)$ . For the  $i$ th grating with period  $d_i$  and  $n \in \mathbb{Z}$ , these coefficients are

defined as

$$B_n^{(i)}(\xi) = \frac{1}{d_i} \int_0^{d_i} dx \int dp e^{-2\pi i n x / d_i - i p \xi d_i / \hbar} T_i(x, p) \quad (8)$$

and taken to be 0 for  $n \notin \mathbb{Z}$ . Assuming that the width of  $D(p)$  is much greater than the grating momenta  $\hbar/d_i$  (and that  $X_0 \rightarrow \infty$ ),  $P_n$  can be expressed as [53]

$$P_n = e^{2\pi i \varphi_n} B_n^{(1)}(0) B_{-n(T_1+T_2)d_2/(T_2d_1)}^{(2)} \left( -n \frac{\hbar T_1}{m d_1 d_2} \right), \quad (9)$$

where  $\hbar$  is the Planck constant and the phase shift due to external force is

$$\varphi_n = \frac{n a (T_1 + T_2) T_1}{2 d_1}. \quad (10)$$

In all cases considered in this paper the acceleration will be due to the Coriolis force

$$a = 2\Omega_{\parallel} v, \quad (11)$$

where  $\Omega_{\parallel}$  is the vertical component of Earth's angular velocity at the lab's latitude and  $v$  is the forward velocity of the molecule<sup>3</sup>.

A three-grating interferometer has one more grating after the second propagation, which can be moved perpendicularly to the fringes. This allows one to detect the presence of the pattern by measuring the flux of the transmitted particles as a function of the transverse position  $x_S$  of the last grating. This is useful because many detection techniques lack the spatial resolution sufficient for direct imaging of the interference pattern.

The probability that the molecule transverses a three-grating interferometer is

$$S(x_S) = \int dx dp dp_2 T_3(x - x_S, p - p_2) w_2'(x, p_2). \quad (12)$$

In the wide-illumination limit  $X_0 \rightarrow \infty$ , the signal approaches a periodic function with a Fourier decomposition

$$S(x_S) = \sum_{n=-\infty}^{\infty} \exp\left(-2\pi i n \frac{T_1 x_S}{T_2 d_1}\right) S_n. \quad (13)$$

$S_n$  can be expressed as [53]

$$S_n = P_n B_{n T_1 d_3 / (T_2 d_1)}^{(3)}(0). \quad (14)$$

## 2.2. Classical description

In the classical description, the state of the particle is described with a phase-space probability distribution  $f(x, p)$ . Before the first grating,  $f$  coincides with  $w_0$ , given in equation (2). Upon traversing a grating,  $f$  undergoes a transformation of the same form as given in equation (3), but with a classical kernel  $\mathcal{K}_1(x, p)$  instead of  $T_1(x, p)$

$$\mathcal{K}_1(x, p) = |t_1(x)|^2 \delta(p - q_1(x)), \quad (15)$$

where  $q_1(x)$  is the momentum kick experienced by the particle traversing the first grating at position  $x$  [53].

Using a decomposition of  $\mathcal{K}_i(x, p)$  analogous to equation (8) with coefficients denoted  $C_n^{(i)}$ , we can express the Fourier coefficients of the classical pattern and signal in a form analogous to equations (9) and (14), but with  $B_n^{(i)}$  replaced by  $C_n^{(i)}$  [50]. These coefficients will be denoted  $P_n^{\text{cl}}$  and  $S_n^{\text{cl}}$ , respectively.

## 2.3. Figure of merit

A primary goal of an interference experiment with massive particles is to demonstrate their quantum behavior by producing a fringe pattern significantly more pronounced than predicted by classical theory. To quantify how well an interferometer performs at this task, we will calculate the difference between the quantum and the classical fringe modulation and compare it to the relevant noise scale<sup>4</sup>.

We assume that the particle detection rate in the absence of gratings is constant and equal to  $N/T$ , where  $T$  is the total data-taking time. In a two-grating interferometer, the mean number of counts registered in a pixel of size  $\Delta x$  is then

$$N \Delta x \langle P(x) \rangle. \quad (16)$$

The averaging of the probability density  $P(x)$  is done over the distribution of the velocities in the beam, and we have assumed that  $\Delta x$  is smaller than the length scale at which  $P(x)$  varies appreciably. Using equation (7) to expand  $P(x)$  we find that the difference between the amplitude of  $n$ th order fringes as predicted by quantum and classical theory is

$$\frac{2N \Delta x}{X_0} (|\langle P_n \rangle| - |\langle P_n^{\text{cl}} \rangle|). \quad (17)$$

The noise in our measurements is due to Poissonian counting statistics and its standard deviation can be estimated as<sup>5</sup>

$$\frac{\Delta x}{X_0} \sqrt{N P_0}. \quad (18)$$

This noise is identical in the quantum and classical models and velocity-independent, hence no averaging is necessary.

We define our figure of merit as the number of counts  $N$  for which the amplitudes of the lowest-order quantum and classical fringes differ by two shot noise amplitudes.  $N$  can then be obtained by equating the ratio of expressions (17) and (18) to 2, yielding

$$N = \frac{P_0}{(|\langle P_n \rangle| - |\langle P_n^{\text{cl}} \rangle|)^2}, \quad (19)$$

where  $n$  is the smallest index such that  $P_n \neq 0$ . In a three-grating interferometer, the integration is done in time bins,

<sup>4</sup> It should be noted that for purely metrological purposes this figure of merit is less relevant. In that case the key parameters are fringe visibility and count rate.

<sup>5</sup> The standard deviation of the number of counts in a single pixel is approximately  $\sqrt{N \Delta x P_0 / X_0}$ . Since we have  $X_0 / \Delta x$  independent pixels, the noise is reduced by a factor of  $\sqrt{X_0 / \Delta x}$ , which gives equation (18).

<sup>3</sup> The horizontal component of Earth's rotation, which depends on the azimuthal orientation of the interferometer, gives rise to a Coriolis force acting along the grating slits and therefore can be neglected.

between which the third grating is moved. By reasoning analogously as above, we arrive at an expression for  $N$  of the same form as equation (19), but with  $P_n$ ,  $P_n^{\text{cl}}$  replaced by  $S_n$ ,  $S_n^{\text{cl}}$ .

The main purpose of the figure of merit  $N$  is to compare the performance of interferometer setups. However, we can also use it as a guide when estimating the number of counts each scheme requires in order to produce a manifestly quantum fringe pattern. These experimentally relevant count numbers are most likely one to two orders of magnitude higher than  $N$ . The additional counts are necessary to offset the imperfections which we neglected in this analysis, such as residual grating vibration and misalignment or non-ionizing photon absorption for biomolecules. Also, a signal-to-noise ratio significantly higher than two is often desired, especially if the experiment is to exclude modifications of quantum mechanics despite significant uncertainty in molecular parameters.

### 3. Long-baseline interferometers for molecules and clusters

In this section, we compare the most promising configurations of a two meter long interferometer for the diffraction of proteins, as well as of metal and amino acid clusters, using the figure of merit  $N$  of section 2.

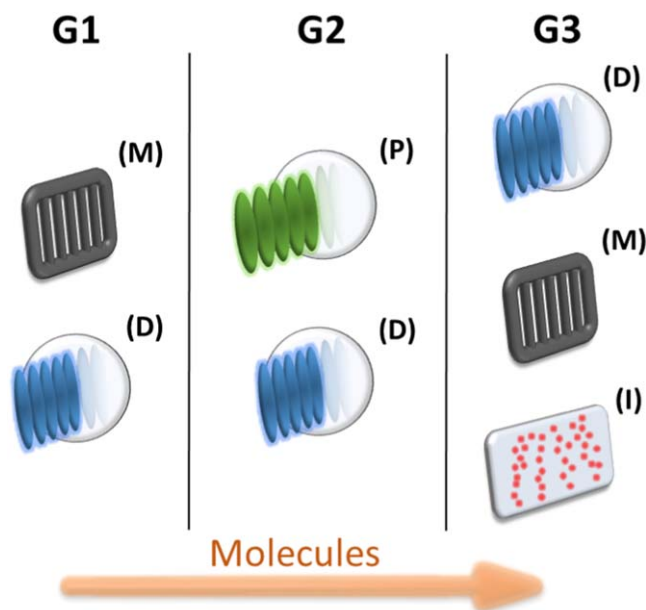
#### 3.1. Grating types

We consider three types of diffraction gratings: nano-machined masks, optical phase gratings, and optical depletion gratings (see figure 1). The Talbot coefficients  $B_n$  and  $C_n$  (see equation (8)) for these grating types can be found in [53].

**3.1.1. Material masks.** A *material grating* ( $M$ ) is a thin nanostructured membrane, which serves to modulate the matter wavefront of atoms, molecules, and clusters alike. This type of grating is the most universal, but suffers from the dispersive influence of the Casimir–Polder (CP) interaction between the particles and the slit wall<sup>6</sup>. When the material mask is used as the middle grating, this leads to strong blurring of the interference pattern [56]. Therefore, we will only consider material masks for the outer gratings, for which the CP-interaction can be approximated as a reduction of the effective slit width [57, 58], as discussed in appendix B. Motivated by previous high-mass experiments [36], we will assume silicon nitride gratings with a period of  $d = 266$  nm.

**3.1.2. Optical phase gratings.** A *phase grating* ( $P$ ) can be realized as a standing wave of laser light, which imprints a periodic phase onto the matter-wave via the dipole interaction [39, 59]. This type of grating is perfectly transmissive, does not clog, and is compatible with high-mass interference despite the dependence of the imprinted phase on the particle's velocity [60]. However, the outer gratings will

<sup>6</sup> In naming the dispersion forces, we follow the nomenclature of [55].



**Figure 1.** The interferometer configurations in this survey consist of up to three gratings, based on up to three different mechanisms. The first grating ( $G1$ ) must be absorptive to establish spatial coherence. It can be realized as material mask ( $M$ ) or a standing light wave depleting the molecular beam ( $D$ ). The second grating ( $G2$ ) can be a pure phase grating ( $P$ ). Interference detection can be achieved either by scanning an absorptive grating ( $G3$ ), or by direct imaging ( $I$ ) of the molecules deposited on a surface. In our study  $M$  and  $P$  gratings are defined to have a period of 266 nm, while  $D$  gratings have half the period.

always be assumed to be absorptive masks, as required to prepare coherence ( $G1$ ) and to analyze the resulting density pattern ( $G3$ ).

In our analysis, we assume 532 nm light for a phase grating with period  $d = 266$  nm. For highly transparent dielectric materials, such as  $\text{SiO}_2$  spheres, this period could be further reduced by a factor of two by using UV light.

**3.1.3. Optical depletion gratings.** A *photo-depletion grating* ( $D$ ) can be implemented as a standing light wave which ionizes [41] or dissociates [61] the particles passing near its anti-nodes. Provided that only the neutral or intact particles are counted, these photo-processes lead to periodic molecular beam depletion. This idea can be applied to tryptophan clusters [62], a vast range of biomolecules [63], and many metal clusters [64]. In cases where the ionization energy exceeds the available photon energy, photo-cleavage ionization can be implemented by appropriate functionalization of the molecules [54]. Photo-fragmentation gratings are also expected to work for beams of native RNA and DNA [65], which undergo intense fragmentation upon UV irradiation. Depletion gratings may also be realized via optical transfer of the particles to undetectable internal states, which removes them from the detected ensemble without actually depleting the molecular beam [66, 67]. In our analysis, we assume a 266 nm UV-light depletion grating, which yields a period of 133 nm.

**Table 1.** Molecules and clusters used in this study and their parameters: polarizability volumes  $\alpha$  and absorption cross sections  $\sigma$  at 266 and 532 nm. The absorption cross sections of insulin and GFP correspond to that of the photo-cleavable group [54]. The remaining values are estimated as described in appendix A.

	$m$ (kDa)	$\alpha_{266}$ ( $\text{\AA}^3$ )	$\sigma_{266}$ ( $\text{cm}^2$ )	$\alpha_{532}$ ( $\text{\AA}^3$ )	$\sigma_{532}$ ( $\text{cm}^2$ )
Insulin	5.8	600	$4 \times 10^{-17}$	600	0
Trp <sub>50</sub> [68]	10	1000	$9.1 \times 10^{-16}$	1000	0
GFP <sup>a</sup>	27	2700	$4 \times 10^{-17}$	2700	0
Silver	100	2500	$6.9 \times 10^{-15}$	5200	$2.1 \times 10^{-16}$
Cesium	100	−2200	$6.5 \times 10^{-15}$	−22000	$2.4 \times 10^{-14}$
Silver	300	7400	$2.1 \times 10^{-14}$	15400	$6.2 \times 10^{-16}$
Cesium	300	−6700	$1.9 \times 10^{-14}$	−65000	$7.2 \times 10^{-14}$

<sup>a</sup> Green fluorescent protein.

### 3.2. Particle species, sources, and detectors

We analyze various interferometer configurations in combination with seven prototypical biomolecules, amino acid clusters and metal clusters (see table 1). This is an exemplary and certainly not exhaustive list of potential candidates up to 300 000 Da. Biomolecules are especially interesting for metrological purposes, while metal clusters or certain dielectric nanoparticles promise the simplest implementation of photo-depletion gratings and are suitable for high-mass interference.

One of the greatest challenges in matter-wave experiments is preparing a sufficiently intense, mass-selected, cold, and directed particle beam. While many native and functionalized organic molecules—from fullerenes and tailored tripeptides [69] to native vitamins [34]—can still be evaporated in a Knudsen cell, molecular beams of complex amino acid clusters and high-mass polypeptides can be prepared by laser desorption into a noble gas jet [70]. We expect that photo-neutralization of singly charged biopolymers [54] and aggregated metal clusters [71] will facilitate the preparation of neutral particle beams.

On the detector side, a key challenge is to efficiently ionize neutral massive particles. While hot-wire detection [72] is a simple and efficient tool for metal clusters with a low work function, single-photon ionization offers high efficiency for a larger range of metals and allows for excellent time resolution. Post-ionization of large amino acid clusters [62] has been observed but the detection of neutral proteins has remained a grand challenge in physical chemistry [73]. This is being tackled using functionalization and photo-cleavage [54].

In most molecule interferometers to date, ionizing detectors count the molecules transmitted through the interferometer and the required spatial resolution is provided by scanning a grating across the interference pattern. For some setups in this study, we propose instead the adsorption of the interferogram on a transparent surface, followed by high resolution imaging using electron or optical super-resolution microscopy [74–76].

### 3.3. Survey results

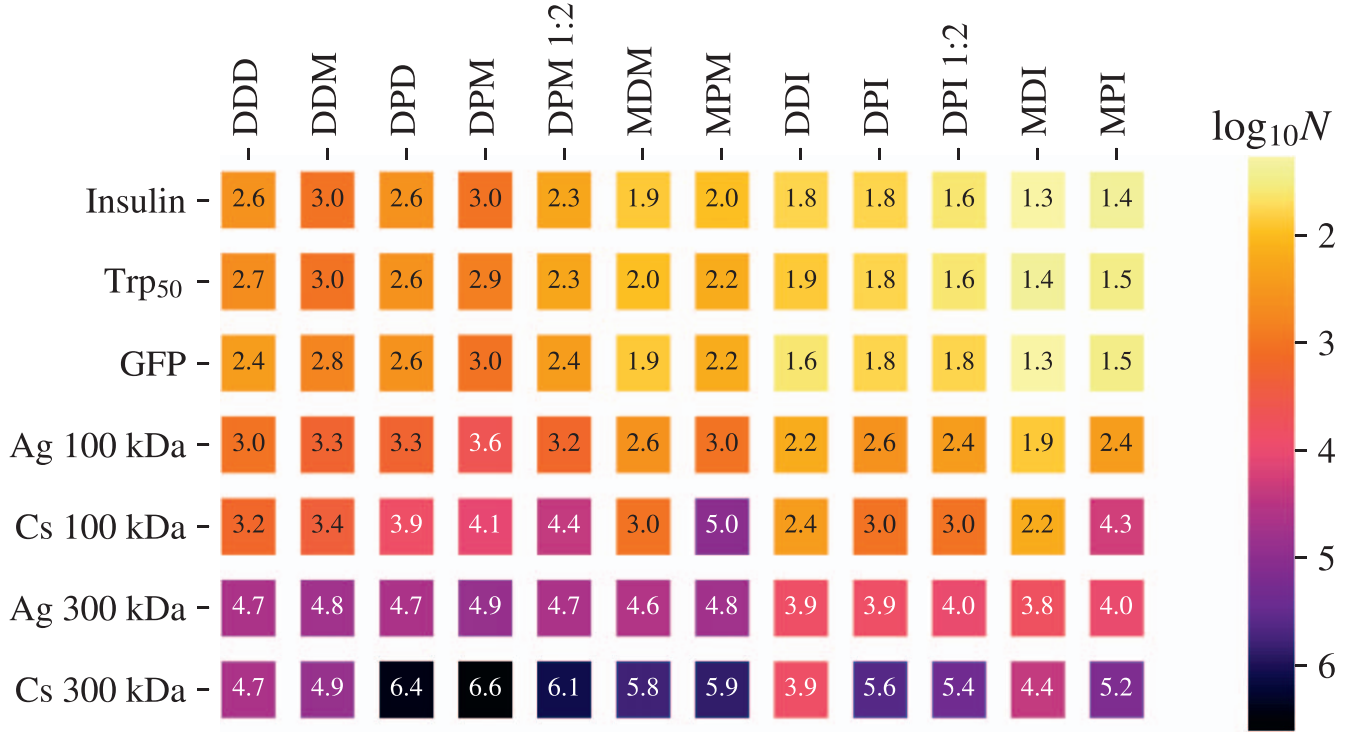
In order to compare the interferometer setups we numerically compute and optimize the figure of merit  $N$  (see

equation (19)) for each combination of grating configuration and particle species. The optimization is carried out over the average velocity of the particles and the powers of the laser gratings. For configurations with multiple laser gratings, the powers of the outer gratings are held equal. The results are summarized in figure 2.

For the biomolecules in our list, we find that all of the setups considered offer similar performance. The greatest difference can be seen between the imaging and the inter-grating-detection setups, the latter typically requiring about an order of magnitude<sup>7</sup> more counts to achieve the same degree of distinguishability between the classical and the quantum model. Within both groups, optimal performance is offered by the material-depletion setups (MDM and MDI), followed closely by the material-phase (MPM and MPI) and the asymmetric depletion-phase configurations (DPM 1:2 and DPI 1:2). The MPM configuration is close to optimal among these setups. The DPM 1:2 and DPI 1:2 setups are the best alternatives should clogging of the material grating become a problem. The calculated values of  $N$  suggest that all proposed setups are viable with biomolecules if one can detect and accumulate a total of several ten thousand molecular counts.

For 100 kDa metal clusters we find that, similar to biomolecules, the material-depletion setups offer the best performance. Also, replacing the last grating with a spatially-resolving detector has again the effect of lowering the required numbers of counts by about an order of magnitude. We find that some configurations are better for silver than for cesium, because of the high polarizability of the cesium cluster at 532 nm. In that case the best discrimination between the quantum and the classical model would nominally be achieved at low velocities, where for the same reason a material grating becomes almost opaque. This is especially pronounced for the setups MPM and MPI with a material grating in  $G1$  and a phase grating in  $G2$ . All considered setups are viable with 100 kDa silver clusters for a few hundred

<sup>7</sup> The exact factor can be estimated analytically in the following way. Note that the removal of the last grating improves the transmission of the interferometer by  $1/B_0^{(3)}(0)$ , while the pattern amplitude changes by  $1/B_{n\ell_1 d_3/(T_2 d_1)}^{(3)}(0)$  in the quantum and by  $1/C_{n\ell_1 d_3/(T_2 d_1)}^{(3)}(0)$  in the classical model (see equation (14)). One can show that  $B_k^{(3)}(0) = C_k^{(i)}(0)$  and therefore, when  $B_k^{(3)}$  is velocity-independent or when the velocity spread is small,  $N$  changes by a factor  $[B_{n\ell_1 d_3/(T_2 d_1)}^{(3)}(0)]^2/B_0^{(3)}(0)$ .



**Figure 2.** Distinguishability of the quantum and the (hypothetical) classical pattern for various interferometer configurations and particle species, as quantified by the count number  $N$  of equation (19) (smaller is better).  $D$ ,  $M$ , and  $P$  stand for depletion, material, and phase grating, respectively, and the letter  $I$  denotes spatially-resolving detection; e.g. by fluorescence imaging of surface-adsorbed molecules. The numbers following the setup names specify the ratio of distances between the gratings,  $L_1 = \overline{G1G2}$  and  $L_2 = \overline{G2G3}$ , with  $L_1:L_2 = 1:1$  if not otherwise mentioned. These results are obtained assuming a Gaussian velocity spread in the particle beam with a standard deviation equal to 5% of the average velocity. The latter is optimized for minimal  $N$  over the 30–600 m s<sup>-1</sup> range.

thousand counts. This also holds for 100 kDa cesium clusters if  $G2$  is a depletion grating.

For clusters with a mass of 300 000 Da an imaging interferometer can achieve the same discrimination between a quantum and a classical model as a non-imaging scheme, but it achieves that feat with ten times fewer counts. The high polarizability of the cesium clusters is even more apparent here, significantly affecting the performance of all configurations with a phase grating in  $G2$ . For 300 kDa silver clusters a few million counts will be required, when the Coriolis force is not compensated.

In all cases considered, the asymmetric depletion-phase-material (DPM 1:2) performs better than its symmetric counterpart. Because of the longer distance between  $G2$  and  $G3$ , low-order diffraction at  $G2$  is already sufficient to close the interferometer paths at  $G3$ . This is true for all Talbot–Lau interferometers with unequal grating periods.

Figure 2 suggests that the minimal number of counts required to verify the quantumness of the fringe pattern increases with the mass of the particle. This is due to the dephasing caused by the Coriolis force, which is proportional to mass if the interferometer length is fixed. This can be seen from equations (10) and (11) assuming the total transit time is proportional to the Talbot time  $T_T = md^2/h$ . If the Coriolis force is compensated, the particle mass can be increased

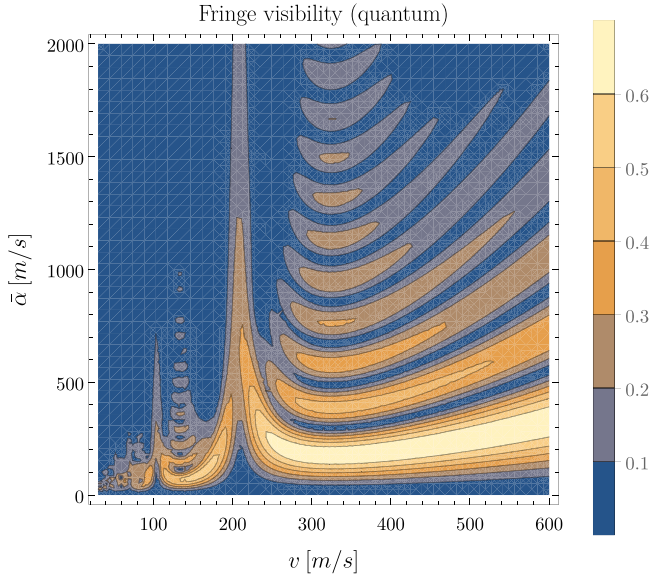
without loss of distinguishability as long as the laser power and the particle’s polarizability and velocity are adjusted accordingly.

In the discussion above we assumed that for each setup the optimal laser intensity can be reached. For insulin and GFP we require more than 20 W of UV light for a laser beam focused to a  $1/e^2$  waist of  $w = 150 \mu\text{m}$ . This is challenging but within reach of intracavity UV power enhancement. For metal clusters, laser intensities as low as 1 W at 266 nm or 15 W at 532 nm are sufficient, even at a waist of  $750 \mu\text{m}$ . These power levels are readily available from commercial light sources.

#### 4. Summary and outlook

Our results suggest that the MPM configuration, as used in the earlier KDTLI interferometer [77] can be suitable for quantum interference of biomolecules as complex as the green fluorescent protein at 27 000 Da (see figure 3) or even silver clusters beyond 300 000 Da, if the interferometer is stretched by a factor of ten to  $L_1 = L_2 = 1\text{m}$ . The arguments in favor of metal clusters also hold for silicon nanoparticles, which may eventually even be prepared by advanced cavity cooling methods in a mass range of  $10^6$ – $10^7$  Da [78].





**Figure 3.** Visibility of green fluorescent protein (GFP) interference fringes in a material-phase-material grating interferometer, as predicted by the quantum model. In the notation of equation (13), the visibility is defined as  $2|S_n|/S_0$ , where  $n$  is the smallest value for which  $S_n \neq 0$ . The velocity distribution in the beam is assumed to be Gaussian with mean  $v$  and  $0.05v$  standard deviation.  $\tilde{\alpha}$  is a measure of the strength of particle-grating interaction, defined as  $\tilde{\alpha} = 8\sqrt{2\pi}\alpha P/(hcw_z)$ , where  $\alpha$  is the polarizability volume,  $P$  is laser power,  $w_z$  is the  $1/e^2$  intensity radius of the beam in the direction of the molecules' propagation, and  $h$ ,  $c$  are the Planck constant and the velocity of light. The phase acquired by particles moving with velocity  $v$  through the antinode of the standing laser wave is then  $2\pi\tilde{\alpha}/v$ . Note, that GFP does not fluoresce in the unsolvated vacuum state, nor can it be photo-ionized using standard techniques. We thus assume that UV photo-cleavage ionization of a small tag can be used [54].

The survey also allows us to identify alternative schemes to overcome foreseeable experimental challenges en route to those goals. The alternative setups include the asymmetric depletion-phase configurations (DPM 1:2 and DPI 1:2), where the nanomask in  $G1$  is substituted by a UV standing light wave and  $G3$  can either be a mechanical grating or an adsorptive surface which is subsequently imaged. Photo-depletion gratings are advisable when clogging of the material mask becomes a limitation. The DDD and DDI configurations are furthermore advantageous over MPM and MDM for high-mass interference, for instance with cesium.

A major constraint to high-mass interference is the dephasing due to the Coriolis force, which can be mitigated in a figure-eight setup, as demonstrated for atoms [79, 80].

For each interferometer setup, we have found the molecular velocity and laser power that minimize the number of counts required to distinguish a quantum fringe pattern from a classical moiré effect. Optimal performance can be achieved when the last grating is replaced by a single-particle imaging detector based on fluorescence [76], STED [81], or highly sensitive scattering imaging for particles beyond about 10 000 Da [82, 83].

These findings will guide future experimental efforts in high-mass interferometry.

## Acknowledgments

This project has received funding from the European Research Council (ERC) under the European Union's Horizon 2020 research and innovation program (Grant Nr. 320694), the Austrian Science Funds within FWF COLMI (P30176), and FWF CoQuS (W 1210-N25).

## Appendix A. Polarizabilities and cross sections of biomolecules and clusters

In the following, we briefly describe how we estimate the polarizability volumes and absorption cross sections shown in table 1. These quantities enter the coefficients  $B_n^{(i)}$  and  $C_n^{(i)}$  describing the particle-grating interaction.

For biomolecules, we use their static polarizabilities, which we estimate by summing the contributions of aromatic amino acids (including histidine), assuming that each contributes  $20 \text{ \AA}^3$ , and non-aromatic amino acids, assuming that each contributes  $10 \text{ \AA}^3$ . To estimate the absorption cross section, we first estimate the molar absorption coefficient  $\epsilon$  as in [84]. The cross section is then obtained as

$$\sigma = \frac{\epsilon \log 10}{N_A}, \quad (\text{A1})$$

where  $N_A$  is the Avogadro number.

Polarizabilities for clusters are estimated based on the experimental values of the real and imaginary part of the complex refractive index [85, 86]. Using those, we calculate the relative permittivity  $\epsilon$  and then the polarizability volume and absorption cross section using the formulas for a sub-wavelength dielectric sphere [53]

$$\alpha = r^3 \text{Re} \frac{\epsilon - 1}{\epsilon + 2}, \quad (\text{A2})$$

$$\sigma = \frac{8\pi^2 r^3}{\lambda} \text{Im} \frac{\epsilon - 1}{\epsilon + 2}. \quad (\text{A3})$$

where  $\lambda$  is the wavelength and  $r$  is the radius of the cluster estimated using the number of atoms and the Wigner–Saitz radii taken from [87, 88].

## Appendix B. Effective opening fraction of material gratings

To estimate the effective slit width in the presence of particle-grating interaction, we assume that the particles which get deflected by more than a fixed angle  $\theta_c$  remain undetected. If the interaction potential is  $V(x)$  and  $b$  is the grating's thickness, the deflection angle to first order in the grating transit time is

$$\theta \approx -\frac{V'(x)b}{mv^2}. \quad (\text{B1})$$

Equation (B1) is a good approximation as long as the higher order term is negligible; that is, as long as

$$\frac{V''(x)v^2 m - (V'(x)^2)(\frac{b}{v})^2}{6m^2v^2} \ll 1. \quad (\text{B2})$$

Substituting the CP potential for  $V(x)$  yields the cutoff distance for a particle with static polarizability volume  $\alpha_0$

$$x_c = \left( \frac{12C_\varepsilon \hbar c \alpha_0 b}{8\pi m v^2 \theta_c} \right)^{\frac{1}{5}}, \quad (\text{B3})$$

where [55]

$$C_\varepsilon = \int_1^\infty d\nu \left[ \left( \frac{2}{\nu^2} - \frac{1}{\nu^4} \right) \frac{\varepsilon \nu - \sqrt{\varepsilon \mu - 1 + \nu^2}}{\varepsilon \nu + \sqrt{\varepsilon \mu - 1 + \nu^2}} - \frac{1}{\nu^4} \frac{\mu \nu - \sqrt{\varepsilon \mu - 1 + \nu^2}}{\mu \nu + \sqrt{\varepsilon \mu - 1 + \nu^2}} \right] \quad (\text{B4})$$

is a constant depending on the static relative permittivities  $\varepsilon$  and  $\mu$  of the grating material. Knowing  $x_c$ , we can calculate the effective opening fraction  $f'$  from the physical value  $f$ .

$$f' = f - \frac{2x_c}{d}. \quad (\text{B5})$$

Using  $f'$ , we can express the Talbot coefficients of the material gratings as [53]

$$B_n(0) = C_n(0) = f' \text{sinc}(\pi n f'). \quad (\text{B6})$$

Many molecules also possess permanent electric dipole moments. Their influence can be estimated using the orientation-averaged, non-retarded potential of a dipole  $D$  in the vicinity of a dielectric half-space


$$V_{D\varepsilon}(x) = -\frac{\varepsilon - 1}{\varepsilon + 1} \frac{D^2}{48\pi\varepsilon_0} \frac{1}{x^3}. \quad (\text{B7})$$

To do this, we take the potential in equation (B1) to be the sum of the dipole potential (B7) and the CP potential.

Assuming parameters similar to those used in previous high-mass experiments [36] ( $f = 0.42$ ,  $\varepsilon = 7.5$  and  $\mu = 1$  for silicon nitride,  $b = 100$  nm, and  $\theta_c = 0.5$  mrad) and the prototypical particles listed in table 1, we find that the influence of the CP interaction is significant at slow velocities ( $v \approx 100$  m s<sup>-1</sup>), often reducing the opening fraction by a factor of two. We further find that, although the dipole and the CP potentials can be comparable, including the former changes  $f'$  only by few percent points. This is because of the very steep dependence of both forces, and thus the deflection angle  $\theta$ , on the particle-grating distance. The contribution of the permanent dipole moments to the particle-grating interaction is therefore neglected in the present analysis.

## ORCID iDs

Klaus Hornberger  <https://orcid.org/0000-0002-3145-1117>

Markus Arndt  <https://orcid.org/0000-0002-9487-4985>

## References

- [1] Cronin A D, Schmiedmayer J and Pritchard D E 2009 *Rev. Mod. Phys.* **81** 1051
- [2] Tino G M and Kasevich M A 2014 *Atom Interferometry* vol 188 (Amsterdam: IOS Press)
- [3] Rosen N 1964 *Am. J. Phys.* **32** 597
- [4] Bassi A, Lochan K, Satin S, Singh T and Ulbricht H 2013 *Rev. Mod. Phys.* **85** 471
- [5] Arndt M and Hornberger K 2014 *Nat. Phys.* **10** 271
- [6] Colella R, Overhauser A W and Werner S A 1975 *Phys. Rev. Lett.* **34** 1472
- [7] Tarallo M G, Mazzoni T, Poli N, Sutyryn D V, Zhang X and Tino G M 2014 *Phys. Rev. Lett.* **113** 023005
- [8] Müntinga H et al 2013 *Phys. Rev. Lett.* **110** 093602
- [9] Nesvizhevsky V V et al 2002 *Nature* **415** 298
- [10] Schlippert D, Hartwig J, Albers H, Richardson L L, Schubert C, Roura A, Schleich W P, Ertmer W and Rasel E M 2014 *Phys. Rev. Lett.* **112** 203002
- [11] Asenbaum P, Overstreet C, Kovachy T, Brown D D, Hogan J M and Kasevich M A 2017 *Phys. Rev. Lett.* **118** 183602
- [12] Hamilton P, Jaffe M, Haslinger P, Simmons Q, Müller H and Khoury J T 2015 *Science* **349** 849
- [13] Schlippert D, Hartwig J, Albers H, Richardson L L, Schubert C, Roura A, Schleich W P, Ertmer W and Rasel E M 2014 *Phys. Rev. Lett.* **112** 203002
- [14] Bonnin A, Zahzam N, Bidel Y and Bresson A 2013 *Phys. Rev. A* **88** 043615
- [15] Zhou L et al 2015 *Phys. Rev. Lett.* **115** 013004
- [16] Rodewald J, Dörre N, Grimaldi A, Geyer P, Felix L, Mayor M, Shayeghi A and Arndt M 2018 *New J. Phys.* **20** 033016
- [17] Riedel C J and Yavin I 2017 *Phys. Rev. D* **96** 023007
- [18] Riedel C J 2015 *Phys. Rev. A* **92** 010101(R)
- [19] Pikovski I, Zych M, Costa F and Brukner C 2015 *Nat. Phys.* **11** 668
- [20] Diosi L 1984 *Phys. Lett. A* **105** 199
- [21] Penrose R 1996 *Gen. Rel. Grav.* **28** 581
- [22] Lamine B, Hervé R, Lambrecht A and Reynaud S 2006 *Phys. Rev. Lett.* **96** 050405
- [23] Giulini D and Großardt A 2013 Gravitationally induced inhibitions of dispersion according to a modified Schrödinger–Newton equation for a homogeneous-sphere potential *Class. Quantum Grav.* **30** 155018
- [24] Bose S, Mazumdar A, Morley G W, Ulbricht H, Toros M, Paternostro M, Geraci A A, Barker P F, Kim M S and Milburn G 2017 *Phys. Rev. Lett.* **119** 240401
- [25] Marletto C and Vedral V 2017 *Phys. Rev. Lett.* **119** 240402
- [26] Bonifacio P M, Wang C H T, Mendonça J T and Bingham R 2009 *Class. Quantum Grav.* **26** 145013
- [27] Nimmrichter S and Hornberger K 2013 *Phys. Rev. Lett.* **110** 160403
- [28] Gustavson T L, Landragin A and Kasevich M A 2000 *Class. Quantum Grav.* **17** 2385
- [29] Geiger R et al 2011 *Nat. Commun.* **2** 474
- [30] Dutta I, Savoie D, Fang B, Venon B, Garrido Alzar C L, Geiger R and Landragin A 2016 *Phys. Rev. Lett.* **116** 183003
- [31] Hornberger K, Gerlich S, Haslinger P, Nimmrichter S and Arndt M 2012 *Rev. Mod. Phys.* **84** 157
- [32] Arndt M 2014 *Phys. Today* **67** 30
- [33] Hackermüller L, Hornberger K, Gerlich S, Gring M, Ulbricht H and Arndt M 2007 *Appl. Phys. B* **89** 469
- [34] Mairhofer L, Eibenberger S, Cotter J P, Romirer M, Shayeghi A and Arndt M 2017 *Angew. Chem., Int. Ed.* **56** 10947
- [35] Eibenberger S, Gerlich S, Arndt M, Tüxen J and Mayor M 2011 *New J. Phys.* **13** 043033



- [36] Eibenberger S, Cheng X, Cotter J P and Arndt M 2014 *Phys. Rev. Lett.* **112** 250402
- [37] Gerlich S, Gring M, Ulbricht H, Hornberger K, Tüxen J, Mayor M and Arndt M 2008 *Angew. Chem., Int. Ed.* **47** 6195
- [38] Tüxen J, Gerlich S, Eibenberger S, Arndt M and Mayor M 2010 *Chem. Commun.* **46** 4145
- [39] Gerlich S *et al* 2007 *Nat. Phys.* **3** 711
- [40] Eibenberger S, Gerlich S, Arndt M, Mayor M and Tüxen J 2013 *Phys. Chem. Chem. Phys.* **15** 14696
- [41] Haslinger P, Dörre N, Geyer P, Rodewald J, Nimmrichter S and Arndt M 2013 *Nat. Phys.* **9** 144
- [42] Dörre N, Rodewald J, Geyer P, von Issendorff B, Haslinger P and Arndt M 2014 *Phys. Rev. Lett.* **113** 233001
- [43] Talbot W H F 1836 *Phil. Mag.* **9** 401
- [44] Lau E 1948 *Ann. Phys.* **437** 417
- [45] Patorski K 1989 *Progress in Optics* ed E Wolf vol 27 (Amsterdam: Elsevier) ch 1 pp 1–108
- [46] Berry M, Marzoli I and Schleich W 2001 *Phys. World* **14** 39
- [47] Kazemi P, Chaturvedi S, Marzoli I, O'Connell R F and Schleich W P 2013 *New J. Phys.* **15** 013052
- [48] Clauser J F and Li S 1994 *Phys. Rev. A* **49** R2213
- [49] Batelaan H, Bernet S, Oberthaler M K, Rasel E M, Schmiedmayer J and Zeilinger A 1997 Classical and quantum atom fringes *Atom Interferometry* ed P R Berman (New York: Academic)
- [50] Hornberger K, Sipe J E and Arndt M 2004 *Phys. Rev. A* **70** 053608
- [51] Cotter J P, Eibenberger S, Mairhofer L, Cheng X, Asenbaum P, Arndt M, Walter K, Nimmrichter S and Hornberger K 2015 *Nat. Commun.* **6** 7336
- [52] Schleich W P 2011 *Quantum Optics in Phase Space* (New York: Wiley)
- [53] Nimmrichter S 2013 Macroscopic matter-wave interferometry *PhD Thesis* University of Vienna
- [54] Debiossac M, Schatti J, Kriegleder M, Geyer P, Shayeghi A, Mayor M, Arndt M and Köhler V 2018 *Phys. Chem. Chem. Phys.* **20** 11412
- [55] Buhmann S Y 2012 *Dispersion Forces I (Springer Tracts in Modern Physics)* vol 247 1st edn (Berlin: Springer)
- [56] Brezger B, Arndt M and Zeilinger A 2003 *J. Opt. B* **5** S82
- [57] Grisenti R E, Schöllkopf W, Toennies J P, Hegerfeldt G C, Köhler T and Stoll M 2000 *Phys. Rev. Lett.* **85** 2284
- [58] Brand C *et al* 2015 *Nat. Nanotechnol.* **10** 845–8
- [59] Nairz O, Brezger B, Arndt M and Zeilinger A 2001 *Phys. Rev. Lett.* **87** 160401
- [60] Eibenberger S, Gerlich S, Arndt M, Mayor M and Tüxen J 2013 *Phys. Chem. Chem. Phys.* **15** 14696
- [61] Dörre N, Rodewald J, Geyer P, von Issendorff B, Haslinger P and Arndt M 2014 *Phys. Rev. Lett.* **113** 233001
- [62] Marksteiner M, Haslinger P, Sclafani M, Ulbricht H and Arndt M 2009 *J. Phys. Chem. A* **113** 9952
- [63] Polfer N C and Dugourd P 2015 *Laser Photodissociation and Spectroscopy of Mass-Separated Biomolecular Ions* (Berlin: Springer)
- [64] Sattler K D 2011 *Handbook of Nanophysics: Clusters and Fullerenes* (Boca Raton, FL; London: CRC Press; Taylor and Francis)
- [65] Gabelica V, Rosu F, Pauw E D, Antoine R, Tabarin T, Broyer M and Dugourd P 2007 *J. Am. Soc. Mass Spectrom.* **18** 1990
- [66] Abfalterer R, Keller C, Bernet S, Oberthaler M K, Schmiedmayer J and Zeilinger A 1997 *Phys. Rev. A* **56** R4365
- [67] Fray S, Diez C A, Hänsch T W and Weitz M 2004 *Phys. Rev. Lett.* **93** 240404
- [68] Marksteiner M, Haslinger P, Ulbricht H, Sclafani M, Oberhofer H, Dellago C and Arndt M 2008 *J. Am. Soc. Mass Spectrom.* **19** 1021
- [69] Schätti J, Sezer U, Pedalino S, Cotter J P, Arndt M, Mayor M and Köhler V 2017 *J. Mass Spectrom.* **52** 550
- [70] Geyer P, Sezer U, Rodewald J, Mairhofer L, Dörre N, Haslinger P, Eibenberger S, Brand C and Arndt M 2014 *Phys. Scr.* **91** 063007
- [71] Haberland H, Karrais M and Mall M 1991 *Z. Phys. D* **20** 413
- [72] Taylor J B and Langmuir I 1933 *Phys. Rev.* **44** 423
- [73] Hanley L and Zimmermann R 2009 *Anal. Chem.* **81** 4174
- [74] Hell S W and Wichmann J 1994 *Opt. Lett.* **19** 780
- [75] Betzig E, Patterson G H, Sougrat R, Lindwasser O W, Olenych S, Bonifacino J S, Davidson M W, Lippincott-Schwartz J and Hess H F 2006 *Science* **313** 1642
- [76] Juffmann T, Milic A, Müllneritsch M, Asenbaum P, Tsukernik A, Tüxen J, Mayor M, Cheshnovsky O and Arndt M 2012 *Nat. Nanotechnol.* **7** 297
- [77] Gerlich S, Eibenberger S, Tomandl M, Nimmrichter S, Hornberger K, Fagan P, Tüxen J, Mayor M and Arndt M 2011 *Nat. Commun.* **2** 263
- [78] Kuhn S, Wachter G, Wieser F-F, Millen J, Schneider M, Schalko J, Schmid U, Trupke M and Arndt M 2017 *Appl. Phys. Lett.* **111** 253107
- [79] Clauser J F 1989 *NASA Conf. Publication* vol 3046 ed R W Hellings
- [80] McGuirk J M, Foster G T, Fixler J B, Snadden M J and Kasevich M A 2002 *Phys. Rev. A* **65** 033608
- [81] Hell S W and Wichmann J 1994 *Opt. Lett.* **19** 780
- [82] Piliarik M and Sandoghdar V 2014 *Nat. Commun.* **5** 4495
- [83] Tzang O, Pevzner A, Marvel R E, Haglund R F and Cheshnovsky O 2015 *Nano Lett.* **15** 1362
- [84] Pace C N, Vajdos F, Fee L, Grimsley G and Gray T 1995 *Protein Sci.* **4** 2411
- [85] Lynch D W and Hunter W 1997 *Handbook of Optical Constants of Solids* ed E D Palik (Burlington, MA: Academic) pp 275–367
- [86] Inagaki T and Arakawa E 1997 *Handbook of Optical Constants of Solids* ed E D Palik (Burlington, MA: Academic) pp 341–50
- [87] Limberger H G and Martin T P 1989 *J. Chem. Phys.* **90** 2979
- [88] Ashcroft N and Mermin N 1976 *Solid State Physics* (San Diego, CA: Harcourt College Publishers)



## Bragg Diffraction of Large Organic Molecules

Christian Brand<sup>1,2</sup>, Filip Kiałka<sup>1,3</sup>, Stephan Troyer<sup>1</sup>, Christian Knobloch<sup>1</sup>, Ksenija Simonović<sup>1</sup>,Benjamin A. Stickler<sup>3,4</sup>, Klaus Hornberger<sup>3</sup>, and Markus Arndt<sup>1,\*</sup><sup>1</sup>University of Vienna, Faculty of Physics, Boltzmannngasse 5, A-1090 Vienna, Austria<sup>2</sup>German Aerospace Center (DLR), Institute of Quantum Technologies, Söflinger Straße 100, 89077 Ulm, Germany<sup>3</sup>Faculty of Physics, University of Duisburg-Essen, Lotharstraße 1, 47048 Duisburg, Germany<sup>4</sup>QOLS, Blackett Laboratory, Imperial College London, SW7 2AZ London, United Kingdom

(Received 14 June 2019; accepted 12 June 2020; published 16 July 2020)

We demonstrate Bragg diffraction of the antibiotic ciprofloxacin and the dye molecule phthalocyanine at a thick optical grating. The observed patterns show a single dominant diffraction order with the expected dependence on the incidence angle as well as oscillating population transfer between the undiffracted and diffracted beams. We achieve an equal-amplitude splitting of  $14\hbar k$  (photon momenta) and maximum momentum transfer of  $18\hbar k$ . This paves the way for efficient, large-momentum beam splitters and mirrors for hot and complex molecules.

DOI: 10.1103/PhysRevLett.125.033604

**Introduction.**—Matter-wave diffraction and interference have numerous applications across the natural sciences. Electron and neutron diffraction are key techniques in condensed-matter physics and materials science [1,2], while atom interferometers are utilized in tests of fundamental physics, as well as for measuring physical constants and inertial forces [3,4]. Extending matter-wave interference experiments to large molecules enabled quantum-assisted studies of molecular properties [5,6] as well as the interference of biomolecules [7,8] and particles with masses beyond 25000 u [9].

One of the major techniques used in matter-wave interferometry is Bragg diffraction. It employs thick gratings [10] to coherently scatter the impinging particles into a single diffraction order. This allows for the realization of efficient matter-wave mirrors and beam splitters [11,12]. Bragg diffraction stands in contrast to Raman-Nath diffraction at thin gratings [13–15], which produces several diffraction orders arranged symmetrically around the incoming particle beam. Bragg diffraction was first demonstrated for neutrons [16] and later for atoms [17], Bose-Einstein condensates [18], electrons [19], and diatomic molecules [20].

Here, we report on the first Bragg diffraction of complex organic molecules. We show that the antibiotic ciprofloxacin and the dye molecule phthalocyanine [see Fig. 1(a)] can be reliably diffracted, despite being in a highly excited rotational state and possessing more than 100 vibrational degrees of freedom thermalized at 700–1000 K. This is an important step towards efficient coherent manipulation of functional, hot, and polar molecules.

**Experimental setup.**—The experimental setup is shown in Fig. 1(b): the molecules are evaporated by a focused laser beam, diffracted at a thick optical grating and collected on a

quartz slide at the end of the vacuum chamber. In detail, a thin film of molecules is evaporated from the entrance window of a vacuum chamber by focusing a 420 nm laser beam down to a waist of  $1.3(1) \mu\text{m}$ . We have used mass spectrometry to verify that molecular fragmentation can be neglected in the evaporation process [21]. After 1505 mm of free flight the molecular beam is transversely collimated with a piezocontrolled slit  $S_x$ , which we set to about  $14 \mu\text{m}$ . After an additional 35 mm, the molecules are diffracted at a standing light wave, realized by retroreflecting a laser beam with wavelength  $\lambda = 532 \text{ nm}$ , power  $P \leq 14.6(2) \text{ W}$ , and waist along the flight direction  $w_z = 7.04(5) \text{ mm}$ . The waist along  $y$  at the position of the molecular beam is set to  $w_y = 55\text{--}65 \mu\text{m}$  as measured with a fiber-based beam profiler [27]. The angle between the mirror surface and the molecular beam  $\theta_{\text{grat}}$  is determined with an accuracy of about  $5 \mu\text{rad}$ . This is achieved by finding the zero-incidence position of the actively stabilized piezo mirror mount and tilting it by the desired  $\theta_{\text{grat}}$  before each run. Free fall in the gravitational field leads to a vertical dispersion of the molecular velocity at the detector surface. To ensure good velocity separation, a vertical slit  $S_y$  with an opening of  $25 \mu\text{m}$  is placed about 20 mm in front of the grating. The slit is aligned with respect to the grating with an accuracy of  $10 \mu\text{m}$  using the fiber-based profiler. The molecular diffraction pattern is collected on a quartz plate, 570 mm behind the grating and imaged using fluorescence microscopy [21]. The experiment is conducted at a pressure below  $10^{-7}$  mbar to avoid collisional decoherence.

Ciprofloxacin is a polar biomolecule with a mass of  $m = 331 \text{ u}$  and a negligible absorption cross section of  $\sigma_{\text{abs}} \ll 10^{-18} \text{ cm}^2$  for  $\lambda \geq 400 \text{ nm}$  [28]. It interacts with the light grating via its optical polarizability volume  $\alpha'_{532} = 38.9 \text{ \AA}^3$ , which we calculated for the ground state

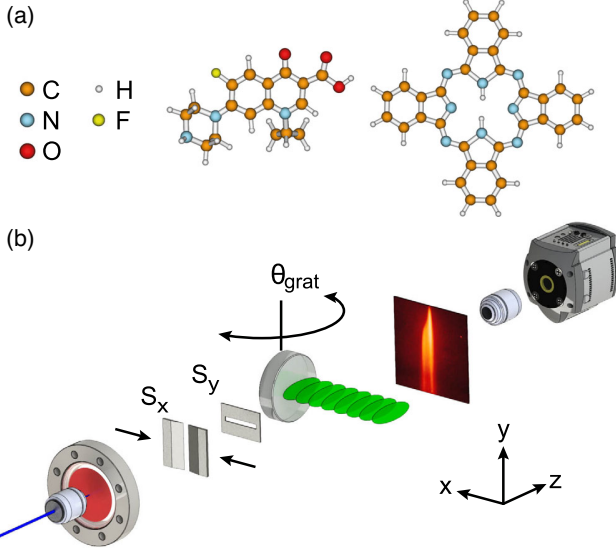


FIG. 1. (a) The experiments are performed with the antibiotic ciprofloxacin (left) and the organic dye phthalocyanine (right). (b) A thermal beam of molecules is produced by microevaporation and collimated vertically ( $S_x$ ) and horizontally ( $S_y$ ). After 1.5 m of free flight the molecules are diffracted at a thick laser grating created by retroreflecting a 532 nm laser at a highly reflective mirror. The angle of the mirror with respect to the molecular beam  $\theta_{\text{grat}}$  can be controlled with  $\mu$  rad precision. The molecular diffraction pattern is recorded after further 0.57 m of free flight by laser-induced fluorescence microscopy.

geometry at the PBE0/Def2TZVPP level. Phthalocyanine is a nonpolar dye molecule with a mass of  $m = 515$  u and a static polarizability volume  $\alpha' = 101 \text{ \AA}^3$  [29]. In contrast to ciprofloxacin, it has a non-negligible absorption cross section of  $\sigma_{\text{abs}} = 9 \times 10^{-18} \text{ cm}^2$  at 532 nm [30]. This allows us to observe the effect of absorption of the grating photons on the diffraction process.

**Theoretical model.**—Atomic and molecular Bragg diffraction follows from the induced dipole interaction of a polarizable point particle with a thick light grating. The particle moves initially with a velocity  $\mathbf{v} = (v_x, v_y, v_z)$ , where  $v_z \gg v_x, v_y$ . Since the forward momentum  $mv_z$  and the kinetic energy  $mv^2/2$  are much bigger than, respectively, the photon momentum  $\hbar k = 2\pi\hbar/\lambda$  and the potential depth, the motion in the  $z$  direction is virtually unchanged by the grating and can be treated classically. The same can be assumed about the  $y$  motion. Furthermore, the high  $v_z$  allows us to neglect the free fall during the particle's passage through the grating. All this reduces the problem to the 1D dynamics along the  $x$  axis.

In a frame moving with the velocity  $v_x$  the particle is initially at rest while the grating is moving. The Hamiltonian can then be written as

$$\hat{H} = -\frac{\hbar^2}{2m} \frac{\partial^2}{\partial x^2} - V(t) \cos^2[k(x + v_x t)], \quad (1)$$

where  $V(t) = 16P\alpha'/(cw_z w_y) \exp(-2v_z^2 t^2/w_z^2)$ . The time-dependent Schrödinger equation  $i\hbar \partial_t \psi(t, x) = \hat{H} \psi(t, x)$  can be solved using the ansatz

$$\phi(t, x) \equiv \exp\left(-\frac{i}{2\hbar} \int_{-\infty}^t dt' V(t')\right) \psi(t, x + \pi/2k) \quad (2)$$

$$= \sum_{j=-\infty}^{\infty} c_j(t) e^{ikjx/n}, \quad (3)$$

where  $n \in \mathbb{N}$  is an arbitrary integer which determines the spacing between the basis states. For plane-wave illumination an  $n = 1$  ansatz is sufficient; for numerical simulation with finite collimation, however,  $n \gg 1$  is necessary. Substituting Eq. (3) into the Schrödinger equation yields the Raman-Nath equations [31],

$$ic'_j = \left(\frac{j}{n}\right)^2 c_j + \frac{\gamma}{4} e^{-2\tau^2/\sigma^2} [c_{j-2n} e^{4ip_{\text{tr}}\tau} + c_{j+2n} e^{-4ip_{\text{tr}}\tau}], \quad (4)$$

where a prime denotes a derivative over  $\tau = \omega_r t$ ,  $\omega_r = \hbar k^2/2m$ , and

$$\gamma = \frac{V(0)}{\hbar\omega_r}, \quad \sigma = \frac{w_z \omega_r}{v_z}, \quad p_{\text{tr}} = \frac{mv_x}{\hbar k}. \quad (5)$$

These correspond to dimensionless grating strength, interaction time, and momentum of the incident particle. The interaction time parameter is close to the ratio of the grating waist radius  $w_z$  and the characteristic length scale of near-field diffraction, the Talbot length  $L_T = \lambda^2 mv/4\hbar$  [32], for we have  $\sigma = \pi w_z/4L_T$ .

The Raman-Nath equations have approximate, closed-form solutions in the short-interaction and in the weak-potential limits. The thin-grating (or Raman-Nath) approximation amounts to dropping the kinetic term in Eq. (1), which is possible when the motion of the particle inside the grating can be neglected. This requires  $\sigma p_{\text{tr}} \ll 1$  and  $\sigma\sqrt{\gamma} \ll 1$ . In this regime the diffraction pattern is symmetric and independent of the incidence angle. The weak-grating (or Bragg) approximation amounts to the adiabatic elimination of all but two of the Raman-Nath equations. This is possible when the depth of the grating potential is small compared to the recoil energy, such that only transfer to the Bragg-reflected state is allowed by energy conservation. For  $p_{\text{tr}} > 1$  this is the case when  $\gamma \ll 8(p_{\text{tr}} - 1)$  [33]. In this regime, the interaction time necessary to achieve high-order diffraction grows like a factorial  $\Gamma(p_{\text{tr}})$ , as the particle has to tunnel through increasingly many energy-forbidden states.

When the above approximations cannot be used, the solution can be obtained either via adiabatic expansion [33] or numerically. In our experiments with ciprofloxacin  $\gamma \simeq 55$ ,  $\sigma \simeq 0.38$ , and  $p_{\text{tr}} \simeq 5$  (at 250 m/s), which lies in

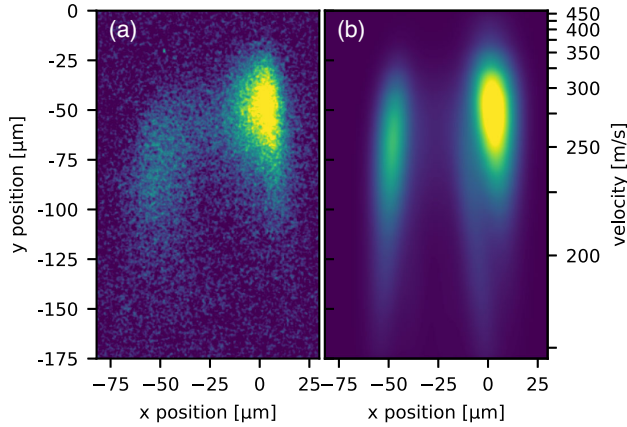


FIG. 2. False color image of the experimental (a) and simulated (b) Bragg diffraction pattern of the antibiotic ciprofloxacin. The laser grating waists are  $w_z = 7.04(5)$  mm,  $w_y = 55(5)$   $\mu\text{m}$ , and the collimation slit is set to 14  $\mu\text{m}$ .

this intermediate regime. We resort to numerical solution, since the convergence of the adiabatic expansion is slow. We note that in the intermediate regime both Raman-Nath-like and Bragg-like (also called quasi-Bragg [33]) diffraction can occur, depending on the intensity profile and the thickness of the grating [34]. We use a smooth Gaussian profile with sufficient thickness to demonstrate Bragg-like diffraction. The latter differs from diffraction in the weak-potential limit in that the intermediate diffraction orders are populated during the transit through the grating. This can lead to losses if the interaction time and strength are not optimally chosen. Finally, we note that classical dynamics of particles in sinusoidal potentials can give rise to analogous beam-splitting behavior [35]; however, a quantum model is generalizable and appropriate in the absence of plausible decoherence channels.

**Diffraction of ciprofloxacin.**—In Fig. 2(a) we show the pattern obtained by diffracting ciprofloxacin molecules at an incidence angle  $\theta_{\text{grat}} = -43(5)$   $\mu\text{rad}$ . The y position in the image determines the forward velocity of the particles, which in turn determines the transverse momentum  $p_{\text{tr}}$  and the particle-grating interaction time  $\sigma$ .

For velocities above 300 m/s the interaction time is short compared to the inverse of the characteristic frequencies of the resonant Bragg transitions, and thus no diffraction occurs. As the characteristic frequencies increase sharply with decreasing  $p_{\text{tr}}$  [33], a relatively sudden onset of diffraction is observed at about 300 m/s. In the 300–150 m/s velocity range the molecules become consecutively resonant with the 6th–4th Bragg transition. The expected momentum transfer in a Bragg transition of order  $l$  is  $2l\hbar k \propto v_z$ . Since the flight time between the grating and the detector is inversely proportional to the forward velocity, we expect an approximately constant separation between the diffracted and the undiffracted beams. The slight bend in the diffracted beam results from the

fact that the 6th order transition is dominant and thus contributes also at nonresonant velocities.

As the Bragg condition is relaxed by the limited interaction time, we observe no diffraction-free regions in between the resonances. Nevertheless, the appearance of a single diffracted beam and the asymmetry of the pattern help distinguish the observed phenomenon from stochastic photon absorption or Raman-Nath diffraction. We finally note that at  $v_z \simeq 210$  m/s the amplitude of the diffracted beam matches that of the undiffracted one, demonstrating a  $10\hbar k$  equal-amplitude beam splitter.

Numerical simulation using the Raman-Nath equations (4) [Fig. 2(b)] qualitatively reproduces the observed pattern [21]. The experimental and the simulated images are vertically aligned by matching the heights at which the diffracted peaks reach half of their maximal intensities. This determines the most probable velocity in the molecular beam of about 250 m/s.

**Diffraction of phthalocyanine.**—To explore the universality of molecular Bragg diffraction and its robustness to absorption, we switch to the dye molecule phthalocyanine. We quantify the absorption by setting  $\theta_{\text{grat}}$  to an angle for which we do not expect diffraction and observing the broadening of the molecular beam. From the width of the beam we infer that on average one photon is absorbed inside the grating [21]. Despite the absorption, we obtain diffraction images of phthalocyanine, which are qualitatively similar to those of ciprofloxacin [see Fig. 3(a)]. The images exhibit oscillating population transfer [see Fig. 3(b)] reminiscent of the Pendellösung oscillations predicted by the theory of weak-potential Bragg diffraction and demonstrated with neutrons [36] and atoms [37]. Similar oscillations can be seen in the power dependence of the diffraction patterns [21].

To investigate the dependence of Bragg diffraction on the incidence angle, we record a series of diffraction images in which we vary  $\theta_{\text{grat}}$  (see Fig. 4). In agreement with the expectations, we find the molecules diffracted to either side of the incoming beam, depending on the sign of the incidence angle. Similarly as for ciprofloxacin, the diffracted molecules form a slanted stripe indicating a single dominant transition. This transition is broadened by the 12  $\mu\text{rad}$  collimation of the molecular beam [21], which results in deviations from specular reflection seen in Figs. 3 and 4. The highest momentum transfer recorded was  $18\hbar k$  with an efficiency of 10% [Fig. 4(c)], and equal-amplitude splitting was realized for a momentum separation of  $14\hbar k$  [Fig. 4(a)].

**Discussion and outlook.**—We have demonstrated Bragg diffraction for the complex organic molecules phthalocyanine and ciprofloxacin. As our data is in qualitative agreement with a simple polarizable-point-particle model, we expect that this technique can be applied without modification to any molecule of comparable size and absorption cross section. That is irrespective of the details



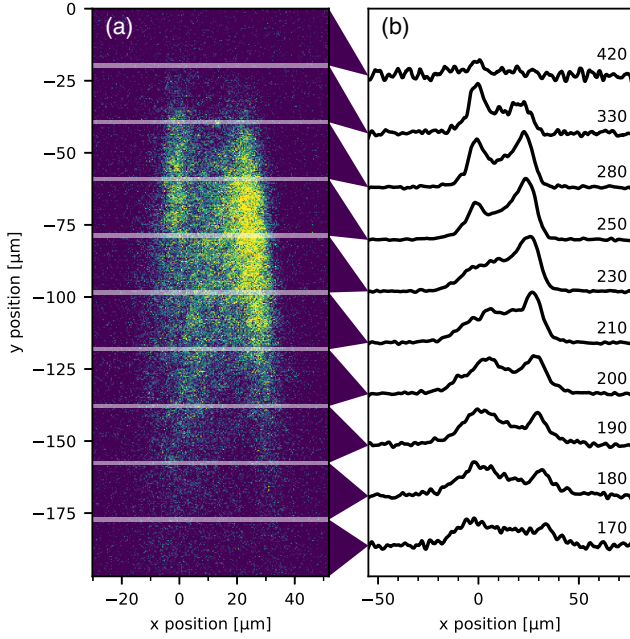


FIG. 3. Bragg diffraction pattern of the organic dye molecule phthalocyanine at an incidence angle  $\theta_{\text{grat}} = 5(5) \mu\text{rad}$ . Panel (a) shows the false color diffraction image. Panel (b) shows the averages of  $20 \mu\text{m}$  high stripes, smoothed with median and Savitzky–Golay [38] filters, and annotated with their corresponding velocities in m/s. The velocities are determined by comparison with a diffraction pattern produced by a material grating [21]. The laser grating waist for this measurement is  $w_y = 57(3) \mu\text{m}$  and the collimation slit width is  $11.5 \mu\text{m}$ .

of its electronic structure, dipole moment, etc. We have demonstrated a balanced beam splitter with a momentum separation of  $14\hbar k$ , which is to the best of our knowledge the largest equal-amplitude splitting demonstrated for molecules using optical gratings. Although with sufficient laser power similar or even greater splitting could be achieved with a thin optical grating, this would typically reduce the particle flux by a factor of 10 as only two of the many populated output beams have to be selected. The same problem applies to mechanical gratings, which additionally are incompatible with polar molecules due to rotational averaging.

Further development should increase the particle-grating interaction time in order to decrease losses and sharpen the Bragg resonances. A promising approach to achieve this is slowing the molecules using buffer gas cells [39]. This could ultimately allow for Mach-Zehnder interferometry with large molecules. The possibility to selectively address the arms in such a setup would, in turn, enable new interference schemes utilizing the molecules' chirality, conformation, and possibly entanglement between the molecules' internal and external degrees of freedom. Efficient Bragg diffraction could also enable pulsed Bloch oscillation beam splitters to realize even larger momentum transfers [40].

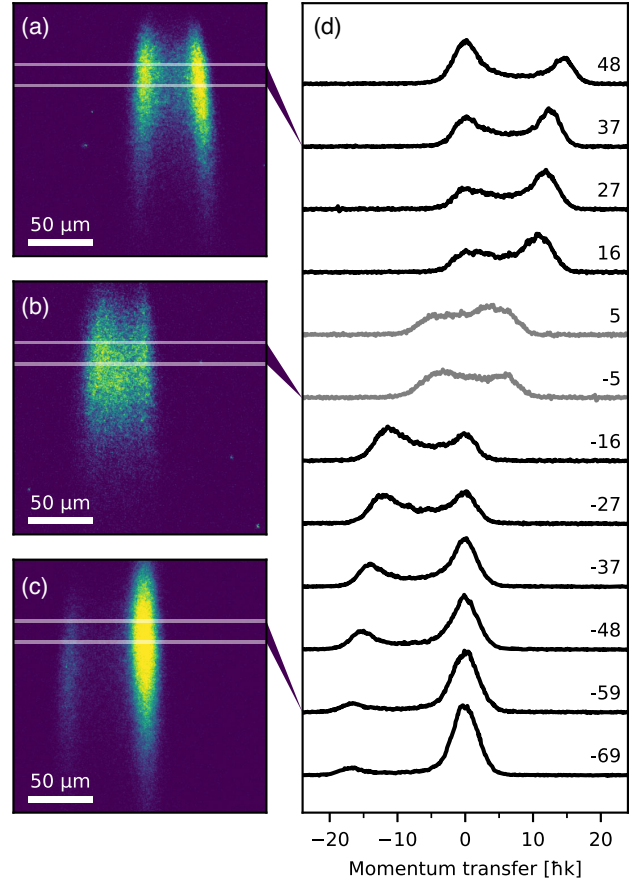


FIG. 4. Angular dependence of Bragg diffraction of the dye molecule phthalocyanine. Panels (a)–(c) show diffraction images for the incidence angles  $48$  (a),  $-5$  (b) and  $-69 \mu\text{rad}$  (c). The images are  $197$  by  $197 \mu\text{m}$  and the scale bars are  $50 \mu\text{m}$  long. Panel (d) shows the integrated intensity profiles for the incidence angle varying from  $-69$  to  $48 \mu\text{rad}$  in steps of  $10 \mu\text{rad}$ . The profiles are averages of  $16 \mu\text{m}$  high stripes of the diffraction images corresponding to a velocity range of  $234$  to  $255$  m/s. The curves are horizontally aligned to center the undiffracted beam (which is the right peak for negative incidence and the left peak for positive incidence). For  $\pm 5 \mu\text{rad}$  we observe diffraction to both sides of the initial beam and hence align the traces with respect to their center of gravity. The laser grating waist for this measurement is  $w_y = 65(5) \mu\text{m}$  and the collimation slit width is  $14.8 \mu\text{m}$ .

This project has received funding from the European Research Council (ERC) under the European Union's Horizon 2020 research and innovation program (Grant No. 320694) and the Austrian Science Fund (FWF) within Projects No. P-30176 and W1210-N25. We thank the Fetzer Pioneers' Fund (Project No. P#2018-1) for financial support, Armin Shayeghi for calculating the polarizability of ciprofloxacin, and Martin Fally for fruitful discussions. B. A. S. acknowledges funding from the European Union's Horizon 2020 research and innovation programme under the Marie Skłodowska-Curie Grant Agreement No. 841040.

\*markus.arndt@univie.ac.at

- [1] M. VanHove, W. Weinberg, and C. Chan, Low-Energy Electron Diffraction: Experiment, Theory and Surface Structure Determination, *Springer Series in Surface Sciences*, Vol. 6 (Springer-Verlag, Berlin, Heidelberg, 1986).
- [2] Neutron Diffraction, *Topics in Current Physics*, edited by H. Dachs (Springer, Heidelberg, 1978).
- [3] A. D. Cronin, J. Schmiedmayer, and D. E. Pritchard, Optics and interferometry with atoms and molecules, *Rev. Mod. Phys.* **81**, 1051 (2009).
- [4] Atom Interferometry, in , *Proceedings of the International School of Physics "Enrico Fermi"*, edited by G. M. Tino and M. A. Kasevich (IOS Press, Amsterdam, Netherlands, 2014), Vol. 188.
- [5] J. Tüxen, S. Gerlich, S. Eibenberger, M. Arndt, and M. Mayor, Quantum interference distinguishes between constitutional isomers, *Chem. Commun.* **46**, 4145 (2010).
- [6] S. Eibenberger, X. Cheng, J. P. Cotter, and M. Arndt, Absolute Absorption Cross Sections from Photon Recoil in a Matter-Wave Interferometer, *Phys. Rev. Lett.* **112**, 250402 (2014).
- [7] L. Mairhofer, S. Eibenberger, J. P. Cotter, M. Romirer, A. Shayeghi, and M. Arndt, Quantum-assisted metrology of neutral vitamins in the gas phase, *Angew. Chem. Int. Ed.* **56**, 10947 (2017).
- [8] A. Shayeghi, P. Rieser, G. Richter, U. Sezer, J. H. Rodewald, P. Geyer, T. J. Martinez, and M. Arndt, Matter-wave interference of a native polypeptide, *Nat. Commun.* **11**, 1447 (2020).
- [9] Y. Y. Fein, P. Geyer, P. Zwick, F. Kiałka, S. Pedalino, M. Mayor, S. Gerlich, and M. Arndt, Quantum superposition of molecules beyond 25 kDa, *Nat. Phys.* **15**, 1242 (2019).
- [10] T. K. Gaylord and M. G. Moharam, Thin and thick gratings: terminology clarification, *Appl. Opt.* **20**, 3271 (1981).
- [11] H. Müller, S.-w. Chiow, Q. Long, S. Herrmann, and S. Chu, Atom Interferometry with up to 24-Photon-Momentum-Transfer Beam Splitters, *Phys. Rev. Lett.* **100**, 180405 (2008).
- [12] S.-w. Chiow, T. Kovachy, H.-C. Chien, and M. A. Kasevich,  $102\hbar k$  Large Area Atom Interferometers, *Phys. Rev. Lett.* **107**, 130403 (2011).
- [13] P. L. Gould, G. A. Ruff, and D. E. Pritchard, Diffraction of atoms by light: The near-resonant Kapitza-Dirac effect, *Phys. Rev. Lett.* **56**, 827 (1986).
- [14] O. Nairz, B. Brezger, M. Arndt, and A. Zeilinger, Diffraction of Complex Molecules by Structures Made of Light, *Phys. Rev. Lett.* **87**, 160401 (2001).
- [15] D. L. Freimund, K. Aflatoon, and H. Batelaan, Observation of the Kapitza-Dirac effect, *Nature* **413**, 142 (2001).
- [16] D. P. Mitchell and P. N. Powers, Bragg reflection of slow neutrons, *Phys. Rev.* **50**, 486 (1936).
- [17] P. J. Martin, B. G. Oldaker, A. H. Miklich, and D. E. Pritchard, Bragg scattering of atoms from a standing light wave, *Phys. Rev. Lett.* **60**, 515 (1988).
- [18] M. Kozuma, L. Deng, E. W. Hagley, J. Wen, R. Lutwak, K. Helmerson, S. L. Rolston, and W. D. Phillips, Coherent Splitting of Bose-Einstein Condensed Atoms with Optically Induced Bragg Diffraction, *Phys. Rev. Lett.* **82**, 871 (1999).
- [19] D. L. Freimund and H. Batelaan, Bragg Scattering of Free Electrons Using the Kapitza-Dirac Effect, *Phys. Rev. Lett.* **89**, 283602 (2002).
- [20] J. R. Abo-Shaeer, D. E. Miller, J. K. Chin, K. Xu, T. Mukaiyama, and W. Ketterle, Coherent Molecular Optics Using Ultracold Sodium Dimers, *Phys. Rev. Lett.* **94**, 040405 (2005).
- [21] See Supplemental Material at <http://link.aps.org/supplemental/10.1103/PhysRevLett.125.033604> for details and Refs. [22–26] included therein.
- [22] C. Knobloch, Coherent matter-wave manipulation techniques, Ph.D. thesis, University of Vienna, Austria, 2019.
- [23] T. Juffmann, A. Milic, M. Müllneritsch, P. Asenbaum, A. Tsukernik, J. Tüxen, M. Mayor, O. Cheshnovsky, and M. Arndt, Real-time single-molecule imaging of quantum interference, *Nat. Nanotechnol.* **7**, 297 (2012).
- [24] J. P. Cotter, C. Brand, C. Knobloch, Y. Lilach, O. Cheshnovsky, and M. Arndt, In search of multipath interference using large molecules, *Sci. Adv.* **3**, e1602478 (2017).
- [25] J. Johansson, P. Nation, and F. Nori, QuTiP: An open-source Python framework for the dynamics of open quantum systems, *Comput. Phys. Commun.* **183**, 1760 (2012).
- [26] J. Johansson, P. Nation, and F. Nori, QuTiP 2: A Python framework for the dynamics of open quantum systems, *Comput. Phys. Commun.* **184**, 1234 (2013).
- [27] C. Brand, K. Simonović, F. Kiałka, S. Troyer, P. Geyer, and M. Arndt, A fiber-based beam profiler for high-power laser beams in confined spaces and ultra-high vacuum, *Opt. Express* **28**, 6164 (2020).
- [28] C.-C. Lin and M.-S. Wu, Degradation of ciprofloxacin by UV/S2O8<sup>2-</sup> process in a large photoreactor, *J. Photochem. Photobiol. A* **285**, 1 (2014).
- [29] R. Ramprasad and N. Shi, Polarizability of phthalocyanine based molecular systems: A first-principles electronic structure study, *Appl. Phys. Lett.* **88**, 222903 (2006).
- [30] H. Du, R.-C. A. Fuh, J. Li, L. A. Corkan, and J. S. Lindsey, PhotochemCAD: A computer-aided design and research tool in photochemistry, *Photochem. Photobiol.* **68**, 141 (1998).
- [31] C. V. Raman and N. S. Nagendra Nath, The diffraction of light by high frequency sound waves: Part IV, *Proc. Indian Acad. Sci.* **3**, 119 (1936).
- [32] H. F. Talbot, Facts relating to optical science. No. IV, *Lond. Edinb. Dubl. Philos. Mag.* **9**, 401 (1836).
- [33] H. Müller, S.-w. Chiow, and S. Chu, Atom-wave diffraction between the Raman-Nath and the Bragg regime: Effective Rabi frequency, losses, and phase shifts, *Phys. Rev. A* **77**, 023609 (2008).
- [34] C. Keller, J. Schmiedmayer, A. Zeilinger, T. Nonn, S. Dürr, and G. Rempe, Adiabatic following in standing-wave diffraction of atoms, *Appl. Phys. B* **69**, 303 (1999).
- [35] P. Ryyty and M. Kaivola, Pulsed Standing-Wave Mirror for Neutral Atoms and Molecules, *Phys. Rev. Lett.* **84**, 5074 (2000).
- [36] C. G. Shull, Observation of Pendellösung Fringe Structure in Neutron Diffraction, *Phys. Rev. Lett.* **21**, 1585 (1968).

- [37] M.K. Oberthaler, R. Abfalterer, S. Bernet, C. Keller, J. Schmiedmayer, and A. Zeilinger, Dynamical diffraction of atomic matter waves by crystals of light, *Phys. Rev. A* **60** 456, (1999).
- [38] A. Savitzky and M.J.E. Golay, Smoothing and differentiation of data by simplified least squares procedures, *Anal. Chem.* **36**, 1627 (1964).
- [39] J. Piskorski, D. Patterson, S. Eibenberger, and J.M. Doyle, Cooling, Spectroscopy and Non-Sticking of trans-Stilbene and Nile Red, *Chem. Phys. Chem.* **15**, 3800 (2014).
- [40] M. Ben Dahan, E. Peik, J. Reichel, Y. Castin, and C. Salomon, Bloch Oscillations of Atoms in an Optical Potential, *Phys. Rev. Lett.* **76**, 4508 (1996).



## Supplemental Material for Bragg diffraction of large organic molecules

Christian Brand,<sup>1,2</sup> Filip Kiałka,<sup>1,3</sup> Stephan Troyer,<sup>1</sup> Christian Knobloch,<sup>1</sup> Ksenija Simonović,<sup>1</sup> Benjamin A. Stickler,<sup>3,4</sup> Klaus Hornberger,<sup>3</sup> and Markus Arndt<sup>1,\*</sup>

<sup>1</sup>University of Vienna, Faculty of Physics, Boltzmannngasse 5, A-1090 Vienna, Austria

<sup>2</sup>German Aerospace Center (DLR), Institute of Quantum Technologies, Söflinger Straße 100, 89077 Ulm, Germany

<sup>3</sup>Faculty of Physics, University of Duisburg-Essen, Lotharstraße 1, 47048 Duisburg, Germany

<sup>4</sup>QOLS, Blackett Laboratory, Imperial College London, SW7 2AZ London, United Kingdom

(Dated: June 17, 2020)

### LASER DESORPTION

We employ a tightly focused laser beam to thermally evaporate the molecules. This results in a high thermal load which may lead to thermal decomposition of ciprofloxacin, especially the detachment of the carboxyl group ( $-\text{COOH}$ ). As the experimental setup offers no mass resolution, this might deteriorate the contrast of the observed pattern. To test whether fragmentation occurs in our source, we desorbed ciprofloxacin in high vacuum and collected the material 8 mm behind the source. This sample was analyzed using matrix-assisted laser desorption/ionization mass spectrometry and compared to the pristine sample from the supplier. The mass spectra show that the laser evaporation leaves more than 99% of ciprofloxacin intact. For phthalocyanine this has been tested with the same result [22].

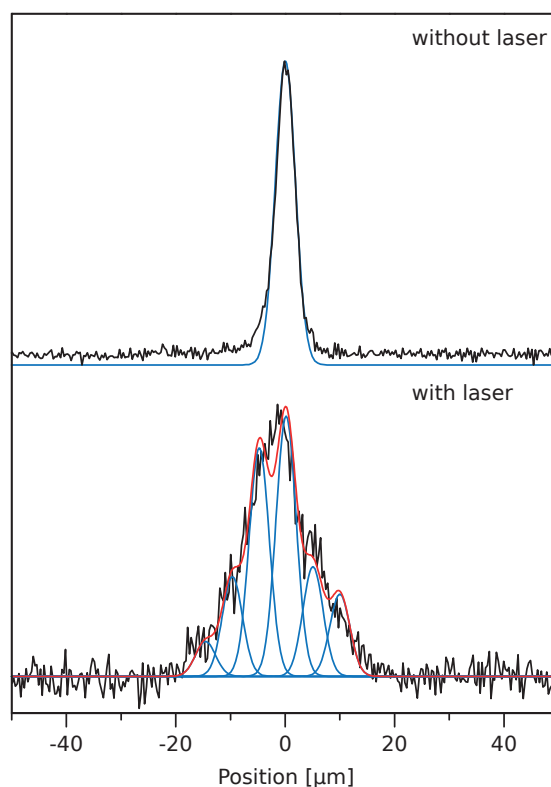
### FLUORESCENCE IMAGING

To visualize the diffraction images of ciprofloxacin, we illuminate the pattern with about 100 mW of 266 nm light generated by a SIRAH WAVETRAIN 2 pumped by a COHERENT VERDI V10. We use a rotating diffuser to achieve uniform illumination at a grazing angle of incidence. The fluorescence photons are collected via a 20-fold microscope objective (ZEISS PLANEO FLUAR,  $\text{NA} = 0.5$ ) and separated from the background via a bandpass filter transmitting light in the range between 505 and 595 nm. The images are recorded with a UV enhanced EMCCD camera (ANDOR IXON DV885 - K(S-VP)), using a multiplication factor of 1 and an integration time of 20 s. Background-correction was achieved by subtracting images under identical illumination with and without molecules.

The patterns of phthalocyanine are recorded by illuminating the pattern with 661 nm light and recording the fluorescence in the range between 700 and 725 nm. For more details see Refs. [23, 24].

### DATA PROCESSING — CIPROFLOXACIN

We perform data processing of all diffraction images using the SCI-PY stack. For Fig. 2a) we averaged 6 individual images of the deposited pattern and denoised the result with



Suppl. Fig. 1. a) Collimating a beam of phthalocyanine with the  $S_x$  delimiter set to  $4\text{ }\mu\text{m}$  leads to a Gaussian signal with a  $1/e^2$  radius of  $w_x = 4.4(1)\text{ }\mu\text{m}$  at the detector. b) Inside a 30 W laser beam the molecules absorb a mean number of 2 to 3 photons for  $v = 140\text{ m/s}$  resulting in a broadened pattern. The spacing of the peaks ( $4.9\text{ }\mu\text{m}$ ) matches the recoil of a single 532 nm photon and the resolved substructure suggests that re-emission after absorption is not the dominant deexcitation mechanism.

a Gaussian filter with a radius of 1 camera pixel. We then perform background correction (in addition to the background subtraction done after image acquisition) by masking the diffraction pattern, averaging the image along the  $y$ -direction, fitting a smoothing spline, and subtracting the noise floor. The same process is repeated along the  $x$ -axis. To find the horizontal center of the diffraction pattern we fit a Gaussian to a  $y$ -averaged,  $16\text{ }\mu\text{m}$  wide horizontal stripe at the top of the diffraction pattern.

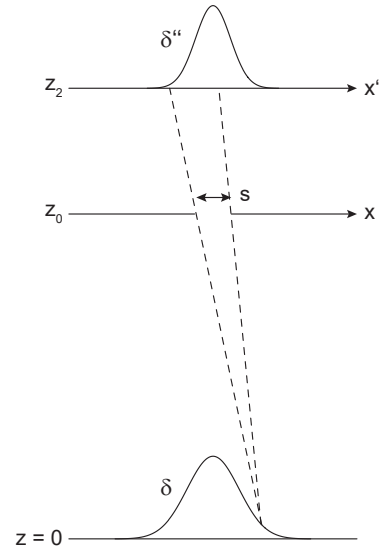
## DATA PROCESSING — PHTHALOCYANINE

We determine the forward velocities in the images by comparison with a phthalocyanine diffraction pattern obtained with a material grating in Ref. [24]. The patterns are aligned by maximizing the overlap of their intensity distributions, which are obtained by integrating the images horizontally. For a material grating the diffraction orders are clearly separated, and the position- as well as momentum-space separation between them is known, which allows us to calculate the forward velocities.

To align the profiles in Fig. 4d) we fit them with a sum of three Gaussians, two narrow ones for the peaks and a broad one to account for the losses. The profiles and images are then horizontally aligned with respect to the rightmost Gaussian for negative incidence angles and the leftmost Gaussian for positive incidence angles. By taking into account the molecules' forward velocity, we convert the horizontal axis from pixel to  $\hbar k$ .

## NUMERICAL SIMULATION — CIPROFLOXACIN

The diffraction image shown in Fig. 2b) is simulated line-by-line (horizontally) by solving the Raman-Nath equations (4) using QUTIP [25, 26]. We truncate the infinite set of equations to those with  $|j| < 2^{13}$  and choose  $n = 700$ . The initial state is Gaussian in position space with a parabolic phase and a standard deviation of the probability amplitude equal to  $4.6 \mu\text{m}$ . The latter is chosen so that the width of the undiffracted beam at the top of the experimental image matches that in the simulation with the laser turned off. The parabolic phase, in turn, is that of a paraxially-approximated spherical wave with the source located  $1505 \text{ mm}$  (the distance between the source and the  $S_x$  delimiter) away. We start by transforming the initial state to momentum space via FFT and evolving it using QUTIP's `sesolve` with a time-dependent, band-diagonal Hamiltonian. We integrate the Schrödinger equation over a time interval of  $6\sigma\omega_p^{-1}$ , after which free propagation in momentum space (by multiplication with the transfer function in Fresnel approximation) is performed. The result is then transformed back to position space. The resulting lines of the simulation are stacked vertically and multiplied by the intensity of the corresponding data line. Then, a Gaussian filter is applied in the vertical direction to the obtained image to account for the finite height of  $S_y$ . To account for the horizontal extent of the source (and thus finite transverse coherence), we calculate 50 diffraction patterns for point sources with different  $x$  positions and average the images by intensity with Gaussian weights corresponding to an estimated source radius of  $12 \mu\text{m}$  standard deviation.



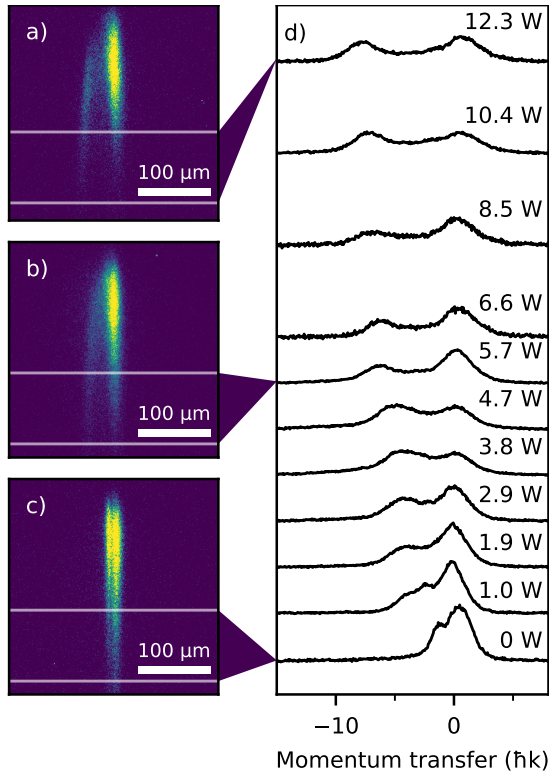
Suppl. Fig. 2. Estimating the effective source size  $\delta$  and the collimation radius of the molecular beam from the known on-screen stripe radius  $\delta''$  and collimation slit width  $s$ . The Gaussian peaks represent the (approximately Gaussian) molecular densities in the source and detector planes.

## ABSORPTION INSIDE THE GRATING

To estimate the number of photons phthalocyanine absorbs inside the laser grating, we limit the transverse velocity spread in the molecular beam to about the recoil velocity by closing the  $S_x$  delimiter to  $4 \mu\text{m}$ . For molecules traveling at  $140 \text{ m/s}$ , this leads to a most probable transverse velocity of  $0.4 \text{ mm/s}$ , which corresponds to a kinetic energy of about  $5 \text{ nK}$  in this degree of freedom. With the laser grating turned off, the signal at the detector has a  $1/e^2$  radius of  $4.4(1) \mu\text{m}$  as shown in Suppl. Fig. 1a). Turning on the grating with a power of  $30 \text{ W}$ , vertical radius  $w_y = 44(1) \mu\text{m}$ , and incidence angle  $\theta_{\text{grat}} = 1.25 \text{ mrad}$ , for which we expect no diffraction, results in a broadening of the beam as shown in Suppl. Fig. 1b). The lineshape exhibits a substructure whose spacing matches the recoil of a  $532 \text{ nm}$  photon for molecules travelling at  $140 \text{ m/s}$ , assuming that the width of the individual peaks remains constant. From the shape we infer that the mean number of absorbed photons is about  $2.5$  at this laser intensity, and thus in the range  $0.8\text{--}1.0$  at the intensities used in the diffraction experiments.

## MOLECULAR BEAM COLLIMATION

To estimate the collimation radius of the molecular beam, we first estimate the source size using ray optics, as illustrated in Suppl. Fig. 2. For an infinitely narrow collimation slit at  $z = z_0$  and Gaussian source (at  $z = 0$ ) with standard deviation  $\delta$ , we would expect a Gaussian stripe on screen with



Suppl. Fig. 3. Power dependence of Bragg diffraction of phthalocyanine. Panels (a) and (b) show the diffraction patterns for laser grating powers of 12.3 (a) and 5.7 W (b). The double peak visible at 0 W (c) is an artifact caused by the collimation slit. Panel (d) shows intensity profiles integrated over a region corresponding to a velocity range of 143–175 m/s.

width

$$\delta' = \frac{z_2 - z_0}{z_0} \delta. \quad (\text{SI.1})$$

If the slit has finite width described by a transmission function  $t(x)$ , the stripe on screen will be a convolution of the  $\delta'$ -wide Gaussian with a projection of the slit,  $t((z_0/z_2)x')$ . To obtain a simple analytical estimate of the stripe width, we approximate a boxcar-shaped  $t(x)$  with a Gaussian with a standard deviation of  $s/4$ . The stripe is then also Gaussian with a standard deviation

$$\delta'' = \sqrt{\left(\frac{sz_2}{4z_0}\right)^2 + \left(\frac{z_2 - z_0}{z_0} \delta\right)^2}. \quad (\text{SI.2})$$

Eq. (SI.2) is easily inverted, allowing us to estimate  $\delta$  knowing  $s$  and  $\delta''$ . With a known source size  $\delta$  and slit size  $s$  we can estimate the one-sigma collimation radius to be

$$\frac{1}{z_0} \left( \delta + \frac{s}{2} \right). \quad (\text{SI.3})$$

Using Eq. (SI.2) we estimate the source sizes to be 12 and 10  $\mu\text{m}$  for the data in Figs. 3 and 4, respectively. This gives one-sigma collimation radii of 12  $\mu\text{rad}$  in both cases (the two-sigma collimation radii are 20 and 19  $\mu\text{rad}$ , respectively).

### EFFECT OF GRATING POWER

To study the influence of the potential depth on the diffraction efficiency, we record diffraction patterns at grating powers ranging from 0 up to 12.3 W, as shown in Suppl. Fig. 3. The profiles in panel (d) show the intensity oscillating between the diffracted and the undiffracted beams. Additionally, the distance between the peaks increases as a function of power, corresponding to a change in  $\theta_{\text{grat}}$  of about 20  $\mu\text{rad}$ . We attribute this to residual thermal drift in the experimental setup.

---

\* markus.arndt@univie.ac.at

- [22] C. Knobloch, *Coherent matter-wave manipulation techniques*, Ph.D. thesis (2019).
- [23] T. Juffmann, A. Milic, M. Müllneritsch, P. Asenbaum, A. Tsukernik, J. Tüxen, M. Mayor, O. Cheshnovsky, and M. Arndt, *Nat. Nanotechnol.* **7**, 297 (2012).
- [24] J. P. Cotter, C. Brand, C. Knobloch, Y. Lilach, O. Cheshnovsky, and M. Arndt, *Sci. Adv.* **3**, e1607478 (2017).
- [25] J. Johansson, P. Nation, and F. Nori, *Comput. Phys. Commun.* **183**, 1760 (2012).
- [26] J. Johansson, P. Nation, and F. Nori, *Comput. Phys. Commun.* **184**, 1234 (2013).



# Orbital angular momentum interference of trapped matter waves

Filip Kiałka,<sup>1,2</sup> Benjamin A. Stickler,<sup>3,2</sup> and Klaus Hornberger<sup>2</sup>

<sup>1</sup>Faculty of Physics, University of Vienna, Boltzmanngasse 5, A-1090 Vienna, Austria

<sup>2</sup>Faculty of Physics, University of Duisburg-Essen, Lotharstraße 1, 47048 Duisburg, Germany

<sup>3</sup>Quantum Optics and Laser Science, Imperial College London, SW72AZ London, United Kingdom



(Received 7 November 2019; revised manuscript received 9 April 2020; accepted 15 April 2020; published 6 May 2020)

We introduce a matter wave interference scheme based on the quantization of orbital angular momentum in a ring trap. It operates without beam splitters, is sensitive to geometric phases induced by external gauge fields, and allows measuring interatomic scattering lengths. We argue that orbital angular momentum interferometry offers a versatile platform for quantum coherent experiments with cold atoms and Bose-Einstein condensates using state-of-the-art technology.

DOI: 10.1103/PhysRevResearch.2.022030

**Introduction.** Trapped interference experiments [1–8] are promising platforms for the next generation of force and acceleration sensors. Guiding matter waves enables atom interferometers with long interrogation times, while providing considerable freedom for choosing the geometry [9–12]. Toroidal traps are particularly attractive for fundamental quantum experiments [13–18] and for precision sensing [19–21] with ultracold gases or fluids. The ring geometry implies that the orbital angular momentum of the revolving particles is conserved. As argued in the following, its fundamental quantization can be exploited to realize trapped interference schemes requiring no beam splitters.

We note that the free quantum dynamics in a ring geometry exhibit *quantum revivals*. An initially well-localized wave packet quickly disperses along the ring on a timescale determined by the orbital angular momentum spread. Only after a much longer quantum revival time, which is independent of the initial state, does the localized wave packet briefly reappear due to the quantization of orbital angular momentum [22]. Similar revival effects are encountered in the orientation of revolving molecules [23–25], and they have been proposed for electromagnetic pulse shaping in semiconductors [26] as well as for macroscopic quantum superposition tests with nanorotors [27].

Here, we propose an interference scheme which exploits the brief emergence of a balanced superposition at half the revival time. By imprinting a relative phase on the superposition, one can coherently control at which antipode the wave packet reappears after the full revival time. The presence of an additional gauge field induces a rotation of the revival determined by the accumulated geometric phase. In contrast to many existing proposals for interference in ring

traps [19,28,29], orbital angular momentum interference does not rely on atomic spin states or collective excitations. It is thus applicable to all matter-wave experiments with a toroidal geometry, ranging from electrons in solid state quantum rings [30] to nanoparticles in optomechanical traps [31]. Here we discuss the special case of optically trapped atomic clouds or Bose-Einstein condensates (BECs), and show that this scheme is sufficiently resilient to be realizable with state-of-the-art technology.

**Interference scheme.** In order to explain the interference scheme we first consider the idealized case of a point particle of mass  $m$  confined to a circle of radius  $R$ . Its Hamiltonian reads  $H = L_z^2/2mR^2$ . Since the eigenvalues of the orbital angular momentum operator  $L_z$  are integer multiples of  $\hbar$ , with eigenstates  $|\ell\rangle$ , the time evolution operator  $U_0(t) = \sum_{\ell \in \mathbb{Z}} \exp(-i\hbar t \ell^2/2mR^2) |\ell\rangle \langle \ell|$  is unity for all even multiples of the revival time

$$T_{\text{rev}} = \frac{2\pi m R^2}{\hbar}. \quad (1)$$

A straightforward calculation shows that the evolution for the revival time performs a  $\pi$  rotation,  $U_0(nT_{\text{rev}}) = \exp(in\pi L_z/\hbar)$ , with  $n \in \mathbb{N}_0$ . In a similar fashion, free evolution for  $T_{\text{rev}}/2$  acts as a beam splitter, preparing a balanced superposition of the initial state and its  $\pi$ -rotated version [24,32],

$$U_0\left(\frac{T_{\text{rev}}}{2}\right) = \frac{e^{-i\pi/4}}{\sqrt{2}} (\mathbb{1} + ie^{i\pi L_z/\hbar}), \quad (2)$$

where  $\mathbb{1}$  is the unity operator.

An initially tightly confined wave packet thus first disperses on a short timescale determined by its initial angular momentum uncertainty. The state then remains delocalized over the ring for most of time, showing fractional revivals such as Eq. (2) at fractions of the revival time. The lifetime of these fractional and full revivals is determined by the initial dispersion time, and is thus typically orders of magnitude smaller than the revival time itself.

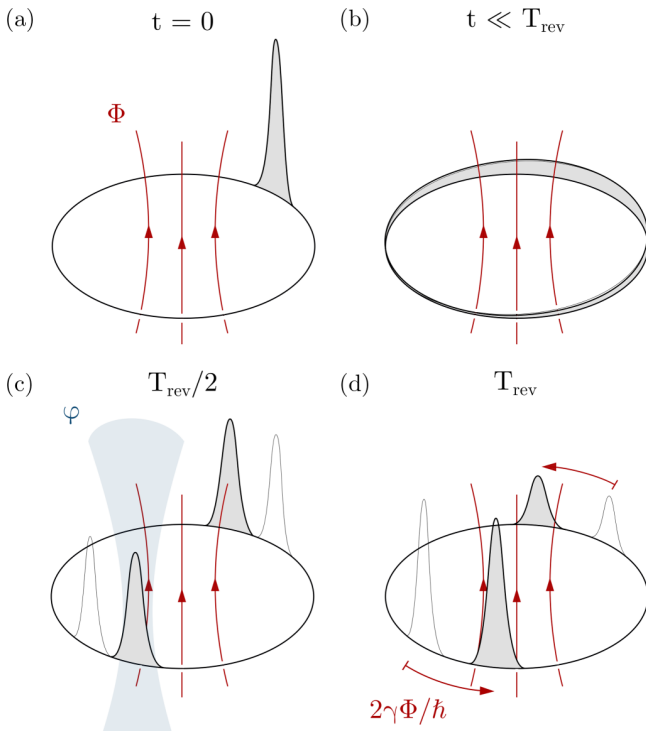


FIG. 1. Schematic illustration of the orbital angular momentum interference effect. A localized wave packet (a) quickly disperses (b), before reappearing (c) at  $T_{\text{rev}}/2$  for a short period of time in a balanced superposition of the original and mirrored locations; see (1) and (2). Applying a relative phase  $\varphi$  between the two superposition components controls final population imbalance at the antipodes (d) after further time evolution for  $T_{\text{rev}}/2$ . If a gauge field is turned on quickly after releasing the wave packet, the interference pattern (black) is rotated with respect to the field-free case (gray) by an angle  $2\gamma\Phi/\hbar$ , equal to the Aharonov-Bohm phase [see Eq. (3)].

The dynamical beam splitting described by (2) is exploited by the following interference scheme; see Fig. 1(a): The particle is initially prepared in a well-localized state  $|\psi_0\rangle$ . After dispersing on a short timescale, the localized state reappears at half of the revival time in a balanced superposition  $(|\psi_0\rangle + i|\psi_\pi\rangle)/\sqrt{2}$ , with the  $\pi$ -rotated initial state  $|\psi_\pi\rangle = \exp(i\pi L_z/\hbar)|\psi_0\rangle$ . Then a relative phase  $\varphi$  is induced between the two wave packets, for instance gravitationally by tilting the ring, optically via laser illumination, or in the case of an atomic cloud via magnetic control of the scattering length. After imprinting the phase, the state evolves freely for another  $T_{\text{rev}}/2$ , yielding the final state  $|\psi_f\rangle = \cos(\varphi/2)|\psi_\pi\rangle + i\sin(\varphi/2)|\psi_0\rangle$ . The final position of the particle is thus determined interferometrically.

**Gauge fields and external potentials.** The interference effect depends sensitively on the interaction with external gauge fields. If the field  $\mathbf{A}(\mathbf{r})$  is minimally coupled to the kinetic angular momentum  $L_z$ , the canonical angular momentum is  $L_z - \gamma R A(\hat{\alpha})$ . Here  $\gamma$  is the gauge coupling and  $A(\alpha) = \mathbf{A}(\mathbf{R}\mathbf{e}_\rho(\alpha)) \cdot \mathbf{e}_\alpha(\alpha)$  is the azimuthal component of the gauge field evaluated at the angular position  $\alpha$ .

The presence of  $\mathbf{A}(\mathbf{r})$  implies a gauge-invariant flux  $\Phi = R \oint d\alpha A(\alpha)$  piercing the ring interferometer and thus

modifying the free time evolution of the matter wave. The unitary time evolution operator becomes

$$U_\Phi(t) = V^\dagger \exp\left(i \frac{2\gamma\Phi}{\hbar} \frac{t}{T_{\text{rev}}} \frac{L_z}{\hbar}\right) U_0(t) V, \quad (3)$$

where  $V = \exp(-i\gamma\Phi\hat{\alpha}/2\pi\hbar + i\gamma R/\hbar \int_0^{\hat{\alpha}} d\alpha' A(\alpha'))$  can always be set to unity by choosing an appropriate gauge (symmetric gauge in the case of a constant field). Thus, a finite flux induces a rotation of the recurring wave packet by the Aharonov-Bohm-type phase  $2\gamma\Phi/\hbar$ .

For example, if the particles are electrically charged,  $\gamma = q$ , a magnetic flux  $\Phi$  through the ring will shift the energy levels [32,33] causing the wave packet to rotate. In a similar fashion, the Aharonov-Casher phase [34] can be measured if a magnetic dipole  $\mathbf{m} = m_0\mathbf{e}_z$  evolves in presence of the electrostatic field  $\mathbf{E}(\mathbf{R}\mathbf{e}_\rho) = E_0\mathbf{e}_\rho$  produced by a line charge. In this case one has  $\gamma\mathbf{A} = \mathbf{m} \times \mathbf{E}/c^2$ , implying  $\gamma\Phi = 2\pi R E_0 m_0/c^2$ . Likewise, geometric phases can result for a permanent or induced electric dipole  $\mathbf{p}$  in a magnetostatic field  $\mathbf{B}$ , so that  $\gamma\mathbf{A} = \mathbf{p} \times \mathbf{B}$  [35], or for a massive particle in a noninertial frame rotating with angular frequency  $\omega$  around the trap center, so that  $\gamma\mathbf{A} = mR^2\omega$ .

The presence of a weak external potential  $V(\alpha) = V_0 \cos(\alpha - \alpha_0)$ , such as that arising from a constant tilt of the ring, leads to phase dispersion. To leading order in  $V_0$ , the energies are shifted by

$$\Delta E_\ell^{(\text{pot})} \approx \frac{mR^2 V_0^2}{4\hbar^2} \left( \ell^2 - \frac{1}{4} \right)^{-1}. \quad (4)$$

Since this is not proportional to  $\ell^2$ , a conservative torque affects the shape of the recurring wave packet. This is in contrast to gauge fields, which only shift the position of the revival.

**Revivals in 3D torus traps.** The evolution of a particle in a real-world (three-dimensional) torus trap differs from the idealized situation described so far. The dynamics transverse to the ring tangent affect the angular dynamics even if the transverse motion remains in its ground state, since the centrifugal force distorts the level spacing. Shape imperfections and excitations of the transverse degrees of freedom can further affect the interference. We will show next that the proposed orbital angular momentum interference protocol is nevertheless surprisingly robust and remains feasible for realistic trap geometries.

To study the dynamics in a real-world torus trap, we expand the full 3D Hamiltonian of a particle in a torus trap and consider leading-order corrections in the transverse size of the wave packet. For this sake, we use a Frenet-Serret coordinate system  $(s, u, v)$  with arc length  $s$  and two transverse coordinates  $u, v$ . Thus, the position vector is  $\mathbf{r} = \mathbf{R}(s) + u\mathbf{n}(s) + v\mathbf{b}(s)$ , where  $\mathbf{R}(s)$  traces the center line of the torus trap, while  $\mathbf{n}(s) = \mathbf{R}''(s)/\kappa$  and  $\mathbf{b}(s) = \mathbf{R}'(s) \times \mathbf{n}(s)$  span the transverse plane at each position [36,37]. Here,  $\kappa = |\mathbf{R}''(s)|$  is the curvature, where prime denotes derivative with respect to  $s$ .

Since the new coordinate system  $(s, u, v)$  is curved, coordinate-space normalization of the wave function includes the root of the metric determinant (Jacobian)  $h$ . Expressing the latter as  $h = 1 - \kappa u$  and assuming that the trapping potential



is separable in the transverse direction yields the Hamiltonian [36,37]

$$H_s = -\frac{\hbar^2}{2m} \left[ \partial_s^2 \frac{\partial_s}{h^2} + \partial_u^2 + \partial_v^2 + \frac{\kappa^2}{4h^2} + \frac{5(h')^2}{4h^4} - \frac{h''}{2h^3} \right] + V_u(u) + V_v(v), \quad (5)$$

which acts on the rescaled wave function  $\chi = \sqrt{h}\psi$ .

If the radially confining potential is harmonic with frequency  $\omega_\perp$  and assuming that centrifugal distortions and small deviations from the ideal circular trap can be described by expanding the Hamiltonian to first order in the small quantities  $\kappa\sigma_u$ ,  $\kappa'\sigma_u/\kappa$ , and  $\kappa''\sigma_u/\kappa^2$  (with  $\sigma_u = \sqrt{\hbar/m\omega_\perp}$  the width of the transverse ground state),

$$H_s \approx -\frac{\hbar^2}{2m} \left[ (1 + 2\kappa u) \left( \partial_s^2 + \frac{\kappa^2}{4} \right) + 2\kappa' u (1 + 3\kappa u) \partial_s + \frac{\kappa'' u}{2} + \partial_u^2 + \partial_v^2 \right] + \frac{m\omega_\perp^2}{2} u^2 + V_v(v). \quad (6)$$

*Centrifugal energy corrections.* For an ideal torus where  $\kappa = 1/R$  the stationary Schrödinger equation becomes separable. It admits solutions of the form

$$\chi_{\ell kn}(s, u, v) = \frac{1}{\sqrt{2\pi R}} e^{i\ell s/R} \xi_{\ell k}(u) \Psi_n(v), \quad (7)$$

with eigenenergies  $E_{\ell kn} = \hbar^2 \ell^2 / 2mR^2 + E_{\ell k}^{(u)} + E_n^{(v)}$  where  $k, n \in \mathbb{N}_0$ . Here,  $\Psi_n(v)$  are normalized eigenstates of the harmonic motion out of the ring plane, whose eigenenergies  $E_n^{(v)}$  are independent of  $\ell$  and thus do not affect the revival structure of the matter wave.

The radially confining harmonic potential in the Schrödinger equation for  $\xi_{\ell k}(u)$  is centrifugally shifted by  $u_\ell = \hbar^2(\ell^2 - 1/4)/m^2\omega_\perp^2 R^3$ ,

$$\left[ -\frac{\hbar^2}{2m} \partial_u^2 + \frac{m\omega_\perp^2}{2} (u^2 + 2uu_\ell) \right] \xi_{\ell k}(u) = E_{\ell k}^{(u)} \xi_{\ell k}(u). \quad (8)$$

Thus, the eigenenergies

$$E_{\ell k}^{(u)} = \hbar\omega_\perp \left( k + \frac{1}{2} \right) - \frac{\hbar^4}{2m^3\omega_\perp^2 R^6} \left( \ell^2 - \frac{1}{4} \right)^2 \quad (9)$$

are lowered due to the centrifugal barrier.

The  $\ell$  dependence in the eigenenergies (9) can shift and diminish the revival. Specifically, the  $\ell^2$  term in Eq. (9) delays the revival without affecting its visibility, while the  $\ell^4$  correction decreases the fidelity of the revival and may further modify the revival time. The optimal recurrence time can be determined numerically from this equation.

*Shape imperfections.* In practice, deviations from the perfect circular shape of the torus trap are the most important source of imperfections for optical traps. In particular, residual astigmatism in the focusing optics may introduce a finite ellipticity to the trap, which can be quantified with the help of (6).

We replace the arc length with the eccentric anomaly  $\beta \in [-\pi, \pi)$  used for the standard parametrization of the ellipse. Thus,  $\partial_s = h_\varepsilon^{-1}(\beta) \partial_\beta / R$ , where  $R$  and  $\varepsilon$  are the semimajor axis and the eccentricity and  $h_\varepsilon(\beta) = \sqrt{1 - \varepsilon^2 \cos^2 \beta}$  is the Jacobi

determinant of the ellipse. In lowest order of  $\varepsilon$ , the Hamiltonian reads as  $H_\beta = h_\varepsilon^{1/2} H_s h_\varepsilon^{-1/2} \approx H_\beta^{(0)} + \varepsilon^2 H_\beta^{(\varepsilon)}$ , where  $H_\beta^{(0)}$  describes the motion on the circle and

$$H_\beta^{(\varepsilon)} = \frac{\hbar^2}{2mR^2} \left[ 1 + \frac{6u}{R} - 2 \left( 1 + \frac{5u}{R} \right) \cos(2\beta) \right] \partial_\beta^2 + \frac{\hbar^2}{2mR^2} \left( 1 + \frac{5u}{R} + \frac{9u^2}{R^2} \right) \sin(2\beta) \partial_\beta - \frac{\hbar^2}{16mR^2} \left[ 1 + \frac{3u}{R} - \left( 1 + \frac{11u}{R} \right) \cos(2\beta) \right]. \quad (10)$$

This implies that the eccentricity-induced energy shift reads in first-order perturbation theory

$$\Delta E_\ell^{(\varepsilon)} = \frac{\hbar^2 \varepsilon^2}{4mR^2} \left( 1 + \frac{3u_\ell}{R} \right) \left( \frac{1}{4} - \ell^2 \right). \quad (11)$$

Here we expressed the position expectation value of the radial state by the centrifugal shift of the harmonic potential (8),  $\langle u \rangle = -u_\ell$ . The first-order influence of a finite eccentricity is thus to decrease the revival time, while further diminishing the revival due to the  $\ell$  dependence of the radial potential minimum  $u_\ell$ .

*Implementation with BECs.* We are now in a position to argue that the orbital angular momentum interference scheme can be realistically carried out with weakly interacting BECs in an optical torus trap. For concreteness, we consider a condensate of  $^{39}\text{K}$  in a trap formed by two coaxial Gaussian beams, one repulsive and one attractive, intersected with an attractive light sheet, as in Ref. [19]. The wavelengths of the red- and blue-detuned laser beams are assumed to be 830 and 532 nm, respectively, with powers of 2 and 2.5 mW as well as waists of 13 and 5.5  $\mu\text{m}$ . The light sheet with the same wavelength as the red-detuned laser has a power of 10 mW and waists of 5 and 200  $\mu\text{m}$ , so that the trap radius is  $R \approx 5.9 \mu\text{m}$  and the transverse confining frequency  $\omega_\perp \approx 6.4 \text{ kHz}$ . The necessary coherence time of  $T_{\text{rev}} \approx 135 \text{ ms}$  is experimentally within reach [8].

Figure 2 shows the simulated dynamics of the orbital angular momentum interference protocol for (a) a noninteracting and (b) a weakly interacting BEC of  $N = 2 \times 10^4$   $^{39}\text{K}$  atoms. We assume in both cases that the Feshbach resonances of  $^{39}\text{K}$  [38] are used to make the interactions (a) negligibly small or (b) equivalent to a scattering length of one Bohr radius. The tightly confined initial wave packet, loaded from three-dimensional harmonic trap of frequency  $\omega_\perp$ , quickly disperses around the torus. It then reappears in a superposition after approximately 65 ms. The presence of interactions diminishes the revival signal. However, even at a realistic transverse confinement and interaction strength, the effect is still clearly visible in the population imbalance displayed in panel (c). The latter shows that the interference visibility exhibits almost the ideal dependence on the imprinted phase. The numerical calculations are based on the Trotter-Suzuki expansion [39–41].

For this setup, the centrifugal energy shift (9) amounts to a few percent of the rotational energy for the highest-populated  $\ell$  eigenstates ( $\ell \simeq 25$ ). The corresponding correction to the revival time is at a permille level, but, given the quick dispersion time, exact timing on the scale of a few microseconds is required to imprint the phase and to observe the revival.

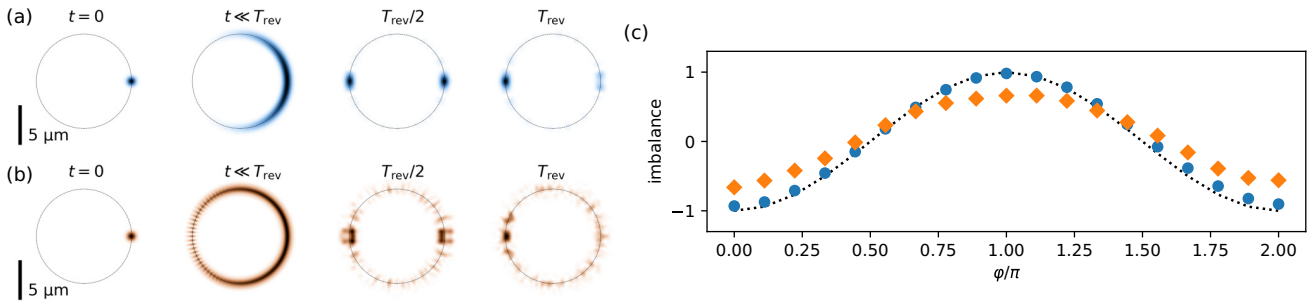


FIG. 2. Mean-field simulation of the interference scheme shown in Fig. 1(a) realized with a BEC of  $^{39}\text{K}$  in an optical trap. (a) Snapshots of the time evolution for a noninteracting condensate: initial particle density, dispersion, recurrent superposition at half of the revival time, and final interferometrically controlled revival with  $\varphi = \pi/3$ . The external phase of  $\exp(i\varphi \cos^2 \alpha)$  is applied on the left part of the ring at  $T_{\text{rev}}/2$ . The revival time  $T_{\text{rev}} \approx 135.8$  ms is found by maximizing the overlap between the initial and final states for  $\varphi = 0$ . (b) As in (a) but with interatomic interactions characterized by the scattering length of one Bohr radius for a BEC of  $N = 2 \times 10^4$  atoms. As a result of the interactions the revival time changes to  $T_{\text{rev}} \approx 136.2$  ms. (c) Interference signal as a function of external phase  $\varphi$  in the noninteracting [as in (a), circles] and interacting [as in (b), diamonds] cases, as compared to the ideal situation (dotted line). The population imbalance is defined as  $(N_R - N_L)/(N_R + N_L)$ , where  $N_R$ ,  $N_L$  are the numbers of atoms on the right and left sides of the ring, weighted with  $\cos^2 \alpha$ .

In a similar fashion, the corrections of the revival time due to interactions must be accounted for, as has been done numerically in Fig. 2(a).

The relative phase  $\varphi$  can be imprinted, e.g., optically, via tilting of the apparatus, or via induced interatomic interactions. For example, if the trap is briefly tilted at  $T_{\text{rev}}/2$  the gravitational potential yields the phase  $\varphi_g \approx 2mgRt_d \sin \theta / \hbar$ , where  $\theta$  is the tilt angle and  $t_d$  is the revival lifetime. The latter is the dispersion timescale  $t_d \approx 1/\omega_{\perp}$  of the initial wave packet of width  $\sqrt{\hbar/\omega_{\perp}m}$ . For the above example, this requires tilting with a precision of hundreds of microradians.

Likewise, if the magnetic field on one side of the ring is detuned from the zero crossing of the Feshbach resonance, the matter wave acquires a relative phase  $\varphi_a \approx 4\pi \hbar a n_{\text{BEC}} t_d / m$ , where  $a$  is the induced scattering length and  $n_{\text{BEC}}$  is the particle density in the initial state. With this one can measure the scattering length with precision  $\Delta a \approx 0.2a_0$  (with  $a_0$  the Bohr radius), on par with state-of-the-art time-of-flight [42] and spectroscopic [43] measurements for  $^{39}\text{K}$ .

**Conclusions.** We introduced orbital angular momentum interference as an attractive platform for trapped matter-wave interferometry in toroidal geometries. Since the proposed

scheme relies on the universal property of orbital momentum quantization, realizations with many different systems can be readily envisioned, e.g., single atoms or BECs in optical traps, ions in electric traps, electrons in solid state quantum rings, as well as molecules and nanoparticles in optical or electrical traps. For the case of a BEC in an optical trap, we have shown that the protocol is feasible with present-day technology.

The interference effect is sensitive to the presence of gauge fields. In the presence of a magnetic field flux  $\Phi$ , for instance, the revival of particles with charge  $q$  will be displaced by the angle  $2q\Phi/\hbar$ . Assuming that displacements on the size of the initial wave packet can be angularly resolved, fields below  $10^{-7}$  T level can be detected with the setup described above.

**Acknowledgments.** We thank Markus Arndt, Thorsten Schumm, and Philipp Haslinger for helpful discussions. F.K. acknowledges support by the Austrian Science Fund (FWF) Project No. W1210-N25, B.A.S. acknowledges funding from the European Union's Horizon 2020 research and innovation programme under the Marie Skłodowska-Curie grant agreement No. 841040.

- [1] Y.-J. Wang, D. Z. Anderson, V. M. Bright, E. A. Cornell, Q. Diot, T. Kishimoto, M. Prentiss, R. A. Saravanan, S. R. Segal, and S. Wu, Atom Michelson Interferometer on a Chip Using a Bose-Einstein Condensate, *Phys. Rev. Lett.* **94**, 090405 (2005).
- [2] O. Garcia, B. Deissler, K. J. Hughes, J. M. Reeves, and C. A. Sackett, Bose-Einstein-condensate interferometer with macroscopic arm separation, *Phys. Rev. A* **74**, 031601(R) (2006).
- [3] M. Horikoshi and K. Nakagawa, Suppression of Dephasing Due to a Trapping Potential and Atom-Atom Interactions in a Trapped-Condensate Interferometer, *Phys. Rev. Lett.* **99**, 180401 (2007).
- [4] M. Karski, L. Förster, J.-M. Choi, A. Steffen, W. Alt, D. Meschede, and A. Widera, Quantum walk in position space with single optically trapped atoms, *Science* **325**, 174 (2009).
- [5] T. Berrada, S. van Frank, R. Bücke, T. Schumm, J.-F. Schaff, and J. Schmiedmayer, Integrated Mach-Zehnder interferometer for Bose-Einstein condensates, *Nat. Commun.* **4**, 2077 (2013).
- [6] B. Rauer, S. Erne, T. Schweigler, F. Cataldini, M. Tajik, and J. Schmiedmayer, Recurrences in an isolated quantum many-body system, *Science* **360**, 307 (2018).
- [7] E. Urban, N. Glikin, S. Mouradian, K. Krimmel, B. Hemmerling, and H. Häefner, Coherent Control of the Rotational Degree of Freedom of a Two-Ion Coulomb Crystal, *Phys. Rev. Lett.* **123**, 133202 (2019).
- [8] V. Xu, M. Jaffe, C. D. Panda, S. L. Kristensen, L. W. Clark, and H. Müller, Probing gravity by holding atoms for 20 seconds, *Science* **366**, 745 (2019).



- [9] O. Zobay and B. M. Garraway, Two-Dimensional Atom Trapping in Field-Induced Adiabatic Potentials, *Phys. Rev. Lett.* **86**, 1195 (2001).
- [10] T. A. Bell, J. A. P. Glidden, L. Humbert, M. W. J. Bromley, S. A. Haine, M. J. Davis, T. W. Neely, M. A. Baker, and H. Rubinsztein-Dunlop, Bose-Einstein condensation in large time-averaged optical ring potentials, *New J. Phys.* **18**, 035003 (2016).
- [11] J. L. Ville, T. Bienaimé, R. Saint-Jalm, L. Corman, M. Aidelburger, L. Chomaz, K. Kleinlein, D. Perconte, S. Nascimbène, J. Dalibard, and J. Beugnon, Loading and compression of a single two-dimensional Bose gas in an optical accordion, *Phys. Rev. A* **95**, 013632 (2017).
- [12] S. Pandey, H. Mas, G. Drougakis, P. Thekkepatt, V. Bolpasi, G. Vasilakis, K. Poullos, and W. von Klitzing, Hypersonic Bose-Einstein condensates in accelerator rings, *Nature (London)* **570**, 205 (2019).
- [13] S. Gupta, K. W. Murch, K. L. Moore, T. P. Purdy, and D. M. Stamper-Kurn, Bose-Einstein Condensation in a Circular Waveguide, *Phys. Rev. Lett.* **95**, 143201 (2005).
- [14] C. Ryu, M. F. Andersen, P. Cladé, V. Natarajan, K. Helmerson, and W. D. Phillips, Observation of Persistent Flow of a Bose-Einstein Condensate in a Toroidal Trap, *Phys. Rev. Lett.* **99**, 260401 (2007).
- [15] A. Ramanathan, K. C. Wright, S. R. Muniz, M. Zelan, W. T. Hill, C. J. Lobb, K. Helmerson, W. D. Phillips, and G. K. Campbell, Superflow in a Toroidal Bose-Einstein Condensate: An Atom Circuit With a Tunable Weak Link, *Phys. Rev. Lett.* **106**, 130401 (2011).
- [16] A. Das, J. Sabbatini, and W. H. Zurek, Winding up superfluid in a torus via Bose-Einstein condensation, *Sci. Rep.* **2**, 352 (2012).
- [17] S. Eckel, J. G. Lee, F. Jendrzejewski, N. Murray, C. W. Clark, C. J. Lobb, W. D. Phillips, M. Edwards, and G. K. Campbell, Hysteresis in a quantized superfluid ‘atomtronic’ circuit, *Nature (London)* **506**, 200 (2014).
- [18] S. Eckel, A. Kumar, T. Jacobson, I. B. Spielman, and G. K. Campbell, A Rapidly Expanding Bose-Einstein Condensate: An Expanding Universe in the Lab, *Phys. Rev. X* **8**, 021021 (2018).
- [19] G. E. Marti, R. Olf, and D. M. Stamper-Kurn, Collective excitation interferometry with a toroidal Bose-Einstein condensate, *Phys. Rev. A* **91**, 013602 (2015).
- [20] S. Ragole and J. M. Taylor, Interacting Atomic Interferometry for Rotation Sensing Approaching the Heisenberg Limit, *Phys. Rev. Lett.* **117**, 203002 (2016).
- [21] J. L. Helm, T. P. Billam, A. Rakonjac, S. L. Cornish, and S. A. Gardiner, Spin-Orbit-Coupled Interferometry with Ring-Trapped Bose-Einstein Condensates, *Phys. Rev. Lett.* **120**, 063201 (2018).
- [22] R. W. Robinett, Quantum wave packet revivals, *Phys. Rep.* **392**, 1 (2004).
- [23] T. Seideman, Revival Structure of Aligned Rotational Wave Packets, *Phys. Rev. Lett.* **83**, 4971 (1999).
- [24] M. Spanner, E. A. Shapiro, and M. Ivanov, Coherent Control of Rotational Wave-Packet Dynamics Via Fractional Revivals, *Phys. Rev. Lett.* **92**, 093001 (2004).
- [25] M. D. Poulsen, E. Peronne, H. Stapelfeldt, C. Z. Bisgaard, S. S. Viftrup, E. Hamilton, and T. Seideman, Nonadiabatic alignment of asymmetric top molecules: Rotational revivals, *J. Chem. Phys.* **121**, 783 (2004).
- [26] A. S. Moskalenko, A. Matos-Abiague, and J. Berakdar, Revivals, collapses, and magnetic-pulse generation in quantum rings, *Phys. Rev. B* **74**, 161303(R) (2006).
- [27] B. A. Stickler, B. Papendell, S. Kuhn, B. Schirski, J. Millen, M. Arndt, and K. Hornberger, Probing macroscopic quantum superpositions with nanorotors, *New J. Phys.* **20**, 122001 (2018).
- [28] P. Navez, S. Pandey, H. Mas, K. Poullos, T. Fernholz, and W. von Klitzing, Matter-wave interferometers using TAAP rings, *New J. Phys.* **18**, 075014 (2016).
- [29] G. Pelegrí, J. Mompart, and V. Ahufinger, Quantum sensing using imbalanced counter-rotating Bose-Einstein condensate modes, *New J. Phys.* **20**, 103001 (2018).
- [30] V. M. Fomin, *Physics of Quantum Rings* (Springer, Berlin, 2013).
- [31] J. Millen, T. S. Monteiro, R. Pettit, and A. N. Vamivakas, Optomechanics with levitated particles, *Rep. Prog. Phys.* **83**, 026401 (2020).
- [32] G. A. Vugalter, A. K. Das, and V. A. Sorokin, A charged particle on a ring in a magnetic field: Quantum revivals, *Eur. J. Phys.* **25**, 157 (2003).
- [33] A. Lorke, R. J. Johannes Luyken, A. O. Govorov, J. P. Kotthaus, J. M. Garcia, and P. M. Petroff, Spectroscopy of Nanoscopic Semiconductor Rings, *Phys. Rev. Lett.* **84**, 2223 (2000).
- [34] Y. Aharonov and A. Casher, Topological Quantum Effects for Neutral Particles, *Phys. Rev. Lett.* **53**, 319 (1984).
- [35] H. Wei, R. Han, and X. Wei, Quantum Phase of Induced Dipoles Moving in a Magnetic Field, *Phys. Rev. Lett.* **75**, 2071 (1995).
- [36] P. Leboeuf and N. Pavloff, Bose-Einstein beams: Coherent propagation through a guide, *Phys. Rev. A* **64**, 033602 (2001).
- [37] S. Schwartz, M. Cozzini, C. Menotti, I. Carusotto, P. Bouyer, and S. Stringari, One-dimensional description of a Bose-Einstein condensate in a rotating closed-loop waveguide, *New J. Phys.* **8**, 162 (2006).
- [38] C. Chin, R. Grimm, P. Julienne, and E. Tiesinga, Feshbach resonances in ultracold gases, *Rev. Mod. Phys.* **82**, 1225 (2010).
- [39] C. S. Bederián and A. D. Dente, Boosting quantum evolutions using Trotter-Suzuki algorithms on GPUs, in *Proceedings of HPCLatAm-11, 4th High-Performance Computing Symposium*, edited by N. Wolovick and G. Hernández (Sociedad Argentina de Informática (SADIO), Buenos Aires, 2011), pp. 63–75.
- [40] P. Wittek and F. M. Cucchietti, A second-order distributed Trotter-Suzuki solver with a hybrid CPU-GPU kernel, *Comput. Phys. Commun.* **184**, 1165 (2013).
- [41] P. Wittek and L. Calderaro, Extended computational kernels in a massively parallel implementation of the Trotter-Suzuki approximation, *Comput. Phys. Commun.* **197**, 339 (2015).
- [42] C. D’Errico, M. Zaccanti, M. Fattori, G. Roati, M. Inguscio, G. Modugno, and A. Simoni, Feshbach resonances in ultracold  $^{39}\text{K}$ , *New J. Phys.* **9**, 223 (2007).
- [43] S. Falke, H. Knöckel, J. Friebe, M. Riedmann, E. Tiemann, and C. Lisdat, Potassium ground-state scattering parameters and Born-Oppenheimer potentials from molecular spectroscopy, *Phys. Rev. A* **78**, 012503 (2008).